TECHNISCHE UNIVERSITÄT MÜNCHEN

Lehrstuhl für Numerische Mechanik

A Computational Approach to Coupled Poroelastic Media Problems

Anh-Tu Vuong

Vollständiger Abdruck der von der Fakultät für Maschinenwesen der Technischen Universität München zur Erlangung des akademischen Grades eines

Doktor-Ingenieurs (Dr.-Ing.)

genehmigten Dissertation.

Vorsitzender: Univ.-Prof. Dr.-Ing. Veit Senner

Prüfer der Dissertation:

1. Univ.-Prof. Dr.-Ing. Wolfgang A. Wall
2. Univ.-Prof. Bernhard Schrefler, Ph.D.
   Università degli Studi di Padova, Italien

Die Dissertation wurde am 18. Mai 2016 bei der Technischen Universität München eingereicht und durch die Fakultät für Maschinenwesen am 19. November 2016 angenommen.

Abstract

Porous media problems are very common in many fields of engineering. Classical applications can be found in civil engineering and geomechanics, where fluid flow through soil or other porous structures is considered. Material sciences, lightweight engineering and chemical engineering may serve as further examples. Of particular interest in this work is the huge potential of porous media approaches to models in biomechanics. In this thesis, a computational approach to saturated porous media problems is presented. Therein, large deformations in two- and three-dimensional settings are considered. The porous flow field is either governed by the Darcy or the Darcy-Brinkman equation. Special emphasis lies on a formulation capable of using different constitutive laws and at the same time incorporating a full coupling of the two phases. An arbitrary potential-based strain energy represents the material behavior. The coupling comprises varying flow resistance caused by changes of the porosity and permeability and additional mechanical stresses within the solid phase in accordance with the loading state of the fluid. The complete set of partial differential equations is discretized with the finite element method. The resulting system of non-linear equations is solved by a Newton-Raphson scheme using a monolithic approach, accounting for the strongly coupled nature of the problem.

One of the main contributions of this thesis comprises different forms of the finite element discretization. Darcy-Brinkman flow with large deformations of the skeleton requires an accurate evaluation of the spatial gradient of the porosity. The influence of those porosity variations on the convergence behavior of the numerical solution scheme is investigated and based on this, two suitable approaches are proposed: an isogeometric approach using the C^1-continuity of NURBS functions and a mixed approach, directly discretizing the porosity. It is shown that both approaches fulfill the necessary requirements for convergence. Furthermore, a special technique to include complex boundary conditions into the monolithic system via the (dual) Lagrange multiplier method is discussed. The degrees of freedom associated with the Lagrange multipliers are condensed out of the linear system, restoring the original system size. Also, a novel volume coupling approach is applied to the fluid and skeleton problem to enable non-matching volume discretizations.

The second major part of this thesis is dedicated to the extension to multi-field problems. The coupling between Navier-Stokes flow and a porous medium is demonstrated. The finite element framework is enriched by this additional problem scenario by introducing the corresponding balance equation and sensible conservation constraints, most importantly the Beavers-Joseph condition. The second example of a multi-field problem is the interaction between a porous medium and an impervious solid. The considered constraints are either a static mesh tying or a dynamic contact zone scenario. Both coupling constraints are established with the dual Lagrange multiplier method, well-known from mesh tying and contact solid mechanics. The respective conditions for the porous fluid at the interface are formulated and enforced in a consistent manner. Additionally, the governing equations for transport within a porous medium are formulated and solved within a partitioned scheme. This methodology is included in a new model for pericellular proteolysis. It comprised a computational model for the interaction of surface- and volume-bound scalar transport and reaction processes with a deformable porous medium. The model is applied to a special form of a mechanical-biochemical coupling phenomenon in cell and tissue mechanics, originating from the degradation process of a strained extracellular matrix.

Zusammenfassung

Poröse Medien sind in vielen Gebieten des Ingenieurwesens sehr verbreitet. Klassische Anwendungsgebiete finden sich im Bauingenieurwesen und der Geomechanik, worin Strömungen durch Böden und anderen Strukturen betrachtet werden. Materialwissenschaften, Leichtbau und Chemieingenieurwesen sind weitere Beispiele. In dieser Arbeit sind die vielfältigen Anwendungsmöglichkeiten im Bereich der Biomechanik von besonderem Interesse. Im Rahmen der vorliegenden Arbeit wird ein numerisches Lösungsverfahren zur Analyse gesättigter poröser Medien entwickelt. Dabei werden zwei- und drei-dimensionale Probleme unter großen Deformationen betrachtet. Die poröse Strömung wird entweder durch die Darcy- oder die Darcy-Brinkman-Gleichung beschrieben. Ein besonderer Fokus liegt hierbei auf einer Formulierung, in welcher ist verschiedenste komplexe konstitutive Beziehungen verwendet werden können als auch die vollständige Kopplung der beiden Phasen berücksichtigt ist. Ein allgemeinenes, Potential-basiertes Materialgesetz modelliert das Materialverhalten. Die Kopplung beinhaltet einen veränderlichen Strömungswiderstand, der durch Variationen der Porosität und der Permeabilität hevorgerufen wird und ebenso komplexe, interagierende Spannungszustände innerhalb beider Phasen. Die partiellen Differentialgleichungen werden mittels der Finiten Elemente Methode diskretisiert. Das entstandene nicht-lineare Gleichungssystem wird unter Berücksichtigung der starken Kopplung der Felder innerhalb eines monolithischen Ansatzes mit der Newton-Raphson Methode gelöst.

Ein Hauptaspekt dieser Arbeit besteht in der Analyse verschiedener Formen der Finite Elemente Diskretisierung. Die Kopplung zwischen der Darcy-Brinkman Strömung und großen Deformationen des porösen Skeletts erfordern eine korrekte Auswertung von räumlichen Gradienten der Porosität. Der Einfluss dieser Porositätsvariationen auf das Konvergenzverhalten des numerischen Ansatzes wird analysiert und auf dessen Basis zwei passende Formulierungen vorgeschlagen: ein isogeometrischer Ansatz, der die C^1-Kontinuität von NURBS Funktionen verwendet, und ein gemischter Ansatz, in welchem die Porosität separat approximiert wird. Es wird gezeigt, dass beide Ansätze die notwendigen Konvergenzkriterien erfüllen. Außerdem wird eine Technik zur Aufbringung komplexer Randbedingungen mittels der (dualen) Lagrange-Multiplikator-Methode diskutiert. Die zusätzlichen Freiheitsgrade des Lagrange Multiplikators werden aus dem linearen Gleichungssystem auskondensiert, womit die ursprüngliche Problemgröße erhalten bleibt. Zusätzlich wird ein neuer Ansatz zur Volumenkopplung, welcher nicht passende Volumendiskretisierungen ermöglicht, auf das vorliegende Fluid-Struktur Interaktionsproblem angewandt.

Der zweite Teil der vorliegenden Arbeit befasst sich mit der Erweiterung in Richtung Mehrfeldproblemen. Die Kopplung zwischen einer Navier-Stokes Strömung und einem porösen Medium wird vorgestellt. Die Finite Elemente Formulierung wird durch Integration der zugehörigen Bilanz- und Erhaltungsgleichungen, insbesondere der Beavers-Joseph Gleichung, um diese Problemstellung erweitert. Das zweite Beispiel eines Mehrfeldproblems ist die Interaktion zwischen einem porösem Medium und einer undurchlässigen Struktur. Die Nebenbedingungen sind hierbei entweder eine statische Netzkopplung oder ein dynamisches Kontaktproblem. Beide Bedingungen werden mittels der insbesondere aus der Strukturmechanik bekannten, dualen Lagrange-Multiplikator-Methode erfüllt. Die zugehörigen Bedingungen auf der Grenzfläche werden hierbei auf einer konsistenten Art und Weise erfüllt. Außerdem werden die Bilanzgleichungen für den Transport skalarer Größen innerhalb eines porösen Mediums vorgestellt und mittels eines

partitionierten Verfahrens gelöst. Dieser Lösungsansatz ist Teil eines neuen Modells für perizelluläre Proteolyse. Letzteres beinhaltet zusätzlich die Interaktion von Oberflächen- und Volumengebundenen skalaren Größen und deren Reaktionen mit einem deformierenden porösen Medium. Dieses Modell wird für eine spezielle Form eines mechanisch-biochemischen Kopplungsphänomens – dem Degradationsprozess einer gedehnten extrazellulären Matrix – angewandt.

Contents

Nomenclature

Abbreviations

ALE	Arbitrary-Lagrangean-Eulerian
B-spline	Basis spline
CAD	Computer Aided Design
FE	Finite Element
FEM	Finite Element Method
FPSI	Fluid-Porous-Structure Interaction
FSI	Fluid-Structure Interaction
GMRES	Generalized Minimal Residual
IBVP	Initial Boundary Value Problem
NURBS	Non-Uniform Rational Basis Spline
PSPG	Pressure Stabilizing Petrov-Galerkin
REV	Representative Elementary Volume
SUPG	Streamline Upwind Petrov-Galerkin
TCAT	Thermodynamically Constrained Averaging Theory

Configurations, Domains and Boundaries

Γ^{c}	Constrained boundary
Γ_t^{D}	Dirichlet boundary in current configuration
Γ_t^{N}	Neumann boundary in current configuration
Γ_0^{D}	Dirichlet boundary in material configuration
Γ_0^{N}	Neumann boundary in material configuration
χ	Mapping between reference and material configuration
Ω_t	Current configuration
Ω_0	Material configuration
Ω_{R}	Reference configuration
Ξ	Mapping between reference and current configuration

Continuum Mechanics

α_{BJ}	Beavers-Joseph coefficient
Γ_t	Current boundary
$\mathrm{d}\boldsymbol{X}$	Infinitesimal line element in material configuration
$\mathrm{d}\boldsymbol{x}$	Infinitesimal line element in current configuration
$\mathrm{d}\boldsymbol{A}$	Infinitesimal area element in material configuration

$\mathrm{d}\boldsymbol{a}$	Infinitesimal area element in current configuration
$\boldsymbol{\varepsilon}$	Deformation rate
ΔA	Surface Area
δ_{ij}	Kronecker delta
$\dot{\boldsymbol{E}}$	Rate of Green-Lagrange strain
η	Penalty parameter
κ	Bulk modulus
λ^{s},μ^{s}	Lamé coefficients
φ	Motion of body
μ^{f}	Dynamic viscosity
ν	Poisson's ratio
p^{f}	Fluid pressure
Φ	Dissipation
ϕ	Current porosity
Φ^{th}	Thermal part of Helmholtz free energy
Ψ	Strain energy function
$\boldsymbol{Q}^{\mathrm{th}}$	Material heat flux
$\boldsymbol{q}^{\mathrm{th}}$	Current heat flux
ρ	Current density
ρ_0	Material density
σ	Reaction term
$\boldsymbol{\sigma}^{\mathrm{f}}_{\mathrm{visc}}$	Viscous part of fluid Cauchy stress
$\mathbf{1}$	Identity tensor
$\boldsymbol{\sigma}$	Cauchy stress tensor
$\boldsymbol{a}$	Current acceleration
$\boldsymbol{b}$	Body force
$\boldsymbol{b}_{\mathrm{B}}$	Biot tangent
$\boldsymbol{C}$	Right Cauchy-Green deformation tensor
$\boldsymbol{C}_{\mathrm{mat}}$	Material tangent
$\boldsymbol{d}$	Displacement
$\boldsymbol{E}$	Green-Lagrange strain tensor
$\boldsymbol{F}$	Deformation gradient
$\boldsymbol{f}$	Force vector
$\boldsymbol{K}$	Material permeability
$\boldsymbol{k}$	Current permeability
$\boldsymbol{N}$	Material outward pointing normal
$\boldsymbol{n}$	Current outward pointing normal
$\boldsymbol{P}$	First Piola-Kirchhoff stress tensor
$\boldsymbol{q}$	Current flux
$\boldsymbol{S}$	Second Piola-Kirchhoff stress tensor
$\boldsymbol{T}$	Material boundary traction
$\boldsymbol{t}$	Current boundary traction
$\boldsymbol{v}$	Current velocity
$\boldsymbol{X}$	Material Coordinate
$\boldsymbol{x}$	Current Coordinate

$\boldsymbol{v}^{\mathrm{c}}$	Convective velocity
$\boldsymbol{v}^{\mathrm{g}}$	Grid ALE velocity
$\boldsymbol{W}^{\mathrm{f}}$	Material relative fluid mass flux
$\boldsymbol{w}^{\mathrm{f}}$	Current relative fluid mass flux
$\boldsymbol{\mathcal{X}}$	Reference Coordinate
c	Scalar quantity
D	Diffusivity
E	Young's modulus
e	Internal specific energy
E_0	Material energy density
g	Specific free enthalpy/Gibbs potential
h	Specific enthalpy
J	Determinant of the deformation gradient
M	Molar mass
m	Mass
N	Biot modulus
P_{int}	Inner mechanical power
S	Material entropy
s	Specific entropy
T	Temperature
W_{ti}	Total internal energy

Computational Solution Approach

α_{f}, α_{m}, γ, β, ρ_∞	Parameter of generalized-α time integration scheme
Δt	Time step size
$\mathbf{d}^{\mathrm{s}}_k$	Nodal displacement of node k
$\mathbf{d}^{\mathrm{s}}$	Global nodal displacement
$\mathbf{p}^{\mathrm{f}}_k$	Nodal fluid pressure of node k
$\mathbf{p}^{\mathrm{f}}$	Global nodal fluid pressure
$\boldsymbol{\phi}_k$	Nodal porosity of node k
$\mathbf{v}^{\mathrm{f}}_k$	Nodal fluid velocity of node k
$\mathbf{v}^{\mathrm{f}}$	Global nodal fluid velocity
$\mathbf{X}$	Global nodal current coordinates
$\mathbf{x}$	Global nodal current coordinates
$\mathbf{X}_{,k}$	Material coordinate displacement of node k
$\mathbf{x}_{,k}$	Current coordinate displacement of node k
B^d_i	i-th B-spline basis function of order p
N_k	Shape function of node k
R^p_i	i-th NURBS basis function of order p
$\mathbf{C}(u)$	NURBS curve
$\mathbf{N}$	Matrix of shape functions
$\mathbf{S}(u,v)$	NURBS surface
$\mathbf{u}$	Knot vector for definition of B-spline polynomial
$\boldsymbol{d}^{\mathrm{s,h}}$	Global approximation of the displacement field

$\boldsymbol{X}^{\mathsf{h}}$	Global approximation of the material coordinate
$\boldsymbol{x}^{\mathsf{h}}$	Global approximation of the current coordinate
$\lambda, \boldsymbol{\lambda}$	Lagrange multiplier
$\mu^{\mathrm{s}}_{\mathrm{eff}}$	Effective shear modulus of the skeleton
$\mathrm{n}_{\mathrm{ele}}$	Number of elements of spatial discretization
$\mathrm{n}_{\mathrm{node}}$	Number of nodes of spatial discretization
ω_i	i-th weight of NURBS basis function
$p^{\mathrm{f},\mathsf{h}}$	Global approximation of the fluid pressure field
ϕ^{h}	Global approximation of the porosity field
ϵ^{s}, ϵ^{f}	Tolerances of Newton-Scheme
τ_{B}	Stabilization parameter for stabilization of Biot system
τ_{M}	Stabilization parameter for PSPG and stabilization due to reactive term
θ	Parameter of one-step-θ time integration scheme
$\boldsymbol{v}^{\mathrm{f},\mathsf{h}}$	Global approximation of the fluid velocity field
h	Characteristic element size

Indizes

$(\bullet)^{\mathrm{f}}$	Averaged fluid phase
$(\bullet)^{\mathrm{s}}$	Averaged solid phase
$(\bullet)^{\mathsf{h}}$	Spatially discretized quantity
$(\bullet)_{\mathrm{NH}}$	Neo-Hooke
$(\bullet)_{\mathrm{SVK}}$	Saint–Venant–Kirchhoff
$(\bullet)_{\mathrm{in}}$	Intrinsic quantity
$(\bullet)_n$	Quantity evaluated at discrete time t_n
$(\bullet)^{\mathrm{s}}$	Macroscopic solid/skeleton phase

Dimensionless Numbers

C	Courant number
Da	Darcy number
Pe_e	Element Péclet number
Re	Reynolds number
St	Strouhal number

Operators

$\det(\bullet)$	Determinant of $(\bullet)$
$\boldsymbol{\nabla}\cdot$	Current divergence
$\boldsymbol{\nabla}_0\,\cdot$	Material divergence
$\boldsymbol{\nabla}$	Current gradient
$\boldsymbol{\nabla}_0$	Material Gradient
$\overset{\circ}{(\bullet)} = \left.\dfrac{\partial(\bullet)}{\partial t}\right\vert_{\boldsymbol{X}}$	Time derivative with fixed material skeleton coordinate
$\otimes$	Dyadic product

$\left.\dfrac{\partial(\bullet)}{\partial t}\right\vert_{\boldsymbol{x}}$	Partial time derivative of $(\bullet)$ with respect to reference coordinate
$(\bullet)^{-1}$	Inverse of $(\bullet)$
$(\bullet)^{-1}$	Transpose of $(\bullet)$
$(\bullet)^{-\mathrm{T}}$	Inverse of transpose of $(\bullet)$
$\dfrac{\mathrm{d}(\bullet)}{\mathrm{d}t} = \dot{(\bullet)}$	Total/material time derivative of $(\bullet)$
$\dfrac{\mathrm{d}^{\mathrm{f}}(\bullet)}{\mathrm{d}t}$	Total time derivative of $(\bullet)$ with respect to fluid phase
$\dfrac{\mathrm{d}^{\mathrm{s}}(\bullet)}{\mathrm{d}t}$	Total time derivative of $(\bullet)$ with respect to skeleton phase
$\mathrm{tr}\,(\bullet)$	Trace of $(\bullet)$

1. Introduction

1.1. Motivation

In principle, every material on earth is porous. It all depends on how close you look at it. The pores of a sponge are visible to the naked eye and its remarkable mechanical integrity is noticeable when squeezed. Ranging from atomic to geodesic scales, examples of porous structures can be found everywhere. Some examples are depicted in Figure 1.1. The fragility of limestone is based on its porous nature, and one reason why the hydrological cycle on earth is working are porous sands and voids within soil, granting space for groundwater to flow. Also seemingly solid and compact materials like stone and metal do actually exhibit an internal structure on a very small scale. In many cases it is still very sensible to model such materials as one-component solids. If the pores are closed and not interconnected, representing the whole solid by a macroscopic material law is most often reasonable. In a way, the material properties are 'smeared' over the solid body and its pores. However, a too 'coarse' description might lead to neglecting some potentially decisive effects. Microscopic pores and cracks can have a significant influence on the macroscopic behavior and could cause, for instance, damage and eventually failure. Even more than dead material, living matter exhibits porous characteristics. Virtually all kinds of biological substances display a large volume fraction filled with fluid. The actual solid phase is a complex of interlinked fibers. They provide stability and at the same time leave sufficient space for water or blood to flow. This mechanism is crucial for the transport of nutrients to supply organs within the vascular systems of animals and plants. Such systems can be observed in the trunk of a tree as well as on a cellular scale within the fiber matrix composing any kind of tissue.

Clearly, just as porous media can frequently be found in nature, they are also omnipresent in engineering. Experiments analyzing natural and artificial porous structures have been performed for almost two centuries, and also theoretical investigations are an intrinsic part of continuum mechanics theory. Classical applications range from civil engineering and soil mechanics to material sciences and lightweight structures in aerospace applications and battery models in chemical engineering. Therein, macroscopic descriptions of the material behavior resulting from a porous structure are developed and applied to the physical system at hand. Besides elastodynamics, such investigations can also include the analysis of flow and transport phenomena. The interplay of deformation and flow within are porous system is called consolidation. Naturally, the theory of consolidation has a huge impact on biomechanics, where mechanical theory is applied to biological systems. Such models in particular have become increasingly large and complex. The non-linear, coupled systems arising from these models are impossible to solve analytically. This emphasizes the necessity to investigate computational models for porous media mechanics, which is the topic of this thesis.

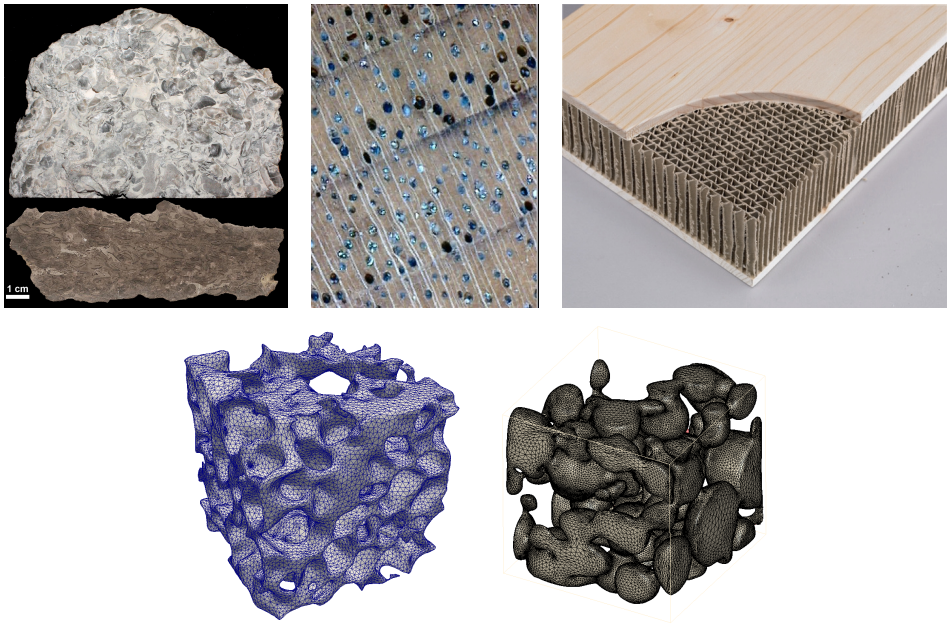

Figure 1.1: Porous media in nature and engineering. Top row (left to right): limestone [2], magnified cross section of wood [3], lightweight structure [1]. Bottom row (left to right): reconstructed tomography scan of alveolar microstructure [208], X-ray-scan of porous electrode battery structure.

1.2. Fundamental Approaches to Porous Media Modeling and Simulation

In the last view decades porous media problems have gained more and more attention in various fields of engineering. Some examples will be listed in the following. In geophysics such problems occur for example in melting of ice or snow layers [176]. Additionally, the analysis of seismic attenuation [165] is of interest in this field. In civil engineering, applications include flow in porous media, e.g. when analyzing seepage through soil, walls of water reservoirs, embankments or dams [105, 106]. In chemical engineering, such approaches are used to model fluid-solid reaction [213], mass and heat transfer through membranes in fuel cells [263] or in packed-bed reactor columns [178]. Also, a large number of models for acoustic and poroelastic wave propagation have been developed [136, 167]. In biomechanics, porous media models have been utilized to model bones or soft tissues (see, e.g. [9, 68]) and recently to model parts of the human lung [29]. On a smaller scale, porous media models have successfully been applied to tumor growth models [206, 223] and cell mechanics [174, 230].

Arguably one of most famous historic names associated with porous media theory is Henri-Philibert Darcy (1803–1858). The civil engineer born in France was the first to perform detailed experimental investigations of water flow through natural sand [71]. He discovered a proportionality between the total amount of filtrating liquid volume and the loss of pressure. This relation for flow of a fluid through a rigid porous solid is still known today as Darcy's law. It represents the most basic flow equation and will also be referred to in a generalized form in this thesis. At

the beginning of the 20th century, the Viennese professor Karl von Terzaghi (1883–1963) made decisive contributions to the theory of porous media and is therefore often named as the founder of soil mechanics. He analyzed fundamental mechanical properties of saturated porous systems. The interested reader is referred to [233] for an original work written in German and to [234] for a textbook in English. Terzaghi was the first to consider deformation of the porous medium and developed the one-dimensional consolidation theory. His principle of effective stress is still present in modern soil mechanics. Based on Terzaghi's findings, Maurice Anthony Biot (1905–1985) derived a complete formulation for three-dimensional problems [33, 38]. The Belgian aeronautic engineer generalized Terzaghi's theory and integrated dynamic loading effects. In the following years, he extended his formulation to anisotropy and linear visco-elasticity of the solid and also acoustic propagation, see e.g. [34–37, 39]. Many practical problems can be solved with Biot's consolidation theory and a quite large number of the modern formulations are still based on his insights and derivations. Besides those three 'pioneers', there are many more important names and contributions to be mentioned concerning the history of porous media theory, which are not given here. For a more thorough review of the development of the theory, the interested reader is referred to [73, 74] and the references therein.

1.2.1. Mathematical Basis: Homogenization

Porous media are composed of one solid phase (the skeleton) and one or several fluid phases, flowing through connected pores. The geometry of the pore structure is very complex and in many application unknown. Thus, a fully resolved model in the sense of a surface coupled fluid-structure interaction system is computationally highly demanding. Yet, in many cases such detailed resolution is not needed to answer the relevant questions. For instance, the knowledge of the precise distribution of the fluid flux within the pores might not be necessary, as long as it can be obtained in an averaged sense. Therefore, continuum mechanics of porous media concentrates on a description on the macroscopic level, which is larger than the pore scale. Such theories lead to a continuous description of the porous medium. The fluid and solid are perceived as overlapping continua and, hence, the interface between the phases is not resolved explicitly. Finally, a volume-coupled fluid-structure interaction problem is derived. Following this methodology, the porous medium can be modeled without presuming detailed knowledge of the pore geometry.

To obtain a macroscopic description, one has to bridge the distance from microscale to macroscale. This not only holds for the governing equations and the variables of interest, like filtration velocity and deformation, but also for model and material parameters. Such a procedure is often referred to as *homogenization* or *averaging*. Note that these terminologies are sometimes used for one specific method. Here, they will be used as umbrella terms for all methodologies resulting in a macroscopic description. The homogenization process is shown schematically for a fully saturated porous medium in Figure 1.2. Starting from a resolved scale, incorporating the interface between solid and fluid, averaging gives a smeared continuum formulation, where every point is composed of both phases with a volume ratio defined by the *porosity* ϕ. It relates the current fluid volume $\mathrm{d}\Omega_t^{\mathrm{f}}$ to the current total volume $\mathrm{d}\Omega_t$:

$$\phi \, \mathrm{d}\Omega_t = \mathrm{d}\Omega_t^{\mathrm{f}}. \tag{1.1}$$

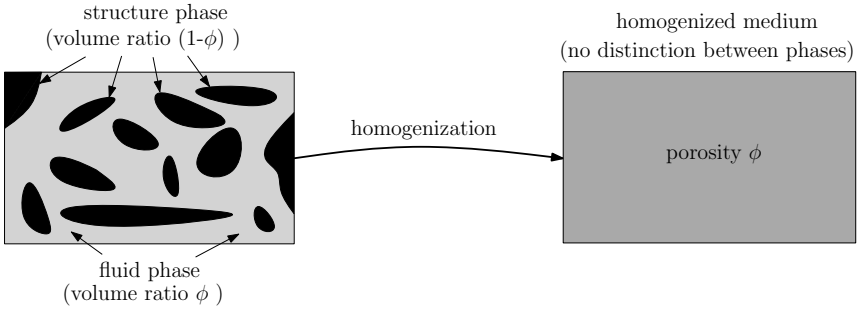

Figure 1.2: Schematic of the homogenization process applied to porous media, taken from [243].

In porous media modeling, many methods have been developed to obtain a homogenized formulation. Some of them will be reviewed briefly in the following. Most methods imply the existence of a so called *representative elementary volume* (REV) big enough to include the basic geometry information of the porous medium and yet small enough to resolve all physical effects of interest with a sensible level of accuracy. The fraction of the porous medium in Figure 1.2 can be interpreted as a REV.

The method of *volume averaging* has been advanced primarily in [249–252]. A similar averaging approach can be found in detail in [25]. Therein, spatial averages are formulated on the microscale and a closure relation is postulated to perform the coupling of scales. Closure relations most often include some assumptions regarding the problem. Simply speaking, it gives the missing relation between some microscropic and macroscopic variables. For instance, a constitutive law for the permeability tensor depending only on macroscopic variables is the result of a closure relation, see [253].

The mathematical method of *asymptotic expansion* has also been applied successfully to porous media problems (see e.g. [16, 124, 214]). Here, the porous medium is assumed to be a spatially periodic structure, with the REV (often also called microcell) representing the smallest composite. The method is based on a multiscale perturbation theory. The solution variables are approximated by a power series of contributions from different scales. By inserting them into the governing equations on the microscale and comparing orders of magnitude of different terms, eventually macroscopic equations are obtained.

Thermodynamically Constrained Averaging Theory (TCAT) (see, e.g. [112, 113, 115]) includes thermodynamic constraints into the averaging process. In [114] a review of TCAT is given. All conservation and balance equations are first formulated on the microscale. The general upscaling procedure is similar to volume averaging. However, the thermodynamic laws are considered on the microscale and treated as constraints on the governing equations. This leads to a more complex and extensive mathematical derivation of the homogenized model. In the end, the conservation properties of the model are very clear by construction. This is the major difference to volume averaging approaches, where most often thermodynamic considerations are restricted to the macroscale, where the physical meaning of some smeared quantities might not be precisely defined.

All methods are capable of reproducing a general form of Darcy's law. The differences in the final equations frequently stem from the constitutive equations and the interpretation of macroscopic values. See [122] for a theoretical comparison between volume averaging and asymptotic

expansion, where it was shown that volume averaging can for certain cases be formulated as a first-order asymptotic expansion method.

1.2.2. Computational Approaches

The method of choice predominantly used for solving porous medium problems is the finite element method (FEM). Other approaches, like the finite difference method and the finite volume method, were also utilized, e.g. in [4, 90, 138, 139]. However, the considered problems are usually restricted to flow through a rigid porous medium there. For consolidation problems, i.e. the coupled problem of deformation and flow, the FEM is the most prominent method. Another popular approach, especially in environmental engineering, is a coupled finite volume and finite element formulation [57, 85, 126]. For textbooks specifically about porous media and FEM analysis the reader is referred to [158, 242].

The first computational approaches concerning porous media can be traced back to the late 1960s and early 1970s. Based on Biot's theory, several FE approaches were proposed during this period of time, see e.g. [60, 131, 216, 262]. Two- and three-dimensional consolidation of linear-elastic solids was simulated. In [108, 266] the method was extended towards compressibility of the fluid and the solid grains. In [227, 266] computational models for visco-elasticity and plasticity were proposed. Permeability changes during consolidation were analyzed in [159] and large deformations were treated in [52]. In the 1980s important contributions were made in [264, 265, 268] and [194–196]. Non-linear dynamic effects including complex material behavior were considered there. Extensions of the porous media model in the form of non-isothermal effects were studied in [5, 41, 160]. Most of the approaches presented above use the pore pressure and the displacements as primary variables. Although being computationally cheap, such methods often lack accuracy regarding the fluid velocity, fluxes and mass conservation. A valid remedy are methodologies involving post-processing of the velocity and enforcing mass conservation [63, 67]. However, more recently, mixed formulations including the fluid velocities as primary solution variables have become increasingly popular. They are based on the general theory of mixed methods, see e.g. the standard textbook [43]. The theory of mixed finite elements was applied to porous flow in [84], originally designed for multiphase flow through a rigid porous medium. Therein, stable Raviart-Thomas spaces [203] were chosen as solution spaces. Equal-order interpolations using residual-based stabilization techniques were proposed in [17, 166]. In [17] a stabilization method, which will also be used in this thesis, based on the variational multiscale decomposition of the Darcy flow problem was considered. This analysis was restricted to a non-deforming solid phase. Small deformations of the solid phase were included in [18]. A more general formulation for a porous media problem was given in [54]. Large strains were considered and a generalized hyperelastic free energy potential was proposed there. Similar theoretical analysis was performed in [102], further including compressible flow. In [103] finite element schemes for this general formulation were presented. Mixed formulations with higher-order interpolations for solid displacements and fluid flow representing stable finite element spaces were applied to one- and two-dimensional settings.

In conclusion, one can state that very general continuum mechanics formulations of porous media models exists. The theory of non-linear effects and the coupling to other fields have been considered. Many of those aspects have also been treated numerically. However, the simulation

of the full coupling between flow and deformation for large deformations and non-linear material behavior still remains a challenge.

1.3. Research Objective

The undeniable importance of porous media in a huge number of scientific fields is the motivation of this work. The objective is to realize a general computational approach for a huge number of problem classes fully or partially consisting of porous media. The numerical method of choice is the finite element method, as it has proven capabilities to solve both non-linear solid and fluid problems as well as complex coupled problems.

1.3.1. Specification of Requirements

Motivated by the overview and explanations given before, the most essential requirements of the work this thesis is based on are listed in the following.

- **General and flexible formulation of porous medium model including large deformations**
  Many concepts and formulations of computational models for porous media exist in the literature. Even though very general theory is available, most of the numerical realizations are in some way restricted to certain assumptions. This frequently means either small deformations, a linear constitutive model or fully or partially stationary behavior. This is very reasonable in classical soil mechanics, for instance, as large deformations and highly dynamic processes only occur in special scenarios. However, when thinking of biomechanics and other fields, large strains are not extraordinary, but rather the default case. Actually, including large deformations introduces further intricacies. As known from classical elastodynamics, non-linear kinematics – not compulsorily, but very often – imply a likewise non-linear constitutive behavior. Hence, there are two further aspects to be accounted for. First, the relation between strain and stress of the skeleton needs to be flexible. It should not be restricted to one certain material law, but expressed in a generic fashion. Second, the relations for the porous media characteristics (e.g. porosity, permeability) need to be exchangeable and possibly the governing equations themselves need to be adapted, if the application demands it. This need for flexibility holds for both the theoretical basis, i.e. continuum mechanics, and for the implementation. In conclusion, the most important goal of this thesis is to provide a generic and flexible numerical solution framework for flow through a deformable porous medium undergoing large deformations, with as few restricting assumptions as possible, giving credit to the complex, coupled nature of the problem.

- **Finite element formulation of porous medium problem**
  Once the formulation is set, it has to be solved. For this, the finite element method is utilized. Particular approaches are to be designed for porous media problems. A significant aspect is the treatment of non-constant porosities in time and space. This is an effect not often considered in classical porous media applications. However, in the large deformation regime this very easily occurs. As will be pointed out in the computational part of this thesis, this leads to some special requirements concerning the finite element ansatz space

in certain cases. The numerical framework further comprises discretization in time and non-linear solution schemes. Suitable and robust methods need to be chosen and applied to the given problem.

- **Extendable formulation and implementation regarding multi-field problems**
  Many realistic scenarios are not single-field (e.g. pure solid), not two-field (e.g. porous solid and porous fluid), but multi-field problems. Flow over a porous bed is a classical example. A fluid field for the free flow is coupled with the two fields comprising the porous medium. Although the development of a solution framework for a pure porous medium problem is the main goal, the extension to multi-field problems is a natural next step. These do not only include interface-coupled problems, as the flow example given before, but also volume-coupled problems. Suitable coupling conditions need to be formulated and included in the finite element framework.

- **Specific application to cell and tissue mechanics**
  Even though it was already stated that the goal is a general formulation, the applications in mind are clearly biomechanical problems, that is, the modeling of cell migration. The environment surrounding a cell is called the extracellular matrix (ECM) and is mainly composed of collagen and elastin fibers and interstitial fluid. Thus, it can almost be denoted as a classical porous medium. More precisely, it is a porous medium with a high fluid volume fraction and potential constitutive anisotropy due to the fibers composing the solid phase. And obviously, at the latest when there is significant interaction between the cell and the ECM, it becomes a multi-field problem. From reviewing the biological literature it becomes clear that the main goal to implement a general framework is not excluding, but rather supporting the aim for a model of cell mechanics. As many biological and biochemical details are not yet fully understood, a flexible formulation gives the opportunity to adapt certain parts of the model once deeper insight is granted. Therefore, the application of the solution scheme to cell and tissue mechanics is a motivation in itself and also a validation of the flexibility of the developed framework.

1.3.2. Proposal of Numerical Approach

The methods presented in this thesis address the aforementioned requirements. The main novelty comprises the generality of the approach, the presented and analyzed discretization techniques and the continuum-mechanical model for cell mechanics including a porous medium. They are summarized in the following scientific contributions:

- Solution of a general formulation for poromechanics in the large deformation regime using the FEM and implementation for 2D and 3D problems [243]. This includes the capability to incorporate an arbitrary potential-based constitutive law for the skeleton phase.

- Analysis of the numerical properties of Darcy and Darcy-Brinkman flow regarding the finite element method and developement of specific approaches for non-constant porosities [244]. Therein, the application of complex boundary conditions is also considered.

- Demonstration of the numerical flexibility in terms of finite element discretization regarding standard Lagrange or NURBS discretizations and non-matching fluid and skeleton discretizations [91, 244].
- Capability to embed the porous medium framework into different, complex multi-field problems [201, 245].
- First applications to cell and tissue mechanics comprising a specific model for biochemical-mechanical coupling [201, 245].

The whole algorithm has been implemented in the in-house C++ code of the Institute for Computational Mechanics at the Technical University of Munich. The basic data structures like already implemented parallelization and linear solver algorithms, were reused. Other modules have been adapted or were written completely from scratch.

1.4. Outline

The remainder of this thesis is structured as follows: In **Chapter 2** the basic equations governing the most important continuum-mechanical problems relevant for this thesis are given. These include classical non-linear elastodynamics, fluid dynamics and transport of scalar quantities. As those equations are basic knowledge, they will only be stated in such a form to be comprehensive, without going into details about mathematical basics and derivations. In **Chapter 3**, the continuum mechanics of porous media is reviewed. This thesis introduces poroelasticity to the Institute of Computational Mechanics, and therefore the descriptions will be more detailed (however without claiming to be complete). All the governing equations will be written on a macroscopic scale. In the subsequent **Chapter 4** the computational approach to solve the porous media problem is presented. It includes different forms of finite element discretizations, specifically designed for non-constant porosities and the flow equations considered. In particular, a natural approach involving skeleton displacements, fluid pressure and fluid velocity is compared with a mixed approach with the porosity as additional primary variable. Continuity requirements on the finite element solution spaces are analyzed. Following this, a NURBS-based approach is proposed. Also, time discretization, stabilization, application of complex boundary conditions and solution techniques are described. At the end of the chapter, the results are illustrated with numerical examples. **Chapter 5** is dedicated to multi-field problems including a porous medium. It will be shown how the interaction between a pure solid and a porous medium can be modeled and solved numerically. Also, examples of fluid-porous-media interaction and passive scalar transport within a porous medium will be displayed. A large part of this chapter will treat the application to cell and tissue mechanics. For this purpose, a framework for scalar transport on curved, moving surfaces has been implemented and will be presented. Thereafter, a model for biochemical-mechanical interaction designed to represent pericellular proteolysis will be proposed. All multi-field applications will be illustrated with numerical examples. Lastly, in **Chapter 6** a summary and an outlook towards potential future work are given.

2. Governing Equations of 'Classical' Non-linear Continuum Mechanics

The basics concepts of non-linear continuum mechanics are reviewed in this chapter. The theory presented here will partly be explicitly used in the succeeding chapters or form the basis of extensions towards porous media models. In the following, the governing equations for solid dynamics, fluid dynamics, and advective-diffusive-reactive transport of scalar quantities will be presented. Detailed theory will only be given when it is considered to be useful for understanding the subsequent exposition of the continuum mechanics of porous media. Otherwise, it will be stated in a matter-of-fact fashion. For more theory and derivations it is referred to the abundant literature on continuum mechanics, like [21, 40, 111, 120].

2.1. Configurations: Eulerian, Lagrangean and Arbitrary-Lagrangean-Eulerian

As a various number of physics and fields are considered in this thesis, a clear distinction between the different configurations and observers is crucial for the comprehensiveness of the theory. Two domains are commonly used in continuum mechanics: The *material configuration* Ω_0 and the *current or spatial configuration* Ω_t. The material configuration describes the position of the *material points* $\boldsymbol{X}$ at the initial time $t = 0$, while the current configuration is composed of all *current points* $\boldsymbol{x}$ at a given time t. The *Lagrangean* observer follows the material particles in their motion. Thus, he is linked to the material configuration and the corresponding governing equations are written in terms of the material coordinates $\boldsymbol{X}$. The Lagrangean formulation is commonly used in structural dynamics and significantly computationally advantageous when considering problems with history-depended variables, like in visco-elasticity and plasticity, for instance. In fluid dynamics, however, most often an *Eulerian* formulation is preferred. Therein, the observer, and thus the computational grid, is fixed. The governing equations are written in terms of the current coordinates $\boldsymbol{x}$. As a consequence, large material deformations like vortices, which could lead to infeasible mesh distortion in a Lagrangean formulation, can be captured. In Fluid-Structure Interaction (FSI) and – as will be shown later – in some sense also in poromechanics, a generalized viewpoint, the so called *Arbitrary-Lagrangean-Eulerian* (ALE) description is used. The corresponding *reference coordinates* are denoted by $\boldsymbol{\mathcal{X}}$. The basic idea is to allow for mesh movement, like in the Lagrangean formulation, but still be decoupled from the motion of the particles, like in the Eulerian formulation. For this purpose, a third configuration, denoted as *reference configuration* Ω_{R}, is introduced. In Figure 2.1 the configurations and the corresponding mappings are illustrated. The *motion* φ is a bijective map between the material

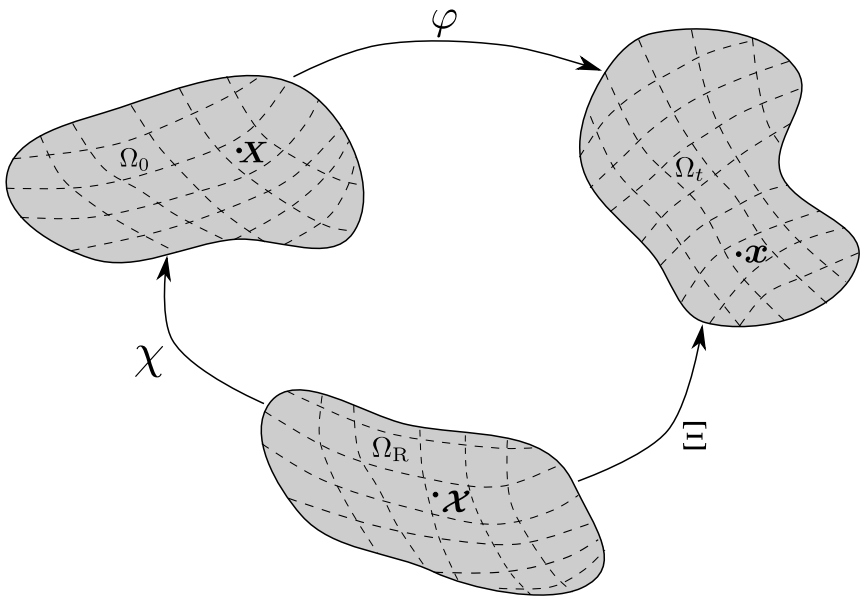

Figure 2.1: Configurations: Reference configuration Ω_{R}, material configuration Ω_0 and current configuration Ω_t and corresponding mappings.

configuration Ω_0 and the current configuration Ω_t:

$$\varphi : \begin{cases} \Omega_0 \to \Omega_t(t), \quad (\boldsymbol{X}, t) \to \boldsymbol{x}, \\ \varphi(\boldsymbol{X}, t) = \boldsymbol{x}(\boldsymbol{X}, t). \end{cases} \tag{2.1}$$

Similarly, the bijective mapping between the reference and the current configuration is defined as

$$\Xi : \begin{cases} \Omega_{\mathrm{R}}(t) \to \Omega_t(t), \quad (\boldsymbol{\mathcal{X}}, t) \to \boldsymbol{x}, \\ \Xi(\boldsymbol{\mathcal{X}}, t) = \boldsymbol{x}(\boldsymbol{\mathcal{X}}, t), \end{cases} \tag{2.2}$$

and the bijective mapping between the reference and the material configuration is written as

$$\chi = \varphi^{-1} \circ \Xi : \begin{cases} \Omega_{\mathrm{R}}(t) \to \Omega_0, \quad (\boldsymbol{\mathcal{X}}, t) \to \boldsymbol{X}, \\ \chi(\boldsymbol{\mathcal{X}}, t) = \boldsymbol{X}(\boldsymbol{\mathcal{X}}, t). \end{cases} \tag{2.3}$$

Note, that the only configuration independent of the time t is the material configuration. An important aspect of equations in ALE formulation is the expression of the total, material time derivative. The material time derivative of a spatial quantity $g(\boldsymbol{x}, t)$ can be written as

$$\frac{\mathrm{d}g(\boldsymbol{x}, t)}{\mathrm{d}t} = \left.\frac{\partial g(\boldsymbol{\mathcal{X}}, t)}{\partial t}\right|_{\boldsymbol{\mathcal{X}}} + \frac{\partial g(\boldsymbol{\mathcal{X}}, t)}{\partial \boldsymbol{\mathcal{X}}} \cdot \left.\frac{\partial \boldsymbol{\mathcal{X}}}{\partial t}\right|_{\boldsymbol{X}} = \left.\frac{\partial g}{\partial t}\right|_{\boldsymbol{\mathcal{X}}} + \frac{\partial g}{\partial \boldsymbol{x}} \cdot \frac{\partial \boldsymbol{x}}{\partial \boldsymbol{\mathcal{X}}} \cdot \left.\frac{\partial \boldsymbol{\mathcal{X}}}{\partial t}\right|_{\boldsymbol{X}}. \tag{2.4}$$

Here, it was used that g can be written in terms of any of the three coordinates. The velocity $\boldsymbol{v}$ of the material particle can be calculated as

$$\boldsymbol{v} = \frac{\mathrm{d}\boldsymbol{x}}{\mathrm{d}t} = \left.\frac{\partial \boldsymbol{x}(\boldsymbol{\mathcal{X}}, t)}{\partial t}\right|_{\boldsymbol{\mathcal{X}}} + \frac{\partial \boldsymbol{x}}{\partial \boldsymbol{\mathcal{X}}} \cdot \left.\frac{\partial \boldsymbol{\mathcal{X}}}{\partial t}\right|_{\boldsymbol{X}}. \tag{2.5}$$

Solving equation (2.5) for the second summand, and substituting this expression in (2.4) yields

$$\frac{\mathrm{d}g(\boldsymbol{x},t)}{\mathrm{d}t} = \left.\frac{\partial g(\boldsymbol{\mathcal{X}},t)}{\partial t}\right|_{\boldsymbol{x}} + (\boldsymbol{v}-\boldsymbol{v}^{\mathrm{g}})\cdot\boldsymbol{\nabla} g = \left.\frac{\partial g(\boldsymbol{\mathcal{X}},t)}{\partial t}\right|_{\boldsymbol{x}} + \boldsymbol{v}^{\mathrm{c}}\cdot\boldsymbol{\nabla} g, \tag{2.6}$$

where $\boldsymbol{v}^{\mathrm{c}} = \boldsymbol{v} - \boldsymbol{v}^{\mathrm{g}}$ denotes the *ALE convective velocity*, i.e. the relative velocity of the particle with respect to the *grid velocity* $\boldsymbol{v}^{\mathrm{g}}$. Equation (2.6) is also known as *fundamental ALE equation*. The material derivative is expressed in terms of a time derivative for fixed reference coordinates. Essentially, this is done by introducing the additional convective term $-\boldsymbol{v}^{\mathrm{g}}\cdot\boldsymbol{\nabla} g$ originating from the movement of the observer.

2.2. Non-linear Kinematics, Strain and Stress

A brief overview of non-linear kinematics, strain, and stress measures, forming the basis of elastodynamics, is given here. A classic Boltzmann continuum in three dimensions is considered. From now on, it is assumed that both the material and the current configuration are formulated with respect to one global Cartesian coordinate system $\{\boldsymbol{e}_1, \boldsymbol{e}_2, \boldsymbol{e}_3\}$, see Figure 2.2. Note, that in

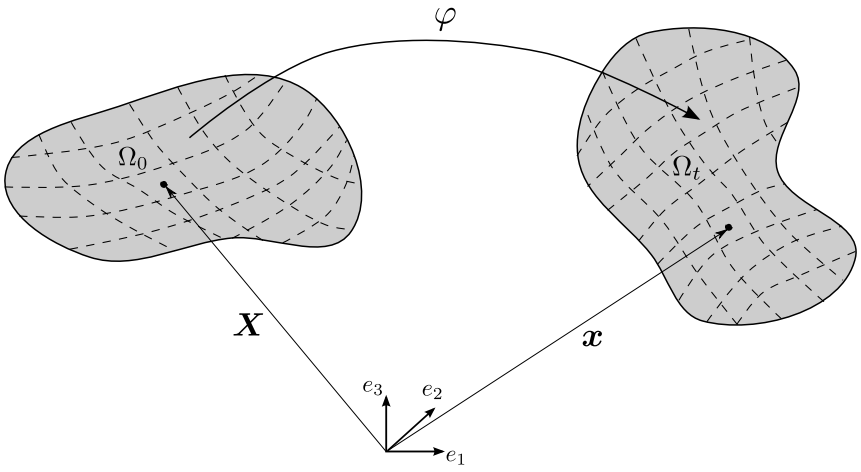

Figure 2.2: The motion φ as mapping between material Ω_0 and current configuration Ω_t, formulated in one global Cartesian coordinate system. In common elastodynamics, no distinction between material configuration and reference configuration, i.e. $\Omega_0 = \Omega_{\mathrm{R}}$, is made.

common elastodynamics no distinction between material and reference configuration is necessary. The *displacement* $\boldsymbol{d}$ is the difference between spatial and material position:

$$\boldsymbol{d} = \boldsymbol{x} - \boldsymbol{X}. \tag{2.7}$$

The *deformation gradient* $\boldsymbol{F}$ is the gradient of the current position with respect to the material position:

$$\boldsymbol{F}(\boldsymbol{X},t) = \frac{\partial \boldsymbol{x}(\boldsymbol{X},t)}{\partial \boldsymbol{X}} = \boldsymbol{\nabla}_0 \boldsymbol{x}. \tag{2.8}$$

It describes the mapping of the infinitesimal line element $\mathrm{d}\boldsymbol{X}$ in the material configuration to the infinitesimal line element $\mathrm{d}\boldsymbol{x}$ in the current configuration, that is

$$\boldsymbol{F} \cdot \mathrm{d}\boldsymbol{X} = \mathrm{d}\boldsymbol{x}. \tag{2.9}$$

The *determinant* J of the deformation gradient

$$J = \det \boldsymbol{F} \tag{2.10}$$

can be interpreted as the relative volume change between an infinitesimal volume element $\mathrm{d}\Omega_0$ in the material configuration and an infinitesimal volume element $\mathrm{d}\Omega_t$ in the spatial configuration. It holds

$$\mathrm{d}\Omega_t = J\,\mathrm{d}\Omega_0. \tag{2.11}$$

Due to the bijectivity and smoothness of the motion, the determinant is guaranteed to be positive, i.e. $J > 0$. For an incompressible body, the determinant of the deformation gradient is equal to 1. For the mapping of an infinitesimal area element $\mathrm{d}\boldsymbol{A}$ in material configuration to a current area element $\mathrm{d}\boldsymbol{a}$, *Nanson's formula* is used:

$$\mathrm{d}\boldsymbol{a} = J\boldsymbol{F}^{-\mathrm{T}} \cdot \mathrm{d}\boldsymbol{A}. \tag{2.12}$$

In order to describe the kinematics of a body, derivatives in time are needed. The *velocity* $\boldsymbol{v}$ and the *acceleration* $\boldsymbol{a}$ of a point are defined as the total time derivatives of the displacements

$$\boldsymbol{v} = \left.\frac{\partial \boldsymbol{d}}{\partial t}\right|_{\boldsymbol{X}} = \frac{\mathrm{d}\boldsymbol{d}}{\mathrm{d}t}, \tag{2.13}$$

$$\boldsymbol{a} = \left.\frac{\partial \boldsymbol{v}}{\partial t}\right|_{\boldsymbol{X}} = \frac{\mathrm{d}^2\boldsymbol{d}}{\mathrm{d}t^2}. \tag{2.14}$$

The rate of the deformation gradient can be calculated as

$$\dot{\boldsymbol{F}} = \frac{\mathrm{d}}{\mathrm{d}t}\left(\frac{\partial \boldsymbol{x}}{\partial \boldsymbol{X}}\right) = \frac{\partial \boldsymbol{v}}{\partial \boldsymbol{X}} = \boldsymbol{\nabla v} \cdot \boldsymbol{F}^{-1}. \tag{2.15}$$

As a measure for strain in non-linear solid mechanics, the *Green-Lagrange strain tensor*

$$\boldsymbol{E} = \frac{1}{2}(\boldsymbol{C} - \boldsymbol{1}) = \frac{1}{2}\left(\boldsymbol{F}^{\mathrm{T}} \cdot \boldsymbol{F} - \boldsymbol{1}\right), \tag{2.16}$$

with the *right Cauchy-Green deformation tensor*

$$\boldsymbol{C} = \boldsymbol{F}^{\mathrm{T}} \cdot \boldsymbol{F}, \tag{2.17}$$

is often used. The Green-Lagrange strains fulfill the natural request for zero strain in the undeformed state, that is $\boldsymbol{E} = \boldsymbol{0}$ for $\boldsymbol{F} = \boldsymbol{1}$. The Green-Lagrange strains are a suitable choice in the moderate stretch and compression regime. Alternative strain measures are for instance the Euler-Almansi and the logarithmic strains, see the textbooks referenced at the beginning of this chapter for details.

For non-rigid bodies, deformation in general induces stress. As the strains, the stresses are not uniquely defined in the theory of large deformations. Instead, different stress measures are possible, depending on the problem formulation used and the configurations considered. The *boundary traction* $\boldsymbol{t}$ in the current configuration is defined as the limit value of the resulting force $\Delta \boldsymbol{f}$ on a vanishing surface area Δa:

$$\boldsymbol{t} = \lim_{\Delta a \to 0} \frac{\Delta \boldsymbol{f}}{\Delta a}. \tag{2.18}$$

The *Cauchy stress tensor* $\boldsymbol{\sigma}$ then gives the current boundary traction $\boldsymbol{t}$ to a respective current outward pointing normal $\boldsymbol{n}$ of a boundary as

$$\boldsymbol{t} = \boldsymbol{\sigma}(\boldsymbol{x}, t) \cdot \boldsymbol{n}. \tag{2.19}$$

The *first Piola-Kirchhoff stress tensor* $\boldsymbol{P}$ is defined as

$$\boldsymbol{P} = J\boldsymbol{\sigma} \cdot \boldsymbol{F}^{-\mathrm{T}}. \tag{2.20}$$

Like the deformation gradient, the first Piola–Kirchhoff stress tensor is a so-called two point tensor, being a mapping from the material to the current configuration. It maps a material normal to a current boundary traction. The *second Piola-Kirchhoff stress tensor* $\boldsymbol{S}$ is a pure material stress measure and defined as the pull-back of the Cauchy stress

$$\boldsymbol{S} = J\boldsymbol{F}^{-1} \cdot \boldsymbol{\sigma} \cdot \boldsymbol{F}^{-\mathrm{T}}. \tag{2.21}$$

It gives the material boundary traction $\boldsymbol{T}$ to a respective material outward pointing normal $\boldsymbol{N}$ of a boundary

$$\boldsymbol{T} = \boldsymbol{S} \cdot \boldsymbol{N}. \tag{2.22}$$

For viscous effects and also for general thermodynamic analysis, rates of strain measures, i.e. their total time derivatives, are needed. The rate $\dot{\boldsymbol{E}}$ of the Green-Lagrange strains can be calculated as

$$\dot{\boldsymbol{E}} = \frac{\mathrm{d}}{\mathrm{d}t}\left(\frac{1}{2}\left(\boldsymbol{F}^{\mathrm{T}} \cdot \boldsymbol{F} - \boldsymbol{1}\right)\right) = \frac{1}{2}\left(\dot{\boldsymbol{F}}^{\mathrm{T}} \cdot \boldsymbol{F} + \boldsymbol{F}^{\mathrm{T}} \cdot \dot{\boldsymbol{F}}\right). \tag{2.23}$$

An objective spatial strain rate is the *deformation rate* $\boldsymbol{\varepsilon}$. It is defined as the push-forward of the rate of the Green-Lagrange strain:

$$\boldsymbol{\varepsilon} = \boldsymbol{F}^{-\mathrm{T}} \cdot \dot{\boldsymbol{E}} \cdot \boldsymbol{F}^{-1} = \frac{1}{2}\left(\boldsymbol{\nabla}\boldsymbol{v} + (\boldsymbol{\nabla}\boldsymbol{v})^{\mathrm{T}}\right). \tag{2.24}$$

All the definitions and relations stated here will be used in the following sections for formulating governing equations in non-linear continuum mechanics.

2.3. Governing Equations of Elastodynamics

The dynamics of elastic solids will either be considered as one component of a porous medium in Chapter 3 (for which similar but slightly different equations hold) or as part of a multi-physics

system in Section 5.1. The mechanical laws, that are typically used for characterizing a structural system, are the balance of mass, linear and angular momentum and energy. All balance equations can be formulated in a global, integral manner or in a local, point-wise form. The balance of angular momentum is implicitly fulfilled by the symmetry of the Cauchy stress tensor and the balance of energy is a direct consequence of the balance of linear momentum for isothermal solids. As the balance of angular momentum and energy do not play a crucial role in the context of this thesis, they will not be addressed further. They can be found in any continuum mechanics textbook mentioned at the beginning of this chapter. Instead, only the conservation of mass and the balance of linear momentum will be stated here. In addition, the constitutive equation for the stresses of a hyperelastic solid are given.

2.3.1. Conservation of Mass

Assuming no mass generation or loss, i.e. no growth and no degradation, the *solid mass* m^{s} needs to be conserved. Thus, the balance of mass can be written as

$$\frac{\mathrm{d}m^{\mathrm{s}}}{\mathrm{d}t} = \frac{\mathrm{d}}{\mathrm{d}t}\int \rho^{\mathrm{s}}\ \mathrm{d}\Omega_t = \int \dot{\rho}^{\mathrm{s}} + \rho^{\mathrm{s}}\boldsymbol{\nabla}\cdot\boldsymbol{v}^{\mathrm{s}}\ \mathrm{d}\Omega_t = 0, \tag{2.25}$$

with the *current solid density* ρ^{s}. Symbols that will be used later also for other fields, like ρ^{f} and $\boldsymbol{v}^{\mathrm{f}}$ for the density and velocity of a fluid, are marked with the superscript $(\bullet)^{\mathrm{s}}$ explicitly denoting their correspondence to the structure field here. The Reynolds' theorem was used to obtain the above equation. The corresponding global form in the material configuration reads

$$\frac{\mathrm{d}m^{\mathrm{s}}}{\mathrm{d}t} = \frac{\mathrm{d}}{\mathrm{d}t}\int J\rho^{\mathrm{s}}\ \mathrm{d}\Omega_0 = \int \dot{\rho}_0^{\mathrm{s}}\ \mathrm{d}\Omega_0 = 0, \tag{2.26}$$

with the *material solid density* $\rho_0^{\mathrm{s}} = J\rho^{\mathrm{s}}$. The local forms of the balance of mass follow immediately, as the global equations have to hold for any arbitrary sub-part of the domain, as

$$\dot{\rho}^{\mathrm{s}} + \rho^{\mathrm{s}}\boldsymbol{\nabla}\cdot\boldsymbol{v}^{\mathrm{s}} = 0, \tag{2.27}$$

for the current configuration and

$$\dot{\rho}_0^{\mathrm{s}} = 0, \tag{2.28}$$

for the material configuration.

2.3.2. Balance of Linear Momentum

The global balance of linear momentum states that its temporal change is equivalent to the sum of forces acting on the body:

$$\frac{\mathrm{d}}{\mathrm{d}t}\int \rho^{\mathrm{s}}\boldsymbol{v}^{\mathrm{s}}\ \mathrm{d}\Omega_t = \int \boldsymbol{b}^{\mathrm{s}}\ \mathrm{d}\Omega_t + \int \boldsymbol{t}^{\mathrm{s}}\ \mathrm{d}\Gamma_t, \tag{2.29}$$

where $\boldsymbol{b}^{\mathrm{s}}$ represents the external *body forces*. The traction forces $\boldsymbol{t}^{\mathrm{s}}$ are acting on the *current boundary* Γ_t. Using Reynolds' transport theorem, the definition of the Cauchy stresses (2.19)

and the conservation of mass (2.28) gives

$$\int \rho^{\mathrm{s}} \boldsymbol{a}^{\mathrm{s}} \, \mathrm{d}\Omega_t = \int \boldsymbol{\nabla} \cdot \boldsymbol{\sigma}^{\mathrm{s}} + \boldsymbol{b}^{\mathrm{s}} \, \mathrm{d}\Omega_t. \tag{2.30}$$

The local form follows in a straightforward way as

$$\rho^{\mathrm{s}} \boldsymbol{a}^{\mathrm{s}} = \boldsymbol{\nabla} \cdot \boldsymbol{\sigma}^{\mathrm{s}} + \boldsymbol{b}^{\mathrm{s}}. \tag{2.31}$$

Similarly, the global balance of linear momentum in the material configuration can be written as

$$\int \rho_0^{\mathrm{s}} \boldsymbol{a}^{\mathrm{s}} \, \mathrm{d}\Omega_0 = \int \boldsymbol{\nabla}_0 \cdot \boldsymbol{P} + \boldsymbol{b}_0^{\mathrm{s}} \, \mathrm{d}\Omega_0 \tag{2.32}$$

and equivalently its local form as

$$\rho_0^{\mathrm{s}} \boldsymbol{a}^{\mathrm{s}} = \boldsymbol{\nabla}_0 \cdot \boldsymbol{P} + \boldsymbol{b}_0^{\mathrm{s}}. \tag{2.33}$$

To complete the problem, a suitable constitutive model to relate stresses and strains and consistent initial and boundary conditions need to be formulated.

2.3.3. Constitutive Relations

For *hyperelastic materials* the existence of a *strain energy function* Ψ is postulated. Considering purely elastic, isothermal conditions, the second law of thermodynamics reads

$$\boldsymbol{P} \cdot \dot{\boldsymbol{F}} - \dot{\Psi} \geq 0. \tag{2.34}$$

The term $\boldsymbol{P} \cdot \dot{\boldsymbol{F}}$ accounts for the internal mechanical power. Assuming that the strain energy function only depends on the deformation state, i.e. $\Psi = \Psi(\boldsymbol{F})$, equation (2.34) can be reformulated as

$$\left(\boldsymbol{P} - \frac{\partial \Psi}{\partial \boldsymbol{F}} \right) \cdot \dot{\boldsymbol{F}} \geq 0. \tag{2.35}$$

Since $\dot{\boldsymbol{F}}$ can vary arbitrarily, the first term in equation (2.35) has to vanish in order to the dissipation inequality to hold. Thus, the following constitutive relation is obtained

$$\boldsymbol{P} = \frac{\partial \Psi}{\partial \boldsymbol{F}}. \tag{2.36}$$

In practice, the strain energy function is often not written in terms of the deformation gradient, but instead in terms of the right Cauchy-Green deformation tensor. The stresses can thereby be calculated via the following constitutive relations:

$$\boldsymbol{\sigma} = 2J^{-1} \boldsymbol{F} \cdot \frac{\partial \Psi(\boldsymbol{C})}{\partial \boldsymbol{C}} \cdot \boldsymbol{F}^{\mathrm{T}}, \quad \boldsymbol{P} = 2\boldsymbol{F} \cdot \frac{\partial \Psi(\boldsymbol{C})}{\partial \boldsymbol{C}}, \quad \boldsymbol{S} = \frac{\partial \Psi(\boldsymbol{E})}{\partial \boldsymbol{E}} = 2\frac{\partial \Psi(\boldsymbol{C})}{\partial \boldsymbol{C}}. \tag{2.37}$$

In particular for finite element approaches, the *material tangent* $\boldsymbol{C}_{\mathrm{mat}}$ is needed for building the stiffness matrix. This fourth-order tensor is defined as

$$\boldsymbol{C}_{\mathrm{mat}} = \frac{\partial^2 \Psi}{\partial \boldsymbol{E}^2} = 2\frac{\partial^2 \Psi}{\partial \boldsymbol{C}^2}. \tag{2.38}$$

The choice of the strain energy function determines the constitutive behavior. One of the simplest model is the *Saint-Venant-Kirchhoff* material. It is the natural extension of linear constitutive theory formulated for large deformations. The strain energy function reads

$$\Psi_{\mathrm{SVK}} = \frac{\lambda^{\mathrm{s}}}{2}\big(\mathrm{tr}\boldsymbol{E}\big)^2 + \mu^{\mathrm{s}}\boldsymbol{E} : \boldsymbol{E}, \tag{2.39}$$

with the *Lamé coefficients* λ^{s} and μ^{s}. The second Piola-Kirchhoff stress tensor follows as

$$\boldsymbol{S}_{\mathrm{SVK}} = \lambda^{\mathrm{s}}\mathrm{tr}(\boldsymbol{E})\boldsymbol{1} + 2\mu^{\mathrm{s}}\boldsymbol{E}, \tag{2.40}$$

and the material tangent of the Saint-Venant-Kirchhoff material reads in index notation

$$C^{ABCD}_{\mathrm{mat,SVK}} = \mu^{\mathrm{s}}(\delta^{AC}\,\delta^{BD} + \delta^{AD}\,\delta^{BC}) + \lambda^{\mathrm{s}}\delta^{AB}\,\delta^{CD}. \tag{2.41}$$

Inspired by linear theory, the material law can also be expressed in terms of the *Young's modulus* E and the *Poisson's ratio* ν. The Lamé coefficients can be calculated from the Young's modulus and the Poisson's ratio as

$$\lambda^{\mathrm{s}} = \frac{E\nu}{(1+\nu)(1-2\nu)}, \qquad \mu^{\mathrm{s}} = \frac{E}{2(1+\nu)}. \tag{2.42}$$

Another popular material law, which will also be used in this thesis, is the *Neo-Hooke* model, with the strain energy function

$$\Psi_{\mathrm{NH}} = \frac{\mu^{\mathrm{s}}}{2}\big(\mathrm{tr}\boldsymbol{C} - 3\big) - \mu^{\mathrm{s}}\ln(J) + \frac{\lambda^{\mathrm{s}}}{2}\big(\ln(J)\big)^2, \tag{2.43}$$

and the corresponding second Piola-Kirchhoff stress

$$\boldsymbol{S}_{\mathrm{NH}} = \mu^{\mathrm{s}}\big(\boldsymbol{1} - \boldsymbol{C}^{-1}\big) + \lambda^{\mathrm{s}}\ln(J)\,\boldsymbol{C}^{-1}. \tag{2.44}$$

The material tangent can be derived as

$$\boldsymbol{C}_{\mathrm{mat,NH}} = \lambda^{\mathrm{s}}\boldsymbol{C}^{-1}\otimes\boldsymbol{C}^{-1} + 2\big(\mu^{\mathrm{s}} - \lambda^{\mathrm{s}}\ln(J)\big)\boldsymbol{D}, \tag{2.45}$$

with the dyadic product $\otimes$ and the fourth-order tensor

$$D^{ABCD} = -\frac{\partial (C^{-1})^{AB}}{\partial C^{CD}} = \frac{1}{2}\left((C^{-1})^{AC}(C^{-1})^{BD} + (C^{-1})^{AD}(C^{-1})^{BC}\right). \tag{2.46}$$

For further, more sophisticated material laws it is referred to the standard textbooks of continuum mechanics listed at the beginning of this chapter.

2.4. Governing Equations of Incompressible Newtonian Flow

The dynamics of fluids are presented as preliminary analysis for flow in porous media and as basis of the multi-physics system of flow over a deformable porous structure. The governing equations of instationary, incompressible flow of a Newtonian fluid in a moving fluid domain are presented in this section. Basically, the equations are the same as in elastodynamics, i.e. the balance of linear momentum and the conservation of mass. However, they are usually written in the current configuration. The Cauchy stress $\boldsymbol{\sigma}^{\mathrm{f}}$ tensor is composed of the *fluid pressure* p^{f} and the *viscous stresses* $\boldsymbol{\sigma}^{\mathrm{f}}_{\mathrm{visc}}$ depending on the *fluid velocity* $\boldsymbol{v}^{\mathrm{f}}$:

$$\boldsymbol{\sigma}^{\mathrm{f}} = -p^{\mathrm{f}}\mathbf{1} + \boldsymbol{\sigma}^{\mathrm{f}}_{\mathrm{visc}} = -p^{\mathrm{f}}\mathbf{1} + 2\mu^{\mathrm{f}}\boldsymbol{\nabla}\cdot\boldsymbol{\varepsilon}^{\mathrm{f}}(\boldsymbol{v}^{\mathrm{f}}), \tag{2.47}$$

where $\boldsymbol{\varepsilon}^{\mathrm{f}}(\boldsymbol{v}^{\mathrm{f}}) = \frac{1}{2}\left(\boldsymbol{\nabla}\boldsymbol{v}^{\mathrm{f}} + (\boldsymbol{\nabla}\boldsymbol{v}^{\mathrm{f}})^{\mathrm{T}}\right)$ denotes the strain rate tensor of the Newtonian fluid and μ^{f} its *dynamic viscosity*. The balance of momentum in ALE formulation then reads

$$\rho^{\mathrm{f}}\left.\frac{\partial \boldsymbol{v}^{\mathrm{f}}}{\partial t}\right|_{\boldsymbol{x}} + \rho^{\mathrm{f}}\left(\boldsymbol{v}^{\mathrm{c}}\cdot\boldsymbol{\nabla}\right)\boldsymbol{v}^{\mathrm{f}} - 2\mu^{\mathrm{f}}\boldsymbol{\nabla}\cdot\boldsymbol{\varepsilon}(\boldsymbol{v}^{\mathrm{f}}) + \boldsymbol{\nabla}p^{\mathrm{f}} = \rho^{\mathrm{f}}\boldsymbol{b}^{\mathrm{f}}, \tag{2.48}$$

$$\boldsymbol{\nabla}\cdot\boldsymbol{v}^{\mathrm{f}} = 0, \tag{2.49}$$

with the *fluid density* ρ^{f}, the *body forces* $\boldsymbol{b}^{\mathrm{f}}$ and the convective velocity $\boldsymbol{v}^{\mathrm{c}} = \boldsymbol{v}^{\mathrm{f}} - \boldsymbol{v}^{\mathrm{g}}$, depending on the grid velocity $\boldsymbol{v}^{\mathrm{g}}$. The convective velocity appears due to the application of the fundamental ALE equation (2.6). Equation (2.49) states the conservation of mass given that the fluid density ρ^{f} is constant. Suitable initial and boundary conditions need to be chosen in order to complete the problem formulation.

2.5. Governing Equations of Advective-Diffusive-Reactive Transport of Scalar Quantities

Advection-diffusion-reaction processes of scalars will be viewed in the sense of mass transport. However, the application of the theory to transport of temperature/heat or energy is straightforward. Later, the theory presented in this section will be extended to transport in porous media in Section 5.3 and transport on curved surfaces in Section 5.4.1. The balance of mass of a *scalar quantity* c with the *molar mass* M reads

$$\frac{\mathrm{d}}{\mathrm{d}t}\int Mc\ \mathrm{d}\Omega_t = -\int M\boldsymbol{q}\ \mathrm{d}\Gamma_t + \int M\sigma(c)\ \mathrm{d}\Omega_t, \tag{2.50}$$

with the *flux* $\boldsymbol{q}$ and the *reaction term* σ. The reaction term is acting as mass source or sink and is often used for modeling the effects of chemical reactions. It is closely linked to kinetics of the reactions. More details with respect to specific forms of the reaction terms for modeling chemical reaction in the context of cell mechanics are given in Section 5.4.3. Assuming a constant molar

mass, the balance of a scalar quantity c can be written in local form as

$$\left.\frac{\partial c}{\partial t}\right|_{\boldsymbol{x}} + \boldsymbol{\nabla}\cdot\boldsymbol{q} - \sigma(c) = 0. \tag{2.51}$$

For classical transport processes, the flux is composed of a convective and a diffusive part:

$$\boldsymbol{q} = \underbrace{c\boldsymbol{v}}_{\text{convective}} \underbrace{-D\boldsymbol{\nabla}c}_{\text{diffusive}}, \tag{2.52}$$

with the *diffusivity* D. The transport velocity $\boldsymbol{v}$ is the velocity of the particle the scalar is associated with. In the context of this thesis, this will be either a solid particle or a fluid particle. Inserting equation (2.52) into equation (2.50) leads to the conservative form of the transport equation:

$$\left.\frac{\partial c}{\partial t}\right|_{\boldsymbol{x}} + \boldsymbol{\nabla}\cdot(c\boldsymbol{v} - D\boldsymbol{\nabla}c) - \sigma(c) = 0. \tag{2.53}$$

The transport equation is written in the spatial, Eulerian configuration. For applications in coupled problems, like passive transport in FSI, or, as will be shown later, for transport in porous media, it is more convenient to rewrite the above equation with respect to a moving domain. In ALE formulation the transport equation reads

$$\left.\frac{\partial c}{\partial t}\right|_{\boldsymbol{\mathcal{X}}} - \boldsymbol{v}^{\mathrm{g}}\cdot\boldsymbol{\nabla}c + \boldsymbol{\nabla}\cdot(c\boldsymbol{v} - D\boldsymbol{\nabla}c) - \sigma(c) = 0. \tag{2.54}$$

As for the ALE formulation of the Navier-Stokes equations, the local time derivative is recast with respect to the arbitrary mesh coordinate using the fundamental ALE equation (2.6). This leads to an additional convective term. In order to obtain the convective form, the divergence term is further expanded using the product rule

$$\left.\frac{\partial c}{\partial t}\right|_{\boldsymbol{\mathcal{X}}} - \boldsymbol{v}^{\mathrm{g}}\cdot\boldsymbol{\nabla}c + c\boldsymbol{\nabla}\cdot\boldsymbol{v} + \boldsymbol{v}\cdot\boldsymbol{\nabla}c - \boldsymbol{\nabla}\cdot(D\boldsymbol{\nabla}c) - \sigma(c) = 0. \tag{2.55}$$

If the transport velocity is divergence-free, like for incompressible flow, for instance, the respective term can be canceled. One obtains

$$\left.\frac{\partial c}{\partial t}\right|_{\boldsymbol{\mathcal{X}}} + (\boldsymbol{v} - \boldsymbol{v}^{\mathrm{g}})\cdot\boldsymbol{\nabla}c - \boldsymbol{\nabla}\cdot(D\boldsymbol{\nabla}c) - \sigma(c) = 0. \tag{2.56}$$

3. Continuum Mechanics of Porous Media

In the following, a compact survey of the theory of porous media will be given. In particular, the governing equations for fluid flow through a deforming porous medium under finite deformations will be introduced. Using the basic principles of contiuum mechanics reviewed in the preceding chapter, the Darcy and the Darcy-Brinkman equation are presented. The constitutive equations are based on macroscopic thermodynamical arguments. This short summary of the most important concepts was already published by the author in a condensed form in [243, 244]. A more extensive review of mechanics of porous media can be found in the textbooks [66], [73] and [158] among others.

3.1. Nomenclature and Scales

Porous structures consist of a solid phase, the so called *matrix*, and a pore space. The latter is possibly filled with fluid. In general, the matrix is assumed to be impermeable. When observing porous media in a continuum sense, one has to distinguish between two phases which compose the infinitesimal volume: the *skeleton phase* and the *fluid phase*. The skeleton phase is formed by the matrix and the connected porous space emptied of fluid. The fluid phase is formed by the fluid filling the porous space (see Figure 3.1). In this thesis the porous media is assumed to be fully saturated, i.e. all pores are completely filled with fluid, and all pores are connected.

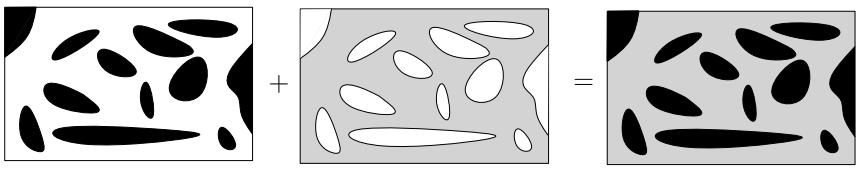

Figure 3.1: Porous media as superposition of skeleton and fluid phase, taken from [243].

The scale, where a local distinction between the phases can be made, will be denoted as *microscale* throughout this thesis. On the microscale the interface between fluid and structure is resolved and the physical laws hold according to classic continuum mechanics. Thus, it is still bigger than the atomic scale, which is not considered here. The scale of main interest for porous media is a larger scale and will be denoted as *macroscale*. On this scale, the two phases can no longer be distinguished. In general, porous media are characterized on the macroscale. In many applications, high resolution methods to identify the geometry of the microscale experimentally

are not available, not efficient or not of interest. Thus, values like porosity, tortuosity or permeability (quantities that will be explained in detail in the following sections) representing the macroscopic characteristics of the porous medium are measured in a macroscopic sense instead of analyzing the microgeometry. From a modelers point of view, it is therefore sensible to derive a formulation which is based on the macroscale, where information can be obtained and parameters are likely to be identified.

Physical quantities are classified into intrinsic, averaged microscopic, and averaged macroscopic. *Intrinsic* quantities are the true quantities on the microscale. Such quantities do not appear in the homogenized equations of porous media. They are replaced by averaged quantities during the derivations of the governing equations. Some exemplary derivations based on volume averaging can be found in Appendix A.1. *Averaged microscopic* quantities are averaged intrinsic quantities over the phase volume they are associated with. *Averaged macroscopic* quantities refer to whole porous volume. Both types of averaged quantities are either not marked explicitly or, if associated to a phase, with a corresponding superscript. For instance, the Green-Lagrange strains $\boldsymbol{E}$ are written without superscript, to emphasize that it refers to whole porous domain and not only the solid phase, whereas the averaged solid and fluid velocities are written as $\boldsymbol{v}^{\mathrm{s}}$ and $\boldsymbol{v}^{\mathrm{f}}$, respectively. The final equations are given in terms of averaged microscopic and/or macroscopic quantities. For single phase equations, as for pure solid or pure fluid dynamics, there is no difference between all three classifications.

3.2. Material Derivatives

One of the main specialties of porous media mechanics compared to classical continuum mechanics is the presence of two phases within one domain. Although mathematically sound, the simultaneous presence of skeleton and fluid phase at every point within the continuum can seem rather non-intuitive or unusual at first glance. A simple example is the effect of incompressibility. Even if structure and fluid phase are assumed to behave incompressible, the determinant of the deformation gradient is not necessarily equal to 1, as one with a traditional solid continuum mechanics background could expect. For instance, the volume can change due to in- and outflow without microscopic volume change, see Figure 3.2. Instead, incompressibility implies a direct relation between porosity and the Jacobian determinant J, see Section 4.4.1 for details.

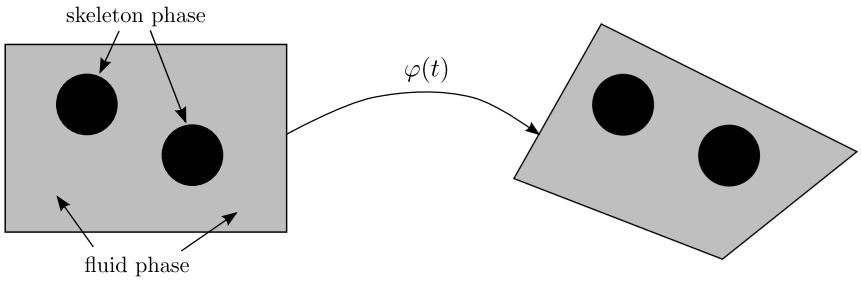

Figure 3.2: Macroscopic deformation without deformation of the microscopic structure.

Skeleton and fluid phases can deform independently, despite the fact that they could have occupied the same material volume in the initial configuration (see Figure 3.3). In this section,

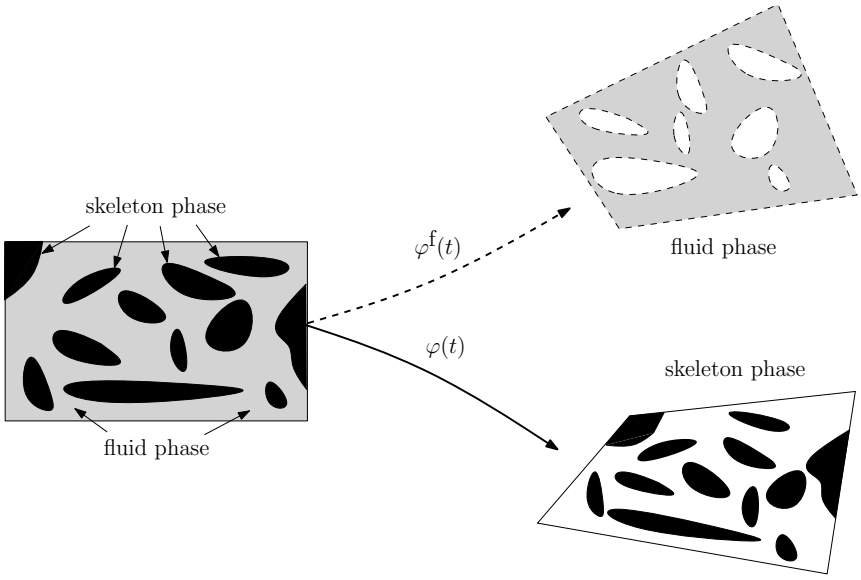

Figure 3.3: Independent deformation of skeleton phase φ (black) and fluid phase φ^{f} (grey), taken from [243].

a mathematical specialty arising from this continuum approach is considered, namely the occurrence of two material time derivatives. In classical continuum mechanics, the material time derivative is defined to follow the Lagrangean observer. Thus it describes the change in time of a physical particle's property. In a way, this is the time derivative with the most evident physical interpretation, when thinking of quantities as the density or the temperature in solid mechanics, for instance. As porous media consist of two types of phases at least, two different material time derivatives have to be distinguished: *the material time derivative with respect to the skeleton*, following the skeleton particle and *the material time derivative with respect to the fluid phase*, following the fluid particle. The total time derivative with respect to the skeleton phase $\mathrm{d}^{\mathrm{s}}/\,\mathrm{d}t$ of a material quantity $(\bullet)\,(\boldsymbol{X},t)$ is given as

$$\frac{\mathrm{d}^{\mathrm{s}}(\bullet)\,(\boldsymbol{X},t)}{\mathrm{d}t} = \left.\frac{\partial(\bullet)\,(\boldsymbol{X},t)}{\partial t}\right|_{\boldsymbol{X}}, \tag{3.1}$$

and the total time derivative of a spatial quantity $(\bullet)\,(\boldsymbol{x},t)$ as

$$\frac{\mathrm{d}^{\mathrm{s}}(\bullet)\,(\boldsymbol{x}(\boldsymbol{X},t),t)}{\mathrm{d}t} = \left.\frac{\partial(\bullet)\,(\boldsymbol{x},t)}{\partial t}\right|_{\boldsymbol{x}} + \boldsymbol{\nabla}\,(\bullet)\cdot\boldsymbol{v}^{\mathrm{s}}, \tag{3.2}$$

using the *velocity of the skeleton* $\boldsymbol{v}^{\mathrm{s}} = \partial\boldsymbol{x}/\partial t|_{\boldsymbol{X}}$. The Lagrangean observer of the porous continuum is defined to follow the skeleton phase. Hence, this material derivative is the same as the material derivative in classical solid mechanics. With respect to the fluid, the material coordinates $\boldsymbol{X}$ of the skeleton can be interpreted as an independently moving material configuration, as the movement of the skeleton is different from the movement of the fluid. In this context $\boldsymbol{X}\left(\boldsymbol{X}^{\mathrm{f}},t\right)$ is depending both on time and the material coordinates $\boldsymbol{X}^{\mathrm{f}}$ associated with the fluid phase. Such a setting is similar to a description based on an ALE formulation. Concerning

porous media, the observer is not arbitrary, but the Lagrangean observer of the skeleton phase. For the fluid, the basic idea yet stays the same. The similarity is even more evident in practice, as in ALE formulations, the mesh displacement is often determined by solving an elastostatic problem. The material derivative with respect to the fluid phase of a spatial quantity $(\bullet)\,(\boldsymbol{x}(\boldsymbol{X},t),t)$ can be written as

$$\begin{aligned}\frac{\mathrm{d}^{\mathrm{f}}(\bullet)\,(\boldsymbol{x},t)}{\mathrm{d}t} &= \frac{\partial(\bullet)\,(\boldsymbol{x}(\boldsymbol{X},t),t)}{\partial t}\bigg|_{\boldsymbol{X}} + \frac{\partial\,(\bullet)\,(\boldsymbol{x}(\boldsymbol{X},t),t)}{\partial \boldsymbol{X}} \cdot \frac{\partial \boldsymbol{X}}{\partial t}\bigg|_{\boldsymbol{X}^{\mathrm{f}}} \\ &= \frac{\partial(\bullet)}{\partial t}\bigg|_{\boldsymbol{X}} + \frac{\partial\,(\bullet)}{\partial \boldsymbol{x}} \cdot \frac{\partial \boldsymbol{x}}{\partial \boldsymbol{X}} \cdot \frac{\partial \boldsymbol{X}}{\partial t}\bigg|_{\boldsymbol{X}^{\mathrm{f}}}. \end{aligned} \tag{3.3}$$

Consequently, the velocity of the fluid is given as

$$\boldsymbol{v}^{\mathrm{f}} = \frac{\mathrm{d}^{\mathrm{f}}\boldsymbol{x}}{\mathrm{d}t} = \frac{\partial \boldsymbol{x}(\boldsymbol{X},t)}{\partial t}\bigg|_{\boldsymbol{X}} + \frac{\partial \boldsymbol{x}}{\partial \boldsymbol{X}} \cdot \frac{\partial \boldsymbol{X}}{\partial t}\bigg|_{\boldsymbol{X}^{\mathrm{f}}}. \tag{3.4}$$

Solving (3.4) for the second summand, and substituting this expression in (3.3) yields

$$\frac{\mathrm{d}^{\mathrm{f}}(\bullet)\,(\boldsymbol{x},t)}{\mathrm{d}t} = \frac{\partial(\bullet)\,(\boldsymbol{X},t)}{\partial t}\bigg|_{\boldsymbol{X}} + (\boldsymbol{v}^{\mathrm{f}} - \boldsymbol{v}^{\mathrm{s}}) \cdot \boldsymbol{\nabla}\,(\bullet)\,, \tag{3.5}$$

where $\partial \boldsymbol{x}(\boldsymbol{X},t)/\partial t|_{\boldsymbol{X}} = \boldsymbol{v}^{\mathrm{s}}$ has been utilized. Note, that this equation and its derivation is equivalent to the fundamental ALE equation (2.6), if the skeleton coordinates $\boldsymbol{X}$ are interpreted as reference coordinates of the fluid and therefore $\boldsymbol{v}^{\mathrm{s}}$ as grid velocity.

The material derivative of an integral quantity can be evaluated as

$$\begin{aligned}&\frac{\mathrm{d}^{\pi}}{\mathrm{d}t}\int (\bullet)\;\mathrm{d}\Omega_t = \int \frac{\mathrm{d}^{\pi}}{\mathrm{d}t}((\bullet)\,J)\,\mathrm{d}\Omega_0 = \\ &\quad = \int J\,\frac{\partial(\bullet)}{\partial t}\bigg|_{\boldsymbol{x}} + J\boldsymbol{\nabla}\,(\bullet)\cdot\boldsymbol{v}^{\pi} + J\,(\bullet)\,\boldsymbol{\nabla}\cdot\boldsymbol{v}^{\pi}\,\mathrm{d}\Omega_0 = \int \frac{\partial(\bullet)}{\partial t}\bigg|_{\boldsymbol{x}} + \boldsymbol{\nabla}\cdot((\bullet)\,\boldsymbol{v}^{\pi})\,\mathrm{d}\Omega_t. \end{aligned} \tag{3.6}$$

Therein, the chain rule and the material derivative of the Jacobian determinant

$$\frac{\mathrm{d}^{\pi}J}{\mathrm{d}t} = J\boldsymbol{\nabla}\cdot\boldsymbol{v}^{\pi}, \tag{3.7}$$

were used, with the index $\pi = \mathrm{s},\mathrm{f}$ denoting the respective phase.

Remark 3.1 *One has to keep in mind, that both time derivative with respect to skeleton and fluid phase can - and actually will - be applied to any type of quantity, disregarding if the quantity itself belongs to the skeleton or the fluid. The physical interpretation of a material derivative only holds, if time derivative and quantity match, hence for instance for the material time derivative with respect to the fluid phase of a quantity of the fluid (e.g. its density). If this is not the case, a clear physical interpretation becomes elusive.*

3.3. Conservation of Mass

The balance of mass for both phases will be derived in the following. In the absence of sources or sinks, the mass in the domain Ω_t occupied by the porous medium at time t has to be conserved, i.e.

$$\frac{\mathrm{d}^{\mathrm{s}}}{\mathrm{d}t} \int \rho^{\mathrm{s}}(1-\phi)\ \mathrm{d}\Omega_t = 0, \tag{3.8}$$

$$\frac{\mathrm{d}^{\mathrm{f}}}{\mathrm{d}t} \int \rho^{\mathrm{f}}\phi\ \mathrm{d}\Omega_t = 0, \tag{3.9}$$

where ρ^{s} and ρ^{f} denote the averaged microscopic density of the respective phase. Equation (3.8) is the balance of mass of skeleton, (3.10) the balance of mass of the fluid. As ϕ and $(1-\phi)$ denote the volume fraction of the fluid and skeleton phase, respectively, $\rho^{\mathrm{s}}(1-\phi)$ and $\rho^{\mathrm{f}}\phi$ can be interpreted as macroscopic densities. Applying equation (3.6) the local balance of mass can be formulated as

$$\left.\frac{\partial(\rho^{\mathrm{s}}(1-\phi))}{\partial t}\right|_{\boldsymbol{x}} + \boldsymbol{\nabla}\cdot(\rho^{\mathrm{s}}(1-\phi)\boldsymbol{v}^{\mathrm{s}}) = 0, \tag{3.10}$$

$$\left.\frac{\partial\left(\rho^{\mathrm{f}}\phi\right)}{\partial t}\right|_{\boldsymbol{x}} + \boldsymbol{\nabla}\cdot(\rho^{\mathrm{f}}\phi\boldsymbol{v}^{\mathrm{f}}) = 0. \tag{3.11}$$

The balance of mass of the skeleton (3.10) is preferably written in the material configuration, yielding

$$J\rho^{\mathrm{s}}(1-\phi) = \rho_0^{\mathrm{s}}(1-\phi_0) = m_0^{\mathrm{s}}, \tag{3.12}$$

where ρ_0^{s}, ϕ_0 and m_0^{s} denote the *initial skeleton density, porosity, and mass*, respectively. Alternatively, the balance of mass is often written in terms of macroscopic masses or densities. Inserting equation (3.2) into equation (3.11) gives

$$\left.\frac{\partial(\rho^{\mathrm{f}}\phi)}{\partial t}\right|_{\boldsymbol{X}} \underbrace{-\boldsymbol{\nabla}(\rho^{\mathrm{f}}\phi)\cdot\boldsymbol{v}^{\mathrm{s}}}_{\rho^{\mathrm{f}}\phi\boldsymbol{\nabla}\boldsymbol{v}^{\mathrm{s}}-\boldsymbol{\nabla}\cdot(\rho^{\mathrm{f}}\phi\boldsymbol{v}^{\mathrm{s}})} + \boldsymbol{\nabla}\cdot(\rho^{\mathrm{f}}\phi\boldsymbol{v}^{\mathrm{f}}) = 0. \tag{3.13}$$

The term beneath the brackets follows from the product rule. Using equation (3.7) one can reformulate equation (3.13) to obtain the following alternative form of the continuity equation:

$$\frac{1}{J}\frac{\mathrm{d}^{\mathrm{s}}m^{\mathrm{f}}}{\mathrm{d}t} + \boldsymbol{\nabla}\cdot\boldsymbol{w}^{\mathrm{f}} = 0, \tag{3.14}$$

with the *local fluid mass*

$$m^{\mathrm{f}} = \rho^{\mathrm{f}}\phi J, \tag{3.15}$$

and the *relative fluid mass flux*

$$\boldsymbol{w}^{\mathrm{f}} = \rho^{\mathrm{f}}\phi\left(\boldsymbol{v}^{\mathrm{f}} - \boldsymbol{v}^{\mathrm{s}}\right). \tag{3.16}$$

Introducing the *material relative fluid mass flux*

$$\boldsymbol{W}^{\mathrm{f}} = J\boldsymbol{F}^{-1}\cdot\boldsymbol{w}^{\mathrm{f}}, \tag{3.17}$$

the continuity equation in material configuration follows as

$$\frac{\mathrm{d}^{\mathrm{s}} m^{\mathrm{f}}}{\mathrm{d}t} + \boldsymbol{\nabla}_0 \cdot \boldsymbol{W}^{\mathrm{f}} = 0. \tag{3.18}$$

This form of the balance of mass will be used for some thermodynamic considerations in Section 3.5. The equations that actually will be used in the final non-linear system are the equations (3.11) and (3.12).

Remark 3.2 *The pull-back of $\boldsymbol{w}^{\mathrm{f}}$ in equation* (3.17) *is not defined as the pull-back of line elements in equation* (2.9) *but via the Piola transform as used for area elements in equation* (2.12)*. This definition is more suitable as $\boldsymbol{w}^{\mathrm{f}}$ and $\boldsymbol{W}^{\mathrm{f}}$ are representing fluxes. From equation* (3.17) *it follows that $\boldsymbol{\nabla} \cdot \boldsymbol{w}^{\mathrm{f}} = \boldsymbol{\nabla}_0 \cdot \boldsymbol{W}^{\mathrm{f}}$, i.e. the Piola transform conserves the flux between material and spatial configuration.*

Remark 3.3 *Note that even when assuming the density to be constant, there will still be a transient term in the continuity equation of the fluid* (3.11)*, as the porosity can and will change in time due to finite deformations. Therefore, the macroscopic continuity equation for the fluid phase shows characteristics of a compressible flow, even if the microscopic flow is assumed to be incompressible.*

3.4. Balance of Linear Momentum

The balance of momentum for the whole porous medium in the spatial configuration can be written as

$$\int \rho \hat{\boldsymbol{b}} - \rho^{\mathrm{s}}(1-\phi)\boldsymbol{a}^{\mathrm{s}} - \rho^{\mathrm{f}}\phi\boldsymbol{a}^{\mathrm{f}} \,\mathrm{d}\Omega_t + \int \boldsymbol{\sigma} \cdot \boldsymbol{n} \,\mathrm{d}\Gamma_t = \boldsymbol{0}, \tag{3.19}$$

where $\boldsymbol{a}^{\mathrm{s}}$ and $\boldsymbol{a}^{\mathrm{f}}$ denote the *averaged microscopic skeleton* and *fluid acceleration*, respectively. The macroscopic Cauchy stress tensor $\boldsymbol{\sigma}$ represents the loading state of the whole porous medium, i.e. both phases. The body forces per spatial unit volume $\hat{\boldsymbol{b}}$ refer to the *macroscopic total density* given by

$$\rho = \rho^{\mathrm{s}}(1-\phi) + \rho^{\mathrm{f}}\phi. \tag{3.20}$$

Equation (3.19) seems to be intuitive, as it resembles the balance of linear momentum (2.29) known from classical elastodynamics. However, its derivation starting from the microscopic equations is non-trivial. An approach based on volume averaging is sketched in Appendix A.1.1. After application of Gauss' divergence theorem, the local balance of momentum in spatial configuration can be obtained as

$$\nabla \cdot \boldsymbol{\sigma} + \rho^{\mathrm{s}}(1-\phi)\left(\hat{\boldsymbol{b}} - \boldsymbol{a}^{\mathrm{s}}\right) + \rho^{\mathrm{f}}\phi\left(\hat{\boldsymbol{b}} - \boldsymbol{a}^{\mathrm{f}}\right) = \boldsymbol{0}. \tag{3.21}$$

Transforming this equation to the material frame leads to

$$\nabla_0 \cdot (\boldsymbol{F} \cdot \boldsymbol{S}) + J\rho^{\mathrm{s}}(1-\phi)\left(\hat{\boldsymbol{b}} - \boldsymbol{a}^{\mathrm{s}}\right) + J\rho^{\mathrm{f}}\phi\left(\hat{\boldsymbol{b}} - \boldsymbol{a}^{\mathrm{f}}\right) = \boldsymbol{0}. \tag{3.22}$$

An alternative form of the local balance of momentum in the material configuration is obtained by introducing the conservation of mass of the skeleton phase (3.12) as

$$\nabla_0 \cdot (\boldsymbol{F} \cdot \boldsymbol{S}) + m_0^{\mathrm{s}} \left(\hat{\boldsymbol{b}} - \boldsymbol{a}^{\mathrm{s}} \right) + J \rho^{\mathrm{f}} \phi \left(\hat{\boldsymbol{b}} - \boldsymbol{a}^{\mathrm{f}} \right) = \boldsymbol{0}. \tag{3.23}$$

In this form the nature of equation as the balance of linear momentum of the mixture is evident. Two acceleration terms account for the inertia of the skeleton and the fluid respectively. The other contributions, i.e. the stress contribution and the body forces, are not written separately for the two phases. The body force is applied on the whole mixture and distributed by the corresponding mass fraction. The stress and the deformation gradient are written with respect to the macroscopic, averaged deformation. Hence, the constitutive law for the stress tensor will include both structural and fluid contributions. Note, that this stress tensor differs from the effective stress, which is a quantity commonly used in soil mechanics, see Section 3.5.2.1.

3.5. Constitutive Equations

In this section different versions of constitutive laws will be derived. It is based on thermodynamic principles and can be found in more detail in [66, chap. 3]. Even though isothermal conditions will be assumed in the subsequent chapters, this section includes the more general case of changing temperatures. This is helpful for the comprehension of the thermodynamics of porous media and also for the understanding of the model used for incorporating reactive porosities in Section 5.4.3, where chemical reactions are included into the general thermodynamical equations of state.

3.5.1. Basic Formulation

First, some basic thermodynamical relations are introduced. The *internal specific energy* e^{f} of the fluid depends on the variables of state as following:

$$e^{\mathrm{f}} = e^{\mathrm{f}} \left(\frac{1}{\rho^{\mathrm{f}}}, s^{\mathrm{f}} \right) : \qquad p^{\mathrm{f}} = - \frac{\partial e^{\mathrm{f}}}{\partial \left(\frac{1}{\rho^{\mathrm{f}}} \right)}, \qquad T = \frac{\partial e^{\mathrm{f}}}{\partial s^{\mathrm{f}}}. \tag{3.24}$$

Therein, s^{f} and T denote the *entropy* and the *temperature*, respectively. Alternative formulations can be obtained by introducing the *specific enthalpy* h^{f}, the *specific Helmholtz free energy* ψ^{f} and the *specific free enthalpy or Gibbs potential* g^{f}:

$$h^{\mathrm{f}} = e^{\mathrm{f}} + \frac{p^{\mathrm{f}}}{\rho^{\mathrm{f}}}, \tag{3.25}$$

$$\psi^{\mathrm{f}} = e^{\mathrm{f}} - T s^{\mathrm{f}}, \tag{3.26}$$

$$g^{\mathrm{f}} = \psi^{\mathrm{f}} + \frac{p^{\mathrm{f}}}{\rho^{\mathrm{f}}} = h^{\mathrm{f}} - T s^{\mathrm{f}}. \tag{3.27}$$

The alternative equations of state then read

$$h^{\mathrm{f}} = h^{\mathrm{f}}\left(p^{\mathrm{f}}, s^{\mathrm{f}}\right): \qquad \frac{1}{\rho^{\mathrm{f}}} = \frac{\partial h^{\mathrm{f}}}{\partial p^{\mathrm{f}}}, \qquad T = \frac{\partial h^{\mathrm{f}}}{\partial s^{\mathrm{f}}}, \tag{3.28}$$

$$\psi^{\mathrm{f}} = \psi^{\mathrm{f}}\left(\frac{1}{\rho^{\mathrm{f}}}, T\right): \qquad p^{\mathrm{f}} = -\frac{\partial \psi^{\mathrm{f}}}{\partial\left(\frac{1}{\rho^{\mathrm{f}}}\right)}, \qquad s^{\mathrm{f}} = -\frac{\partial \psi^{\mathrm{f}}}{\partial T}, \tag{3.29}$$

$$g^{\mathrm{f}} = g^{\mathrm{f}}\left(p^{\mathrm{f}}, T\right): \qquad \frac{1}{\rho^{\mathrm{f}}} = \frac{\partial g^{\mathrm{f}}}{\partial p^{\mathrm{f}}}, \qquad s^{\mathrm{f}} = -\frac{\partial g^{\mathrm{f}}}{\partial T}. \tag{3.30}$$

Having those quantities at hand, the constitutive equations can be derived. Therefore, the first principle of thermodynamics is used: Neglecting internal heat sources, the total time derivative of the *total internal energy* $\mathrm{d}W_{\mathrm{ti}}/\,\mathrm{d}t$ needs to be equal to the sum of the *inner mechanical power* P_{int} and the *heat flux* $\boldsymbol{q}^{\mathrm{th}}$ over the boundary Γ_t of the domain Ω_t

$$\frac{\mathrm{d}}{\mathrm{d}t} W_{\mathrm{ti}} = P_{\mathrm{int}} + \int \boldsymbol{q}^{\mathrm{th}} \cdot \boldsymbol{n}\ \mathrm{d}\Gamma_t. \tag{3.31}$$

In the following, $\mathrm{d}W_{\mathrm{ti}}/\,\mathrm{d}t$ and P_{int} will expressed in terms of kinematic and kinetic quantities. According to [66, chap. 2.4.1] the inner mechanical power of a porous medium can be calculated as follows:

$$P_{\mathrm{int}} = \int (1-\phi)\boldsymbol{\sigma}^{\mathrm{s}} : \boldsymbol{\varepsilon} + \phi\boldsymbol{\sigma}^{\mathrm{f}} : \boldsymbol{\varepsilon}^{\mathrm{f}} + \boldsymbol{f}^{\mathrm{f}}_{\mathrm{sf}} \cdot \left(\boldsymbol{v}^{\mathrm{s}} - \boldsymbol{v}^{\mathrm{f}}\right)\ \mathrm{d}\Omega_t, \tag{3.32}$$

with the *averaged interface traction* $\boldsymbol{f}^{\mathrm{f}}_{\mathrm{sf}}$ analogously to equation (A.8). The strain rates are given as

$$\boldsymbol{\varepsilon} = \boldsymbol{F}^{-\mathrm{T}} \cdot \dot{\boldsymbol{E}} \cdot \boldsymbol{F}^{-1} = \frac{1}{2}\left(\boldsymbol{\nabla}\boldsymbol{v}^{\mathrm{s}} + \left(\boldsymbol{\nabla}\boldsymbol{v}^{\mathrm{s}}\right)^{\mathrm{T}}\right), \tag{3.33}$$

$$\boldsymbol{\varepsilon}^{\mathrm{f}} = \boldsymbol{F}^{-\mathrm{T}} \cdot \dot{\boldsymbol{E}}^{\mathrm{f}} \cdot \boldsymbol{F}^{-1} = \frac{1}{2}\left(\boldsymbol{\nabla}\boldsymbol{v}^{\mathrm{f}} + \left(\boldsymbol{\nabla}\boldsymbol{v}^{\mathrm{f}}\right)^{\mathrm{T}}\right). \tag{3.34}$$

Hence, the inner mechanical power of a porous medium is composed of the inner mechanical power of the skeleton and the fluid phase, weighted with the respective volume fraction, and the mechanical power of the interface traction. For the following derivation, it is convenient to express the interface traction $\boldsymbol{f}^{\mathrm{f}}_{\mathrm{sf}}$ in terms of the fluid pressure p^{f}. The averaged balance of linear of momentum of the fluid phase, see also equation (A.9) with $\pi = f$, reads

$$\boldsymbol{\nabla}\cdot\left(\phi\boldsymbol{\sigma}^{\mathrm{f}}\right) + \rho^{\mathrm{f}}\phi\left(\hat{\boldsymbol{b}} - \boldsymbol{a}^{\mathrm{f}}\right) + \boldsymbol{f}^{\mathrm{f}}_{\mathrm{sf}} = \boldsymbol{0}. \tag{3.35}$$

Inserting equation (3.35) in equation (3.32) gives

$$\begin{aligned} P_{\mathrm{int}} &= \int \underbrace{\left[(1-\phi)\boldsymbol{\sigma}^{\mathrm{s}} + \phi\boldsymbol{\sigma}^{\mathrm{f}}\right]}_{\boldsymbol{\sigma}} : \boldsymbol{\varepsilon} + \phi\boldsymbol{\sigma}^{\mathrm{f}} : \left(\boldsymbol{\varepsilon}^{\mathrm{f}} - \boldsymbol{\varepsilon}\right) + \boldsymbol{\nabla}\cdot(\phi\boldsymbol{\sigma}^{\mathrm{f}}) \cdot \left(\boldsymbol{v}^{\mathrm{f}} - \boldsymbol{v}^{\mathrm{s}}\right) + \left(\hat{\boldsymbol{b}} - \boldsymbol{a}^{\mathrm{f}}\right)\boldsymbol{w}^{\mathrm{f}}\ \mathrm{d}\Omega_t \\ &= \int \boldsymbol{\sigma} : \boldsymbol{\varepsilon} + \phi\boldsymbol{\sigma}^{\mathrm{f}} : \left(\boldsymbol{\nabla}\left(\boldsymbol{v}^{\mathrm{f}} - \boldsymbol{v}^{\mathrm{s}}\right)\right) + \boldsymbol{\nabla}\cdot(\phi\boldsymbol{\sigma}^{\mathrm{f}}) \cdot \left(\boldsymbol{v}^{\mathrm{f}} - \boldsymbol{v}^{\mathrm{s}}\right) + \left(\hat{\boldsymbol{b}} - \boldsymbol{a}^{\mathrm{f}}\right) \cdot \boldsymbol{w}^{\mathrm{f}}\ \mathrm{d}\Omega_t, \end{aligned} \tag{3.36}$$

with the relative mass flux $\boldsymbol{w}^{\mathrm{f}} = \rho^{\mathrm{f}}\phi\left(\boldsymbol{v}^{\mathrm{f}} - \boldsymbol{v}^{\mathrm{s}}\right)$ from equation (3.16). The second term in the above equation was reformulated using the symmetry of $\boldsymbol{\sigma}^{\mathrm{f}}$:

$$\begin{aligned}\phi\boldsymbol{\sigma}^{\mathrm{f}} : \left(\boldsymbol{\varepsilon}^{\mathrm{f}} - \boldsymbol{\varepsilon}\right) &= \phi\boldsymbol{\sigma}^{\mathrm{f}} : \frac{1}{2}\left(\left(\boldsymbol{\nabla}\boldsymbol{v}^{\mathrm{f}} - \boldsymbol{\nabla}\boldsymbol{v}^{\mathrm{s}}\right) + \left(\boldsymbol{\nabla}\boldsymbol{v}^{\mathrm{f}} - \boldsymbol{\nabla}\boldsymbol{v}^{\mathrm{s}}\right)^{\mathrm{T}}\right) \\ &= \phi\boldsymbol{\sigma}^{\mathrm{f}} : \left(\boldsymbol{\nabla}\left(\boldsymbol{v}^{\mathrm{f}} - \boldsymbol{v}^{\mathrm{s}}\right)\right).\end{aligned}$$

Using the product rule one finally obtains

$$P_{\mathrm{int}} = \int \boldsymbol{\sigma} : \boldsymbol{\varepsilon} + \boldsymbol{\nabla}\cdot\left(\frac{1}{\rho^{\mathrm{f}}}\boldsymbol{\sigma}^{\mathrm{f}} \cdot \boldsymbol{w}^{\mathrm{f}}\right) + \left(\hat{\boldsymbol{b}} - \boldsymbol{a}^{\mathrm{f}}\right) \cdot \boldsymbol{w}^{\mathrm{f}} \, \mathrm{d}\Omega_t. \tag{3.37}$$

This identity is an expression for the inner mechanical power depending on spatial quantities only. Next, the left side of equation (3.31) is considered. The time derivative of the total internal energy W_{ti} of a porous continuum can be expressed by the *spatial specific internal energies* e^{s} and e^{f} using equation (3.6) as

$$\begin{aligned}\frac{\mathrm{d}W_{\mathrm{ti}}}{\mathrm{d}t} &= \frac{\mathrm{d}^{\mathrm{s}}}{\mathrm{d}t}\int \rho^{\mathrm{s}}(1-\phi)e^{\mathrm{s}} \, \mathrm{d}\Omega_t + \frac{\mathrm{d}^{\mathrm{f}}}{\mathrm{d}t}\int \rho^{\mathrm{f}}\phi e^{\mathrm{f}} \, \mathrm{d}\Omega_t \\ &= \int \frac{\mathrm{d}^{\mathrm{s}}e}{\mathrm{d}t} + e\boldsymbol{\nabla}\cdot\boldsymbol{v}^{\mathrm{s}} + \boldsymbol{\nabla}\cdot(e^{\mathrm{f}}\boldsymbol{w}^{\mathrm{f}}) \, \mathrm{d}\Omega_t,\end{aligned} \tag{3.38}$$

wherein $e = \rho^{\mathrm{s}}(1-\phi)e^{\mathrm{s}} + \rho^{\mathrm{f}}\phi e^{\mathrm{f}}$ denotes the *total internal energy* per unit volume in the deformed state. Inserting the above derived expressions for the internal mechanical power (3.37) and the total internal energy (3.38) into the balance of energy (3.31), one obtains by applying the divergence theorem on the heat term, splitting the fluid stress $\boldsymbol{\sigma}^{\mathrm{f}} = -p^{\mathrm{f}}\mathbf{1} + \boldsymbol{\sigma}^{\mathrm{f}}_{\mathrm{visc}}$, inserting equation (3.25) and some algebraic rearrangements

$$\boldsymbol{\sigma} : \boldsymbol{\varepsilon} + \boldsymbol{\nabla}\cdot\left(-h^{\mathrm{f}}\boldsymbol{w}^{\mathrm{f}} + \frac{1}{\rho^{\mathrm{f}}}\boldsymbol{\sigma}^{\mathrm{f}}_{\mathrm{visc}} \cdot \boldsymbol{w}^{\mathrm{f}} + \boldsymbol{q}^{\mathrm{th}}\right) + \left(\hat{\boldsymbol{b}} - \boldsymbol{a}^{\mathrm{f}}\right) \cdot \boldsymbol{w}^{\mathrm{f}} - \frac{\mathrm{d}^{\mathrm{s}}e}{\mathrm{d}t} - e\boldsymbol{\nabla}\cdot\boldsymbol{v}^{\mathrm{s}} = 0. \tag{3.39}$$

This equation represents the balance of energy of a porous medium formulated in the current configuration. Now, the energy balance will be reformulated with respect to the material configuration. In order to do so, some definitions and rearrangements of terms will be performed first. The *material heat flux* $\boldsymbol{Q}^{\mathrm{th}}$ is defined via the Piola transform (see Remark 3.2) as

$$\boldsymbol{Q}^{\mathrm{th}} = J\boldsymbol{F}^{-1} \cdot \boldsymbol{q}^{\mathrm{th}}. \tag{3.40}$$

The viscous stress contribution in equation (3.39) is rewritten as follows

$$\boldsymbol{\nabla}\cdot\left(\frac{1}{\rho^{\mathrm{f}}}\boldsymbol{\sigma}^{\mathrm{f}}_{\mathrm{visc}} \cdot \boldsymbol{w}^{\mathrm{f}}\right) = \frac{1}{\phi\rho^{\mathrm{f}}}\boldsymbol{w}^{\mathrm{f}} \cdot \left(\boldsymbol{\nabla}\cdot\left(\phi\boldsymbol{\sigma}^{\mathrm{f}}_{\mathrm{visc}}\right)\right) + \phi\boldsymbol{\sigma}^{\mathrm{f}}_{\mathrm{visc}} : \boldsymbol{\nabla}\left(\frac{1}{\phi\rho^{\mathrm{f}}}\boldsymbol{w}^{\mathrm{f}}\right). \tag{3.41}$$

Furthermore, the second summand of above equation is reformulated with the definition of $\boldsymbol{w}^{\mathrm{f}}$ and due to symmetry of $\boldsymbol{\sigma}^{\mathrm{f}}_{\mathrm{visc}}$ as

$$\begin{aligned}\phi\boldsymbol{\sigma}^{\mathrm{f}}_{\mathrm{visc}} : \boldsymbol{\nabla}\left(\frac{1}{\phi\rho^{\mathrm{f}}}\boldsymbol{w}^{\mathrm{f}}\right) &= \phi\boldsymbol{\sigma}^{\mathrm{f}}_{\mathrm{visc}} : \left(\boldsymbol{\nabla}\left(\boldsymbol{v}^{\mathrm{f}} - \boldsymbol{v}^{\mathrm{s}}\right)\right) \\ &= \phi\boldsymbol{\sigma}^{\mathrm{f}}_{\mathrm{visc}} : \frac{1}{2}\left(\left(\boldsymbol{\nabla}\boldsymbol{v}^{\mathrm{f}} - \boldsymbol{\nabla}\boldsymbol{v}^{\mathrm{s}}\right) + \left(\boldsymbol{\nabla}\boldsymbol{v}^{\mathrm{f}} - \boldsymbol{\nabla}\boldsymbol{v}^{\mathrm{s}}\right)^{\mathrm{T}}\right) \\ &= \phi\boldsymbol{\sigma}^{\mathrm{f}}_{\mathrm{visc}} : \left(\boldsymbol{\varepsilon}^{\mathrm{f}} - \boldsymbol{\varepsilon}\right). \end{aligned} \tag{3.42}$$

Using equations (3.7), (3.17), (3.41) , and (3.42) the energy balance with respect to the material configuration with the *material energy density* $E_0 = Je$ can be derived as

$$\begin{aligned}\boldsymbol{S} : \dot{\boldsymbol{E}} + \boldsymbol{\nabla}_0 \cdot\left(-h^{\mathrm{f}}\boldsymbol{W}^{\mathrm{f}} + \boldsymbol{Q}^{\mathrm{th}}\right) + \frac{1}{\phi\rho^{\mathrm{f}}}\left(\boldsymbol{\nabla}_0 \cdot\left(\phi\boldsymbol{P}^{\mathrm{f}}_{\mathrm{visc}}\right)\right)\cdot\boldsymbol{F}\cdot\boldsymbol{W}^{\mathrm{f}} \\ +\phi\boldsymbol{S}^{\mathrm{f}}_{\mathrm{visc}} : \left(\dot{\boldsymbol{E}}^{\mathrm{f}} - \dot{\boldsymbol{E}}\right) + \left(\hat{\boldsymbol{b}} - \boldsymbol{a}^{\mathrm{f}}\right)\cdot\boldsymbol{F}\cdot\boldsymbol{W}^{\mathrm{f}} - \frac{\mathrm{d}^{\mathrm{s}}E_0}{\mathrm{d}t} = 0. \end{aligned} \tag{3.43}$$

Relation (3.43) represents the local energy balance of a porous medium depending on material quantities. Now, the material energy density E_0 will be expressed by the strain energy and the entropy. Therefore the second principle of thermodynamics is used. The second principle of thermodynamics, the balance of entropy, reads

$$\frac{\mathrm{d}^{\mathrm{s}}}{\mathrm{d}t}\int \rho^{\mathrm{s}}(1-\phi)s^{\mathrm{s}}\,\mathrm{d}\Omega_t + \frac{\mathrm{d}^{\mathrm{f}}}{\mathrm{d}t}\int \rho^{\mathrm{f}}\phi s^{\mathrm{f}}\,\mathrm{d}\Omega_t \geq \int \frac{\boldsymbol{q}^{\mathrm{th}}}{T}\cdot\boldsymbol{n}\,\mathrm{d}\Gamma_t. \tag{3.44}$$

Analogue derivation as for equation (3.43) and by introducing the *total material entropy density* $S = J\left(\rho^{\mathrm{s}}(1-\phi)s^{\mathrm{s}} + \rho^{\mathrm{f}}\phi s^{\mathrm{f}}\right)$ leads to the local material form of the entropy balance

$$\frac{\mathrm{d}^{\mathrm{s}}S}{\mathrm{d}t} \geq -\boldsymbol{\nabla}_0 \cdot\left(s^{\mathrm{f}}\boldsymbol{W}^{\mathrm{f}} + \frac{\boldsymbol{Q}^{\mathrm{th}}}{T}\right). \tag{3.45}$$

Giving the material Helmholtz free energy $\Psi = E_0 - TS$ and replacing s^{f} and $\boldsymbol{Q}$ using equation (3.27) and (3.45), equation (3.43) can be split into a skeleton, fluid and temperature dependent part

$$\Phi = \Phi^{\mathrm{s}} + \Phi^{\mathrm{f}} + \Phi^{\mathrm{th}} \geq 0, \tag{3.46}$$

with

$$\Phi^{\mathrm{s}} = \boldsymbol{S} : \dot{\boldsymbol{E}} - g^{\mathrm{f}}\cdot\boldsymbol{\nabla}_0\cdot\boldsymbol{W}^{\mathrm{f}} - \phi\boldsymbol{S}^{\mathrm{f}}_{\mathrm{visc}} : \dot{\boldsymbol{E}} - S\left.\frac{\partial T}{\partial t}\right|_{\boldsymbol{X}} - \left.\frac{\partial \Psi}{\partial t}\right|_{\boldsymbol{X}}, \tag{3.47}$$

$$\Phi^{\mathrm{f}} = \left[-\boldsymbol{\nabla}_0\, g^{\mathrm{f}}\big|_T + \frac{1}{\phi\rho^{\mathrm{f}}}\left(\boldsymbol{\nabla}_0 \cdot\left(\phi\boldsymbol{P}^{\mathrm{f}}_{\mathrm{visc}}\right)\right)\cdot\boldsymbol{F} + \left(\hat{\boldsymbol{b}} - \boldsymbol{a}^{\mathrm{f}}\right)\boldsymbol{F}\right]\cdot\boldsymbol{W}^{\mathrm{f}} + \phi\boldsymbol{S}^{\mathrm{f}}_{\mathrm{visc}} : \dot{\boldsymbol{E}}^{\mathrm{f}}, \tag{3.48}$$

$$\Phi^{\mathrm{th}} = -\frac{\boldsymbol{Q}^{\mathrm{th}}}{T}\cdot\boldsymbol{\nabla}_0\, T, \tag{3.49}$$

where Φ can be identified as *dissipation term*. The inequality (3.46) is the *Clausius-Duhem inequality of porous continua* (see [66, chap. 3.2.3]). In order to identify Φ^{s} as dissipation of

the skeleton phase, equation (3.47) is further rearranged. First, the continuity equation (3.18) is inserted

$$\Phi^{\mathrm{s}} = \boldsymbol{S} : \dot{\boldsymbol{E}} - \phi \boldsymbol{S}^{\mathrm{f}}_{\mathrm{visc}} : \dot{\boldsymbol{E}} + g^{\mathrm{f}} \frac{\mathrm{d}^{\mathrm{s}} m^{\mathrm{f}}}{\mathrm{d}t} - S \frac{\mathrm{d}^{\mathrm{s}} T}{\mathrm{d}t} - \frac{\mathrm{d}^{\mathrm{s}} \Psi}{\mathrm{d}t}. \tag{3.50}$$

Furthermore, due to the additive characteristic of energy and entropy, both can be split into skeleton and fluid part:

$$\Psi = \Psi^{\mathrm{s}} + m^{\mathrm{f}} \psi^{\mathrm{f}}, \qquad S = S^{\mathrm{s}} + m^{\mathrm{f}} s^{\mathrm{f}}. \tag{3.51}$$

Using equations (3.25)–(3.30) and the definition $m^{\mathrm{f}} = \rho^{\mathrm{f}} J \phi$ one can easily derive the following form:

$$\frac{\mathrm{d}^{\mathrm{s}} \Psi}{\mathrm{d}t} = \frac{\mathrm{d}^{\mathrm{s}} \Psi^{\mathrm{s}}}{\mathrm{d}t} + \frac{\mathrm{d}^{\mathrm{s}} \left(m^{\mathrm{f}} \psi^{\mathrm{f}} \right)}{\mathrm{d}t} = \frac{\mathrm{d}^{\mathrm{s}} \Psi^{\mathrm{s}}}{\mathrm{d}t} + g^{\mathrm{f}} \frac{\mathrm{d}^{\mathrm{s}} m^{\mathrm{f}}}{\mathrm{d}t} - p^{\mathrm{f}} \frac{\mathrm{d}^{\mathrm{s}} (J\phi)}{\mathrm{d}t} + m^{\mathrm{f}} s^{\mathrm{f}} \frac{\mathrm{d}^{\mathrm{s}} T}{\mathrm{d}t}. \tag{3.52}$$

Inserting this into equation (3.50) leads to

$$\Phi^{\mathrm{s}} = \boldsymbol{S} : \dot{\boldsymbol{E}} - \phi \boldsymbol{S}^{\mathrm{f}}_{\mathrm{visc}} : \dot{\boldsymbol{E}} + p^{\mathrm{f}} \frac{\mathrm{d}^{\mathrm{s}} (J\phi)}{\mathrm{d}t} - S^{\mathrm{s}} \frac{\mathrm{d}^{\mathrm{s}} T}{\mathrm{d}t} - \frac{\mathrm{d}^{\mathrm{s}} \Psi^{\mathrm{s}}}{\mathrm{d}t}. \tag{3.53}$$

From this, it becomes clear, that the strain energy rate $\mathrm{d}^{\mathrm{s}} \Psi^{\mathrm{s}} / \mathrm{d}t$ of the skeleton is composed of the strain energy rate $\boldsymbol{S} : \dot{\boldsymbol{E}}$ of a conventional structure, the power $\phi \boldsymbol{S}^{\mathrm{f}}_{\mathrm{visc}} : \dot{\boldsymbol{E}}$ and $p^{\mathrm{f}} \, \mathrm{d}^{\mathrm{s}} (J\phi) / \mathrm{d}t$ transferred by the viscous forces and the pore pressure, respectively, and a thermal contribution $S^{\mathrm{s}} \, \mathrm{d}^{\mathrm{s}} T / \mathrm{d}t$. The dissipation of the fluid phase (3.48) and the dissipation due to temperature gradients (3.49) can also be written in the spatial configuration:

$$\Phi^{\mathrm{s}} = \boldsymbol{S} : \dot{\boldsymbol{E}} - \phi \boldsymbol{S}^{\mathrm{f}}_{\mathrm{visc}} : \dot{\boldsymbol{E}} + p^{\mathrm{f}} \frac{\mathrm{d}^{\mathrm{s}} (J\phi)}{\mathrm{d}t} - S^{\mathrm{s}} \frac{\mathrm{d}^{\mathrm{s}} T}{\mathrm{d}t} - \frac{\mathrm{d}^{\mathrm{s}} \Psi^{\mathrm{s}}}{\mathrm{d}t} \geq 0, \tag{3.54}$$

$$\Phi^{\mathrm{f}} = \left[-\boldsymbol{\nabla} p + \frac{1}{\phi} \boldsymbol{\nabla} \cdot \left(\phi \boldsymbol{\sigma}^{\mathrm{f}}_{\mathrm{visc}} \right) + \rho^{\mathrm{f}} \left(\hat{\boldsymbol{b}} - \boldsymbol{a}^{\mathrm{f}} \right) \right] \cdot \phi \left(\boldsymbol{v}^{\mathrm{f}} - \boldsymbol{v}^{\mathrm{s}} \right) + \phi \boldsymbol{\sigma}^{\mathrm{f}}_{\mathrm{visc}} : \boldsymbol{\varepsilon}^{\mathrm{f}} \geq 0, \tag{3.55}$$

$$\Phi^{\mathrm{th}} = -\frac{\boldsymbol{q}^{\mathrm{th}}}{T} \cdot \boldsymbol{\nabla} T \geq 0. \tag{3.56}$$

The above three inequalities are the basic energy equations for the three considered fields. For the derivation of a constitutive equation for the skeleton, the dissipation of the skeleton phase is considered. The dissipation of the fluid phase will be used in Section 3.6 for deducing a valid flow equation. As only isothermal processes are considered, the thermal dissipation will not be further analyzed in this thesis.

Remark 3.4 *For sake of completeness, a comment on the thermal dissipation Φ^{th} is made. Equation* (3.56) *states a constraint for the relation between the heat flux $\boldsymbol{q}^{\mathrm{th}}$ and the temperature gradient $\boldsymbol{\nabla} T$. The simplest law fulfilling the dissipation inequality is* Fick's law $\boldsymbol{q}^{\mathrm{th}} = -D^{\mathrm{th}} \boldsymbol{\nabla} T$, *with the positive thermal diffusion coefficient D^{th}. Heat transport will not be treated within this thesis.*

It is assumed, that the strain energy Ψ^{s} of the skeleton only depends on the deformation state, the porosity and the temperature (and not on internal states, as for instance in plastic media). It holds

$$\frac{\mathrm{d}^{\mathrm{s}} \Psi^{\mathrm{s}}(\boldsymbol{E}, J\phi, T)}{\mathrm{d}t} = \frac{\partial \Psi^{\mathrm{s}}}{\partial \boldsymbol{E}} : \frac{\mathrm{d}^{\mathrm{s}} \boldsymbol{E}}{\mathrm{d}t} + \frac{\partial \Psi^{\mathrm{s}}}{\partial (J\phi)} \cdot \frac{\mathrm{d}^{\mathrm{s}} (J\phi)}{\mathrm{d}t} + \frac{\partial \Psi^{\mathrm{s}}}{\partial T} \cdot \frac{\mathrm{d}^{\mathrm{s}} T}{\mathrm{d}t}. \tag{3.57}$$

Then, equation (3.54) can be rearranged:

$$\left(\boldsymbol{S} - \phi \boldsymbol{S}^{\mathrm{f}}_{\mathrm{visc}} - \frac{\partial \Psi^{\mathrm{s}}}{\partial \boldsymbol{E}}\right) : \dot{\boldsymbol{E}} + \left(p^{\mathrm{f}} - \frac{\partial \Psi^{\mathrm{s}}}{\partial (J\phi)}\right) \cdot \frac{\mathrm{d}^{\mathrm{s}}(J\phi)}{\mathrm{d}t} - \left(S^{\mathrm{s}} - \frac{\partial \Psi^{\mathrm{s}}}{\partial T}\right) \cdot \frac{\mathrm{d}^{\mathrm{s}} T}{\mathrm{d}t} \geq 0. \quad (3.58)$$

Since $\boldsymbol{E}$, $J\phi$ and T can vary independently and their time derivative can have arbitrary sign and absolute values, all terms in brackets in equation (3.58) have to vanish. One obtains the following constitutive equations for the skeleton phase of a porous medium:

$$\boldsymbol{S} = \phi \boldsymbol{S}^{\mathrm{f}}_{\mathrm{visc}} + \frac{\partial \Psi^{\mathrm{s}}(\boldsymbol{E}, J\phi, T)}{\partial \boldsymbol{E}}, \qquad p^{\mathrm{f}} = \frac{\partial \Psi^{\mathrm{s}}(\boldsymbol{E}, J\phi, T)}{\partial (J\phi)}, \qquad S^{\mathrm{s}} = \frac{\partial \Psi^{\mathrm{s}}(\boldsymbol{E}, J\phi, T)}{\partial T}. \quad (3.59)$$

Alternatively, it is also possible to choose $\boldsymbol{E}$, m^{f} and T as independent variables. Starting from equation (3.50) instead of equation (3.54) one can derive [66] after analogous calculations the following alternative set of constitutive equations:

$$\boldsymbol{S} = \phi \boldsymbol{S}^{\mathrm{f}}_{\mathrm{visc}} + \frac{\partial \Psi^{\mathrm{s}}(\boldsymbol{E}, m^{\mathrm{f}}, T)}{\partial \boldsymbol{E}}, \qquad g^{\mathrm{f}} = \frac{\partial \Psi^{\mathrm{s}}(\boldsymbol{E}, m^{\mathrm{f}}, T)}{\partial m^{\mathrm{f}}}, \qquad S = \frac{\partial \Psi^{\mathrm{s}}(\boldsymbol{E}, m^{\mathrm{f}}, T)}{\partial T}. \quad (3.60)$$

A third alternative can be formulated with the definition

$$G^{\mathrm{s}} = \Psi^{\mathrm{s}} - p^{\mathrm{f}} J\phi \quad (3.61)$$

as

$$\boldsymbol{S} = \phi \boldsymbol{S}^{\mathrm{f}}_{\mathrm{visc}} + \frac{\partial G^{\mathrm{s}}(\boldsymbol{E}, p^{\mathrm{f}}, T)}{\partial \boldsymbol{E}}, \qquad J\phi = -\frac{\partial G^{\mathrm{s}}(\boldsymbol{E}, p^{\mathrm{f}}, T)}{\partial p^{\mathrm{f}}}, \qquad S^{\mathrm{s}} = -\frac{\partial G^{\mathrm{s}}(\boldsymbol{E}, p^{\mathrm{f}}, T)}{\partial T}. \quad (3.62)$$

Further forms and derivations can be found in [66].

Remark 3.5 *The energy terms in the constitutive equations* (3.59) *include the term $J\phi$ and not solely the porosity ϕ. This is due to the fact, that the constitutive laws are formulated depending on* material *quantities. The porosity, however, is a spatial quantity. Considering equation* (1.1) *and* (2.11) *it becomes clear, that $J\phi$ can be interpreted as material porosity, denoting the ratio of current fluid volume to material volume*

$$J\phi \cdot \mathrm{d}\Omega_0 = \mathrm{d}\Omega^{\mathrm{f}}_t. \quad (3.63)$$

3.5.2. Some Concepts from Geo and Soil Mechanics

In this section, selected terminologies originating from geo and soil mechanics are introduced. Terzaghi's principle of effective stress in Section 3.5.2.1 is well-known in this field. Porous materials are classically characterized by the Biot moduli, described in Section 3.5.2.2. Lastly, drained and undrained conditions are commented in Section 3.5.2.3.

3.5.2.1. Terzaghi's Principle of Effective Stress

Terzaghis principle of effective stress will be introduced in this section, as it is often referred to, especially in classical soil mechanics (see e.g. [45, 73, 220]). The comments given here are a compact version of the explanations in [66, sec. 3.4.1].

The *effective stress* $\boldsymbol{S}^{\mathrm{eff}}$ of a porous medium is defined as the sum of the total stress of the mixture and the hydrostatic pressure

$$\boldsymbol{S}^{\mathrm{eff}} = \boldsymbol{S} + p^{\mathrm{f}} J \boldsymbol{C}^{-1}. \tag{3.64}$$

The effective stress defines the mechanical state of loading, which actually induces macroscopic deformation in case of a (nearly) incompressible skeleton phase. The density of the skeleton phase is assumed to be constant and the change of volume is uniquely defined by the change of porosity. Then, it follows from the balance of mass of the skeleton phase (3.12), that

$$J\phi = J + \phi_0 - 1. \tag{3.65}$$

Using the identity

$$\frac{\mathrm{d}^{\mathrm{s}} J}{\mathrm{d}t} = J \boldsymbol{C}^{-1} : \dot{\boldsymbol{E}}, \tag{3.66}$$

and neglecting viscous effects, one obtains from the dissipation inequality (3.54)

$$\Phi^{\mathrm{s}} = \left(\boldsymbol{S} + p^{\mathrm{f}} J \boldsymbol{C}^{-1}\right) : \dot{\boldsymbol{E}} - S^{\mathrm{s}} \frac{\mathrm{d}^{\mathrm{s}} T}{\mathrm{d}t} - \frac{\mathrm{d}^{\mathrm{s}} \Psi^{\mathrm{s}}}{\mathrm{d}t} \geq 0, \tag{3.67}$$

and finally the following constitutive relations, similar to equation (3.59)

$$\boldsymbol{S}^{\mathrm{eff}} = \boldsymbol{S} + p^{\mathrm{f}} J \boldsymbol{C}^{-1} = \frac{\partial \Psi(\boldsymbol{E}, T)}{\partial \boldsymbol{E}}, \qquad S = \frac{\partial \Psi(\boldsymbol{E}, T)}{\partial T}. \tag{3.68}$$

From the first constitutive equation in (3.68) one can conclude that the effective stress can be modeled as derivative of a strain energy function in the same way as in classical elastodynamics. Due to these relations, the complexity of systems, where Terzaghi's principle of effective stress is applicable, is reduced significantly.

3.5.2.2. Linear Poroelasticity: Biot Modulus and Biot Tangent

Next to the known material elasticity tensor, which gives the material response to macroscopic strain, there are commonly two additional stiffness measures: the *Biot modulus* and the *Biot tangent*. In linear theory those moduli characterize the stress response due to change of porosity and pore pressure and were also used for postulating non-linear constitutive laws (see e.g. [48, 55]). Even though they do not play a central role in this thesis, they will be shortly reviewed in the following, as they are often referred to in the literature. The definitions given here are a short summary of [66, sec. 4.1.2].

As infinitesimal changes of state are considered, the distinction between different strain and stress measures is dropped here. The constitutive equation (3.62) then gives for the isothermal,

non-viscous case

$$\mathrm{d}\sigma_{ij} = C_{ijkl}\,\mathrm{d}\varepsilon_{kl} - b_{ij}\,\mathrm{d}p^{\mathrm{f}}, \tag{3.69a}$$

$$\mathrm{d}(J\phi) = (b_{\mathrm{B}})_{ij}\;\mathrm{d}\varepsilon_{ij} + \frac{\mathrm{d}p^{\mathrm{f}}}{N}. \tag{3.69b}$$

Here, the forth-order tensor

$$C_{ijkl} = \frac{\partial^2 G^{\mathrm{s}}}{\partial\varepsilon_{ij}\partial\varepsilon_{kl}} \tag{3.70}$$

denotes the material elasticity tensor and G^{s} the free enthalpy of the skeleton, see equation (3.61). The symmetric, second-order tensor

$$(b_{\mathrm{B}})_{ij} = -\frac{\partial^2 G^{\mathrm{s}}}{\partial\varepsilon_{ij}\partial p^{\mathrm{f}}} \tag{3.71}$$

denotes the Biot tangent. It relates changes of porosity with changes of strains as well as changes of the pore pressure with changes of stress at a constant strain state. Second, the scalar value

$$\frac{1}{N} = -\frac{\partial^2 G^{\mathrm{s}}}{\left(\partial p^{\mathrm{f}}\right)^2} \tag{3.72}$$

is the inverse Biot modulus. It gives the behavior of the pore pressure at variations of the porosity. Both quantities are constant in case of linear theory. In the special case of an incompressible matrix, the volume change of the porous medium $\epsilon = \varepsilon_{ii}$ is uniquely determined by the change of material porosity:

$$\mathrm{d}\epsilon = \mathrm{d}(J\phi). \tag{3.73}$$

Then, it immediately follows from equation (3.69b)

$$(b_{\mathrm{B}})_{ij} = \delta_{ij}, \quad \frac{1}{N} = 0, \tag{3.74}$$

with the Kronecker delta δ_{ij}. Equation (3.69a) then gives

$$\mathrm{d}(\sigma_{ij} + p^{\mathrm{f}}\delta_{ij}) = C_{ijkl}\,\mathrm{d}\epsilon_{kl}, \tag{3.75}$$

which is consistent with the results obtained from the considerations of the effective stress in equation (3.68).

3.5.2.3. Drained and Undrained Conditions

A categorization, which is common in geo and soil mechanics, are so-called drained and undrained conditions. Both terminologies can be applied to a whole problem setting as to a boundary. The behavior of a porous medium is said to be *fully drained*, if the duration of the consolidation process is short compared to the time scale of the problem considered [242]. This means that flow and pressure variations can be neglected. So, in fact, a pure solid problem is investigated. If a fluid boundary is assumed to be drained, it represents a free outflow at reference pressure (most often zero pressure). The other extreme case are *undrained conditions*. There, it

is assumed that the loading is so fast and/or the permeability is so low, that there is hardly any fluid flowing. Then, the fluid will instantly carry a part of the load. From a macroscopic point of view, this case can also be written as pure solid problem with modified material parameters, see e.g. [242, chap. 2.8]. In general, the stiffness is increased due to the resistance of the pore fluid. In this context, it is distinguished between undrained and drained moduli. A problem with impermeable boundaries, i.e. no fluid flux over the boundaries, is also called undrained situation.

3.5.3. An Approach for the Strain Energy Function

The theory presented in the previous sections is well known. Once it is applied to a given problem, the choice of a suitable strain energy function in equation (3.59) is a major difficulty. Often simplifying assumptions are made beforehand. Such simplifications can be incompressibility of both phases, small strains, or very specific strain energy functions, see for instance [16, 48, 55, 219]. Theoretic work seldom proposes a general strain energy function. Some examples can be found in [54, 102, 103]. The approach given here, cf. [243], is based on such a proposal of a general strain energy function.

Naturally, the model presented here is not universal and hence some assumptions still need to be made. First, the model is restricted to Newtonian fluids (see also Section 3.6), as these types of fluids are of main interest in the applications considered. For flow of non-Newtonian fluids through a non deforming porous medium see [93, 228] and the references therein. There are no examples of flow of non-Newtonian fluids through a deforming porous medium known to the author. Besides, the fluid density is assumed to be constant

$$\rho^{\mathrm{f}} = \rho_0^{\mathrm{f}} = \text{constant}, \tag{3.76}$$

and, therefore, can be eliminated from the balance of mass. Note that even though the assumption of incompressible flow is well established in the field of biomechanics, it might be not reasonable in other classical fields of application of porous media, as soil mechanics, for instance. Still, one has to point out, that all formulations given before this section do not assume compressibility or incompressibility and also the model can easily be extended to compressible flow, if needed.

In order to derive an expression of the strain energy function of the porous medium, the strain energy function of the skeleton is rewritten as a function of the determinant of the deformation gradient weighted by the volume ratio of the solid phase

$$J^{\mathrm{s}} = J(1-\phi), \tag{3.77}$$

instead of the volume ratio $J\phi$ of the fluid. By applying the balance of mass (3.12), J^{s} can also be expressed in terms of the ratio of material to spatial solid density, i.e. $J^{\mathrm{s}} = (1-\phi_0)\rho_0^{\mathrm{s}}/\rho^{\mathrm{s}}$. Also, $J^{\mathrm{s}}/(1-\phi_0)$ represents the dilation ratio of the solid skeleton. Using the identity

$$\frac{\mathrm{d}^{\mathrm{s}} J^{\mathrm{s}}}{\mathrm{d}t} = \frac{\mathrm{d}^{\mathrm{s}} J}{\mathrm{d}t} - \frac{\mathrm{d}^{\mathrm{s}}(J\phi)}{\mathrm{d}t} = J\boldsymbol{C}^{-1} : \frac{\mathrm{d}^{\mathrm{s}}\boldsymbol{E}}{\mathrm{d}t} - \frac{\mathrm{d}^{\mathrm{s}}(J\phi)}{\mathrm{d}t}, \tag{3.78}$$

with the right Cauchy-Green deformation tensor $\boldsymbol{C}$, one deduces from equation (3.57)

$$\begin{aligned} \frac{\mathrm{d}^{\mathrm{s}}\Psi^{\mathrm{s}}(\boldsymbol{E}, J^{\mathrm{s}})}{\mathrm{d}t} &= \frac{\partial \Psi^{\mathrm{s}}}{\partial \boldsymbol{E}} : \left.\frac{\partial \boldsymbol{E}}{\partial t}\right|_{\boldsymbol{X}} + \frac{\partial \Psi^{\mathrm{s}}}{\partial J^{\mathrm{s}}} \cdot \frac{\mathrm{d}^{\mathrm{s}} J^{\mathrm{s}}}{\mathrm{d}t} \\ &= \left(\frac{\partial \Psi^{\mathrm{s}}}{\partial \boldsymbol{E}} + \frac{\partial \Psi^{\mathrm{s}}}{\partial J^{\mathrm{s}}} J \boldsymbol{C}^{-1}\right) : \frac{\mathrm{d}^{\mathrm{s}} \boldsymbol{E}}{\mathrm{d}t} - \frac{\partial \Psi^{\mathrm{s}}}{\partial J^{\mathrm{s}}} \cdot \frac{\mathrm{d}^{\mathrm{s}}(J\phi)}{\mathrm{d}t}. \end{aligned} \tag{3.79}$$

Thus, the following constitutive equations for the fluid pressure and the macroscopic second Piola-Kirchhoff stress tensor are obtained:

$$p^{\mathrm{f}} = -\frac{\partial \Psi^{\mathrm{s}}(\boldsymbol{E}, J^{\mathrm{s}})}{\partial J^{\mathrm{s}}}, \tag{3.80}$$

$$\begin{aligned} \boldsymbol{S} &= \phi \boldsymbol{S}^{\mathrm{f}}_{\mathrm{visc}} + \frac{\partial \Psi^{\mathrm{s}}(\boldsymbol{E}, J^{\mathrm{s}})}{\partial \boldsymbol{E}} + \frac{\partial \Psi^{\mathrm{s}}(\boldsymbol{E}, J^{\mathrm{s}})}{\partial J^{\mathrm{s}}} J \boldsymbol{C}^{-1} \\ &= \phi \boldsymbol{S}^{\mathrm{f}}_{\mathrm{visc}} + \frac{\partial \Psi^{\mathrm{s}}(\boldsymbol{E}, J^{\mathrm{s}})}{\partial \boldsymbol{E}} - p^{\mathrm{f}} J \boldsymbol{C}^{-1}. \end{aligned} \tag{3.81}$$

Adapting the approach proposed in [54], the subsequent form for the strain energy function is assumed:

$$\Psi^{\mathrm{s}}(\boldsymbol{E}, J^{\mathrm{s}}) = W^{\mathrm{skel}}(\boldsymbol{E}) + W^{\mathrm{vol}}(J^{\mathrm{s}}) + W^{\mathrm{pen}}(\boldsymbol{E}, J^{\mathrm{s}}). \tag{3.82}$$

W^{skel} denotes the macroscopic strain energy function of the skeleton, while W^{vol} accounts for the macroscopic volume change of the structure due to the pore pressure. It has to be noted, that the additive split of the strain energy function in (3.82) is not a decomposition into an isochoric and a volumetric part, as W^{skel} can, and actually should [54] include a volumetric contribution as well. The following choice of $W^{\mathrm{vol}}(J^{\mathrm{s}})$ will be utilized subsequently

$$W^{\mathrm{vol}}(J^{\mathrm{s}}) = \kappa \left(\frac{J^{\mathrm{s}}}{1-\phi_0} - 1 - \ln\left(\frac{J^{\mathrm{s}}}{1-\phi_0}\right)\right), \tag{3.83}$$

with the *bulk modulus of the skeleton* κ. The penalty function W^{pen}, needed to maintain positive porosities, is here chosen to be

$$W^{\mathrm{pen}}(\boldsymbol{E}, J^{\mathrm{s}}) = \eta \left(-\ln\left(\frac{J\phi}{\phi_0}\right) + \frac{J\phi}{\phi_0} - \frac{1}{\phi_0}\right), \tag{3.84}$$

with a *penalty parameter* η. In contrast to [54] the additional summand $\eta J\phi/\phi_0$ is added to circumvent a pressure jump at the initial state at $\phi = \phi_0$ and $J = 1$. Hence, it is assured that $\partial W^{\mathrm{pen}}/\partial J^{\mathrm{s}} = 0$ in the undeformed state. Using equations (3.82)–(3.84), the constitutive equations (3.80) and (3.81) can be written as

$$p^{\mathrm{f}} = -\frac{\partial W^{\mathrm{vol}}(J^{\mathrm{s}})}{\partial J^{\mathrm{s}}} - \frac{\partial W^{\mathrm{pen}}(\boldsymbol{E}, J^{\mathrm{s}})}{\partial J^{\mathrm{s}}}, \tag{3.85}$$

$$\boldsymbol{S} = \phi \boldsymbol{S}^{\mathrm{f}}_{\mathrm{visc}} + \frac{\partial W^{\mathrm{skel}}(\boldsymbol{E})}{\partial \boldsymbol{E}} + \frac{\partial W^{\mathrm{pen}}(\boldsymbol{E}, J^{\mathrm{s}})}{\partial \boldsymbol{E}} - p^{\mathrm{f}} J \boldsymbol{C}^{-1}. \tag{3.86}$$

Equation (3.85) gives a relation between the fluid pressure, the porosity and the determinant of the deformation gradient. For instance, using the approach for W^{vol} and W^{pen} in equation (3.83)

and (3.84), one obtains

$$p^{\mathrm{f}} = \kappa \left(-\frac{1}{1-\phi_0} + \frac{1}{J^{\mathrm{s}}} \right) - \eta \left(\frac{1}{J\phi} - \frac{1}{\phi_0} \right). \tag{3.87}$$

This equation will later be used to calculated the porosity depending on the fluid and skeleton state. Note, that the porosity depends on both fluid and skeleton properties. Only in case of a truly incompressible skeleton (i.e. $\kappa \to \infty$), the porosity can be expressed as a function of the Jacobian only and is independent of the fluid pressure.

This formulation of the constitutive law is very convenient, as it allows the integration of any arbitrary hyperelastic material model for the structure phase by choosing W^{skel} accordingly, as long as it includes a volumetric part. As it is pointed out in [54] the additive split of the strain energy function (3.82) holds for nearly incompressible structures. In more detail, this is a consequence of the fact that the energy contribution W^{vol} is not explicitly depending on macroscopic volume changes. In [54] it is shown that this corresponds to a Biot modulus tending to one in linear theory, justifying this approach for nearly incompressible skeleton behavior. In short, it was shown that the Biot tangent $\boldsymbol{b}_B$ defined in equation (3.71) calculated from the constitutive law (3.81) gives

$$\boldsymbol{b}_B = \frac{\partial \boldsymbol{\sigma}}{\partial \varepsilon} = \mathbf{1}, \tag{3.88}$$

which corresponds to the Biot tangent in the case of an incompressible structure phase, justifying the assumption of near incompressibility. The Biot modulus from equation (3.72) is in general unequal to zero, in contrast to truly incompressible material behavior. The interested reader is referred to [54] and [102] for more general formulations, including the truly incompressible case.

Remark 3.6 *Also, in [54] it is concluded, that modeling truly incompressible materials would be easily possible by additionally making W^{vol} an explicit function of the determinant of the deformation gradient. Furthermore, it is worth noting, that following the presented approach without the penalty contribution, the constitutive behavior of the solid phase is split into two parts: the first induced by the stress acting on the solid skeleton included in W^{skel} and the second given by the pore pressure included in W^{vol}. One can think of the first contribution as the constitutive behavior of the skeleton as a structure while maintaining zero fluid pressure and also its response when increasing the fluid pressure while maintaining zero total stresses. On the other hand, the energy contribution W^{vol} will determine the response of the porous structure to volume changes of the solid phase induced by fluid pressure.*

3.5.4. Alternative Constitutive Laws

Equation (3.87) represents a constitutive law for how the porosity changes due to pore pressure and displacements. It is based on a Neo-Hookean-like approach for a volumetric part of the strain energy of the skeleton. As in classical solid mechanics, a huge variety of constitutive laws are feasible. To determine which one is the most appropriate to use for a certain application is a very difficult task. Not only selecting a sensible formulation but also identifying the corresponding parameters is very cumbersome and a field of research by itself. This is not in the scope of this thesis. However, some alternative constitutive laws, which are simple and well-established will be reviewed here.

The first law given originates from linear theory. It can be derived by choosing the following approach for the strain energy Ψ^{s} of the skeleton:

$$\Psi^{\mathrm{s}}\left(\boldsymbol{E}, J\phi\right) = W^{\mathrm{skel}}(\boldsymbol{E}) + \frac{1}{2}N\left(J\phi - \phi_0\right)^2 + \frac{1}{2}Nb^2\left(J(\boldsymbol{E}) - 1\right)^2 - Nb(J\phi)\left(J(\boldsymbol{E}) - 1\right). \quad (3.89)$$

The material constants are the *Biot modulus* N and the *Biot coefficient* b, see also the definition of the Biot tangent (3.71) in Section 3.5.2.2. Inserting this into the constitutive law (3.59) and assuming isothermal conditions, gives

$$\begin{aligned} \boldsymbol{S} &= \phi\boldsymbol{S}^{\mathrm{f}}_{\mathrm{visc}} + \frac{\partial W^{\mathrm{skel}}(\boldsymbol{E})}{\partial \boldsymbol{E}} - bp^{\mathrm{f}}J\boldsymbol{C}^{-1}, & (3.90)\\ p^{\mathrm{f}} &= N\left(J\phi - \phi_0\right) - Nb\left(J(\boldsymbol{E}) - 1\right). & (3.91) \end{aligned}$$

Again, the contribution W^{skel} represents the drained macroscopic strain energy function of the skeleton and $\phi\boldsymbol{S}^{\mathrm{f}}_{\mathrm{visc}}$ the viscous part of fluid stresses, which vanishes for Darcy flow. Solving equation (3.91) for the porosity gives

$$J\phi - \phi_0 = \frac{1}{N}p^{\mathrm{f}} + b\left(J - 1\right). \quad (3.92)$$

This law simply states that the change of material porosity is linear dependent of the pore pressure and the volume change. In the small deformation regime, the difference between Eulerian and Lagrangean porosity can be neglected, i.e. $J\phi \approx \phi$. Further, the determinant of the deformation gradient is approximated by the trace of the linear strains, i.e. $J \approx 1 + \mathrm{tr}(\boldsymbol{\epsilon})$. Then, it follows the well known linear form of the Biot law

$$\phi - \phi_0 = \frac{1}{N}p^{\mathrm{f}} + b\,\mathrm{tr}(\boldsymbol{\epsilon}). \quad (3.93)$$

For many fields of porous media application it can be reasonable to assume an incompressible solid phase. This is a classical assumption in soil mechanics, for instance. As already stated in Section 3.5.2.1, for an incompressible solid phase the following identity follows from the balance of mass (3.12) of the skeleton:

$$J\phi - \phi_0 = J - 1. \quad (3.94)$$

By comparing this equation to the Biot relation (3.92) it becomes clear that incompressibility corresponds to a Biot modulus $N \to \infty$ and a Biot coefficient $b = 1$. Equation (3.94) describes incompressibility for large deformations. Note, that there is a non-linear dependence between the current porosity ϕ and the Jacobian determinant J. In case of linear kinematics, this reduces to a likewise linear relation

$$\phi - \phi_0 = \mathrm{tr}(\boldsymbol{\epsilon}). \quad (3.95)$$

Obviously, this relation, and also the linear Biot law (3.93), are only reasonable for small strains and small changes of the porosity. This can be seen in the fact, that there, the value of the porosity is not bounded by 1 for large volumetric expansion. Note, however, that none of the laws given in this section, including the non-linear ones, is made for large compression, as the porosity is

allowed to become negative. One remedy for this is an additional penalty term in the respective strain energy, like the one given before in equation (3.84).

3.6. Flow Equation: Darcy and Darcy-Brinkman Equation

When not only deformations of the solid phase are of interest, but also the behavior of the fluid phase, the flow equations are of major importance. In this thesis, the Darcy and the Darcy-Brinkman flow model are utilized, which will be reviewed and compared in the following.

3.6.1. Strong Form

The Clausius–Duhem inequality for the fluid phase (3.55) is recalled as

$$\Phi^{\mathrm{f}} = \underbrace{\left[-\boldsymbol{\nabla} p^{\mathrm{f}} + \frac{1}{\phi}\boldsymbol{\nabla}\cdot\left(\phi\boldsymbol{\sigma}^{\mathrm{f}}_{\mathrm{visc}}\right) + \rho^{\mathrm{f}}\left(\hat{\boldsymbol{b}} - \boldsymbol{a}^{\mathrm{f}}\right)\right]}_{\mathcal{F}} \cdot \underbrace{\phi\left(\boldsymbol{v}^{\mathrm{f}} - \boldsymbol{v}^{\mathrm{s}}\right)}_{\mathcal{V}} + \underbrace{\phi\boldsymbol{\sigma}^{\mathrm{f}}_{\mathrm{visc}} : \boldsymbol{\varepsilon}^{\mathrm{f}}}_{\mathcal{D}} \geq 0. \tag{3.96}$$

The dissipation of the fluid phase is composed of the dissipation due to the spatial force term $\mathcal{F}$ along the induced spatial relative velocity $\mathcal{V}$ and the viscous dissipation $\mathcal{D}$. For the first flow equation, the viscous contribution is neglected, i.e. $\boldsymbol{\sigma}^{\mathrm{f}}_{\mathrm{visc}} = \mathbf{0}$ and $\mathcal{D} = 0$. This implies that the resistance acting on the flow is dominantly established by adhesion on the interface between the fluid and the structure phase. The dissipation equation then reduces to

$$\Phi^{\mathrm{f}} = \underbrace{\left[-\boldsymbol{\nabla} p^{\mathrm{f}} + \rho^{\mathrm{f}}\left(\hat{\boldsymbol{b}} - \boldsymbol{a}^{\mathrm{f}}\right)\right]}_{\mathcal{F}} \cdot \underbrace{\phi\left(\boldsymbol{v}^{\mathrm{f}} - \boldsymbol{v}^{\mathrm{s}}\right)}_{\mathcal{V}} \geq 0. \tag{3.97}$$

The most simple option to satisfy equation (3.97) is a linear relation between force term and relative flux depending on the positive definite, symmetric, second-order *permeability tensor* $\boldsymbol{k}$:

$$\frac{\boldsymbol{k}}{\mu^{\mathrm{f}}} \cdot \left(-\boldsymbol{\nabla} p^{\mathrm{f}} + \rho^{\mathrm{f}}\left(\hat{\boldsymbol{b}} - \boldsymbol{a}^{\mathrm{f}}\right)\right) = \phi\left(\boldsymbol{v}^{\mathrm{f}} - \boldsymbol{v}^{\mathrm{s}}\right), \tag{3.98}$$

and reformulated in a more common form

$$\rho^{\mathrm{f}}\boldsymbol{a}^{\mathrm{f}} + \boldsymbol{\nabla} p^{\mathrm{f}} - \rho^{\mathrm{f}}\hat{\boldsymbol{b}} + \phi\mu^{\mathrm{f}}\boldsymbol{k}^{-1} \cdot \left(\boldsymbol{v}^{\mathrm{f}} - \boldsymbol{v}^{\mathrm{s}}\right) = \mathbf{0}. \tag{3.99}$$

Equation (3.99) is the so-called *Darcy equation*. The inequality (3.97) holds as the permeability tensor is positive definite. Note, that in equation (3.98) the permeability is divided by the fluid viscosity. By doing so, the permeability becomes a purely geometric quantity, independent of the properties of the Newtonian fluid, see [66, chap. 3.3.1] for further explanations.

Assuming a significant influence of the viscous forces also on the macroscopic scale, one most commonly uses a Newtonian fluid (see equation (2.47)) with $\boldsymbol{\sigma}^{\mathrm{f}}_{\mathrm{visc}} = 2\mu^{\mathrm{f}}\boldsymbol{\varepsilon}^{\mathrm{f}}(\boldsymbol{v}^{\mathrm{f}})$. In this case the

so called *Darcy-Brinkman equation* is obtained as follows

$$\rho^{\mathrm{f}}\boldsymbol{a}^{\mathrm{f}} + \boldsymbol{\nabla} p^{\mathrm{f}} - \rho^{\mathrm{f}}\hat{\boldsymbol{b}} + \phi\mu^{\mathrm{f}}\boldsymbol{k}^{-1}\cdot\left(\boldsymbol{v}^{\mathrm{f}} - \boldsymbol{v}^{\mathrm{s}}\right) - \frac{1}{\phi}\boldsymbol{\nabla}\cdot\left(\phi\boldsymbol{\sigma}^{\mathrm{f}}_{\mathrm{visc}}\right) = \boldsymbol{0}. \tag{3.100}$$

Here, as the positiveness of the viscous dissipation $\mathcal{D}$ is trivial, the dissipation inequality (3.96) is again fulfilled due the positive definiteness of the permeability tensor. The so-called Brinkman term $1/\phi\boldsymbol{\nabla}\cdot\left(\phi\boldsymbol{\sigma}^{\mathrm{f}}_{\mathrm{visc}}\right)$ in equation (3.100) resembles the viscous contribution in the incompressible Navier-Stokes equations. Other approaches account for the viscous stresses by introducing an additional viscous potential in the strain energy function (see e.g. [54, 124, 172, 220]). In the following chapters, both the Darcy and the Darcy-Brinkman equation wil bel used and analyzed.

Remark 3.7 *As the balance of momentum of the mixture before, the presented flow equations are based on considerations mainly on the macroscopic scale. All physical quantities are valid on this scale, i.e. they are implicitly assumed to be the average of the respective microscopic counterparts. A more formal way to derive the flow equations is again based on micro-macro-approaches. In [25], the flow equations were derived based on a volume averaging approach, whereas asymptotic expansion was utilized in [124] and [214]. In both cases, the Darcy and the Darcy-Brinkman equation are derived from the Stokes equation on the microscale assuming a no-slip condition on the fluid-structure interface. Using TCAT, an extended form of Darcy's law was derived in [115].*

Remark 3.8 *As already stated before, other formulations or extensions for flow through a porous medium exists. Many of them are of heuristic nature and motivated by specific applications. One of the most common variant is the so-called* Forchheimer equation *[100]. Either the Darcy or the Darcy-Brinkman equation is extended by an additive non-linear reactive term $\boldsymbol{f}\cdot\boldsymbol{v}^{\mathrm{f}}$, with the Forchheimer correction tensor $\boldsymbol{f}$ depending on the L_2-norm $||\boldsymbol{v}^{\mathrm{f}}||_2$ of the velocity and further porous medium parameters, like permeability and porosity. It is intended to account for effects in the high Reynolds number regime. The Forchheimer extension will not be considered in this thesis. For a theoretical analysis of the Forchheimer equation see [237, 252].*

Remark 3.9 *Note, that the Darcy-Brinkman equation* (3.100) *is divided by the porosity ϕ when compared to the equation given by volume averaging the microscopic balance of momentum. Hence, the actual balance equation reads*

$$\phi\rho^{\mathrm{f}}\boldsymbol{a}^{\mathrm{f}} - \phi\rho^{\mathrm{f}}\hat{\boldsymbol{b}} + \phi\boldsymbol{\nabla} p^{\mathrm{f}} - \boldsymbol{\nabla}\cdot\left(\phi\boldsymbol{\sigma}^{\mathrm{f}}_{\mathrm{visc}}\right) + \mu^{\mathrm{f}}\phi^2\boldsymbol{k}^{-1}\cdot\left(\boldsymbol{v}^{\mathrm{f}} - \boldsymbol{v}^{\mathrm{s}}\right) = \boldsymbol{0}. \tag{3.101}$$

Clearly, this equation is just a reformulation of Darcy-Brinkman equation and thus equivalent. The given form of the Darcy-Brinkman equation in (3.100) *is more convenient as the coupling by porosity appears in less terms, however one has to keep form* (3.101) *in mind for physical interpretation of the linear momentum.*

3.6.2. Comments on Tortuosity and Permeablity

As already mentioned above, the averaging procedure results in the need of some additional assumptions. Some of them can be interpreted as further material parameters of the macroscopic

homogeneous structure. The most prominent material parameters in the porous medium literature are the *permeability* and the *tortuosity*. The permeability accounts for the resistance of the skeleton against porous flow and is in general depending on the microgeometry of the structure and the characteristics of the fluid flow. In the definition given in Section 3.6.1 and considering Newtonian fluids only, it can assumed to be purely geometric [66, chap. 3.3.1]. The tortuosity describes the 'curvedness' of the pores and thus depends on the microstructure. From intuition it becomes clear that both quantities are often inversely related. If the tortuosity rises the permeability likely decreases, as when the pore channels are curved, the flow resistance increases. See [42] and the references therein for some possible relations of tortuosity and porosity. In [66] the tortuosity effect is modeled as an additional inertia term. In Figure 3.4 the tortuosity effect is

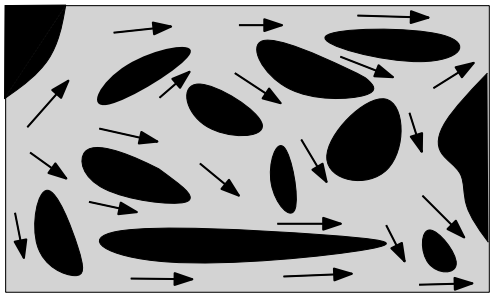

Figure 3.4: Illustration of tortuosity effect: The averaged flow points predominantly from left to right, however tortuosity effects may also induce inertia forces in other directions.

illustrated. The depicted flow field is predominantly pointing from left to right leading to an according averaged velocity. However, due to the curvedness of the microgeometry, inertia forces might also act in other directions. This effect is called strict tortuosity effect. There are also secondary effects due to tortuosity (which are sometimes included in the definition of the general tortuosity effect). Clearly, not only the homogenized inertia, but also other force terms are influenced by a curved pore structure. The direction of microscopic drag forces at the fluid-structure interface and the fluid pressure gradient might vary. Therefore, a second-order tortuosity tensor is often multiplied with the homogenized terms within the balance of momentum to include a 'dispersion' of the respective forces. For a detailed analysis, see for instance [25, 140]. One has to note, that such effects become more important when anisotropy, regarding elasticity and flow, are considered. For more general theory regarding anisotropic porous media, see [69, 118] and the references therein. In this thesis the tortuosity effect is neglected, and therefore the tortuosity does not appear explicitly in the flow equations. Still, it will be later referred to when considering scalar transport in porous media in Section 5.3.

For stationary conditions and a non-deforming porous medium, the permeability can be calculated from the Darcy equation (3.99) as

$$\boldsymbol{k} \cdot \frac{1}{\mu^{\mathrm{f}}} \boldsymbol{\nabla} p^{\mathrm{f}} = -\phi \boldsymbol{v}^{\mathrm{f}}. \tag{3.102}$$

Very simply speaking, the stationary value of the permeability can thus be measured by applying a fixed pressure gradient on the porous medium and measuring the fluid flow, see e.g. [96, 163, 235]. In Table 3.1 the ranges for permeability and porosity of some exemplary materials is listed.

Material	Permeability $[\,\mathrm{m}^2]$	Porosity
marble	10^{-19}	$0,005 - 0,02$
concrete	$10^{-16} - 10^{-21}$	$0,02 - 0,07$
clay	$10^{-16} - 10^{-20}$	$\sim 0,50$
granite	$10^{-16} - 10^{-20}$	$0,002 - 0,04$
leather	$10^{-13} - 10^{-14}$	$0,56 - 0,59$
limestone	$10^{-12} - 10^{-16}$	$0,04 - 0,29$
sandstone	$10^{-11} - 10^{-17}$	$0,08 - 0,38$
soil	$10^{-11} - 10^{-13}$	$0,43 - 0,54$
gravel, sand	$10^{-9} - 10^{-12}$	$0,37 - 0,50$

Table 3.1.: Order of magnitudes of permeability and porosity for different materials, [65, 179]

Also, numerical experiments of flow at the pore scale have been used to evaluate macroscopic characteristics. The geometries are obtained by advanced imaging techniques or statistical reconstruction [142, 183]. The question remains how the permeability depends on deformation. As it is intrinsically geometric, it depends on information of the microscopic geometry on the macroscopic level. Even though precise analytical forms for both tensors can be derived under certain conditions [25] (from which characteristics like symmetry and positive definiteness can be proven), they most often cannot be evaluated in practice, as they depend on the unknown microgeometry. Instead, simplified or heuristic material laws are usually applied. Based on experimental data, a functional relation of the porosity can be fitted. Alternatively, for simple geometries, (semi)-analytical forms can be used. For instance, for flow at low Reynolds numbers, the permeability of a solid matrix formed by the packing of almost regular spheres, the so-called *Carman-Kozeny* relation can be derived [51, 150] as

$$\boldsymbol{k} = k \cdot \mathbf{1}, \qquad k = l^2 \frac{1-\phi^3}{1-\phi^2}, \tag{3.103}$$

with the geometrical constant l. For the large deformation regime the Carman-Kozeny relation will be used to determine the material permeability. Thus, it is reformulated to depend on the material porosity $J\phi$, see Remark 3.5, instead

$$\boldsymbol{K} = K \cdot \mathbf{1}, \qquad K = l^2 \frac{1-(J\phi)^3}{1-(J\phi)^2}. \tag{3.104}$$

Here, k and K denote the scalar value of the isotropic permeability in the current and material configuration, respectively. The current permeability $\boldsymbol{k}$ and material permeability $\boldsymbol{K}$ are related by a push-forward operation

$$\boldsymbol{k} = \frac{1}{J} \boldsymbol{F} \cdot \boldsymbol{K} \cdot \boldsymbol{F}^{\mathrm{T}}. \tag{3.105}$$

The Carman-Kozeny equation is very common in practice, however not undisputed. In [239] its applicability is questioned. The analysis is build on theoretical derivations using volume averaging and numerical experiments. In [141] an alternative law for the permeability of complex

porous structures is proposed. In this thesis, in most numerical examples a constant material permeability is assumed. The spatial permeability changes due to deformation as given in equation (3.105).

3.6.3. Validity and Comparison of the Flow Equations

The Darcy and the Darcy-Brinkman equation just presented in Section 3.6 are the most common ways to describe flow through porous media. However, there exist multiple variations and extensions (see e.g. [24, 25, 79, 179, 185, 247, 251, 252] and Remark 3.8). Nevertheless, even though only the two options presented here are considered, it is desirable to formulate mathematical conditions to evaluate which equation is suitable to model flow through a certain porous medium. In the following, some categorizations will be given. This summary has already been given by the author in [243].

Every flow equation through a porous medium is obtained by homogenizing the microscopic equations. Irrespective of the detailed method used to derive the macroscopic equations, some assumptions concerning microscopic quantities have to be made. For instance, neglecting the viscous forces is the major difference between Darcy and Darcy-Brinkman flow. Thus, every macroscopic description is only an approximation of the smaller scale. None of them is strictly wrong or right, but the application and demanded accuracy determine the model to be used.

One of the most clear and perspicuous ways to categorize phyiscal equations is using dimensionless numbers. Mainly, the results of the mathematical analysis in [25], which is based on volume averaging, are restated in the following. In general, both the Darcy equation and the Darcy-Brinkman equation only hold for small Reynolds numbers

$$\mathrm{Re} = \frac{v_{\mathrm{c}}^{\mathrm{f}} \cdot l_{\mathrm{c}}}{\nu_{\mathrm{c}}^{\mathrm{f}}}, \tag{3.106}$$

with a characteristic fluid velocity $v_{\mathrm{c}}^{\mathrm{f}}$, a characteristic length l_{c}, and a characteristic kinematic viscosity $\nu_{\mathrm{c}}^{\mathrm{f}}$ of the fluid. For porous media, usually an averaged seepage velocity and a characteristic pore size are used as characteristic velocity and length, respectively. The Darcy equation is valid for Reynolds numbers smaller than 1, see [153, 179], thus

$$\mathrm{Re} < 1. \tag{3.107}$$

This condition is consistent with neglecting the convective term, i.e. the approximation that the Stokes equation holds on the microscopic scale, see [124, 249]. A more sophisticated criterion for the validity of the Darcy equation can be formulated using two additional dimensionless numbers, namely the Strouhal number St and the Darcy number Da given by

$$\mathrm{St} = \frac{l_{\mathrm{c}}}{t_c \cdot v_{\mathrm{c}}^{\mathrm{f}}}, \qquad \mathrm{Da} = \frac{\frac{k_{\mathrm{c}}}{\phi_{\mathrm{c}} \cdot \tau_{\mathrm{c}}}}{l_c^2}, \tag{3.108}$$

with k_{c}, t_{c}, ϕ_{c}, and τ_{c} being a characteristic permeability, the length of a characteristic time interval where variations of the velocity occur, a characteristic porosity and a characteristic tortuosity, respectively. The Strouhal number describes the ratio of two time scales. One time scale $l_{\mathrm{c}}/v_{\mathrm{c}}^{\mathrm{f}}$

is the travel time until a significant spatial change in velocity is encountered. The other time interval t_c denotes the time until a similar change is observed at a fixed point. The Darcy number denotes the size of the microscale with respect to the macroscale. According to [25, chap. 2.6.1] the Darcy equation is valid if

$$\mathrm{St} \leq 1 \quad \text{and} \quad \mathrm{Re} \cdot \mathrm{Da}^{\frac{1}{2}} \ll 1, \tag{3.109}$$

whereas the Darcy-Brinkman equation is valid if

$$\mathrm{Re} \cdot \mathrm{Da}^{\frac{1}{2}} \ll 1. \tag{3.110}$$

In addition to this analysis via dimensionless numbers, the similarities between the flow equations and the Navier-Stokes equations will be illustrated with a simple example. A straight channel with a constant pressure gradient of 1 pointing against the flow direction is considered. The solid phase is fixed and the porosity constant. For the Navier-Stokes equation and the Darcy-Brinkman equation a no-slip condition and for the Darcy flow a no-penetration condition is prescribed at the upper and lower boundaries. The stationary flow field for this simple pressure gradient driven channel flow is depicted in Figure 3.5.The solution of the Navier-Stokes equation of this setting is the well known parabolic profile of Poiseuille flow. The solution of the Darcy-Brinkman equation has a similar shape, however the flow profile is more flat and has a smaller maximum velocity. This is due to the additional resistance against flow enforced by the Darcy term. The Darcy flow is constant over the channel height. As a pure Darcy fluid does not exhibit any shear stresses, no curvature of the flow field is produced. Further, in Figure 3.6 the

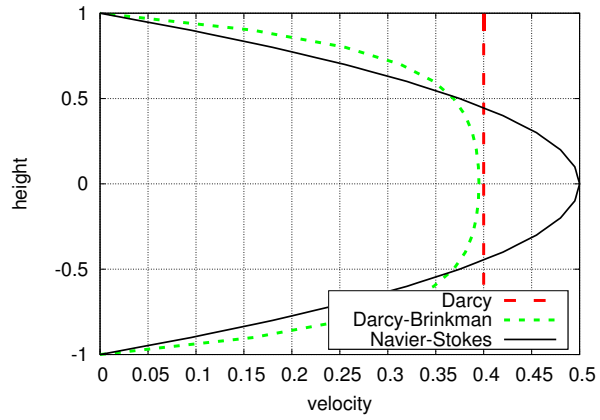

Figure 3.5: Comparison of flow profiles for Poiseuille flow for Darcy, Darcy-Brinkman and Navier-Stokes flow.

interpretation of the Darcy-Brinkman equation as transition between Darcy and Navier-Stokes equations is illustrated. There, it is demonstrated, that Darcy-Brinkman flow converges either to Navier-Stokes flow or Darcy flow, depending on the choice of material parameters. In the left Subfigure 3.6, the porosity is varied, while the permeability is calculated via the Carman-Kozeny relation (3.103) (i.e. $k \to \infty$ when $\phi \to 1$). In this case, the Brinkman solution reproduces the Navier-Stokes solution for porosities near 1. This can be verified easily by inserting these limit

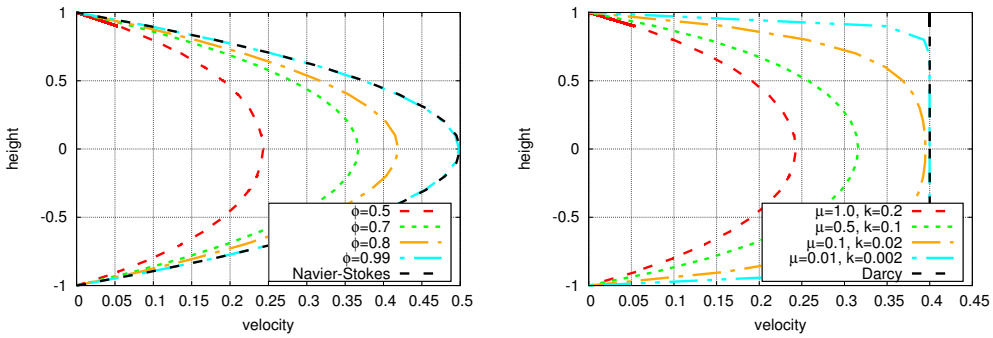

Figure 3.6: Comparison of flow profiles for Poiseuille flow: Darcy-Brinkman flow converges towards Navier-Stokes flow for $\phi \to 1$ and $k \to \infty$ (left figure). Darcy-Brinkman flow converges towards Darcy flow for $\mu \to 0$ and $\mu/k = \text{const}$ (right figure).

values for the porosity and the permeability into the Darcy-Brinkman equations (3.100) and the continuity equation (3.11). On the other hand, when the viscosity is decreased successively, the Darcy-Brinkman solution starts to flatten, see the right Subfigure 3.6. If the coefficient of the Darcy term is held constant, that is $\phi\mu/k = \text{const}$, the solution approaches the Darcy solution with the same Darcy coefficient. However, it can also be seen, that a boundary layer with a large velocity gradient develops in order to fulfill the no-slip condition. This will lead to an ill-conditioned numerical problem. Physically speaking, for vanishing viscosity, the fluid does no longer support shear stresses, which are necessary to maintain a zero tangential velocity. This illustrates, that a no-slip condition for a pure Darcy fluid without viscous term is an ill-posed problem.

3.7. Summary of the Coupled System

The system equations from the previous sections is recalled. Eliminating some depending variables, and in particular assuming incompressible flow, see Section 3.5.3, the following coupled system is obtained:

$$\mathring{\phi} + \phi\, \boldsymbol{\nabla}\cdot\boldsymbol{v}^{\mathrm{s}} + \boldsymbol{\nabla}\cdot\left(\phi\cdot\left(\boldsymbol{v}^{\mathrm{f}} - \boldsymbol{v}^{\mathrm{s}}\right)\right) = 0, \quad \text{in}\,\Omega_t \times [t_0, t_E], \tag{3.111}$$

$$\rho_0^{\mathrm{s}}(1-\phi_0)\boldsymbol{a}^{\mathrm{s}} - \boldsymbol{\nabla}_0\cdot(\boldsymbol{F}\cdot\boldsymbol{S}) - \rho_0^{\mathrm{s}}(1-\phi_0)\hat{\boldsymbol{b}} - \rho_0^{\mathrm{f}} J\phi\left(\hat{\boldsymbol{b}} - \boldsymbol{a}^{\mathrm{f}}\right) = \boldsymbol{0}, \quad \text{in}\,\Omega_0 \times [t_0, t_E], \tag{3.112}$$

with the abbreviation $\mathring{\phi} = \partial\phi/\partial t|_{\boldsymbol{X}}$. Equation (3.111) is the continuity equation derived from equation (3.11), where the material derivative with respect to the fluid phase was recast to the skeleton phase using equation (3.2). Equation (3.112) describes the balance of momentum of the porous medium. For the fluid flow, as stated above, either the Darcy equation

$$\rho_0^{\mathrm{f}}\boldsymbol{a}^{\mathrm{f}} + \mu^{\mathrm{f}}\phi\boldsymbol{k}^{-1}\cdot\left(\boldsymbol{v}^{\mathrm{f}} - \boldsymbol{v}^{\mathrm{s}}\right) + \boldsymbol{\nabla}p^{\mathrm{f}} - \rho_0^{\mathrm{f}}\hat{\boldsymbol{b}} = \boldsymbol{0} \quad \text{in}\,\Omega_t \times [t_0, t_E], \tag{3.113}$$

or the Darcy-Brinkman equation

$$\rho_0^{\mathrm{f}}\boldsymbol{a}^{\mathrm{f}} + \mu^{\mathrm{f}}\phi\boldsymbol{k}^{-1}\cdot\left(\boldsymbol{v}^{\mathrm{f}}-\boldsymbol{v}^{\mathrm{s}}\right) + \boldsymbol{\nabla}p^{\mathrm{f}} - \rho_0^{\mathrm{f}}\hat{\boldsymbol{b}} - \frac{1}{\phi}\boldsymbol{\nabla}\cdot\left(\phi\boldsymbol{\sigma}_{\mathrm{visc}}^{\mathrm{f}}\right) = \boldsymbol{0} \quad \text{in}\,\Omega_t\times[t_0,t_E] \tag{3.114}$$

will be used. The following rearrangements will be performed for the Darcy-Brinkman equation, but of course the same holds for the Darcy equation by dropping the viscous stress term. In order to eliminate the fluid acceleration from the equation (3.112), the Darcy-Brinkman equation (3.114) is transformed to the material configuration and added to equation (3.112) yielding

$$\rho_0^{\mathrm{s}}(1-\phi_0)\boldsymbol{a}^{\mathrm{s}} - \boldsymbol{\nabla}_0\cdot(\boldsymbol{F}\cdot\boldsymbol{S}) - \rho_0^{\mathrm{s}}(1-\phi_0)\hat{\boldsymbol{b}} - \mu^{\mathrm{f}}J\phi^2\boldsymbol{k}^{-1}\cdot\left(\boldsymbol{v}^{\mathrm{f}}-\boldsymbol{v}^{\mathrm{s}}\right) - J\phi\boldsymbol{F}^{-\mathrm{T}}\cdot\boldsymbol{\nabla}_0 p^{\mathrm{f}} = \boldsymbol{0}. \tag{3.115}$$

Note, that the current permeability $\boldsymbol{k}$ usually depends on the material permeability $\boldsymbol{K}$ and the deformation as given in equation (3.105). In a next step, the fluid acceleration $\boldsymbol{a}^{\mathrm{f}}$ in the Darcy equation (3.113) and Darcy-Brinkman equation (3.114) are expressed as a function of the fluid velocity. For this purpose, the fundamental ALE equation (3.5) is utilized. One obtains

$$\boldsymbol{a}^{\mathrm{f}} = \frac{\mathrm{d}^{\mathrm{f}}\boldsymbol{v}^{\mathrm{f}}}{\mathrm{d}t} = \left.\frac{\partial\boldsymbol{v}^{\mathrm{f}}(\boldsymbol{X},t)}{\partial t}\right|_{\boldsymbol{X}} + \left(\left(\boldsymbol{v}^{\mathrm{f}}-\boldsymbol{v}^{\mathrm{s}}\right)\cdot\boldsymbol{\nabla}\right)\boldsymbol{v}^{\mathrm{f}} \approx \mathring{\boldsymbol{v}}^{\mathrm{f}} - \left(\boldsymbol{v}^{\mathrm{s}}\cdot\boldsymbol{\nabla}\right)\boldsymbol{v}^{\mathrm{f}}. \tag{3.116}$$

Note, the abbreviation $\mathring{\boldsymbol{v}}^{\mathrm{f}} = \left.\partial\boldsymbol{v}^{\mathrm{f}}(\boldsymbol{X},t)/\partial t\right|_{\boldsymbol{X}}$. The convective term $\boldsymbol{v}^{\mathrm{f}}\cdot\boldsymbol{\nabla}\boldsymbol{v}^{\mathrm{f}}$ is neglected which corresponds to the assumption of flow at low Reynolds numbers, see Section 3.6.3. Collecting all system equations finally leads to the following strong formulation of the coupled porous medium problem:

$$\left\{\begin{aligned}
\mathring{\phi} + \phi\,\boldsymbol{\nabla}\cdot\boldsymbol{v}^{\mathrm{s}} + \boldsymbol{\nabla}\cdot\left(\phi\left(\boldsymbol{v}^{\mathrm{f}}-\boldsymbol{v}^{\mathrm{s}}\right)\right) &= 0, && \text{in}\,\Omega_t\times[t_0,t_E],\\
\rho_0^{\mathrm{f}}\mathring{\boldsymbol{v}}^{\mathrm{f}} - \rho_0^{\mathrm{f}}\left(\boldsymbol{v}^{\mathrm{s}}\cdot\boldsymbol{\nabla}\right)\boldsymbol{v}^{\mathrm{f}} + \boldsymbol{\nabla}p^{\mathrm{f}} - \rho_0^{\mathrm{f}}\hat{\boldsymbol{b}} +&\\
+\mu^{\mathrm{f}}\phi\boldsymbol{k}^{-1}\cdot\left(\boldsymbol{v}^{\mathrm{f}}-\boldsymbol{v}^{\mathrm{s}}\right) - \frac{1}{\phi}\boldsymbol{\nabla}\cdot\left(\phi\boldsymbol{\sigma}_{\mathrm{visc}}^{\mathrm{f}}\right) &= \boldsymbol{0}, && \text{in}\,\Omega_t\times[t_0,t_E],\\
\rho_0^{\mathrm{s}}(1-\phi_0)\boldsymbol{a}^{\mathrm{s}} - \boldsymbol{\nabla}_0\cdot(\boldsymbol{F}\cdot\boldsymbol{S}) - \rho_0^{\mathrm{s}}(1-\phi_0)\hat{\boldsymbol{b}} +&\\
-J\phi\boldsymbol{F}^{-\mathrm{T}}\cdot\boldsymbol{\nabla}_0 p^{\mathrm{f}} - \mu^{\mathrm{f}}J\phi^2\boldsymbol{k}^{-1}\cdot\left(\boldsymbol{v}^{\mathrm{f}}-\boldsymbol{v}^{\mathrm{s}}\right) &= \boldsymbol{0}, && \text{in}\,\Omega_0\times[t_0,t_E],\\
\boldsymbol{S} = \phi\boldsymbol{S}_{\mathrm{visc}}^{\mathrm{f}} - p^{\mathrm{f}}J\boldsymbol{C}^{-1} + \frac{\partial\Psi^{\mathrm{s}}(\boldsymbol{E},J\phi)}{\partial\boldsymbol{E}} && && \text{in}\,\Omega_0\times[t_0,t_E],\\
p^{\mathrm{f}} = \frac{\partial\Psi^{\mathrm{s}}(\boldsymbol{E},J\phi)}{\partial(J\phi)} && && \text{in}\,\Omega_0\times[t_0,t_E].
\end{aligned}\right. \tag{3.117}$$

In order to obtain a complete description of the problem, suitable initial and boundary condition must be defined. Obviously, as initial conditions, the solid displacements and velocity and the fluid velocity are prescribed

$$\begin{aligned}
\boldsymbol{d}^{\mathrm{s}} &= \hat{\boldsymbol{d}}_0^{\mathrm{s}} && \text{in}\,\Omega_0\times\{0\},\\
\boldsymbol{v}^{\mathrm{s}} &= \hat{\boldsymbol{v}}_0^{\mathrm{s}} && \text{in}\,\Omega_0\times\{0\},\\
\boldsymbol{v}^{\mathrm{f}} &= \hat{\boldsymbol{v}}_0^{\mathrm{f}} && \text{in}\,\Omega_t\times\{0\}.
\end{aligned} \tag{3.118}$$

Defining suitable boundary conditions for porous media problems is a little more intricate, as one condition for each phase is needed at every boundary of the domain. For instance, a Neu-

mann condition can be applied on the global mixture as well as on the pore fluid on the same boundary Γ^{N} in different configurations as

$$\begin{aligned} (\boldsymbol{F}\cdot\boldsymbol{S})\cdot\boldsymbol{N} &= \hat{\boldsymbol{t}}_0 \quad \text{on } \Gamma_0^{\mathrm{N,s}}\times[t_0,t_E], \\ \boldsymbol{\sigma}^{\mathrm{f}}\cdot\boldsymbol{n} &= \hat{\boldsymbol{t}}_t^{\mathrm{f}} \quad \text{on } \Gamma_t^{\mathrm{N,f}}\times[t_0,t_E]. \end{aligned} \tag{3.119}$$

Note that the fluid stress tensor $\boldsymbol{\sigma}^{\mathrm{f}}$ only includes the fluid pressure in the Darcy case, i.e. $\boldsymbol{\sigma}^{\mathrm{f}} = -p^{\mathrm{f}}\boldsymbol{I}$ and in the Brinkman case also viscous effects, i.e. $\boldsymbol{\sigma}^{\mathrm{f}} = -p^{\mathrm{f}}\boldsymbol{I} + \boldsymbol{\sigma}^{\mathrm{f}}_{\mathrm{visc}}$. Analogously, the simplest Dirichlet boundary condition is a prescribed displacement field $\hat{\boldsymbol{d}}^{\mathrm{s}}$ on a part of the structural boundary $\Gamma_0^{\mathrm{D,s}}$ in the material configuration:

$$\boldsymbol{d}^{\mathrm{s}} = \hat{\boldsymbol{d}}^{\mathrm{s}} \quad \text{on } \Gamma_0^{\mathrm{D,s}}\times[t_0,t_E], \tag{3.120}$$

and analogously Dirichlet boundary conditions concerning the fluid velocities on a current boundary $\Gamma_t^{\mathrm{D,f}}$:

$$\begin{aligned} &\text{Darcy:} && \boldsymbol{v}^{\mathrm{f}}\cdot\boldsymbol{n} = \hat{v}_{\perp}^{\mathrm{f}} && \text{on } \Gamma_t^{\mathrm{D,f}}\times[t_0,t_E], \\ &\text{Darcy-Brinkman:} && \boldsymbol{v}^{\mathrm{f}} = \hat{\boldsymbol{v}}^{\mathrm{f}} && \text{on } \Gamma_t^{\mathrm{D,f}}\times[t_0,t_E], \end{aligned} \tag{3.121}$$

with the prescribed normal velocity $\hat{v}_{\perp}^{\mathrm{f}}$ and the prescribed velocity $\hat{\boldsymbol{v}}^{\mathrm{f}}$. However, the respective Dirichlet and Neumann boundaries of both phases need not necessarily be identical. A typical example for this is an impermeability constraint. This implies an equality of the normal components of the velocities in case of Darcy flow and identical velocities for Darcy-Brinkman flow at a part of the boundary Γ_t^{c}:

$$\begin{aligned} &\text{Darcy:} && \phi\boldsymbol{n}\cdot\left(\boldsymbol{v}^{\mathrm{f}}-\boldsymbol{v}^{\mathrm{s}}\right) = 0 && \text{on } \Gamma_t^{c}\times[t_0,t_E], \\ &\text{Darcy-Brinkman:} && \boldsymbol{v}^{\mathrm{f}}-\boldsymbol{v}^{\mathrm{s}} = \boldsymbol{0} && \text{on } \Gamma_t^{\mathrm{c}}\times[t_0,t_E]. \end{aligned} \tag{3.122}$$

These conditions can be combined with a traction boundary for the whole mixture or a Dirichlet boundary on the solid phase. The impermeability constraints are non-trivial to account for in non-linear poroelasticity, especially if a curved boundary is moving and included in a monolithic scheme, which will be further discussed in Section 4.3.2.3.

4. Computational Approach to Porous Media Problems

In order to solve the system of equations numerically, they need to be discretized in time and space. In this thesis, standard proceedings are used for each involved field. In Section 4.1, two basic methods for time discretization will be presented. The semi-discrete form is obtained by applying those methods to the initial boundary value problem (IBVP) in Section 4.2. Following this, the weak form of the given IBVP is derived in Section 4.3 leading to the fully discrete system. The finite element formulation will be elaborated in detail there. Different formulations for Darcy and Darcy-Brinkman flow will be presented. They are particularly designed for the case of non-constant porosities. Finally, the presented approaches will be illustrated numerical examples in Section 4.4.

4.1. Discretization in Time

A various number of methods exist for the temporal discretization of a differential equation. One can differentiate between explicit and implicit methods. While explicit methods allow for a direct extrapolation of a given solution in time, implicit methods in general require solving a set of non-linear equations to find the solution of the next time step. Throughout this thesis only implicit schemes are considered, as they can be proven to be unconditionally stable and allow for larger time steps compared to explicit schemes. The two implicit schemes applied here are the one-step-θ scheme and the generalized-α scheme.

4.1.1. One-Step-θ Scheme

The one-step-θ scheme is a simple, single-step scheme. The methodology will be presented for first- and second-order systems. A first-order differential equation

$$\dot{\boldsymbol{v}} = \boldsymbol{f}\left(\boldsymbol{v}, t\right) \tag{4.1}$$

is discretized in time using the one-step-θ scheme. The terms can be evaluated at the intermediate time step $t_{n+\theta} = (1-\theta)t_n + \theta t_{n+1}$. It holds

$$\dot{\boldsymbol{v}}_{n+\theta} = (1-\theta)\dot{\boldsymbol{v}}_n + \theta\dot{\boldsymbol{v}}_{n+1} = \frac{\boldsymbol{v}_{n+1} - \boldsymbol{v}_n}{\Delta t}, \tag{4.2}$$

$$\boldsymbol{f}_{n+\theta} = (1-\theta)\boldsymbol{f}\left(\boldsymbol{v}_n, t_n\right) + \theta\boldsymbol{f}\left(\boldsymbol{v}_{n+1}, t_{n+1}\right). \tag{4.3}$$

The subscripts n and $n+1$ denote the values at the discrete time t_n and t_{n+1}, respectively. The time step size is denoted by $\Delta t = t_{n+1} - t_n$. The discretized form of the differential equation (4.1)

then reads

$$\dot{\boldsymbol{v}}_{n+\theta} = \boldsymbol{f}_{n+\theta}, \tag{4.4}$$

or, in a more common form, directly solved for the unknown state $\boldsymbol{v}_{n+1}$

$$\boldsymbol{v}_{n+1} = \boldsymbol{v}_n + (1-\theta)\Delta t \underbrace{\boldsymbol{f}\left(\boldsymbol{v}_n, t_n\right)}_{\dot{\boldsymbol{v}}_n} + \theta \Delta t \boldsymbol{f}\left(\boldsymbol{v}_{n+1}, t_{n+1}\right). \tag{4.5}$$

The parameter $\theta \in [0,1]$ determines the behavior of the integration scheme. The method is implicit unless for $\theta = 0$. An unconditionally stable, implicit scheme is obtained for $\theta \in [0.5, 1]$. Second-order accuracy is only achieved for $\theta = 0.5$ (trapezoidal rule). All other values of θ lead to a first-order scheme. Further prominent members of the one-step-θ family are the implicit backward Euler scheme ($\theta = 1$) and the explicit forward Euler scheme ($\theta = 0$).

For a second order system

$$\left\{ \begin{array}{rcl} \dot{\boldsymbol{d}}(t) - \boldsymbol{v}(t) & = & \boldsymbol{0}, \\ \dot{\boldsymbol{v}}(t) - \boldsymbol{a}(t) & = & \boldsymbol{0}, \\ \boldsymbol{M} \cdot \boldsymbol{a}(t) + \boldsymbol{f}\left(\boldsymbol{d}(t), \boldsymbol{v}(t), t\right) + \boldsymbol{f}_{\text{ext}}(t) & = & \boldsymbol{0}, \end{array} \right. \tag{4.6}$$

the discrete states can be written as follows

$$\boldsymbol{v}_{n+1} = \frac{1}{\theta \Delta t}(\boldsymbol{d}_{n+1} - \boldsymbol{d}_n) - \frac{(1-\theta)}{\theta}\boldsymbol{v}_n, \tag{4.7}$$

$$\boldsymbol{a}_{n+1} = \frac{1}{\theta^2 \Delta t^2}(\boldsymbol{d}_{n+1} - \boldsymbol{d}_n) - \frac{1}{\theta^2 \Delta t}\boldsymbol{v}_n - \frac{(1-\theta)}{\theta}\boldsymbol{a}_n. \tag{4.8}$$

The terms are then expressed at the intermediate time step $t_{n+\theta} = (1-\theta)t_n + \theta t_{n+1}$ as

$$\boldsymbol{d}_{n+\theta} = (1-\theta)\boldsymbol{d}_n + \theta \boldsymbol{d}_{n+1}, \tag{4.9}$$

$$\boldsymbol{v}_{n+\theta} = (1-\theta)\boldsymbol{v}_n + \theta \boldsymbol{v}_{n+1}, \tag{4.10}$$

$$\boldsymbol{a}_{n+\theta} = (1-\theta)\boldsymbol{a}_n + \theta \boldsymbol{a}_{n+1}, \tag{4.11}$$

$$\boldsymbol{f}_{n+\theta} = (1-\theta)\boldsymbol{f}(\boldsymbol{d}_n, \boldsymbol{v}_n, t_n) + \theta \boldsymbol{f}(\boldsymbol{d}_{n+1}, \boldsymbol{v}_{n+1}, t_{n+1}), \tag{4.12}$$

$$\boldsymbol{f}_{\text{ext},n+\theta} = (1-\theta)\boldsymbol{f}_{\text{ext}}(t_n) + \theta \boldsymbol{f}_{\text{ext}}(t_{n+1}). \tag{4.13}$$

The final equation then reads

$$\boldsymbol{M} \cdot \boldsymbol{a}_{n+\theta} + \boldsymbol{f}_{n+\theta} + \boldsymbol{f}_{\text{ext},n+\theta} = \boldsymbol{0}. \tag{4.14}$$

Note, that in equation (4.12) it was decided to interpolate $\boldsymbol{f}$ between the two discrete times t_n and t_{n+1}. A valid alternative is interpolating the states instead, i.e. $\boldsymbol{f}_{n+\theta} = \boldsymbol{f}(\boldsymbol{d}_{n+\theta}, \boldsymbol{v}_{n+\theta}, t_{n+\theta})$. Those two expressions differ for non-linear problems. Since none of these versions is clearly better than the other, equation (4.12) is used in the following.

4.1.2. Generalized-α Scheme

The second method used here is the generalized-α scheme. It was introduced for first-order systems with application to Navier-Stokes flow in [137]. The discrete form of a first-order system of differential equations (4.1) given by the generalized-α scheme reads

$$\dot{\boldsymbol{v}}_{n+\alpha_\mathrm{m}} = \boldsymbol{f}\left(\boldsymbol{y}_{n+\alpha_\mathrm{f}}, t_{n+\alpha_\mathrm{f}}\right), \tag{4.15}$$

$$\dot{\boldsymbol{v}}_{n+\alpha_\mathrm{m}} = (1-\alpha_\mathrm{m})\,\dot{\boldsymbol{v}}_n + \alpha_\mathrm{m}\dot{\boldsymbol{v}}_{n+1}, \tag{4.16}$$

$$\boldsymbol{v}_{n+\alpha_\mathrm{f}} = (1-\alpha_\mathrm{f})\,\boldsymbol{v}_n + \alpha_\mathrm{f}\boldsymbol{v}_{n+1}, \tag{4.17}$$

$$\boldsymbol{v}_{n+1} = \boldsymbol{v}_n + \Delta t(1-\gamma)\dot{\boldsymbol{v}}_n + \Delta t\gamma\dot{\boldsymbol{v}}_{n+1}. \tag{4.18}$$

Therein, α_m, α_f and γ are the parameters of the method. Note, that with the two parameters, α_m and α_f two intermediate time levels $t_{n+\alpha_\mathrm{m}} = (1-\alpha_\mathrm{m})t_n + \alpha_\mathrm{m}\, t_{n+1}$ and $t_{n+\alpha_\mathrm{f}} = (1-\alpha_\mathrm{f})t_n + \alpha_\mathrm{f}\, t_{n+1}$ are introduced, where the problem is evaluated. According to [137] the generalized-α scheme for a linear first-order system is stable if

$$\alpha_\mathrm{m} \geq \alpha_\mathrm{f} \geq \frac{1}{2} \tag{4.19}$$

and second-order accurate if

$$\gamma = \frac{1}{2} + \alpha_\mathrm{m} - \alpha_\mathrm{f} \tag{4.20}$$

is fulfilled. In the same reference, a second-order accurate approach with specified high-frequency damping is proposed. It depends on one single parameter $\rho_\infty \in [0,1]$ from which the other parameters can be calculated as

$$\alpha_\mathrm{f} = \frac{1}{1+\rho_\infty}, \qquad \alpha_\mathrm{m} = \frac{3-\rho_\infty}{2+2\rho_\infty}, \qquad \gamma = \frac{1}{2} + \alpha_\mathrm{m} - \alpha_\mathrm{f}. \tag{4.21}$$

For $\rho_\infty = 0$ the highest frequency of a linear problem will be annihilated within one time step. For $\rho_\infty = 1$ no numerical damping is introduced. The one-step-θ method for a first-order system can be reproduced by choosing $\alpha_\mathrm{f} = \alpha_\mathrm{m} = 1$ and $\gamma = \theta$. Also other time integration schemes are included within the generalized-α method. However, as they are not used within this thesis, this will not be discussed further. The interested reader is again referred to [137] for details.

For a second-order system (4.6) the discrete time derivatives can be given [61] as

$$\boldsymbol{v}_{n+1} = \frac{\gamma}{\beta\Delta t}\left(\boldsymbol{d}_{n+1} - \boldsymbol{d}_n\right) - \frac{\gamma-\beta}{\beta}\boldsymbol{v}_n - \frac{\gamma-2\beta}{2\beta}\Delta t\,\boldsymbol{a}_n, \tag{4.22}$$

$$\boldsymbol{a}_{n+1} = \frac{1}{\beta\Delta t^2}\left(\boldsymbol{d}_{n+1} - \boldsymbol{d}_n\right) - \frac{1}{\beta\Delta t}\boldsymbol{v}_n - \frac{1-2\beta}{2\beta}\,\boldsymbol{a}_n. \tag{4.23}$$

Note, that for second-order systems, the additional parameter β is introduced. The terms are evaluated at the intermediate time steps $t_{n+1-\alpha_\mathrm{m}} = \alpha_\mathrm{m} t_n + (1-\alpha_\mathrm{m})\, t_{n+1}$ and $t_{n+1-\alpha_\mathrm{f}} =$

$\alpha_\mathrm{f} t_n + (1-\alpha_\mathrm{f})\, t_{n+1}$:

$$\boldsymbol{d}_{n+1-\alpha_\mathrm{f}} = \alpha_\mathrm{f}\boldsymbol{d}_n + (1-\alpha_\mathrm{f})\boldsymbol{d}_{n+1}, \tag{4.24}$$
$$\boldsymbol{v}_{n+1-\alpha_\mathrm{f}} = \alpha_\mathrm{f}\boldsymbol{v}_n + (1-\alpha_\mathrm{f})\boldsymbol{v}_{n+1}, \tag{4.25}$$
$$\boldsymbol{a}_{n+1-\alpha_\mathrm{m}} = \alpha_\mathrm{m}\boldsymbol{a}_n + (1-\alpha_\mathrm{m})\boldsymbol{a}_{n+1}, \tag{4.26}$$
$$\boldsymbol{f}_{n+1-\alpha_\mathrm{f}} = \alpha_\mathrm{f}\boldsymbol{f}\left(\boldsymbol{v}_n, \boldsymbol{d}_n, t_n\right) + (1-\alpha_\mathrm{f})\boldsymbol{f}\left(\boldsymbol{v}_{n+1}, \boldsymbol{d}_{n+1}, t_{n+1}\right), \tag{4.27}$$
$$\boldsymbol{f}_{\mathrm{ext},n+1-\alpha_\mathrm{f}} = \alpha_\mathrm{f}\boldsymbol{f}_\mathrm{ext}(t_n) + (1-\alpha_\mathrm{f})\boldsymbol{f}_\mathrm{ext}(t_{n+1}). \tag{4.28}$$

The discrete system then reads

$$\boldsymbol{M}\cdot\boldsymbol{a}_{n+1-\alpha_\mathrm{m}} + \boldsymbol{f}_{n+1-\alpha_\mathrm{f}} + \boldsymbol{f}_{\mathrm{ext},n+1-\alpha_\mathrm{f}} = \boldsymbol{0}. \tag{4.29}$$

Remark 4.1 *Note, that the definition of the time level is different for first- and second-order equations ($t_{n+1-\alpha_\mathrm{m}}$ compared to $t_{n+\alpha_\mathrm{m}}$ and $t_{n+1-\alpha_\mathrm{f}}$ compared to $t_{n+\alpha_\mathrm{f}}$). Actually, this is just a change of definition of α_f and α_m from the first-order system to the second-order system. The value of α_f for the first-order system is $1-\alpha_\mathrm{f}$ of the second-order system (and the same for α_m). This is how the respective methods are defined in the original papers [137] and [61]. As this is also the form that is implemented for the fluid equations (first-order system) and the skeleton/structure equations (second-order system), this notation is kept here.*

Again, it was shown in [61] that the generalized-α scheme for linear, second-order systems is unconditionally stable if

$$\alpha_\mathrm{m} \leq \alpha_\mathrm{f} \leq \frac{1}{2}, \quad \beta \geq \frac{1}{4} + \frac{1}{2}(\alpha_\mathrm{f} - \alpha_\mathrm{m}), \tag{4.30}$$

and second-order accurate if

$$\gamma = \frac{1}{2} - \alpha_\mathrm{m} + \alpha_\mathrm{f}. \tag{4.31}$$

Also for second-order systems the high order frequency damping can be controlled with the parameter ρ_∞. The other parameters can then be deduced as

$$\alpha_\mathrm{f} = \frac{\rho_\infty}{1+\rho_\infty}, \quad \alpha_\mathrm{m} = \frac{2\rho_\infty - 1}{\rho_\infty + 1}, \quad \gamma = \frac{1}{2} - \alpha_\mathrm{m} + \alpha_\mathrm{f}, \quad \beta = \frac{1}{4}(1 - \alpha_\mathrm{m} + \alpha_\mathrm{f})^2. \tag{4.32}$$

As for the first-order system, for $\rho_\infty = 1$ a mid-point rule without numerical dissipation is obtained.

4.2. Time-Discrete Form

In the following, two semi-discrete forms of the system (3.117) will be deduced. For time discretization, the one-step-θ is utilized, as this method is used for most examples. Note, that the generalized-α method can be applied in a similar way and is also included in the implementation. For the first version of a time-discrete form, the porosity and its time derivatives are expressed

in terms of the skeleton displacement, velocity and the fluid pressure:

$$\mathring{\phi}(\boldsymbol{d}^{\mathrm{s}}, \boldsymbol{v}^{\mathrm{s}}, p^{\mathrm{f}}, \mathring{p}^{\mathrm{f}}) = \frac{\partial \phi}{\partial p^{\mathrm{f}}}(\boldsymbol{d}^{\mathrm{s}}, p^{\mathrm{f}})\mathring{p}^{\mathrm{f}} + \frac{\partial \phi}{\partial J}(\boldsymbol{d}^{\mathrm{s}}, p^{\mathrm{f}})\mathring{J}(\boldsymbol{d}^{\mathrm{s}}) = \frac{\partial \phi}{\partial p^{\mathrm{f}}}(\boldsymbol{d}^{\mathrm{s}}, p^{\mathrm{f}})\mathring{p}^{\mathrm{f}} + \frac{\partial \phi}{\partial J}(\boldsymbol{d}^{\mathrm{s}}, p^{\mathrm{f}})J(\boldsymbol{d}^{\mathrm{s}})\,\boldsymbol{\nabla}\cdot\boldsymbol{v}^{\mathrm{s}}. \tag{4.33}$$

Inserting this into the strong equations (3.117), the semi-discrete form can be written as

$$\begin{cases} \mathring{p}^{\mathrm{f}}_{n+\theta} + f^{\mathrm{f}}_{\mathrm{C},n+\theta}(\boldsymbol{d}^{\mathrm{s}}_{n+1}, \boldsymbol{v}^{\mathrm{f}}_{n+1}, p^{\mathrm{f}}_{n+1}) &= 0, \\ \rho^{\mathrm{f}}_0 \mathring{\boldsymbol{v}}^{\mathrm{f}}_{n+\theta} + \boldsymbol{f}^{\mathrm{f}}_{\mathrm{M},n+\theta}(\boldsymbol{d}^{\mathrm{s}}, \boldsymbol{v}^{\mathrm{f}}, p^{\mathrm{f}}) &= \boldsymbol{0}, \\ \rho^{\mathrm{s}}_0(1-\phi_0)\boldsymbol{a}^{\mathrm{s}}_{n+\theta} + \boldsymbol{f}^{\mathrm{s}}_{\mathrm{M},n+\theta}(\boldsymbol{d}^{\mathrm{s}}_{n+1}, \boldsymbol{v}^{\mathrm{f}}_{n+1}, p^{\mathrm{f}}_{n+1}) &= \boldsymbol{0}. \end{cases} \tag{4.34}$$

The first equation is the mass balance of the fluid. The other two equations are the flow equation and the balance of linear momentum of the porous medium, respectively. For compactness of notation, the following additional abbreviations were introduced:

$$f^{\mathrm{f}}_{\mathrm{C},n+\theta}(\boldsymbol{d}^{\mathrm{s}}_{n+1}, \boldsymbol{v}^{\mathrm{f}}_{n+1}, p^{\mathrm{f}}_{n+1}) = (1-\theta)\mathring{p}^{\mathrm{f}}_n + \theta f^{\mathrm{f}}_{\mathrm{C}}(\boldsymbol{d}^{\mathrm{s}}_{n+1}, \boldsymbol{v}^{\mathrm{f}}_{n+1}, p^{\mathrm{f}}_{n+1}) \tag{4.35}$$

$$\begin{aligned} f^{\mathrm{f}}_{\mathrm{C}}(\boldsymbol{d}^{\mathrm{s}}, \boldsymbol{v}^{\mathrm{f}}, p^{\mathrm{f}}) = &\left(\frac{\partial \phi}{\partial p^{\mathrm{f}}}(\boldsymbol{d}^{\mathrm{s}}, p^{\mathrm{f}})\right)^{-1} \Bigg(\left(\frac{\partial \phi}{\partial J}(\boldsymbol{d}^{\mathrm{s}}, p^{\mathrm{f}})\right) J(\boldsymbol{d}^{\mathrm{s}})\,\boldsymbol{\nabla}\cdot\boldsymbol{v}^{\mathrm{s}} \\ &+ \phi(\boldsymbol{d}^{\mathrm{s}}, p^{\mathrm{f}})\,\boldsymbol{\nabla}\cdot\boldsymbol{v}^{\mathrm{s}} + \boldsymbol{\nabla}\cdot\left(\phi\left(\boldsymbol{v}^{\mathrm{f}} - \boldsymbol{v}^{\mathrm{s}}\right)\right) \Bigg), \end{aligned} \tag{4.36}$$

$$\boldsymbol{f}^{\mathrm{f}}_{\mathrm{M},n+\theta}(\boldsymbol{d}^{\mathrm{s}}_{n+1}, \boldsymbol{v}^{\mathrm{f}}_{n+1}, p^{\mathrm{f}}_{n+1}) = (1-\theta)\mathring{\boldsymbol{v}}^{\mathrm{f}}_n + \theta \boldsymbol{f}^{\mathrm{f}}_{\mathrm{M}}(\boldsymbol{d}^{\mathrm{s}}_{n+1}, \boldsymbol{v}^{\mathrm{f}}_{n+1}, p^{\mathrm{f}}_{n+1}) \tag{4.37}$$

$$\begin{aligned} \boldsymbol{f}^{\mathrm{f}}_{\mathrm{M}}(\boldsymbol{d}^{\mathrm{s}}, \boldsymbol{v}^{\mathrm{f}}, p^{\mathrm{f}}) = &-\rho^{\mathrm{f}}_0\left(\boldsymbol{v}^{\mathrm{s}}\cdot\boldsymbol{\nabla}\right)\boldsymbol{v}^{\mathrm{f}} + \boldsymbol{\nabla}p^{\mathrm{f}} - \rho^{\mathrm{f}}_0\hat{\boldsymbol{b}} \\ &+ \mu^{\mathrm{f}}\phi(\boldsymbol{d}^{\mathrm{s}}, p^{\mathrm{f}})\boldsymbol{k}^{-1}(\boldsymbol{d}^{\mathrm{s}})\cdot\left(\boldsymbol{v}^{\mathrm{f}} - \boldsymbol{v}^{\mathrm{s}}\right) \\ &- \frac{1}{\phi(\boldsymbol{d}^{\mathrm{s}}, p^{\mathrm{f}})}\boldsymbol{\nabla}\cdot\left(\phi(\boldsymbol{d}^{\mathrm{s}}, p^{\mathrm{f}})\boldsymbol{\sigma}^{\mathrm{f}}_{\mathrm{visc}}(\boldsymbol{d}^{\mathrm{s}}, \boldsymbol{v}^{\mathrm{f}})\right), \end{aligned} \tag{4.38}$$

$$\boldsymbol{f}^{\mathrm{s}}_{\mathrm{M},n+\theta}(\boldsymbol{d}^{\mathrm{s}}_{n+1}, \boldsymbol{v}^{\mathrm{f}}_{n+1}, p^{\mathrm{f}}_{n+1}) = (1-\theta)\boldsymbol{a}^{\mathrm{s}}_n + \theta \boldsymbol{f}^{\mathrm{s}}_{\mathrm{M}}(\boldsymbol{d}^{\mathrm{s}}_{n+1}, \boldsymbol{v}^{\mathrm{f}}_{n+1}, p^{\mathrm{f}}_{n+1}) \tag{4.39}$$

$$\begin{aligned} \boldsymbol{f}^{\mathrm{s}}_{\mathrm{M}}(\boldsymbol{d}^{\mathrm{s}}, \boldsymbol{v}^{\mathrm{f}}, p^{\mathrm{f}}) = &-\boldsymbol{\nabla}_0\cdot\left(\boldsymbol{F}(\boldsymbol{d}^{\mathrm{s}})\cdot\boldsymbol{S}(\boldsymbol{d}^{\mathrm{s}}, \boldsymbol{v}^{\mathrm{f}}, p^{\mathrm{f}})\right) - \rho^{\mathrm{s}}_0(1-\phi_0)\hat{\boldsymbol{b}} \\ &- J(\boldsymbol{d}^{\mathrm{s}})\phi(\boldsymbol{d}^{\mathrm{s}}, p^{\mathrm{f}})\boldsymbol{F}^{-\mathrm{T}}(\boldsymbol{d}^{\mathrm{s}})\cdot\boldsymbol{\nabla}_0 p^{\mathrm{f}} \\ &- \mu^{\mathrm{f}}J(\boldsymbol{d}^{\mathrm{s}})\phi^2(\boldsymbol{d}^{\mathrm{s}}, p^{\mathrm{f}})\boldsymbol{k}^{-1}(\boldsymbol{d}^{\mathrm{s}})\cdot\left(\boldsymbol{v}^{\mathrm{f}} - \boldsymbol{v}^{\mathrm{s}}\right). \end{aligned} \tag{4.40}$$

The necessary discrete time derivatives and end-time skeleton velocity can be calculated in accordance to equations (4.2), (4.8) and (4.11) in terms of known values from the last time step n

and unknown primary variables at time step $n+1$ as

$$\mathring{p}^{\mathrm{f}}_{n+\theta}(p^{\mathrm{f}}_{n+1}) = \frac{p^{\mathrm{f}}_{n+1} - p^{\mathrm{f}}_{n}}{\Delta t}, \tag{4.41}$$

$$\mathring{\boldsymbol{v}}^{\mathrm{f}}_{n+\theta}(\boldsymbol{v}^{\mathrm{f}}_{n+1}) = \frac{\boldsymbol{v}^{\mathrm{f}}_{n+1} - \boldsymbol{v}^{\mathrm{f}}_{n}}{\Delta t}, \tag{4.42}$$

$$\boldsymbol{a}^{\mathrm{s}}_{n+\theta}(\boldsymbol{d}^{\mathrm{s}}_{n+1}) = \frac{1}{\theta\Delta t^2}(\boldsymbol{d}_{n+1} - \boldsymbol{d}_n) - \frac{1}{\theta\Delta t}\boldsymbol{v}_n, \tag{4.43}$$

$$\mathring{p}^{\mathrm{f}}_{n} = f^{\mathrm{f}}_{\mathrm{C}}(\boldsymbol{d}^{\mathrm{s}}_n, \boldsymbol{v}^{\mathrm{f}}_n, p^{\mathrm{f}}_n), \tag{4.44}$$

$$\mathring{\boldsymbol{v}}^{\mathrm{f}}_{n} = \boldsymbol{f}^{\mathrm{f}}_{\mathrm{M}}(\boldsymbol{d}^{\mathrm{s}}_n, \boldsymbol{v}^{\mathrm{f}}_n, p^{\mathrm{f}}_n, t_n), \tag{4.45}$$

$$\boldsymbol{a}^{\mathrm{s}}_{n} = \boldsymbol{f}^{\mathrm{s}}_{\mathrm{M}}(\boldsymbol{d}^{\mathrm{s}}_n, \boldsymbol{v}^{\mathrm{f}}_n, p^{\mathrm{f}}_n, t_n), \tag{4.46}$$

$$\boldsymbol{v}^{\mathrm{s}}_{n+1}(\boldsymbol{d}^{\mathrm{s}}_{n+1}) = \frac{1}{\theta\Delta t}(\boldsymbol{d}_{n+1} - \boldsymbol{d}_n) - \frac{(1-\theta)}{\theta}\boldsymbol{v}_n. \tag{4.47}$$

This form will later be utilized for the weak form of the porous system with Darcy flow in Section 4.3.2.1 and for one variant of a porous system with Darcy-Brinkman flow in Section 4.3.2.2.

An alternative time-discrete form is obtained as follows. If the porosity is not expressed in terms of other variables, but directly discretized in time instead, one concludes

$$\begin{cases} \mathring{\phi}_{n+\theta} + f^{\mathrm{f}}_{\mathrm{C}\phi,n+\theta}(\boldsymbol{d}^{\mathrm{s}}_{n+1}, \boldsymbol{v}^{\mathrm{f}}_{n+1}, p^{\mathrm{f}}_{n+1}, \phi_{n+1}) & = 0, \\ \rho^{\mathrm{f}}_0 \mathring{\boldsymbol{v}}^{\mathrm{f}}_{n+\theta} + \boldsymbol{f}^{\mathrm{f}}_{\mathrm{M}\phi,n+\theta}(\boldsymbol{d}^{\mathrm{s}}_{n+1}, \boldsymbol{v}^{\mathrm{f}}_{n+1}, p^{\mathrm{f}}_{n+1}, \phi_{n+1}) & = \boldsymbol{0}, \\ \rho^{\mathrm{s}}_0(1-\phi_0)\boldsymbol{a}^{\mathrm{s}}_{n+\theta} + \boldsymbol{f}^{\mathrm{s}}_{\mathrm{M}\phi,n+\theta}(\boldsymbol{d}^{\mathrm{s}}_{n+1}, \boldsymbol{v}^{\mathrm{f}}_{n+1}, p^{\mathrm{f}}_{n+1}) & = \boldsymbol{0}, \\ (1-\theta)\left(p^{\mathrm{f}}_n - \dfrac{\partial \Psi^{\mathrm{s}}}{\partial(J\phi)}(\boldsymbol{d}^{\mathrm{s}}_n, p^{\mathrm{f}}_n, \phi_n)\right) & \\ +\theta\left(p^{\mathrm{f}}_{n+1} - \left(\dfrac{\partial \Psi^{\mathrm{s}}}{\partial(J\phi)}(\boldsymbol{d}^{\mathrm{s}}_{n+1}, p^{\mathrm{f}}_{n+1}, \phi_{n+1})\right)\right) & = 0. \end{cases} \tag{4.48}$$

Here, the following notation was used

$$f^{\mathrm{f}}_{\mathrm{C}\phi,n+\theta}(\boldsymbol{d}^{\mathrm{s}}_{n+1},\boldsymbol{v}^{\mathrm{f}}_{n+1},p^{\mathrm{f}}_{n+1},\phi_{n+1}) = (1-\theta)\mathring{\phi}_n + \theta f^{\mathrm{f}}_{\mathrm{C}\phi}(\boldsymbol{d}^{\mathrm{s}}_{n+1},\boldsymbol{v}^{\mathrm{f}}_{n+1},p^{\mathrm{f}}_{n+1}) \tag{4.49}$$

$$f^{\mathrm{f}}_{\mathrm{C}\phi}(\boldsymbol{d}^{\mathrm{s}},\boldsymbol{v}^{\mathrm{f}},p^{\mathrm{f}},\phi) = \phi\,\boldsymbol{\nabla}\cdot\boldsymbol{v}^{\mathrm{s}} + \boldsymbol{\nabla}\cdot\left(\phi\left(\boldsymbol{v}^{\mathrm{f}}-\boldsymbol{v}^{\mathrm{s}}\right)\right), \tag{4.50}$$

$$\boldsymbol{f}^{\mathrm{f}}_{\mathrm{M}\phi,n+\theta}(\boldsymbol{d}^{\mathrm{s}}_{n+1},\boldsymbol{v}^{\mathrm{f}}_{n+1},p^{\mathrm{f}}_{n+1},\phi_{n+1}) = (1-\theta)\mathring{\boldsymbol{v}}^{\mathrm{f}}_n + \theta\boldsymbol{f}^{\mathrm{f}}_{\mathrm{M}\phi}(\boldsymbol{d}^{\mathrm{s}}_{n+1},\boldsymbol{v}^{\mathrm{f}}_{n+1},p^{\mathrm{f}}_{n+1},p^{\mathrm{f}}_{n+1}) \tag{4.51}$$

$$\begin{aligned}\boldsymbol{f}^{\mathrm{f}}_{\mathrm{M}\phi}(\boldsymbol{d}^{\mathrm{s}},\boldsymbol{v}^{\mathrm{f}},p^{\mathrm{f}},\phi) = &-\rho^{\mathrm{f}}_0\left(\boldsymbol{v}^{\mathrm{s}}\cdot\boldsymbol{\nabla}\right)\boldsymbol{v}^{\mathrm{f}} + \boldsymbol{\nabla}p^{\mathrm{f}} - \rho^{\mathrm{f}}_0\hat{\boldsymbol{b}}\\ &+\mu^{\mathrm{f}}\phi\,\boldsymbol{k}^{-1}(\boldsymbol{d}^{\mathrm{s}})\cdot\left(\boldsymbol{v}^{\mathrm{f}}-\boldsymbol{v}^{\mathrm{s}}\right)\\ &-\frac{1}{\phi}\boldsymbol{\nabla}\cdot\left(\phi\boldsymbol{\sigma}^{\mathrm{f}}_{\mathrm{visc}}(\boldsymbol{d}^{\mathrm{s}},\boldsymbol{v}^{\mathrm{f}})\right),\end{aligned} \tag{4.52}$$

$$\boldsymbol{f}^{\mathrm{s}}_{\mathrm{M}\phi,n+\theta}(\boldsymbol{d}^{\mathrm{s}}_{n+1},\boldsymbol{v}^{\mathrm{f}}_{n+1},p^{\mathrm{f}}_{n+1}) = (1-\theta)\boldsymbol{a}^{\mathrm{s}}_n + \theta\boldsymbol{f}^{\mathrm{s}}_{\mathrm{M}\phi}(\boldsymbol{d}^{\mathrm{s}}_{n+1},\boldsymbol{v}^{\mathrm{f}}_{n+1},p^{\mathrm{f}}_{n+1}), \tag{4.53}$$

$$\begin{aligned}\boldsymbol{f}^{\mathrm{s}}_{\mathrm{M}\phi}(\boldsymbol{d}^{\mathrm{s}},\boldsymbol{v}^{\mathrm{f}},p^{\mathrm{f}},\phi) = &-\boldsymbol{\nabla}_0\cdot\left(\boldsymbol{F}(\boldsymbol{d}^{\mathrm{s}})\cdot\boldsymbol{S}(\boldsymbol{d}^{\mathrm{s}},\boldsymbol{v}^{\mathrm{f}},p^{\mathrm{f}})\right) - \rho^{\mathrm{s}}_0(1-\phi_0)\hat{\boldsymbol{b}}\\ &-J(\boldsymbol{d}^{\mathrm{s}})\phi\,\boldsymbol{F}^{-\mathrm{T}}(\boldsymbol{d}^{\mathrm{s}})\cdot\boldsymbol{\nabla}_0 p^{\mathrm{f}}\\ &-\mu^{\mathrm{f}}J(\boldsymbol{d}^{\mathrm{s}})\phi^2\,\boldsymbol{k}^{-1}(\boldsymbol{d}^{\mathrm{s}})\cdot\left(\boldsymbol{v}^{\mathrm{f}}-\boldsymbol{v}^{\mathrm{s}}\right).\end{aligned} \tag{4.54}$$

The discrete time derivative of the porosity is given as

$$\mathring{\phi}_{n+\theta} = \frac{\phi_{n+1}-\phi_n}{\Delta t}, \tag{4.55}$$

$$\mathring{\phi}_n = f^{\mathrm{f}}_{\mathrm{C}\phi}(\boldsymbol{d}^{\mathrm{s}}_n,\boldsymbol{v}^{\mathrm{f}}_n,p^{\mathrm{f}}_n,t_n). \tag{4.56}$$

The semi-discrete form (4.48) consists of one additional equation compared to the semi-discret form (4.34), namely the constitutive equation relating the pore pressure, the displacements and the porosity. This form will later be used for the mixed approach presented in Section 4.3.2.2.2.

4.3. Finite Element Formulation and Solution Approach

In this section, the finite element formulations for porous media utilized in this thesis is presented. A thorough review of fundamental finite element theory is omitted. Instead, only the basic concepts are explained and the notation is introduced. For more details it is referred to common finite element textbooks. For a comprehensive introduction of the FEM in general and in terms of elastodynamics see [27, 129, 269, 270]. Details about the FEM for flow and transport processes can be found in [82, 271]. The FEM for porous media is reviewed in [158, 242]. The most outstanding characteristic of the approaches proposed in this thesis is, that a specific emphasis is laid on the ability of the porous medium model to represent changing porosities and porosity gradients. This leads to special requirements when considering Darcy-Brinkman flow. Those requirements will be analyzed in detail in Section 4.3.1, before stating the weak formulations in Section 4.3.2. Following this, three suitable finite element approaches will be presented in Section 4.3.3: The first is denoted ‘standard’ approach using the displacements, fluid velocities, and pressure as primary fields $(\boldsymbol{d}^{\mathrm{s}},\boldsymbol{v}^{\mathrm{f}},p^{\mathrm{f}})$ representing a natural and very common choice

for the unknown variables. The other two approaches are meant for the correct representation of porosity gradients in case of Darcy-Brinkman flow. A mixed approach and a NURBS based approach are proposed. As all approaches used in this thesis are based on equal-order interpolations and thus do not fulfill the inf-sup stability condition, the finite element formulations need to be stabilized. A residual-based variational multi-scale stabilization will be described. Subsequently, details about the application of impermeability constraints using the dual Lagrange multiplier method are also given. Lastly, the monolithic solution approach is presented in Section 4.3.4. This section includes the manipulation to be made of the linearized system in order to apply complex constraints and to compute on non-matching solid and fluid meshes.

4.3.1. Pre-Analysis: Continuity and Completeness

Before considering the weak form and finite element formulations, some terms appearing in the strong form of the governing equations are re-examined. The analysis stated here was presented by the author in [244].

The highest derivative appearing in the weak form determines the *continuity* and *completeness* (or *compatibility*) requirements of the shape functions. These characteristics are crucial for the convergence of the finite element approach. In classical elastodynamics, the stress divergence is integrated by parts, which leads to the highest derivative of the shape and the weighting function being a first derivative. Completeness then demands non-zero first derivatives and continuity requires C^0-continuous shape functions. Thus, a linear Lagrange element is the simplest element fulfilling the convergence requirements. These requirements can be different for a porous system. The important terms regarding continuity and completeness are porosity gradients, that is, $\boldsymbol{\nabla}\phi$ and $\boldsymbol{\nabla}_0\phi$. If the porosity is to vary in space, those gradients need special consideration. As, in general, the porosity itself depends on the determinant of the deformation gradient, see equation (3.80), the porosity gradient is related to a second derivative in space of the displacement field. Hence, if the porosity appears in the final weak form, the continuity requirements on the displacements are stricter than in an elastodynamic problem. The balance of linear momentum of the mixture (3.115) implicitly depends on the porosity gradient as it included in the stress tensor. A porosity gradient appears in the continuity equation of the fluid phase (3.111), and, when considering Darcy-Brinkman flow (3.114) as fluid equation, it needs to be evaluated to determine the fluid viscous stress term. Only the Darcy equation (3.113) is not directly influenced by spatial variations of the porosity. All appearances of the porosity gradient are listed in the following and evaluated whether this spatial derivative can be circumvented by partial integration.

- Within the mixture equation (3.115), the porosity gradient appears in the stress term, that is, in

$$\boldsymbol{\nabla}_0 \cdot (\boldsymbol{F} \cdot \boldsymbol{S}) = \boldsymbol{\nabla}_0 \cdot \left(\boldsymbol{F} \cdot \left(\phi \boldsymbol{S}^{\mathrm{f}}_{\mathrm{visc}} - p^{\mathrm{f}} J \boldsymbol{C}^{-1} + \frac{\partial \Psi^{\mathrm{s}}(\boldsymbol{E}, J\phi)}{\partial \boldsymbol{E}} \right) \right). \tag{4.57}$$

  As this term is usually partially integrated, it does not lead to a porosity gradient in the weak form.

- Similar argumentation holds for the porosity gradient in the continuity equation (3.111). Therein, the term $\boldsymbol{\nabla} \cdot \left(\phi \left(\boldsymbol{v}^{\mathrm{f}} - \boldsymbol{v}^{\mathrm{s}} \right) \right)$ can be integrated by parts, shifting the derivative

onto the test function. However, note that this partial integration is not usually done for incompressible Navier-Stokes equations and leads to an additional boundary integral, representing the mass flux over the boundary, which needs to be evaluated.

- The actual peculiarity lies within the Darcy-Brinkman equation (3.114). As already stated above, the Darcy equations are non-problematic in that regard. The viscous stress term can be reformulated using the product rule in order to obtain a 'classical' viscous term, also appearing in the Navier-Stokes equations, and an additional viscous stress term:

$$\frac{1}{\phi}\boldsymbol{\nabla}\cdot\left(\phi\boldsymbol{\sigma}^{\mathrm{f}}_{\mathrm{visc}}\right) = \boldsymbol{\nabla}\cdot\left(\boldsymbol{\sigma}^{\mathrm{f}}_{\mathrm{visc}}\right) + \frac{1}{\phi}\boldsymbol{\nabla}\phi\cdot\boldsymbol{\sigma}^{\mathrm{f}}_{\mathrm{visc}}. \tag{4.58}$$

  It becomes obvious that the porosity gradient cannot be eliminated by partial integration in the weak form (it could only be done by multiplying the whole equation by the porosity beforehand, which would lead to similar problems when partially integrating the pressure gradient, which will not be considered here).

In conclusion, assuming Darcy-Brinkman flow and including a varying porosity in space requires special care regarding the continuity requirements. To be more specific, assuming to have displacements, fluid velocities, and pressures as primary fields $(\boldsymbol{d}^{\mathrm{s}}, \boldsymbol{v}^{\mathrm{f}}, p^{\mathrm{f}})$, the shape functions of the displacement field need to have non-zero second derivatives in order to be complete and need to be globally C^1-continuous in order to fulfill the continuity requirements. Note that standard Lagrange elements are globally C^0-continuous, regardless of the order, and therefore convergence cannot be guaranteed for this formulation.

4.3.2. Weak Formulations

In this section, the weak formulations of the porous system will be presented. Therein, it will be differentiated whether Darcy or Darcy-Brinkman flow is considered. As elaborated in Section 4.3.1, different continuity requirements need to be considered for both types of flow. The approach for the Darcy equation is described in Section 4.3.2.1 followed by two alternative approaches for porous media with Darcy-Brinkman flow in Section 4.3.2.2. All the techniques presented in this section were given by the author in [244].

4.3.2.1. 'Standard' Approach for the Darcy Equation

The 'standard' approach describes one the most natural choices of primary fields. For the structural side, the displacement field and for fluid side, the velocity field and the pressure field are chosen as primary variables. Figure 4.1 shows a graphical representation of the governing equations and physical fields in a Tonti-diagram. A common mixed approach is chosen for the fluid phase. In order to formulate the weak form of the problem, the following function spaces $\mathcal{S}$ for the primary variables and the respective weighting function spaces $\mathcal{V}$ are defined

$$\mathcal{S}_{\mathrm{d}} = \left\{ \boldsymbol{d}^{\mathrm{s}} \in \left(\mathcal{H}^2(\Omega_0)\right)^{\mathrm{n_{sd}}} \middle| \, \boldsymbol{d}^{\mathrm{s}} = \hat{\boldsymbol{d}}^{\mathrm{s}} \text{ on } \Gamma_0^{\mathrm{D,s}} \right\}, \tag{4.59}$$

$$\mathcal{V}_{\mathrm{d}} = \left\{ \delta\boldsymbol{d}^{\mathrm{s}} \in \left(\mathcal{H}^1(\Omega_0)\right)^{\mathrm{n_{sd}}} \middle| \, \delta\boldsymbol{d}^{\mathrm{s}} = \boldsymbol{0} \text{ on } \Gamma_0^{\mathrm{D,s}} \right\}, \tag{4.60}$$

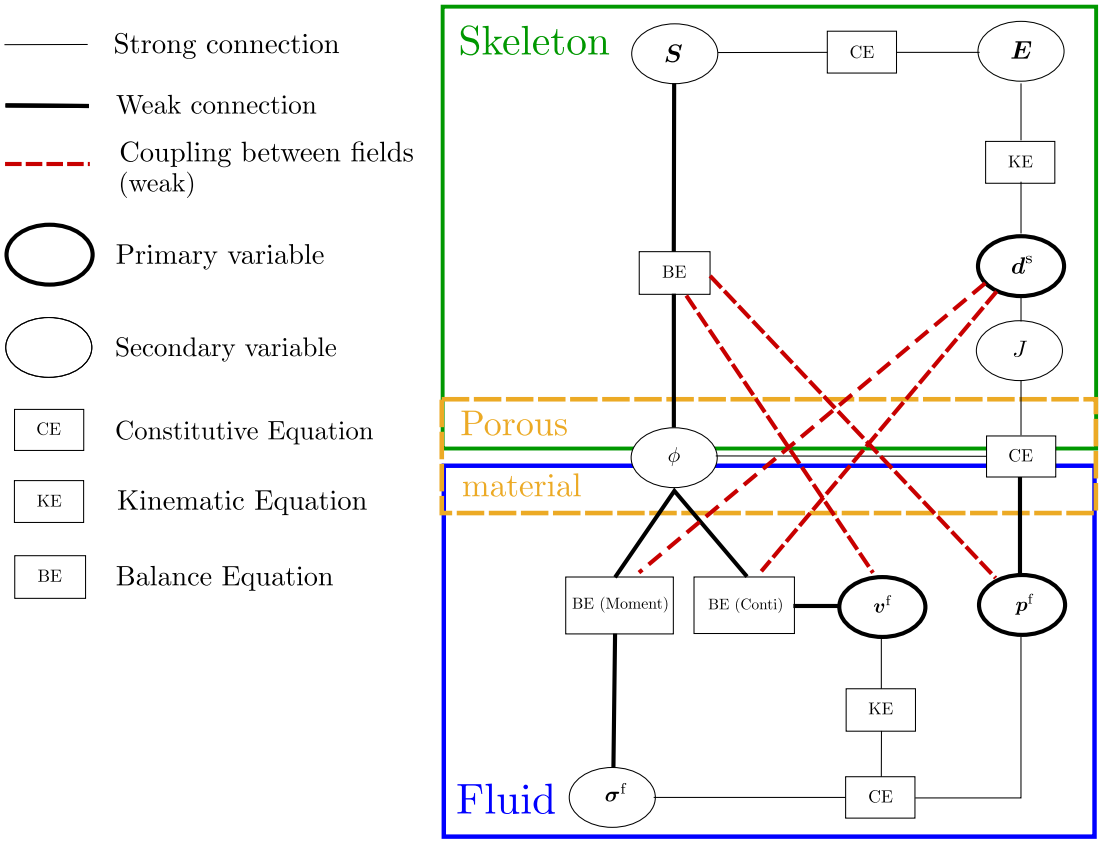

Figure 4.1: Tonti-diagram for 'standard' approach. Boundary conditions are omitted for sake of clarity.

$$\mathcal{S}_{\mathrm{v}} = \left\{ \boldsymbol{v}^{\mathrm{f}} \in \left(\mathcal{H}^1(\Omega_t)\right)^{\mathrm{n_{sd}}} \middle| \, \boldsymbol{v}^{\mathrm{f}} \cdot \boldsymbol{n} = \hat{v}_n^{\mathrm{f}} \text{ on } \Gamma_t^{\mathrm{D,f}} \right\}, \tag{4.61}$$

$$\mathcal{V}_{\mathrm{v}} = \left\{ \delta\boldsymbol{v}^{\mathrm{f}} \in \left(\mathcal{H}^1(\Omega_t)\right)^{\mathrm{n_{sd}}} \middle| \, \delta\boldsymbol{v}^{\mathrm{f}} \cdot \boldsymbol{n} = 0 \text{ on } \Gamma_t^{\mathrm{D,f}} \right\}, \tag{4.62}$$

$$\mathcal{S}_{\mathrm{p}} = \left\{ p^{\mathrm{F}} \in \mathcal{H}^1(\Omega_t) \right\}, \tag{4.63}$$

$$\mathcal{V}_{\mathrm{p}} = \left\{ \delta p^{\mathrm{f}} \in \mathcal{H}^1(\Omega_t) \right\}, \tag{4.64}$$

with $\mathrm{n_{sd}}$, $\mathcal{H}^2$ and $\mathcal{H}^1$ denoting the number of space dimensions, the Sobolev space of square integrable functions with square integrable first and second derivatives and the Sobolev space of square integrable functions with square integrable first derivatives, respectively. The expression

$$(\bullet, \bullet)_\Omega = \int (\bullet) \cdot (\bullet) \, \mathrm{d}\Omega \tag{4.65}$$

denotes the inner $\mathcal{L}_2$ product. The semi-discrete form (4.34) is multiplied with the respective weighting functions and integrated over the domain. By partially integrating the porosity gradient in the balance of linear momentum of the mixture as well as in the continuity equation of the fluid, one obtains to the following weak formulation:

Find $\left(\boldsymbol{d}^{\mathrm{s}}_{n+1}, \boldsymbol{v}^{\mathrm{f}}_{n+1}, p^{\mathrm{f}}_{n+1}\right) \in \mathcal{S}_{\mathrm{d}} \times \mathcal{S}_{\mathrm{v}} \times \mathcal{S}_{\mathrm{p}}$, such that $\forall \left(\delta\boldsymbol{d}^{\mathrm{s}}, \delta\boldsymbol{v}^{\mathrm{f}}, \delta p^{\mathrm{f}}\right) \in \mathcal{V}_{\mathrm{d}} \times \mathcal{V}_{\mathrm{v}} \times \mathcal{V}_{\mathrm{p}}$:

$$\begin{cases} \left(\delta p^{\mathrm{f}}, \left(\dfrac{\partial\phi}{\partial p^{\mathrm{f}}}\right)_{n+1} \mathring{p}^{\mathrm{f}}_{n+\theta}\right)_{\Omega(t_{n+1})} + \mathcal{F}^{\mathrm{f}}_{\mathrm{C},n+\theta}(\delta p^{\mathrm{f}}, \boldsymbol{d}^{\mathrm{s}}_{n+1}, \boldsymbol{v}^{\mathrm{f}}_{n+1}, p^{\mathrm{f}}_{n+1}) = 0, \\ \left(\delta\boldsymbol{v}^{\mathrm{f}}, \rho^{\mathrm{f}}_0 \mathring{\boldsymbol{v}}^{\mathrm{f}}_{n+\theta}\right)_{\Omega(t_{n+1})} + \boldsymbol{\mathcal{F}}^{\mathrm{f}}_{\mathrm{M},n+\theta}(\delta\boldsymbol{v}^{\mathrm{f}}, \boldsymbol{d}^{\mathrm{s}}_{n+1}, \boldsymbol{v}^{\mathrm{f}}_{n+1}, p^{\mathrm{f}}_{n+1}) = 0, \\ \left(\delta\boldsymbol{d}^{\mathrm{s}}, m^{\mathrm{s}}_0 \boldsymbol{a}^{\mathrm{s}}_{n+\theta}\right)_{\Omega_0} + \boldsymbol{\mathcal{F}}^{\mathrm{s}}_{\mathrm{M},n+\theta}(\delta\boldsymbol{d}^{\mathrm{s}}, \boldsymbol{d}^{\mathrm{s}}_{n+1}, \boldsymbol{v}^{\mathrm{f}}_{n+1}, p^{\mathrm{f}}_{n+1}) = 0. \end{cases} \tag{4.66}$$

Similar to the notation in Section 4.2, the following abbreviations were used in the continuity equation:

$$\begin{aligned} \mathcal{F}^{\mathrm{f}}_{\mathrm{C},n+\theta}(\delta p^{\mathrm{f}}, \boldsymbol{d}^{\mathrm{s}}_{n+1}, \boldsymbol{v}^{\mathrm{f}}_{n+1}, p^{\mathrm{f}}_{n+1}) =& (1-\theta)\left(\delta p^{\mathrm{f}}, \left(\frac{\partial\phi}{\partial p^{\mathrm{f}}}\right)_{n+1} \mathring{p}^{\mathrm{f}}_{n}\right)_{\Omega(t_{n+1})} \\ &+ \theta\mathcal{F}^{\mathrm{f}}_{\mathrm{C}}(\delta p^{\mathrm{f}}, \boldsymbol{d}^{\mathrm{s}}_{n+1}, \boldsymbol{v}^{\mathrm{f}}_{n+1}, p^{\mathrm{f}}_{n+1}), \end{aligned} \tag{4.67}$$

$$\begin{aligned} \mathcal{F}^{\mathrm{f}}_{\mathrm{C}}(\delta p^{\mathrm{f}}, \boldsymbol{d}^{\mathrm{s}}, \boldsymbol{v}^{\mathrm{f}}, p^{\mathrm{f}}) =& \left(\delta p^{\mathrm{f}}, \frac{\partial\phi}{\partial J} J\,\boldsymbol{\nabla}\cdot\boldsymbol{v}^{\mathrm{s}}\right)_{\Omega(t_{n+1})} \\ &+ \left(\delta p^{\mathrm{f}}, \phi\,\boldsymbol{\nabla}\cdot\boldsymbol{v}^{\mathrm{s}}\right)_{\Omega(t_{n+1})} \\ &- \left(\boldsymbol{\nabla}\delta p^{\mathrm{f}}, \phi\left(\boldsymbol{v}^{\mathrm{f}} - \boldsymbol{v}^{\mathrm{s}}\right)\right)_{\Omega(t_{n+1})} \\ &+ \left(\delta p^{\mathrm{f}}, \phi\boldsymbol{n}\cdot\left(\boldsymbol{v}^{\mathrm{f}} - \boldsymbol{v}^{\mathrm{s}}\right)\right)_{\Gamma(t_{n+1})}. \end{aligned} \tag{4.68}$$

Note the slight modifications in equation (4.67) due to the pre-multiplication with $(\partial\phi/\partial p^{\mathrm{f}})_{n+1}$. The terms in the flow equation are defined as

$$\boldsymbol{\mathcal{F}}^{\mathrm{f}}_{\mathrm{M},n+\theta}(\delta\boldsymbol{v}^{\mathrm{f}}, \boldsymbol{d}^{\mathrm{s}}_{n+1}, \boldsymbol{v}^{\mathrm{f}}_{n+1}, p^{\mathrm{f}}_{n+1}) = (1-\theta)\left(\delta\boldsymbol{v}^{\mathrm{f}}, \mathring{\boldsymbol{v}}^{\mathrm{f}}_{n}\right)_{\Omega(t_{n+1})} + \theta\boldsymbol{\mathcal{F}}^{\mathrm{f}}_{\mathrm{M}}(\delta\boldsymbol{v}^{\mathrm{f}}, \boldsymbol{d}^{\mathrm{s}}_{n+1}, \boldsymbol{v}^{\mathrm{f}}_{n+1}, p^{\mathrm{f}}_{n+1}), \tag{4.69}$$

$$\begin{aligned} \boldsymbol{\mathcal{F}}^{\mathrm{f}}_{\mathrm{M}}(\delta\boldsymbol{v}^{\mathrm{f}}, \boldsymbol{d}^{\mathrm{s}}, \boldsymbol{v}^{\mathrm{f}}, p^{\mathrm{f}}) =& -\left(\boldsymbol{\nabla}\cdot\delta\boldsymbol{v}^{\mathrm{f}}, p^{\mathrm{f}}\right)_{\Omega(t_{n+1})} - \left(\delta\boldsymbol{v}^{\mathrm{f}}, \rho^{\mathrm{f}}_0\boldsymbol{v}^{\mathrm{s}}\cdot\boldsymbol{\nabla}\boldsymbol{v}^{\mathrm{f}}\right)_{\Omega(t_{n+1})} \\ &+ \left(\delta\boldsymbol{v}^{\mathrm{f}}, \mu^{\mathrm{f}}\phi\boldsymbol{k}^{-1}\cdot\left(\boldsymbol{v}^{\mathrm{f}} - \boldsymbol{v}^{\mathrm{s}}\right)\right)_{\Omega(t_{n+1})} \\ &- \left(\delta\boldsymbol{v}^{\mathrm{f}}, \rho^{\mathrm{f}}_0\boldsymbol{b}\right)_{\Omega(t_{n+1})} - \left(\delta\boldsymbol{v}^{\mathrm{f}}, \hat{\boldsymbol{t}}^{\mathrm{f}}_t\right)_{\Gamma^{\mathrm{N,f}}(t_{n+1})\cup\Gamma^{\mathrm{c,f}}(t_{n+1})}, \end{aligned} \tag{4.70}$$

and in the balance of linear momentum of the mixture as

$$\boldsymbol{\mathcal{F}}^{\mathrm{s}}_{\mathrm{M},n+\theta}(\delta\boldsymbol{d}^{\mathrm{s}}, \boldsymbol{d}^{\mathrm{s}}_{n+1}, \boldsymbol{v}^{\mathrm{f}}_{n+1}, p^{\mathrm{f}}_{n+1}) = (1-\theta)\left(\delta\boldsymbol{d}^{\mathrm{s}}, \boldsymbol{a}^{\mathrm{s}}_{n}\right)_{\Omega_0} + \theta\boldsymbol{\mathcal{F}}^{\mathrm{s}}_{\mathrm{M}}(\delta\boldsymbol{d}^{\mathrm{s}}, \boldsymbol{d}^{\mathrm{s}}_{n+1}, \boldsymbol{v}^{\mathrm{f}}_{n+1}, p^{\mathrm{f}}_{n+1}), \tag{4.71}$$

$$\begin{aligned} \boldsymbol{\mathcal{F}}^{\mathrm{s}}_{\mathrm{M}}(\delta\boldsymbol{d}^{\mathrm{s}}, \boldsymbol{d}^{\mathrm{s}}, \boldsymbol{v}^{\mathrm{f}}, p^{\mathrm{f}}) =& +\left(\delta\boldsymbol{E}, \boldsymbol{S}\right)_{\Omega_0} - \left(\delta\boldsymbol{d}^{\mathrm{s}}, \mu^{\mathrm{f}}J\phi^2\boldsymbol{k}^{-1}\cdot\left(\boldsymbol{v}^{\mathrm{f}} - \boldsymbol{v}^{\mathrm{s}}\right)\right)_{\Omega_0} \\ &- \left(\delta\boldsymbol{d}^{\mathrm{s}}, J\phi\boldsymbol{F}^{-\mathrm{T}}\cdot\boldsymbol{\nabla}_0 p^{\mathrm{f}}\right)_{\Omega_0} \\ &- \left(\delta\boldsymbol{d}^{\mathrm{s}}, m^{\mathrm{s}}_0\boldsymbol{b}\right)_{\Omega_0} \\ &- \left(\delta\boldsymbol{d}^{\mathrm{s}}, \hat{\boldsymbol{t}}_0\right)_{\Gamma^{\mathrm{N,s}}_0\cup\Gamma^{\mathrm{c,s}}_0}. \end{aligned} \tag{4.72}$$

Here, $\delta \boldsymbol{E}$ denotes the variation of the Green-Lagrange strains given by

$$\delta \boldsymbol{E} = \frac{\partial \boldsymbol{E}}{\partial \boldsymbol{d}^{\mathrm{s}}} \delta \boldsymbol{d}^{\mathrm{s}} = \frac{1}{2} \left(\left(\boldsymbol{F}^T \cdot \boldsymbol{\nabla}_0 \delta \boldsymbol{d}^{\mathrm{s}} \right)^T + \boldsymbol{F}^T \cdot \boldsymbol{\nabla}_0 \delta \boldsymbol{d}^{\mathrm{s}} \right). \tag{4.73}$$

Note the partitioning of the material and current boundary into Dirichlet, Neumann and constraint boundary, i.e. $\Gamma_0 = \Gamma_0^{\mathrm{D}} \cup \Gamma_0^{\mathrm{N}} \cup \Gamma_0^{\mathrm{c}}$ and $\Gamma_t = \Gamma_t^{\mathrm{D}} \cup \Gamma_t^{\mathrm{N}} \cup \Gamma_t^{\mathrm{c}}$, as stated in Section 3.7.

4.3.2.2. Approaches for the Darcy-Brinkman Equation

Two semi-discrete forms for the porous medium system with Darcy-Brinkman flow are presented. The first formulation is a $(\boldsymbol{d}^{\mathrm{s}}, \boldsymbol{v}^{\mathrm{f}}, p^{\mathrm{f}})$-approach as for the Darcy equation, but with stricter requirements on the finite element spaces. The second alternative form is a mixed formulation $(\boldsymbol{d}^{\mathrm{s}}, \boldsymbol{v}^{\mathrm{f}}, p^{\mathrm{f}}, \phi)$, which includes the porosity as primary unknown.

4.3.2.2.1. 'Standard' Approach for the Darcy-Brinkman Equation

Here, the same approach as for Darcy flow is used. The only, but crucial, difference is the higher continuity requirement. The function spaces $\mathcal{S}$ for the primary variables, namely the solid displacement $\boldsymbol{d}^{\mathrm{s}}$, the fluid velocity $\boldsymbol{v}^{\mathrm{f}}$, and the fluid pressure p^{f}, as well as the respective weighting function spaces $\mathcal{V}$ are defined as follows

$$\mathcal{S}_{\mathrm{d,DB}} = \left\{ \boldsymbol{d}^{\mathrm{s}} \in \left(\mathcal{H}^2(\Omega_0) \right)^{\mathrm{n_{sd}}} \middle| \, \boldsymbol{d}^{\mathrm{s}} = \hat{\boldsymbol{d}}^{\mathrm{s}} \text{ on } \Gamma_0^{\mathrm{D,s}} \right\}, \tag{4.74}$$

$$\mathcal{V}_{\mathrm{d,DB}} = \left\{ \delta \boldsymbol{d}^{\mathrm{s}} \in \left(\mathcal{H}^1(\Omega_0) \right)^{\mathrm{n_{sd}}} \middle| \, \delta \boldsymbol{d}^{\mathrm{s}} = \boldsymbol{0} \text{ on } \Gamma_0^{\mathrm{D,s}} \right\}, \tag{4.75}$$

$$\mathcal{S}_{\mathrm{v,DB}} = \left\{ \boldsymbol{v}^{\mathrm{f}} \in \left(\mathcal{H}^1(\Omega_t) \right)^{\mathrm{n_{sd}}} \middle| \, \boldsymbol{v}^{\mathrm{f}} = \hat{\boldsymbol{v}}^{\mathrm{f}} \text{ on } \Gamma_t^{\mathrm{D,f}} \right\}, \tag{4.76}$$

$$\mathcal{V}_{\mathrm{v,DB}} = \left\{ \delta \boldsymbol{v}^{\mathrm{f}} \in \left(\mathcal{H}^1(\Omega_t) \right)^{\mathrm{n_{sd}}} \middle| \, \delta \boldsymbol{v}^{\mathrm{f}} = \boldsymbol{0} \text{ on } \Gamma_t^{\mathrm{D,f}} \right\}, \tag{4.77}$$

$$\mathcal{S}_{\mathrm{p,DB}} = \left\{ p^{\mathrm{f}} \in \mathcal{H}^1(\Omega_t) \right\}, \tag{4.78}$$

$$\mathcal{V}_{\mathrm{p,DB}} = \left\{ \delta p^{\mathrm{f}} \in \mathcal{H}^1(\Omega_t) \right\}. \tag{4.79}$$

The additional index 'DB' marks this approach. By partially integrating the porosity gradient in the balance of linear momentum of the mixture as well as in the continuity equation of the fluid, one obtains to the following weak formulation:

Find $\left(\boldsymbol{d}^{\mathrm{s}}, \boldsymbol{v}^{\mathrm{f}}, p^{\mathrm{f}} \right) \in \mathcal{S}_{\mathrm{d,DB}} \times \mathcal{S}_{\mathrm{v,DB}} \times \mathcal{S}_{\mathrm{p,DB}}$, such that $\forall \left(\delta \boldsymbol{d}^{\mathrm{s}}, \delta \boldsymbol{v}^{\mathrm{f}}, \delta p^{\mathrm{f}} \right) \in \mathcal{V}_{\mathrm{d,DB}} \times \mathcal{V}_{\mathrm{v,DB}} \times \mathcal{V}_{\mathrm{p,DB}}$:

$$\begin{cases} \left(\delta p^{\mathrm{f}}, \left(\dfrac{\partial \phi}{\partial p^{\mathrm{f}}} \right)_{n+1}, \mathring{p}^{\mathrm{f}}_{n+\theta} \right)_{\Omega(t_{n+1})} + \mathcal{F}^{\mathrm{f}}_{\mathrm{C,DB},n+\theta}(\delta p^{\mathrm{f}}, \boldsymbol{d}^{\mathrm{s}}_{n+1}, \boldsymbol{v}^{\mathrm{f}}_{n+1}, p^{\mathrm{f}}_{n+1}) = 0. \\ \left(\delta \boldsymbol{v}^{\mathrm{f}}, \rho_0^{\mathrm{f}} \mathring{\boldsymbol{v}}^{\mathrm{f}}_{n+\theta} \right)_{\Omega(t_{n+1})} + \boldsymbol{\mathcal{F}}^{\mathrm{f}}_{\mathrm{M,DB},n+\theta}(\delta \boldsymbol{v}^{\mathrm{f}}, \boldsymbol{d}^{\mathrm{s}}_{n+1}, \boldsymbol{v}^{\mathrm{f}}_{n+1}, p^{\mathrm{f}}_{n+1}) = 0, \\ \left(\delta \boldsymbol{d}^{\mathrm{s}}, m_0^{\mathrm{s}} \boldsymbol{a}^{\mathrm{s}}_{n+\theta} \right)_{\Omega_0} + \boldsymbol{\mathcal{F}}^{\mathrm{s}}_{\mathrm{M,DB},n+\theta}(\delta \boldsymbol{d}^{\mathrm{s}}, \boldsymbol{d}^{\mathrm{s}}_{n+1}, \boldsymbol{v}^{\mathrm{f}}_{n+1}, p^{\mathrm{f}}_{n+1}) = 0. \end{cases} \tag{4.80}$$

The following abbreviations were used in the continuity equation:

$$\begin{aligned}\mathcal{F}^{\mathrm{f}}_{\mathrm{C,DB},n+\theta}(\delta p^{\mathrm{f}}, \boldsymbol{d}^{\mathrm{s}}_{n+1}, \boldsymbol{v}^{\mathrm{f}}_{n+1}, p^{\mathrm{f}}_{n+1}) =& (1-\theta)\left(\delta p^{\mathrm{f}}, \left(\frac{\partial \phi}{\partial p^{\mathrm{f}}}\right)_{n+1} \mathring{p}^{\mathrm{f}}_{n}\right)_{\Omega(t_{n+1})} \\ &+ \theta \mathcal{F}^{\mathrm{f}}_{\mathrm{C,DB}}(\delta p^{\mathrm{f}}, \boldsymbol{d}^{\mathrm{s}}_{n+1}, \boldsymbol{v}^{\mathrm{f}}_{n+1}, p^{\mathrm{f}}_{n+1}), \qquad (4.81)\\ \mathcal{F}^{\mathrm{f}}_{\mathrm{C,DB}}(\delta p^{\mathrm{f}}, \boldsymbol{d}^{\mathrm{s}}, \boldsymbol{v}^{\mathrm{f}}, p^{\mathrm{f}}) =& \left(\delta p^{\mathrm{f}}, \frac{\partial \phi}{\partial J} J\, \boldsymbol{\nabla}\cdot\boldsymbol{v}^{\mathrm{s}}\right)_{\Omega(t_{n+1})} \\ &+ \left(\delta p^{\mathrm{f}}, \phi\, \boldsymbol{\nabla}\cdot\boldsymbol{v}^{\mathrm{s}}\right)_{\Omega(t_{n+1})} \\ &- \left(\boldsymbol{\nabla}\delta p^{\mathrm{f}}, \phi\left(\boldsymbol{v}^{\mathrm{f}} - \boldsymbol{v}^{\mathrm{s}}\right)\right)_{\Omega(t_{n+1})} \\ &+ \left(\delta p^{\mathrm{f}}, \phi \boldsymbol{n}\cdot\left(\boldsymbol{v}^{\mathrm{f}} - \boldsymbol{v}^{\mathrm{s}}\right)\right)_{\Gamma(t_{n+1})}. \qquad (4.82)\end{aligned}$$

Again, note the same modifications in equation (4.81) as in the standard formulation (4.67) due to the pre-multiplication with $(\partial\phi/\partial p^{\mathrm{f}})_{n+1}$. The terms In the flow equation are defined as

$$\begin{aligned}\boldsymbol{\mathcal{F}}^{\mathrm{f}}_{\mathrm{M,DB},n+\theta}(\delta \boldsymbol{v}^{\mathrm{f}}, \boldsymbol{d}^{\mathrm{s}}_{n+1}, \boldsymbol{v}^{\mathrm{f}}_{n+1}, p^{\mathrm{f}}_{n+1}) =& (1-\theta)\left(\delta \boldsymbol{v}^{\mathrm{f}}, \mathring{\boldsymbol{v}}^{\mathrm{f}}_{n}\right)_{\Omega(t_{n+1})} \\ &+ \theta \boldsymbol{\mathcal{F}}^{\mathrm{f}}_{\mathrm{M,DB}}(\delta \boldsymbol{v}^{\mathrm{f}}, \boldsymbol{d}^{\mathrm{s}}_{n+1}, \boldsymbol{v}^{\mathrm{f}}_{n+1}, p^{\mathrm{f}}_{n+1}), \qquad (4.83)\\ \boldsymbol{\mathcal{F}}^{\mathrm{f}}_{\mathrm{M,DB}}(\delta \boldsymbol{v}^{\mathrm{f}}, \boldsymbol{d}^{\mathrm{s}}, \boldsymbol{v}^{\mathrm{f}}, p^{\mathrm{f}}) =& -\left(\boldsymbol{\nabla}\cdot\delta \boldsymbol{v}^{\mathrm{f}}, p^{\mathrm{f}}\right)_{\Omega(t_{n+1})} - \left(\delta \boldsymbol{v}^{\mathrm{f}}, \rho^{\mathrm{f}}_0 \boldsymbol{v}^{\mathrm{s}}\cdot\boldsymbol{\nabla}\boldsymbol{v}^{\mathrm{f}}\right)_{\Omega(t_{n+1})} \\ &+ \left(\delta \boldsymbol{v}^{\mathrm{f}}, \mu^{\mathrm{f}}\phi \boldsymbol{k}^{-1}\cdot\left(\boldsymbol{v}^{\mathrm{f}} - \boldsymbol{v}^{\mathrm{s}}\right)\right)_{\Omega(t_{n+1})} \\ &+ \left(\boldsymbol{\nabla}\delta \boldsymbol{v}^{\mathrm{f}}, \boldsymbol{\sigma}^{\mathrm{f}}_{\mathrm{visc}}\right)_{\Omega(t_{n+1})} \\ &- \left(\delta \boldsymbol{v}^{\mathrm{f}}, \frac{1}{\phi}\boldsymbol{\nabla}\phi\cdot\boldsymbol{\sigma}^{\mathrm{f}}_{\mathrm{visc}}\right)_{\Omega(t_{n+1})} \\ &- \left(\delta \boldsymbol{v}^{\mathrm{f}}, \rho^{\mathrm{f}}_0 \boldsymbol{b}\right)_{\Omega(t_{n+1})} - \left(\delta \boldsymbol{v}^{\mathrm{f}}, \hat{\boldsymbol{t}}^{\mathrm{f}}_t\right)_{\Gamma^{\mathrm{N,f}}(t_{n+1})\cup\Gamma^{\mathrm{c,f}}(t_{n+1})}, \qquad (4.84)\end{aligned}$$

and in the balance of linear momentum of the mixture as

$$\begin{aligned}\boldsymbol{\mathcal{F}}^{\mathrm{s}}_{\mathrm{M,DB},n+\theta}(\delta \boldsymbol{d}^{\mathrm{s}}, \boldsymbol{d}^{\mathrm{s}}_{n+1}, \boldsymbol{v}^{\mathrm{f}}_{n+1}, p^{\mathrm{f}}_{n+1}) =& (1-\theta)\left(\delta \boldsymbol{d}^{\mathrm{s}}, \boldsymbol{a}^{\mathrm{s}}_{n}\right)_{\Omega_0} \\ &+ \theta \boldsymbol{\mathcal{F}}^{\mathrm{s}}_{\mathrm{M,DB}}(\delta \boldsymbol{d}^{\mathrm{s}}, \boldsymbol{d}^{\mathrm{s}}_{n+1}, \boldsymbol{v}^{\mathrm{f}}_{n+1}, p^{\mathrm{f}}_{n+1}, t_{n+1}), \qquad (4.85)\\ \boldsymbol{\mathcal{F}}^{\mathrm{s}}_{\mathrm{M,DB}}(\delta \boldsymbol{d}^{\mathrm{s}}, \boldsymbol{d}^{\mathrm{s}}, \boldsymbol{v}^{\mathrm{f}}, p^{\mathrm{f}}) =& +\left(\delta \boldsymbol{E}, \boldsymbol{S}\right)_{\Omega_0} - \left(\delta \boldsymbol{d}^{\mathrm{s}}, \mu^{\mathrm{f}} J \phi^2 \boldsymbol{k}^{-1}\cdot\left(\boldsymbol{v}^{\mathrm{f}} - \boldsymbol{v}^{\mathrm{s}}\right)\right)_{\Omega_0} \\ &- \left(\delta \boldsymbol{d}^{\mathrm{s}}, J\phi \boldsymbol{F}^{-\mathrm{T}}\cdot\boldsymbol{\nabla}_0 p^{\mathrm{f}}\right)_{\Omega_0} \\ &- \left(\delta \boldsymbol{d}^{\mathrm{s}}, m^{\mathrm{s}}_0 \boldsymbol{b}\right)_{\Omega_0} \\ &- \left(\delta \boldsymbol{d}^{\mathrm{s}}, \hat{\boldsymbol{t}}_0\right)_{\Gamma^{\mathrm{N,s}}_0\cup\Gamma^{\mathrm{c,s}}_0}. \qquad (4.86)\end{aligned}$$

Note that equations (4.80)–(4.86) are almost the same as the standard approach (4.66)–(4.72). The only difference is the inclusion of the Brinkman term in equation (4.84). This form will later be discretized using second order NURBS-based finite elements in Section 4.3.3.4, as second order NURBS fulfill the C^1-continuity requirement. Of course, any other type of shape func-

tion with continuous first derivatives, like Hermite shape functions, for instance, could also be applied.

4.3.2.2.2. 'Mixed' Approach for the Darcy-Brinkman Equation

An alternative approach is choosing the porosity as additional primary variable. The constitutive equation for the porosity is no longer inserted into the other equations, but fulfilled in a weak sense. In Figure 4.2 the respective Tonti-diagram is depicted. There, the porosity is counted among the skeleton's degrees of freedom. This is how the implementation was realized. However, it could also be counted among the fluid field, as the porosity actually belongs to the mixture. In this case the function spaces $\mathcal{S}$ for the primary variables and the respective weighting

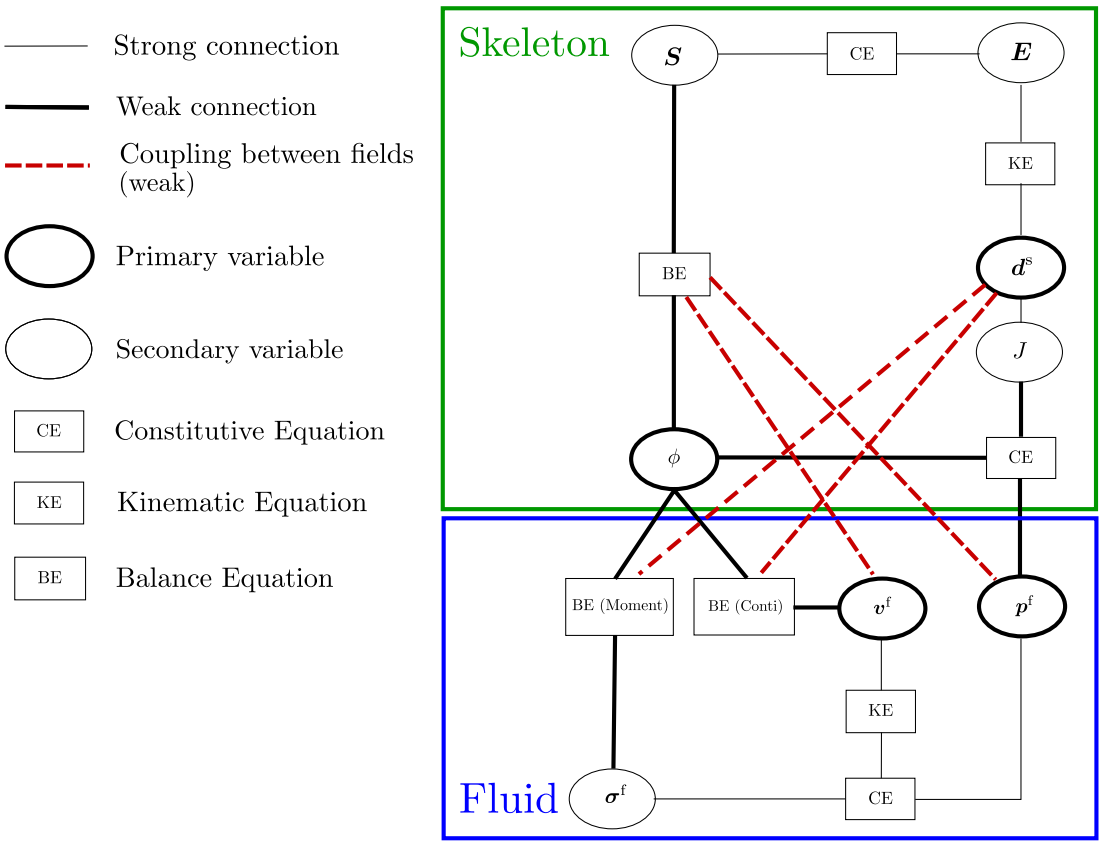

Figure 4.2: Tonti-diagram for 'mixed' approach. Boundary conditions are omitted for sake of clarity.

function spaces $\mathcal{V}$ are defined as follows

$$\mathcal{S}_{\mathrm{d}\phi} = \left\{ \boldsymbol{d}^{\mathrm{s}} \in \left(\mathcal{H}^1(\Omega_0)\right)^{\mathrm{n_{sd}}} \middle| \, \boldsymbol{d}^{\mathrm{s}} = \hat{\boldsymbol{d}}^{\mathrm{s}} \text{ on } \Gamma_0^{\mathrm{D,s}} \right\}, \tag{4.87}$$

$$\mathcal{V}_{\mathrm{d}\phi} = \left\{ \delta\boldsymbol{d}^{\mathrm{s}} \in \left(\mathcal{H}^1(\Omega_0)\right)^{\mathrm{n_{sd}}} \middle| \, \delta\boldsymbol{d}^{\mathrm{s}} = \boldsymbol{0} \text{ on } \Gamma_0^{\mathrm{D,s}} \right\}, \tag{4.88}$$

$$\mathcal{S}_{\mathrm{v}\phi} = \left\{ \boldsymbol{v}^{\mathrm{f}} \in \left(\mathcal{H}^1(\Omega_t)\right)^{\mathrm{n_{sd}}} \middle| \, \boldsymbol{v}^{\mathrm{f}} = \hat{\boldsymbol{v}}^{\mathrm{f}} \text{ on } \Gamma_t^{\mathrm{D,f}} \right\}, \tag{4.89}$$

$$\mathcal{V}_{\mathrm{v}\phi} = \left\{ \delta\boldsymbol{v}^{\mathrm{f}} \in \left(\mathcal{H}^1(\Omega_t)\right)^{\mathrm{n_{sd}}} \middle| \, \delta\boldsymbol{v}^{\mathrm{f}} = \boldsymbol{0} \text{ on } \Gamma_t^{\mathrm{D,f}} \right\}, \tag{4.90}$$

$$\mathcal{S}_{\mathrm{p}\phi} = \left\{ p^{\mathrm{f}} \in \mathcal{H}^1(\Omega_t) \right\}, \tag{4.91}$$

$$\mathcal{V}_{\mathrm{p}\phi} = \left\{ \delta p^{\mathrm{f}} \in \mathcal{H}^1(\Omega_t) \right\}, \tag{4.92}$$

$$\mathcal{S}_{\phi} = \left\{ \phi \in \left(\mathcal{H}^1(\Omega_0)\right) \right\}, \tag{4.93}$$

$$\mathcal{V}_{\phi} = \left\{ \delta\phi \in \left(\mathcal{H}^1(\Omega_0)\right) \right\}. \tag{4.94}$$

Note the additional subscript 'ϕ', which indicates the mixed approach. The weak form can then be formulated as follows:

Find $\left(\boldsymbol{d}^{\mathrm{s}}_{n+1}, \boldsymbol{v}^{\mathrm{f}}_{n+1}, p^{\mathrm{f}}_{n+1}, \phi_{n+1}\right) \in \mathcal{S}_{\mathrm{d}\phi} \times \mathcal{S}_{\mathrm{v}\phi} \times \mathcal{S}_{\mathrm{p}\phi} \times \mathcal{S}_{\phi}$, such that $\forall \left(\delta\boldsymbol{d}^{\mathrm{s}}, \delta\boldsymbol{v}^{\mathrm{f}}, \delta p^{\mathrm{f}}, \delta\phi\right) \in \mathcal{V}_{\mathrm{d}\phi} \times \mathcal{V}_{\mathrm{v}\phi} \times \mathcal{V}_{\mathrm{p}\phi} \times \mathcal{V}_{\phi}$:

$$\begin{cases} \left(\delta p^{\mathrm{f}}, \mathring{\phi}_{n+\theta}\right)_{\Omega(t_{n+1})} + \mathcal{F}^{\mathrm{f}}_{\mathrm{C}\phi,n+\theta}(\delta p^{\mathrm{f}}, \boldsymbol{d}^{\mathrm{s}}_{n+1}, \boldsymbol{v}^{\mathrm{f}}_{n+1}, p^{\mathrm{f}}_{n+1}, \phi_{n+1}) = 0. \\ \left(\delta\boldsymbol{v}^{\mathrm{f}}, \rho^{\mathrm{f}}_0 \mathring{\boldsymbol{v}}^{\mathrm{f}}_{n+\theta}\right)_{\Omega(t_{n+1})} + \boldsymbol{\mathcal{F}}^{\mathrm{f}}_{\mathrm{M}\phi,n+\theta}(\delta\boldsymbol{v}^{\mathrm{f}}, \boldsymbol{d}^{\mathrm{s}}_{n+1}, \boldsymbol{v}^{\mathrm{f}}_{n+1}, p^{\mathrm{f}}_{n+1}, \phi_{n+1}) = 0, \\ \left(\delta\boldsymbol{d}^{\mathrm{s}}, m^{\mathrm{s}}_0 \boldsymbol{a}^{\mathrm{s}}_{n+\theta}\right)_{\Omega_0} + \boldsymbol{\mathcal{F}}^{\mathrm{s}}_{\mathrm{M}\phi,n+\theta}(\delta\boldsymbol{d}^{\mathrm{s}}, \boldsymbol{d}^{\mathrm{s}}_{n+1}, \boldsymbol{v}^{\mathrm{f}}_{n+1}, p^{\mathrm{f}}_{n+1}, \phi_{n+1}) = 0, \\ (1-\theta)\left(\delta\phi, p^{\mathrm{f}}_n - \left(\frac{\partial\Psi^{\mathrm{s}}}{\partial(J\phi)}\right)_n\right)_{\Omega_0} + \theta\left(\delta\phi, p^{\mathrm{f}}_{n+1} - \left(\frac{\partial\Psi^{\mathrm{s}}}{\partial(J\phi)}\right)_{n+1}\right)_{\Omega_0} = 0. \end{cases} \tag{4.95}$$

The terms in the weak form in the continuity equation are defined as

$$\begin{aligned} \mathcal{F}^{\mathrm{f}}_{\mathrm{C}\phi,n+\theta}(\delta p^{\mathrm{f}}, \boldsymbol{d}^{\mathrm{s}}_{n+1}, \boldsymbol{v}^{\mathrm{f}}_{n+1}, p^{\mathrm{f}}_{n+1}, \phi_{n+1}) =& (1-\theta)\left(\delta p^{\mathrm{f}}, \mathring{\phi}_n\right)_{\Omega(t_{n+1})} \\ &+ \theta\mathcal{F}^{\mathrm{f}}_{\mathrm{C}\phi}(\delta p^{\mathrm{f}}, \boldsymbol{d}^{\mathrm{s}}_{n+1}, \boldsymbol{v}^{\mathrm{f}}_{n+1}, p^{\mathrm{f}}_{n+1}, \phi_{n+1}), \end{aligned} \tag{4.96}$$

$$\begin{aligned} \mathcal{F}^{\mathrm{f}}_{\mathrm{C}\phi}(\delta p^{\mathrm{f}}, dS, \boldsymbol{v}^{\mathrm{f}}, p^{\mathrm{f}}, \phi) =& \left(\delta p^{\mathrm{f}}, \phi\, \boldsymbol{\nabla}\cdot\boldsymbol{v}^{\mathrm{s}}\right)_{\Omega(t_{n+1})} - \left(\boldsymbol{\nabla}\delta p^{\mathrm{f}}, \phi\left(\boldsymbol{v}^{\mathrm{f}} - \boldsymbol{v}^{\mathrm{s}}\right)\right)_{\Omega(t_{n+1})} \\ &+ \left(\delta p^{\mathrm{f}}, \phi\boldsymbol{n}\cdot\left(\boldsymbol{v}^{\mathrm{f}} - \boldsymbol{v}^{\mathrm{s}}\right)\right)_{\Gamma(t_{n+1})}, \end{aligned} \tag{4.97}$$

and in the Darcy-Brinkman equation as

$$\begin{aligned}\boldsymbol{\mathcal{F}}^{\mathrm{f}}_{\mathrm{M}\phi,n+\theta}(\delta\boldsymbol{v}^{\mathrm{f}},\boldsymbol{d}^{\mathrm{s}}_{n+1},\boldsymbol{v}^{\mathrm{f}}_{n+1},p^{\mathrm{f}}_{n+1},\phi_{n+1}) =&(1-\theta)\left(\delta\boldsymbol{v}^{\mathrm{f}},\mathring{\boldsymbol{v}}^{\mathrm{f}}_{n}\right)_{\Omega(t_{n+1})}\\ &+\theta\boldsymbol{\mathcal{F}}^{\mathrm{f}}_{\mathrm{M}\phi}(\delta\boldsymbol{v}^{\mathrm{f}},\boldsymbol{d}^{\mathrm{s}}_{n+1},\boldsymbol{v}^{\mathrm{f}}_{n+1},p^{\mathrm{f}}_{n+1},\phi_{n+1},t_{n+1}),\end{aligned}\tag{4.98}$$

$$\begin{aligned}\boldsymbol{\mathcal{F}}^{\mathrm{f}}_{\mathrm{M}\phi}(\delta\boldsymbol{v}^{\mathrm{f}},\boldsymbol{d}^{\mathrm{s}},\boldsymbol{v}^{\mathrm{f}},p^{\mathrm{f}},\phi) =&-\left(\boldsymbol{\nabla}\cdot\delta\boldsymbol{v}^{\mathrm{f}},p^{\mathrm{f}}\right)_{\Omega(t_{n+1})}-\left(\delta\boldsymbol{v}^{\mathrm{f}},\rho^{\mathrm{f}}_{0}\boldsymbol{v}^{\mathrm{s}}\boldsymbol{\nabla}\boldsymbol{v}^{\mathrm{f}}\right)_{\Omega(t_{n+1})}\\ &+\left(\delta\boldsymbol{v}^{\mathrm{f}},\mu^{\mathrm{f}}\phi\boldsymbol{k}^{-1}\cdot\left(\boldsymbol{v}^{\mathrm{f}}-\boldsymbol{v}^{\mathrm{s}}\right)\right)_{\Omega(t_{n+1})}\\ &+\left(\boldsymbol{\nabla}\delta\boldsymbol{v}^{\mathrm{f}},\boldsymbol{\sigma}^{\mathrm{f}}_{\mathrm{visc}}\right)_{\Omega(t_{n+1})}\\ &-\left(\delta\boldsymbol{v}^{\mathrm{f}},\frac{1}{\phi}\boldsymbol{\nabla}\phi\cdot\boldsymbol{\sigma}^{\mathrm{f}}_{\mathrm{visc}}\right)_{\Omega(t_{n+1})}\\ &-\left(\delta\boldsymbol{v}^{\mathrm{f}},\rho^{\mathrm{f}}_{0}\boldsymbol{b}\right)_{\Omega(t_{n+1})}-\left(\delta\boldsymbol{v}^{\mathrm{f}},\hat{\boldsymbol{t}}^{\mathrm{f}}_{t}\right)_{\Gamma^{\mathrm{N,f}}(t_{n+1})\cup\Gamma^{\mathrm{c,f}}(t_{n+1})},\end{aligned}\tag{4.99}$$

and finally in the balance of linear momentum of the mixture as

$$\begin{aligned}\boldsymbol{\mathcal{F}}^{\mathrm{s}}_{\mathrm{M}\phi,n+\theta}(\delta\boldsymbol{d}^{\mathrm{s}},\boldsymbol{d}^{\mathrm{s}}_{n+1},\boldsymbol{v}^{\mathrm{f}}_{n+1},p^{\mathrm{f}}_{n+1},\phi_{n+1}) =&(1-\theta)\left(\delta\boldsymbol{d}^{\mathrm{s}},\boldsymbol{a}^{\mathrm{s}}_{n}\right)_{\Omega(t_{n+1})}\\ &+\theta\boldsymbol{\mathcal{F}}^{\mathrm{s}}_{\mathrm{M}\phi}(\delta\boldsymbol{d}^{\mathrm{s}},\boldsymbol{d}^{\mathrm{s}}_{n+1},\boldsymbol{v}^{\mathrm{f}}_{n+1},p^{\mathrm{f}}_{n+1},\phi_{n+1},t_{n+1}),\end{aligned}\tag{4.100}$$

$$\begin{aligned}\boldsymbol{\mathcal{F}}^{\mathrm{s}}_{\mathrm{M}\phi}(\delta\boldsymbol{d}^{\mathrm{s}},\boldsymbol{d}^{\mathrm{s}},\boldsymbol{v}^{\mathrm{f}},p^{\mathrm{f}},\phi) =&\left(\delta\boldsymbol{E},\boldsymbol{S}\right)_{\Omega_0}-\left(\delta\boldsymbol{d}^{\mathrm{s}},\mu^{\mathrm{f}}J\phi^{2}\boldsymbol{k}^{-1}\cdot\left(\boldsymbol{v}^{\mathrm{f}}-\boldsymbol{v}^{\mathrm{s}}\right)\right)_{\Omega_0}\\ &-\left(\delta\boldsymbol{d}^{\mathrm{s}},J\phi\boldsymbol{F}^{-\mathrm{T}}\cdot\boldsymbol{\nabla}_{0}p^{\mathrm{f}}\right)_{\Omega_0}\\ &-\left(\delta\boldsymbol{d}^{\mathrm{s}},m^{\mathrm{s}}_{0}\boldsymbol{b}\right)_{\Omega_0}-\left(\delta\boldsymbol{d}^{\mathrm{s}},\hat{\boldsymbol{t}}_{0}\right)_{\Gamma^{\mathrm{N,s}}_{0}\cup\Gamma^{\mathrm{c,s}}_{0}}.\end{aligned}\tag{4.101}$$

As consequence of the porosity being an additional primary field, the weak form (4.95) consists of one additional equation, that is, the weighted constitutive relation (3.80). The other equations remain unaltered compared to the first formulation (4.80), but the continuity requirement on the displacement field is reduced here (compare equation (4.59) and (4.87)). In this approach, the displacement field as well as the porosity field need to be C^0-continuous. Due to these reduced continuity requirements, this form can be discretized by first-order Lagrange elements in Section 4.3.3.3.

4.3.2.3. Impermeability Boundary Conditions

The modifications of the system (4.66), (4.80) or (4.95), originating from the impermeability conditions on the boundary Γ^{c}_{t}, for Darcy and Darcy-Brinkman flow will be shown here. Note, that the terms given here are written in time-continuous form for clarity of notation, but the same holds for the semi-discrete form.

For Darcy flow the no-penetration (no-flow) condition and for Darcy-Brinkman flow the no-slip constraint, see equation (3.122), is enforced weakly by a Lagrange multiplier field $\boldsymbol{\lambda}$. First, the impermeability condition for Darcy flow is considered. It reads

$$\left(\delta\lambda_{\perp},\phi\boldsymbol{n}\cdot\left(\boldsymbol{v}^{\mathrm{f}}-\boldsymbol{v}^{\mathrm{s}}\right)\right)_{\Gamma^{\mathrm{c}}_{t}}=0.\tag{4.102}$$

As the no-penetration condition acts in normal direction of the boundary, the Lagrange multiplier needs to point this direction. To ensure the correct orientation of the Lagrange multiplier, all tangential components are forced to vanish by the additional tangential constraint

$$\left(\delta\boldsymbol{\lambda}_{\parallel}, \boldsymbol{T}\cdot\boldsymbol{\lambda}\right)_{\Gamma_t^{\mathrm{c}}} = 0. \tag{4.103}$$

The conditions in normal and tangential direction are multiplied by the corresponding test functions $\delta\lambda_{\perp}$ and $\delta\boldsymbol{\lambda}_{\parallel}$. The tangential vectors on the boundary Γ_t^c are gathered in $\boldsymbol{T}$ to perform the projection of the Lagrange multiplier onto the boundary.

For Darcy-Brinkman flow, the weak no-slip constraint is required. Thus, the fluid velocity needs to be equal to the solid velocity. Hence, the weak form reads

$$\left(\delta\boldsymbol{\lambda}, \boldsymbol{v}^{\mathrm{f}} - \boldsymbol{v}^{\mathrm{s}}\right)_{\Gamma_t^{\mathrm{c}}} = 0. \tag{4.104}$$

After formulating the constraints, in the following it will be shown how they couple into the governing equations. The Lagrange multiplier field can be identified as the fluid traction $\boldsymbol{t}_t^{\mathrm{f}}$ acting on the constraint boundary

$$\boldsymbol{\lambda} = \boldsymbol{t}_t^{\mathrm{f}}, \tag{4.105}$$

which can be inserted into the weak form

$$\left(\delta\boldsymbol{v}^{\mathrm{f}}, \boldsymbol{t}^{\mathrm{f}}\right)_{\Gamma_t^{\mathrm{c}}} = \left(\delta\boldsymbol{v}^{\mathrm{f}}, \boldsymbol{\lambda}\right)_{\Gamma_t^{\mathrm{c}}}. \tag{4.106}$$

The Lagrange multiplier acts explicitly only on the fluid phase. There is no effective contribution of the impermeability condition to the boundary integral of the mixture equation, as it does not apply any external tractions onto the surface. A detailed explanation can be found in [244].

Remark 4.2 *In monolithic FSI systems, the Lagrange multiplier acts on both field equations, see e.g. [168]. In the formulation of the porous medium used here, it acts on the fluid only. This is because the 'solid' equation is actually the balance of linear momentum of the mixture, where balance of solid and fluid tractions at the boundaries is already included. If, however, the governing equations were written differently, that is, the solid part of the balance of momentum would be extracted from the mixture equation by subtracting the fluid equation (see [243] or [54]), the Lagrange multiplier of the impermeability constraint would also appear in both the solid and the fluid equations.*

4.3.3. Discrete System

In this section, the discrete system will be derived. Finite elements are used for the spatial discretization. Following standard procedure, the domain Ω is approximated by a discrete domain Ω^{h}, which is composed of $\mathrm{n_{ele}}$ non-overlapping subdomains Ω_e, $e = 1 \dots \mathrm{n_{ele}}$, denoted as elements. Thus, it holds

$$\Omega \approx \Omega^{\mathrm{h}} = \bigcup_{e=1}^{\mathrm{n_{ele}}} \Omega_e, \text{with} \quad \Omega_e \cap \Omega_f = \emptyset, \text{for } e \neq f. \tag{4.107}$$

The approximation of the solution for each primary field will be formulated in terms of $\mathrm{n}_{\mathrm{node}}$ discrete values at discrete positions called nodes. The nodes form the elements. In the following the three FE formulations based on the time-discrete weak forms from Section 4.3.2 are presented.

4.3.3.1. FE Formulation for Poroelasticity with Darcy Flow

For deforming porous media including Darcy flow, the skeleton displacements, the fluid velocities, and the fluid pressures are discretized. The solution fields for the primary unknowns can be approximated by local shape functions $\mathsf{N}_{\mathsf{d},k}$, $\mathsf{N}_{\mathsf{v},k}$ and $\mathsf{N}_{\mathsf{p},k}$:

$$\boldsymbol{d}^{\mathrm{s}} \approx \boldsymbol{d}^{\mathrm{s},\mathsf{h}} = \sum_{k=1}^{\mathrm{n}_{\mathrm{node}}} \mathsf{N}_{\mathsf{d},k} \mathbf{d}_k^{\mathrm{s}} = \mathbf{N}_{\mathsf{d}} \cdot \mathbf{d}^{\mathrm{s}}, \tag{4.108}$$

$$\boldsymbol{v}^{\mathrm{f}} \approx \boldsymbol{v}^{\mathrm{f},\mathsf{h}} = \sum_{k=1}^{\mathrm{n}_{\mathrm{node}}} \mathsf{N}_{\mathsf{v},k} \mathbf{v}_k^{\mathrm{f}} = \mathbf{N}_{\mathsf{v}} \cdot \mathbf{v}^{\mathrm{f}}, \tag{4.109}$$

$$p^{\mathrm{f}} \approx p^{\mathrm{f},\mathsf{h}} = \sum_{k=1}^{\mathrm{n}_{\mathrm{node}}} \mathsf{N}_{\mathsf{p},k} \mathbf{p}_k^{\mathrm{f}} = \mathbf{N}_{\mathsf{p}} \cdot \mathbf{p}^{\mathrm{f}}. \tag{4.110}$$

The superscript h marks spatially discretized quantities. For instance, $\boldsymbol{d}^{\mathrm{s},\mathsf{h}}$ denotes the global approximation of the displacement field, $\mathbf{d}_k^{\mathrm{s}}$ the nodal displacement of node k and $\mathbf{d}^{\mathrm{s}}$ the global nodal displacements. The interpolation functions are gathered in the matrix $\mathbf{N}$ for matrix-vector products. The weighting functions are approximated in the same way as the respective primary field. That is,

$$\delta\boldsymbol{d}^{\mathrm{s}} \approx \delta\boldsymbol{d}^{\mathrm{s},\mathsf{h}} = \sum_{k=1}^{\mathrm{n}_{\mathrm{node}}} \mathsf{N}_{\mathsf{d},k} \delta\mathbf{d}_k^{\mathrm{s}} = \mathbf{N}_{\mathsf{d}} \cdot \delta\mathbf{d}^{\mathrm{s}}, \tag{4.111}$$

$$\delta\boldsymbol{v}^{\mathrm{f}} \approx \delta\boldsymbol{v}^{\mathrm{f},\mathsf{h}} = \sum_{k=1}^{\mathrm{n}_{\mathrm{node}}} \mathsf{N}_{\mathsf{v},k} \delta\mathbf{v}_k^{\mathrm{f}} = \mathbf{N}_{\mathsf{v}} \cdot \delta\mathbf{v}^{\mathrm{f}}, \tag{4.112}$$

$$\delta p^{\mathrm{f}} \approx \delta p^{\mathrm{f},\mathsf{h}} = \sum_{k=1}^{\mathrm{n}_{\mathrm{node}}} \mathsf{N}_{\mathsf{p},k} \delta\mathbf{p}_k^{\mathrm{f}} = \mathbf{N}_{\mathsf{p}} \cdot \delta\mathbf{p}^{\mathrm{f}}. \tag{4.113}$$

This is referred to as Bubnov-Galerkin approach, compared to the Petrov-Galerkin approach, where the weighting function interpolations are chosen differently from the primary variables. In most cases in this thesis, the same discretization is used for all primary fields, i.e. $\mathsf{N}_{\mathsf{d},k} = \mathsf{N}_{\mathsf{v},k} = \mathsf{N}_{\mathsf{p},k} = \mathsf{N}_k$ and $\mathbf{N}_{\mathsf{d}} = \mathbf{N}_{\mathsf{v}} = \mathbf{N}_{\mathsf{p}} = \mathbf{N}$. Only for non-matching solid and fluid meshes, the shape functions for displacements and porosity differ from the interpolations for fluid velocity and pressure, see Section 4.3.4.3.

Following the isoparametric concept, the material and current coordinates are approximated in the same way as the displacement field:

$$\boldsymbol{X} \approx \boldsymbol{X}^{\mathsf{h}} = \sum_{k=1}^{\mathrm{n_{node}}} \mathsf{N}_{\mathsf{d},k} \mathbf{X}_k = \mathbf{N}_{\mathsf{d}} \cdot \mathbf{X}, \tag{4.114}$$

$$\boldsymbol{x} \approx \boldsymbol{x}^{\mathsf{h}} = \sum_{k=1}^{\mathrm{n_{node}}} \mathsf{N}_{\mathsf{d},k} \mathbf{x}_k = \mathbf{N}_{\mathsf{d}} \cdot \mathbf{x}. \tag{4.115}$$

The global approximations of the primary unknowns are elements of the usual finite element approximation spaces $\mathcal{S}^{\mathsf{h}} \subset \mathcal{S}$ and $\mathcal{V}^{\mathsf{h}} \subset \mathcal{V}$. Standard isoparametric finite elements of first and second order will be used here. This way the primary unknowns can be approximated by the respective discrete nodal values. Then, the discrete form, based on the weak form (4.66), can be formulated as follows:

Find $\left(\boldsymbol{d}^{\mathrm{s,h}}_{n+1}, \boldsymbol{v}^{\mathrm{f,h}}_{n+1}, p^{\mathrm{f,h}}_{n+1}\right) \in \mathcal{S}^{\mathsf{h}}_{\mathrm{d}} \times \mathcal{S}^{\mathsf{h}}_{\mathrm{v}} \times \mathcal{S}^{\mathsf{h}}_{\mathrm{p}}$, such that $\forall \left(\delta\boldsymbol{d}^{\mathrm{s,h}}, \delta\boldsymbol{v}^{\mathrm{f,h}}, \delta p^{\mathrm{f,h}}\right) \in \mathcal{V}^{\mathsf{h}}_{\mathrm{d}} \times \mathcal{V}^{\mathsf{h}}_{\mathrm{v}} \times \mathcal{V}^{\mathsf{h}}_{\mathrm{p}}$:

$$\left\{ \begin{aligned} \left(\delta p^{\mathrm{f,h}}, \frac{\partial \phi}{\partial p^{\mathrm{f}}}\left(\boldsymbol{d}^{\mathrm{s,h}}_{n+1}, p^{\mathrm{f,h}}_{n+1}\right) \cdot \mathring{p}^{\mathrm{f,h}}_{n+\theta}\right)_{\Omega^{\mathsf{h}}(t_{n+1})} &+ \mathcal{F}^{\mathrm{f}}_{\mathrm{C},n+\theta}(\delta p^{\mathrm{f,h}}, \boldsymbol{d}^{\mathrm{s,h}}_{n+1}, \boldsymbol{v}^{\mathrm{f,h}}_{n+1}, p^{\mathrm{f,h}}_{n+1}) = 0, \\ \left(\delta\boldsymbol{v}^{\mathrm{f,h}}, \rho^{\mathrm{f}}_0 \mathring{\boldsymbol{v}}^{\mathrm{f,h}}_{n+\theta}\right)_{\Omega^{\mathsf{h}}(t_{n+1})} &+ \boldsymbol{\mathcal{F}}^{\mathrm{f}}_{\mathrm{M},n+\theta}(\delta\boldsymbol{v}^{\mathrm{f,h}}, \boldsymbol{d}^{\mathrm{s,h}}_{n+1}, \boldsymbol{v}^{\mathrm{f,h}}_{n+1}, p^{\mathrm{f,h}}_{n+1}) = 0, \\ \left(\delta\boldsymbol{d}^{\mathrm{s,h}}, m^{\mathrm{s}}_0 \boldsymbol{a}^{\mathrm{s,h}}_{n+\theta}\right)_{\Omega^{\mathsf{h}}_0} &+ \boldsymbol{\mathcal{F}}^{\mathrm{s}}_{\mathrm{M},n+\theta}(\delta\boldsymbol{d}^{\mathrm{s,h}}, \boldsymbol{d}^{\mathrm{s,h}}_{n+1}, \boldsymbol{v}^{\mathrm{f,h}}_{n+1}, p^{\mathrm{f,h}}_{n+1}) = 0, \end{aligned} \right. \tag{4.116}$$

with the abbreviations given in equations (4.67)–(4.72). Note, that of course not only the discrete approximations at the time step $n+1$, but also at the time step n, i.e. $(\boldsymbol{d}^{\mathrm{s,h}}_n, \boldsymbol{v}^{\mathrm{f,h}}_n, p^{\mathrm{f,h}}_n)$ are used in equations (4.67)–(4.72).

Remark 4.3 *An alternative, also commonly used set of primary variables includes the relative fluid mass flux* $\boldsymbol{w}^{\mathrm{f}} = \rho^{\mathrm{f}}\phi\left(\boldsymbol{v}^{\mathrm{f}} - \boldsymbol{v}^{\mathrm{s}}\right)$ *(see equation* (3.16)*) instead of the fluid velocity* $\boldsymbol{v}^{\mathrm{f}}$*. The governing equations are then rewritten in terms of* $\boldsymbol{w}^{\mathrm{f}}$*, like given in equation* (3.14) *for the balance of mass. For constant densities and porosities and slow motions of the solid, this approach clearly has no significant difference to the one presented here. However, in the general case the approximations differ. Even though it would be interesting to investigate and compare the numerical properties, this variant is not considered here.*

4.3.3.2. FE Formulations for Poroelasticity with Darcy-Brinkman flow

As already explained in Section 4.3.1 special care needs to be taken, if poroelasticity with variable porosity is coupled with Darcy-Brinkman flow. Two approaches dealing with these stricter requirements are presented in the following. The first method reduces the continuity requirements by introducing an additional primary field. The second approach uses higher order finite elements with sufficiently smooth shape functions.

4.3.3.3. Mixed Approach

This approach is based on a mixed formulation. Thereby, not only the solid displacements, the fluid velocity, and fluid pressure are chosen as primary fields (which is, of course, a mixed formulation itself), but an additional unknown field is introduced. That is, the porosity is incorporated as primary variable. The additional equation needed is the constitutive relation between porosity, pressure and displacements. It is tested and enforced in a weak sense, see equation (4.95). Thereby, the continuity requirements are reduced. This means, that occurring porosity gradients can be represented by first-order shape functions for Darcy-Brinkman flow. In general, mixed approaches have already been applied to porous media systems. Most commonly they are used in extended porous medium problems, such as thermo-poroelasticity, transport of chemical substances or multiphase flow within porous media (see, e.g. [149, 223]). Therein, the additional field, being the temperature or a concentration, is discretized. Here, it is the porosity. Hence, in addition to the approximations of displacements, velocities, and pressures in equations (4.108)–(4.110), the following approximations are introduced

$$\phi \approx \phi^{\mathsf{h}} = \sum_{k=1}^{\mathrm{n_{node}}} \mathsf{N}_{\phi,k} \boldsymbol{\phi}_k = \mathbf{N}_{\mathsf{p}} \cdot \boldsymbol{\phi}, \tag{4.117}$$

$$\delta\phi \approx \delta\phi^{\mathsf{h}} = \sum_{k=1}^{\mathrm{n_{node}}} \mathsf{N}_{\phi,k} \delta\boldsymbol{\phi}_k = \mathbf{N}_{\mathsf{p}} \cdot \delta\boldsymbol{\phi}. \tag{4.118}$$

The usual finite-dimensional finite element spaces $\mathcal{S}^{\mathsf{h}} \subset \mathcal{S}$ and $\mathcal{V}^{\mathsf{h}} \subset \mathcal{V}$ are utilized and first- and second-order isoparametric Lagrange elements will be used. Based on the weak form (4.95), the discrete form can then be formulated as follows:

Find $\left(\boldsymbol{d}^{\mathrm{s,h}}_{n+1}, \boldsymbol{v}^{\mathrm{f,h}}_{n+1}, p^{\mathrm{f,h}}_{n+1}, \phi^{\mathsf{h}}_{n+1}\right) \in \mathcal{S}^{\mathsf{h}}_{\mathrm{d}\phi} \times \mathcal{S}^{\mathsf{h}}_{\mathrm{v}\phi} \times \mathcal{S}^{\mathsf{h}}_{\mathrm{p}\phi} \times \mathcal{S}^{\mathsf{h}}_{\phi}$, such that $\forall \left(\delta\boldsymbol{d}^{\mathrm{s,h}}, \delta\boldsymbol{v}^{\mathrm{f,h}}, \delta p^{\mathrm{f,h}}, \delta\phi^{\mathsf{h}}\right) \in \mathcal{V}^{\mathsf{h}}_{\mathrm{v}\phi} \times \mathcal{V}^{\mathsf{h}}_{\mathrm{d}\phi} \times \mathcal{V}^{\mathsf{h}}_{\mathrm{p}\phi} \times \mathcal{V}^{\mathsf{h}}_{\phi}$:

$$\begin{cases} \left(\delta p^{\mathrm{f,h}}, \mathring{\phi}^{\mathsf{h}}_{n+\theta}\right)_{\Omega^{\mathsf{h}}(t_{n+1})} + \mathcal{F}^{\mathrm{f}}_{\mathrm{C}\phi,n+\theta}(\delta p^{\mathrm{f,h}}, \boldsymbol{d}^{\mathrm{s,h}}_{n+1}, \boldsymbol{v}^{\mathrm{f,h}}_{n+1}, p^{\mathrm{f,h}}_{n+1}, \phi^{\mathsf{h}}_{n+1}) = 0. \\ \left(\delta\boldsymbol{v}^{\mathrm{f,h}}, \rho^{\mathrm{f}}_0 \mathring{\boldsymbol{v}}^{\mathrm{f,h}}_{n+\theta}\right)_{\Omega^{\mathsf{h}}(t_{n+1})} + \boldsymbol{\mathcal{F}}^{\mathrm{f}}_{\mathrm{M}\phi,n+\theta}(\delta\boldsymbol{v}^{\mathrm{f,h}}, \boldsymbol{d}^{\mathrm{s,h}}_{n+1}, \boldsymbol{v}^{\mathrm{f,h}}_{n+1} p^{\mathrm{f,h}}_{n+1}, \phi^{\mathsf{h}}_{n+1}) = 0, \\ \left(\delta\boldsymbol{d}^{\mathrm{s,h}}, m^{\mathrm{s}}_0 \boldsymbol{a}^{\mathrm{s,h}}_{n+\theta}\right)_{\Omega^{\mathsf{h}}_0} + \boldsymbol{\mathcal{F}}^{\mathrm{s}}_{\mathrm{M}\phi,n+\theta}(\delta\boldsymbol{d}^{\mathrm{s,h}}, \boldsymbol{d}^{\mathrm{s,h}}_{n+1}, \boldsymbol{v}^{\mathrm{f,h}}_{n+1}, p^{\mathrm{f,h}}_{n+1}, \phi^{\mathsf{h}}_{n+1}) = 0, \\ (1-\theta)\left(\delta\phi^{\mathsf{h}}, p^{\mathrm{f,h}}_n - \left(\frac{\partial\Psi^{\mathrm{s}}}{\partial(J\phi)}\right)(\boldsymbol{d}^{\mathrm{s,h}}_n, p^{\mathrm{f,h}}_n, \phi^{\mathsf{h}}_n)\right)_{\Omega^{\mathsf{h}}_0} \\ +\theta\left(\delta\phi^{\mathsf{h}}, p^{\mathrm{f,h}}_{n+1} - \left(\frac{\partial\Psi^{\mathrm{s}}}{\partial(J\phi)}\right)(\boldsymbol{d}^{\mathrm{s,h}}_{n+1}, p^{\mathrm{f,h}}_{n+1}, \phi^{\mathsf{h}}_{n+1})\right)_{\Omega^{\mathsf{h}}_0} = 0. \end{cases} \tag{4.119}$$

As stated before, in this approach, the displacement field as well as the porosity field need to be C^0-continuous. Hence, even first-order Lagrange elements are applicable. From a practical

point of view, this is a major advantage of the mixed approach compared to the NURBS-based approach, as first order elements are computationally cheaper and easier to be implemented.

4.3.3.4. NURBS-based Approach

The second formulation for a porous system with Darcy-Brinkman flow is based on *Non-Uniform Rational Basis Splines* (NURBS). NURBS have been the industrial standard for CAD-systems (Computer Aided Design). They became increasingly popular also in the computational mechanics community through the work of Hughes et. al. [128] who used them as shape functions in the context of the finite element method. This special version of the FEM is called isogeometric analysis. Since it was first introduced, isogeometric analysis has been applied to a variety of problems. One application that is of special interest to this work is given in [132]. There, isogeometric analysis has been applied to poroelasticity but still was restricted to small deformations. As NURBS basis functions of order p can be up to C^{p-1}-continuous by construction, they perfectly meet the requirements posed by the specific porous medium problem analyzed here. In the following, a brief introduction into the definition of NURBS functions is given. Fundamentals on NURBS are well documented in the literature and a comprehensive discussion can be found in textbooks [190] and [205].

NURBS are based on so called *Basis-splines* (B-splines). For the construction of a B-spline polynomial of order p, a corresponding *knot vector*

$$\mathbf{u} = (\mathsf{u}_1, \mathsf{u}_2, \ldots, \mathsf{u}_{n+p+1}) \tag{4.120}$$

needs to be defined. The knot values u_i, $i = 1, \ldots, n+p+1$ form a set of non-decreasing numbers representing coordinates in the parametric space. The interval $[\mathsf{u}_1, \mathsf{u}_{n+p+1}]$ is called a *patch*, which is composed of the *knot spans* $[\mathsf{u}_i, \mathsf{u}_{i+1}]$. A knot vector is called *uniform*, if all knot values are equally spaced, otherwise non-uniform. A knot vector is open if its first and last knots are repeated $p+1$ times. A B-spline basis function of order 0 is then defined as

$$\mathsf{B}_i^0(u) := \begin{cases} 1 & \text{if} \quad \mathsf{u}_i \leq u < \mathsf{u}_{i+1} \\ 0 & \text{otherwise} \end{cases} \tag{4.121}$$

and recursively B-spline basis functions of order $p > 1$ are defined as

$$\mathsf{B}_i^d(u) := \frac{u - \mathsf{u}_i}{\mathsf{u}_{i+d} - \mathsf{u}_i} \cdot \mathsf{B}_i^{d-1}(u) + \frac{\mathsf{u}_{i+d+1} - u}{\mathsf{u}_{i+d+1} - \mathsf{u}_{i+1}} \cdot \mathsf{B}_{i+1}^{d-1}(u), \quad d = 1, \ldots, p. \tag{4.122}$$

In Figure 4.3 an example of B-spline basis functions is depicted. NURBS basis functions are rational B-spline functions. They are defined by using a set of positive weights ω_i, $i = 1, \ldots, n$ as

$$\mathsf{R}_i^p(u) := \frac{\omega_i \cdot \mathsf{B}_i^p(u)}{\sum_{j=1}^n \omega_j \cdot B_j^p(u)}. \tag{4.123}$$

NURBS basis functions are C^{p-1}-continuous if the internal knots are not repeated. For a knot with multiplicity k, the basis is C^{p-k}-continuous at that knot. NURBS curves of order p are a linear combination of NURBS basis functions of order p and n control points $\mathbf{X}$. Hence, a

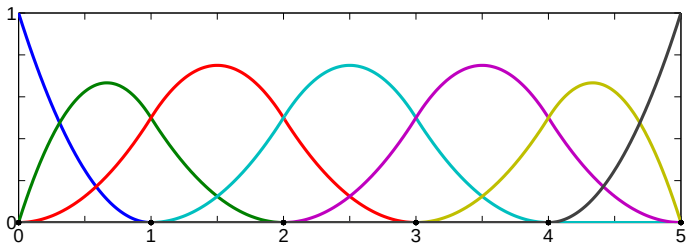

Figure 4.3: B-spline basis functions for $p = 2$ and knot vector $\mathbf{u} = [0, 0, 0, 1, 2, 3, 4, 5, 5, 5]$, taken from [244].

NURBS curve is given as

$$\mathbf{C}(u) = \sum_{i}^{n} \mathsf{R}_i^p \mathbf{X}_i. \tag{4.124}$$

The control points define the control polygon. A generalization of NURBS curves to NURBS surfaces and volumes is based on tensor products of B-spline basis functions. NURBS surfaces are defined as

$$\mathbf{S}(u,v) = \sum_{i}^{n}\sum_{j}^{m} \underbrace{\frac{\mathsf{B}_i^p(u)\mathsf{B}_j^q(v)\omega_{ij}}{\sum_i^n \sum_j^m \mathsf{B}_i^p(u)\mathsf{B}_j^q(v)\omega_{ij}}}_{\mathsf{R}_{ij}} \mathbf{X}_{ij}, \tag{4.125}$$

depending on two parameter coordinates u and v. The B-spline basis functions are for polynomial order p and q and the $n{\cdot}m$ control points form the control net. The corresponding weights ω_{ij} for definition of the NURBS basis do not follow a tensor-product structure and can be chosen arbitrarily, just like the control points $\mathbf{X}_{ij}$. NURBS volumes can be formulated analogously, that is

$$\mathbf{V}(u,v,w) = \sum_{i}^{n}\sum_{j}^{m}\sum_{k}^{o} \frac{\mathsf{B}_i^p(u)\mathsf{B}_j^q(v)\mathsf{B}_k^r(w)\omega_{ijk}}{\sum_i^n \sum_j^m \sum_k^o \mathsf{B}_i^p(u)\mathsf{B}_j^q(v)\mathsf{B}_k^r(w)\omega_{ijk}} \mathbf{X}_{ijk}. \tag{4.126}$$

Derivatives of NURBS parametrizations with respect to the parameter coordinates can easily be derived for any order p of the NURBS basis functions. Again, the interested reader is referred to the common literature and textbooks mentioned above for details.

Now, the weak form (4.80) will be discretized using NURBS. Thus, NURBS basis functions (4.123) are used as shape functions, i.e.

$$\boldsymbol{d}^{\mathrm{s}} \approx \boldsymbol{d}^{\mathrm{s,h}} = \sum_{k=1}^{\mathrm{n_{node}}} \mathsf{R}_{\mathsf{d},k}^p \mathbf{d}_k^{\mathrm{s}}, \tag{4.127}$$

$$\boldsymbol{v}^{\mathrm{f}} \approx \boldsymbol{v}^{\mathrm{f,h}} = \sum_{k=1}^{\mathrm{n_{node}}} \mathsf{R}_{\mathsf{v},k}^p \mathbf{v}_k^{\mathrm{f}}, \tag{4.128}$$

$$p^{\mathrm{f}} \approx p^{\mathrm{f,h}} = \sum_{k=1}^{\mathrm{n_{node}}} \mathsf{R}_{\mathsf{p},k}^p \mathbf{p}_k^{\mathrm{f}}, \tag{4.129}$$

and, following the isoparametric concept, also for the approximation of the geometry

$$\boldsymbol{X} \approx \boldsymbol{X}^{\mathsf{h}} = \sum_{k=1}^{\mathrm{n_{node}}} \mathsf{R}^{p}_{\mathsf{d},k} \mathbf{X}_k, \tag{4.130}$$

$$\boldsymbol{x} \approx \boldsymbol{x}^{\mathsf{h}} = \sum_{k=1}^{\mathrm{n_{node}}} \mathsf{R}^{p}_{\mathsf{d},k} \mathbf{x}_k. \tag{4.131}$$

In this context $\mathrm{n_{node}}$ denotes the number of control points and $\mathbf{X}_k$ and $\mathbf{x}_k$ the material and current coordinate of control point k, respectively. A Bubnov-Galerkin approach is utilized, i.e. the weighting functions are approximated in the same way as the primary fields. This time, the finite-dimensional approximation spaces $\mathcal{S}^{\mathsf{h}}$ and $\mathcal{V}^{\mathsf{h}}$ are spanned by the NURBS basis functions. Second-order NURBS are used in this thesis. Based on the weak form (4.80), the discrete form reads:

Find $\left(\boldsymbol{d}^{\mathrm{s,h}}_{n+1}, \boldsymbol{v}^{\mathrm{f,h}}_{n+1}, p^{\mathrm{f,h}}_{n+1}\right) \in \mathcal{S}^{\mathsf{h}}_{\mathrm{d,DB}} \times \mathcal{S}^{\mathsf{h}}_{\mathrm{v,DB}} \times \mathcal{S}^{\mathsf{h}}_{\mathrm{p,DB}}$, such that $\forall \left(\delta\boldsymbol{d}^{\mathrm{s,h}}, \delta\boldsymbol{v}^{\mathrm{f,h}}, \delta p^{\mathrm{f,h}}\right) \in \mathcal{V}^{\mathsf{h}}_{\mathrm{d,DB}} \times \mathcal{V}^{\mathsf{h}}_{\mathrm{v,DB}} \times \mathcal{V}^{\mathsf{h}}_{\mathrm{p,DB}}$:

$$\begin{cases} \left(\delta p^{\mathrm{f,h}}, \dfrac{\partial \phi}{\partial p^{\mathrm{f}}}\left(\boldsymbol{d}^{\mathrm{s,h}}_{n+1}, p^{\mathrm{f,h}}_{n+1}\right) \cdot \mathring{p}^{\mathrm{f,h}}_{n+\theta}\right)_{\Omega^{\mathsf{h}}(t_{n+1})} + \mathcal{F}^{\mathrm{f}}_{\mathrm{C,DB},n+\theta}(\delta p^{\mathrm{f,h}}, \boldsymbol{d}^{\mathrm{s,h}}_{n+1}, \boldsymbol{v}^{\mathrm{f,h}}_{n+1}, p^{\mathrm{f,h}}_{n+1}) = 0, \\ \left(\delta\boldsymbol{v}^{\mathrm{f,h}}, \rho^{\mathrm{f}}_0 \mathring{\boldsymbol{v}}^{\mathrm{f,h}}_{n+\theta}\right)_{\Omega^{\mathsf{h}}(t_{n+1})} + \boldsymbol{\mathcal{F}}^{\mathrm{f}}_{\mathrm{M,DB},n+\theta}(\delta\boldsymbol{v}^{\mathrm{f,h}}, \boldsymbol{d}^{\mathrm{s,h}}_{n+1}, \boldsymbol{v}^{\mathrm{f,h}}_{n+1}, p^{\mathrm{f,h}}_{n+1}) = 0, \\ \left(\delta\boldsymbol{d}^{\mathrm{s,h}}, m^{\mathrm{s}}_0 \boldsymbol{a}^{\mathrm{s,h}}_{n+\theta}\right)_{\Omega^{\mathsf{h}}_0} + \boldsymbol{\mathcal{F}}^{\mathrm{s}}_{\mathrm{M,DB},n+\theta}(\delta\boldsymbol{d}^{\mathrm{s,h}}, \boldsymbol{d}^{\mathrm{s,h}}_{n+1}, \boldsymbol{v}^{\mathrm{f,h}}_{n+1}, p^{\mathrm{f,h}}_{n+1}) = 0. \end{cases} \tag{4.132}$$

This approach fulfills the requirements for convergence thanks to the higher continuity of NURBS. Thereby the system size is the same as for the standard approach. However, one has to keep in mind, that usually NURBS have a larger stencil compared to Lagrange elements, which increases solver costs.

Remark 4.4 *Since NURBS basis functions are non-interpolatory, the application of non-constant Dirichlet boundary conditions to the degrees of freedom is not straightforward. In general, they can either be applied in a strong or weak sense. In the examples, the non-constant Dirichlet values at the control points are calculated via solving a least squares problem and are applied in a strong sense.*

Remark 4.5 *In addition, as NURBS basis functions are in general rational functions, standard gauss quadrature is not exact. However, it was shown in [129], that it still leads to good and accurate results. Hence, standard quadrature rules will be used in the examples.*

Remark 4.6 *Strictly speaking, the higher continuity of NURBS holds on a so called patch, which is defined by a corresponding set of knot vectors. For many basic geometries one patch is sufficient for its exact description, while for more complex geometries multiple patches assembling the overall domain are necessary. It has to be noted, that maintaining continuity over patch*

boundaries is a non-trivial task. For instance, two NURBS surfaces achieve only C^0-continuity, if they share a common boundary curve. In [64], C^1-continuity between multiple patches was attained by using a constraint equation. An alternative is to use so-called T-Splines, which are a generalization of NURBS. For a comparison between NURBS and T-Splines see [23]. In this thesis, only single patch geometries are considered.

4.3.3.5. Residual-based Variational Multi-Scale Stabilization

When using equal-order interpolations for certain solution variables in a mixed formulation, the finite element approximation violates the Ladyschenskaja-Babuska-Brezzi (LBB) condition. Thus, all discrete forms (4.116), (4.119) and (4.132) need to be stabilized. A residual-based variational multi-scale stabilization is applied, which leads to additional terms in the discrete form. This thesis does not contain any new aspects concerning stabilization, but a common formulation will be summarized and utilized subsequently. The reader is referred to the textbook [82] for general stabilzation techniques for flow with finite elements and [17, 18, 166] for residual-based stabilization of porous flow.

The theory behind residual-based stabilizations is well known. For a given problem, however, detailed investigation are due in order to determine the adequate choice of the stabilization parameters, see e.g. [17] for Darcy flow. This is not the focus of this thesis. Still, the utilized stabilization terms are listed here for the sake of completeness without going into detail about their derivation. Note, that the given stabilization parameters are taken from studies in the literature based on similar, but not identical, problems and thus might not be optimal for the given porous medium problem. Nonetheless, they were used within the numerical examples and performed well. The unresolved scales are approximated via the discrete residual of the flow equation $\boldsymbol{\mathcal{R}}_{\mathrm{M}}^{\mathrm{f,h}}$ and the residual of the balance of linear momentum of the mixture $\boldsymbol{\mathcal{R}}_{\mathrm{M}}^{\mathrm{s,h}}$. Those residuals are calculated by inserting the numerical approximation into the strong form:

$$\boldsymbol{\mathcal{R}}_{\mathrm{M}}^{\mathrm{f,h}} = \mathring{\boldsymbol{v}}_{n+\theta}^{\mathrm{f,h}} + \boldsymbol{f}_{\mathrm{M},n+\theta}^{\mathrm{f}} \left(\boldsymbol{d}_{n+1}^{\mathrm{s,h}}, \boldsymbol{v}_{n+1}^{\mathrm{f,h}}, p_{n+1}^{\mathrm{f,h}} \right), \tag{4.133}$$

$$\boldsymbol{\mathcal{R}}_{\mathrm{M}}^{\mathrm{s,h}} = m_0^{\mathrm{s}} \boldsymbol{a}_{n+\theta}^{\mathrm{s,h}} + \boldsymbol{f}_{\mathrm{M},n+\theta}^{\mathrm{s}} \left(\boldsymbol{d}_{n+1}^{\mathrm{s,h}}, \boldsymbol{v}_{n+1}^{\mathrm{f,h}}, p_{n+1}^{\mathrm{f,h}} \right). \tag{4.134}$$

Here, the residuals are written for the formulation (4.34). For the mixed formulation, the residuals are analogously obtained inserting the approximations into the system (4.48). The choice of the stabilization parameter for the porous flow equations is adopted from [17] and is defined as

$$\tau_{\mathrm{M}} = \frac{h^2}{4h^2 \rho^{\mathrm{f}} \left(\phi \frac{\mu^{\mathrm{f}}}{k} + (\theta \Delta t)^{-1} \right) + 6\mu_{\mathrm{eff}}^{\mathrm{f}}}. \tag{4.135}$$

Therein, h denotes a characteristic element size and k a scalar-valued characteristic permeability. The effective viscosity $\mu_{\mathrm{eff}}^{\mathrm{f}}$ is set zero for Darcy flow and $\mu_{\mathrm{eff}}^{\mathrm{f}} = \mu^{\mathrm{f}}$ for Darcy-Brinkman flow. For the volumetric coupling of solid and fluid an additional stabilization parameter is introduced [18]:

$$\tau_{\mathrm{B}} = c \frac{h^2}{2\mu_{\mathrm{eff}}^{\mathrm{s}}}, \tag{4.136}$$

with the numerical constant c and the effective shear modulus $\mu^{\mathrm{s}}_{\mathrm{eff}}$ of the skeleton. The following stabilization techniques are included in the implementation:

- Pressure Stabilizing Petrov-Galerkin (PSPG)
  PSPG allows for equal-order interpolation of pressure and fluid velocity by relaxing the continuity equation. Stemming from [17], the following contribution is added to the continuity equation of the fluid phase (first equation of (4.66), (4.80) and (4.95))

$$\sum_{e=1}^{\mathrm{n_{ele}}} \left(\boldsymbol{\nabla} \delta p^{\mathrm{f}}_h, \tau_{\mathrm{M}} \boldsymbol{\mathcal{R}}^{\mathrm{f,h}}_{\mathrm{M}} \right)_{\Omega_e} . \tag{4.137}$$

- Stabilization due to reactive term
  Based on the same argumentation as the PSPG term, an additional term is added to the flow equation [17] (second equation of (4.66), (4.80) or (4.95)) weighted by the reactive (Darcy) coefficient

$$\sum_{e=1}^{\mathrm{n_{ele}}} \left(\phi \frac{\mu^{\mathrm{f}}}{k} \delta \boldsymbol{v}^{\mathrm{f}}_h, -\tau_{\mathrm{M}} \boldsymbol{\mathcal{R}}^{\mathrm{f,h}}_{\mathrm{M}} \right)_{\Omega_e} . \tag{4.138}$$

- Biot stabilization
  Further, a special stabilization term for the porous medium system (also called Biot system in linear theory) is included. It becomes relevant, when low permeabilities and dynamic effects are considered. More precisely, when the time derivative of the porosity in the continuity equation is non-zero, unphysical stress and pressure oscillations occur for low-permeability problems. From an engineering perspective, this effect can be interpreted as volumetric locking of the porous system [189]. One possible remedy is the introduction of another stabilization term to the balance of mass of the fluid phase [18]. The following contribution is added to the continuity equation of the fluid phase (first equation of (4.66), (4.80) and (4.95))

$$\sum_{e=1}^{\mathrm{n_{ele}}} \left(\boldsymbol{\nabla} \delta p^{\mathrm{f}}_h, \tau_{\mathrm{B}} \boldsymbol{\mathcal{R}}^{\mathrm{s,h}}_{\mathrm{M}} \right)_{\Omega_e} . \tag{4.139}$$

PSPG and the stabilization due to the reactive term are used within all numerical simulations involving a porous medium. As stated before, the Biot stabilization is only necessary in certain kinds of settings. The Biot stabilization is used and analyzed in the example in Section 4.4.1.

4.3.4. Newton Scheme and Monolithic Approach

After discretization of (4.66), (4.80) or (4.95) in time and space the discrete residuals $\mathbf{R}^{\mathrm{s}} = \mathbf{R}^{\mathrm{s}}(\mathbf{d}^{\mathrm{s}}, \mathbf{v}^{\mathrm{f}})$ and $\mathbf{R}^{\mathrm{f}} = \mathbf{R}^{\mathrm{f}}(\mathbf{d}^{\mathrm{s}}, \mathbf{v}^{\mathrm{f}})$ of the skeleton and fluid equations are obtained. In this context, $\mathbf{d}^{\mathrm{s}}$ and $\mathbf{v}^{\mathrm{f}}$ denote the vectors of nodal displacements (and porosities in case of the mixed approach) and fluid unknowns (i.e., fluid velocities and pressures), respectively. The residuals consist of the discrete form (4.116), (4.80) or (4.95) and the stabilization terms presented in Section 4.3.3.5.

For the solution of this system of non-linear equations at a time step $n+1$

$$\mathbf{R}(\mathbf{d}^{\mathrm{s}}_{n+1}, \mathbf{v}^{\mathrm{f}}_{n+1}) = \begin{pmatrix} \mathbf{R}^{\mathrm{s}}(\mathbf{d}^{\mathrm{s}}_{n+1}, \mathbf{v}^{\mathrm{f}}_{n+1}) \\ \mathbf{R}^{\mathrm{f}}(\mathbf{d}^{\mathrm{s}}_{n+1}, \mathbf{v}^{\mathrm{f}}_{n+1}) \end{pmatrix} = \mathbf{0} \tag{4.140}$$

a Newton-Raphson method is utilized. This fully coupled non-linear problem will be solved within one Newton loop. A so-called monolithic solution scheme is applied, wherein the primary variables of the respective fields will be solved simultaneously. In comparison to partitioned schemes, where an iteration between single field solvers is utilized, this approach has been successfully applied to other multi-field applications and proven to be superior especially for complex biological problems (see, [107, 151]). The corresponding linearized equations at a iteration step i are given as

$$\mathrm{Lin}\ \mathbf{R} = \mathbf{R}(\mathbf{d}^{\mathrm{s},i}_{n+1}, \mathbf{v}^{\mathrm{f},i}_{n+1}) + \left.\frac{\partial \mathbf{R}(\mathbf{d}^{\mathrm{s}}, \mathbf{v}^{\mathrm{f}})}{\partial \mathbf{d}^{\mathrm{s}}}\right|^{i}_{n+1} \Delta\mathbf{d}^{\mathrm{s},i+1}_{n+1} + \left.\frac{\partial \mathbf{R}(\mathbf{d}^{\mathrm{s}}, \mathbf{v}^{\mathrm{f}})}{\partial \mathbf{v}^{\mathrm{f}}}\right|^{i}_{n+1} \Delta\mathbf{v}^{\mathrm{f},i+1}_{n+1} = \mathbf{0}. \tag{4.141}$$

The most important linearizations can be found in Appendix A.2. This system is solved for the unknown increments $\Delta\mathbf{d}^{\mathrm{s},i+1}_{n+1}$ and $\Delta\mathbf{v}^{\mathrm{f},i+1}_{n+1}$. Hence, in compact matrix notation the following linear system is solved

$$\begin{pmatrix} \dfrac{\partial \mathbf{R}(\mathbf{d}^{\mathrm{s}}, \mathbf{v}^{\mathrm{f}})}{\partial \mathbf{d}^{\mathrm{s}}} & \dfrac{\partial \mathbf{R}(\mathbf{d}^{\mathrm{s}}, \mathbf{v}^{\mathrm{f}})}{\partial \mathbf{v}^{\mathrm{f}}} \end{pmatrix}^{i}_{n+1} \begin{pmatrix} \Delta\mathbf{d}^{\mathrm{s}} \\ \Delta\mathbf{v}^{\mathrm{f}} \end{pmatrix}^{i+1}_{n+1} = - \begin{pmatrix} \mathbf{R}^{\mathrm{s}} \\ \mathbf{R}^{\mathrm{f}} \end{pmatrix}^{i}_{n+1}, \tag{4.142}$$

Then, the guess of the nodal values for the next iteration step $i+1$ are obtained as

$$\begin{pmatrix} \mathbf{d}^{\mathrm{s}} \\ \mathbf{v}^{\mathrm{f}} \end{pmatrix}^{i+1}_{n+1} = \begin{pmatrix} \mathbf{d}^{\mathrm{s}} \\ \mathbf{v}^{\mathrm{f}} \end{pmatrix}^{i}_{n+1} + \begin{pmatrix} \Delta\mathbf{d}^{\mathrm{s}} \\ \Delta\mathbf{v}^{\mathrm{f}} \end{pmatrix}^{i+1}_{n+1}. \tag{4.143}$$

The iterative procedure is aborted when a convergence criterion is met, e.g.

$$\left|\left|(\mathbf{R}^{\mathrm{s}})^{i}_{n+1}\right|\right| < \epsilon^{\mathrm{s}} \text{ and } \left|\left|(\mathbf{R}^{\mathrm{f}})^{i}_{n+1}\right|\right| < \epsilon^{\mathrm{f}}, \tag{4.144}$$

where ϵ^{s} and ϵ^{f} are problem specific tolerances. In the following Section 4.3.4.1 comments concerning the solution of linear system are made. Subsequently, some special cases are presented, where the linear system is manipulated before solving. In Section 4.3.4.2 a method for the application of impermeability constraints is proposed. There, the constraints are enforce with the Lagrange multiplier method. The resulting additional degrees of freedom are condensed out of the linear system. In Section 4.3.4.3 non-matching fluid and skeleton meshes are treated. The nodal values are projected from one mesh to the other. This leads to manipulation of the coupling blocks of the linear system.

4.3.4.1. Linear Solver

The main drawback of the monolithic solution approach compared to partitioned schemes is the increased size of the linear system. As both fields are solved simultaneously, the linear system includes the tangential matrices from both residuals as well as the respective linearizations of the coupling terms. This leads to a complex matrix pattern, as exemplarily depicted in Figure 4.4. For large problems the most expensive part of the numerical simulation is the linear

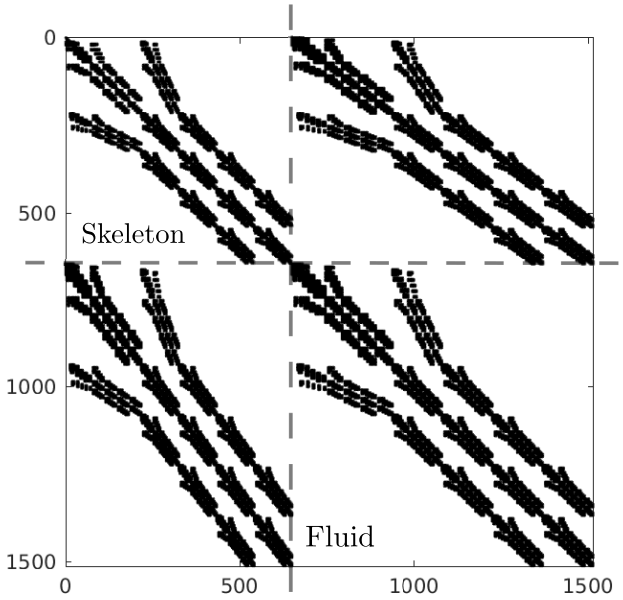

Figure 4.4: Exemplary sparsity pattern of tangent matrix of monolithic porous medium system. Black dot denotes non-zero entry.

solver. In this work, an iterative solution technique known as Generalized Minimal RESidual (GMRES) [211] is applied. In addition, for efficient calculations a block-preconditioner is used. It has been specifically designed for monolithic coupled problems, see [240].

4.3.4.2. Impermeability Constraints

In the following a methodology to apply no-penetration conditions for Darcy flow and no-slip conditions for Darcy-Brinkman flow is presented. This is realized mainly by manipulating the linear system within the Newton scheme. After consistent linearization and before application of those mentioned conditions, the system to be solved in every iteration step $i+1$ of the non-linear

algorithm reads

$$\begin{pmatrix} \mathbf{S}_{\mathrm{II}} & \mathbf{S}_{\mathrm{IC}} & \mathbf{C}_{\mathrm{II}}^{\mathrm{FS}} & \mathbf{C}_{\mathrm{IC}}^{\mathrm{SF}} \\ \mathbf{S}_{\mathrm{CI}} & \mathbf{S}_{\mathrm{CC}} & \mathbf{C}_{\mathrm{CI}}^{\mathrm{SF}} & \mathbf{C}_{\mathrm{CC}}^{\mathrm{SF}} \\ \mathbf{C}_{\mathrm{II}}^{\mathrm{FS}} & \mathbf{C}_{\mathrm{IC}}^{\mathrm{FS}} & \mathbf{F}_{\mathrm{II}} & \mathbf{F}_{\mathrm{IC}} \\ \mathbf{C}_{\mathrm{CI}}^{\mathrm{FS}} & \mathbf{C}_{\mathrm{CC}}^{\mathrm{FS}} & \mathbf{F}_{\mathrm{CI}} & \mathbf{F}_{\mathrm{CC}} \end{pmatrix}^{i}_{n+1} \begin{pmatrix} \Delta\mathbf{d}_{\mathrm{I}}^{\mathrm{s}} \\ \Delta\mathbf{d}_{\mathrm{C}}^{\mathrm{s}} \\ \Delta\mathbf{v}_{\mathrm{I}}^{\mathrm{f}} \\ \Delta\mathbf{v}_{\mathrm{C}}^{\mathrm{f}} \end{pmatrix}^{i+1}_{n+1} = - \begin{pmatrix} \mathbf{R}_{\mathrm{I}}^{\mathrm{s}} \\ \mathbf{R}_{\mathrm{C}}^{\mathrm{s}} \\ \mathbf{R}_{\mathrm{I}}^{\mathrm{f}} \\ \mathbf{R}_{\mathrm{C}}^{\mathrm{f}} \end{pmatrix}^{i}_{n+1}, \tag{4.145}$$

for time step $n+1$. Therein, the degrees of freedom are split into inner degrees of freedom (marked with the subscript I) and conditioned degrees of freedom (marked with subscript C). Note that in this notation all fluid pressure degrees of freedom are counted as inner degrees of freedom, i.e. included in $\Delta\mathbf{v}_{\mathrm{I}}^{\mathrm{f}}$. The individual sub-matrices of the system matrix in equation (4.145) denote the derivatives of the residuals with respect to the degrees of freedom, split into inner and conditioned degrees of freedom, i.e. for instance

$$\mathbf{S}_{\mathrm{CI}} = \frac{\partial \mathbf{R}_{\mathrm{C}}^{\mathrm{s}}}{\partial \mathbf{d}_{\mathrm{I}}^{\mathrm{s}}}, \tag{4.146}$$

$$\mathbf{C}_{\mathrm{CC}}^{\mathrm{SF}} = \frac{\partial \mathbf{R}_{\mathrm{C}}^{\mathrm{s}}}{\partial \mathbf{v}_{\mathrm{C}}^{\mathrm{f}}}, \tag{4.147}$$

$$\mathbf{F}_{\mathrm{II}} = \frac{\partial \mathbf{R}_{\mathrm{I}}^{\mathrm{f}}}{\partial \mathbf{v}_{\mathrm{I}}^{\mathrm{f}}}, \tag{4.148}$$

$$\mathbf{C}_{\mathrm{IC}}^{\mathrm{FS}} = \frac{\partial \mathbf{R}_{\mathrm{I}}^{\mathrm{f}}}{\partial \mathbf{d}_{\mathrm{C}}^{\mathrm{s}}}. \tag{4.149}$$

In case of impermeable boundaries this system is extended by the Lagrange multiplier field and the constraint itself. The most important steps in order to condense them out of the system are sketched in the following.

4.3.4.2.1. No-Penetration Condition for Darcy Equation

In case of Darcy flow, the no-penetration constraints (4.102), (4.103) and (4.106) are demanded in a weak sense. This leads to the discrete residuals $\mathbf{R}_{\mathrm{C}\perp}^{\mathrm{f}} = \mathbf{R}_{\mathrm{C}\perp}^{\mathrm{f}}(\mathbf{d}^{\mathrm{s}}, \mathbf{v}^{\mathrm{f}})$, $\mathbf{R}_{\mathrm{C}\parallel}^{\mathrm{f}} = \mathbf{R}_{\mathrm{C}\parallel}^{\mathrm{f}}(\mathbf{d}^{\mathrm{s}}, \boldsymbol{\lambda})$ and $\mathbf{R}_{\mathrm{C}}^{\mathrm{f},\lambda} = \mathbf{R}_{\mathrm{C}}^{\mathrm{f},\lambda}(\mathbf{d}^{\mathrm{s}}, \boldsymbol{\lambda})$ of the normal, tangential condition and the additional boundary integrals, respectively. Here $\boldsymbol{\lambda}$ denotes the vector of nodal unknown Lagrange multipliers. Including

$$\mathbf{R}_{\mathrm{C}\perp}^{\mathrm{f}} = \mathbf{0}, \tag{4.150}$$

$$\mathbf{R}_{\mathrm{C}\parallel}^{\mathrm{f}} = \mathbf{0} \tag{4.151}$$

into the monolithic system (4.145) and adding the boundary integral residual to the fluid equation (forth line in (4.145))

$$\mathbf{R}_{\mathrm{C}}^{\mathrm{f}} + \mathbf{R}_{\mathrm{C}}^{\mathrm{f},\lambda} \;=\; \mathbf{0}, \tag{4.152}$$

leads after consistent linearization to

$$\begin{pmatrix} \mathbf{S}_{\mathrm{II}} & \mathbf{S}_{\mathrm{IC}} & \mathbf{C}_{\mathrm{II}}^{\mathrm{SF}} & \mathbf{C}_{\mathrm{IC}}^{\mathrm{SF}} & \mathbf{0} \\ \mathbf{S}_{\mathrm{CI}} & \mathbf{S}_{\mathrm{CC}} & \mathbf{C}_{\mathrm{CI}}^{\mathrm{SF}} & \mathbf{C}_{\mathrm{CC}}^{\mathrm{SF}} & \mathbf{0} \\ \mathbf{C}_{\mathrm{II}}^{\mathrm{FS}} & \mathbf{C}_{\mathrm{IC}}^{\mathrm{FS}} & \mathbf{F}_{\mathrm{II}} & \mathbf{F}_{\mathrm{IC}} & \mathbf{0} \\ \mathbf{C}_{\mathrm{CI}}^{\mathrm{FS}} & \mathbf{C}_{\mathrm{CC}}^{\mathrm{FS}} & \mathbf{F}_{\mathrm{CI}} & \mathbf{F}_{\mathrm{CC}} & -\theta\mathbf{D}^{\mathrm{T}} \\ \mathbf{0} & \mathbf{N}_{\mathrm{CC}}^{\mathrm{FS}} & \mathbf{N}_{\mathrm{CI}}^{\mathrm{FF}} & \mathbf{N}_{\mathrm{CC}}^{\mathrm{FF}} & \mathbf{0} \\ \mathbf{0} & \mathbf{T}_{\mathrm{CC}}^{\mathrm{FS}} & \mathbf{0} & \mathbf{0} & \mathbf{T}_{\mathrm{C}}^{\lambda} \end{pmatrix}_{n+1}^{i} \begin{pmatrix} \Delta\mathbf{d}_{\mathrm{I}}^{\mathrm{s}} \\ \Delta\mathbf{d}_{\mathrm{C}}^{\mathrm{s}} \\ \Delta\mathbf{v}_{\mathrm{I}}^{\mathrm{f}} \\ \Delta\mathbf{v}_{\mathrm{C}}^{\mathrm{f}} \\ \boldsymbol{\lambda} \end{pmatrix}_{n+1}^{i+1} = - \begin{pmatrix} \left(\mathbf{R}_{\mathrm{I}}^{\mathrm{s}}\right)_{n+1}^{i} \\ \left(\mathbf{R}_{\mathrm{C}}^{\mathrm{s}}\right)_{n+1}^{i} \\ \left(\mathbf{R}_{\mathrm{I}}^{\mathrm{f}}\right)_{n+1}^{i} \\ \widetilde{\mathbf{R}_{\mathrm{C}}^{\mathrm{f}}} \\ \left(\mathbf{R}_{\mathrm{C}\perp}^{\mathrm{f}}\right)_{n+1}^{i} \\ \mathbf{0} \end{pmatrix}, \tag{4.153}$$

with $\widetilde{\mathbf{R}_{\mathrm{C}}^{\mathrm{f}}} = \left(\mathbf{R}_{\mathrm{C}}^{\mathrm{f}}\right)_{n+1}^{i} - (1-\theta)\left(\mathbf{D}^{\mathrm{T}} \cdot \boldsymbol{\lambda}\right)_{n}$. Thus, the system size is increased by the number of nodal Lagrange multipliers. A noteworthy technical detail, is that in contrast to the other unknown quantities, the system is solved for the discrete Lagrange multiplier $\boldsymbol{\lambda}_{n+1}^{i+1}$, instead of an increment. Also, the time discretized tangential condition is demanded at the time step $n+1$. The additional sub matrices denote the derivatives of the following residuals with respect to the degrees of freedom, i.e. for instance

$$\mathbf{N}_{\mathrm{CC}}^{\mathrm{FF}} = \frac{\partial \mathbf{R}_{\mathrm{C}\perp}^{\mathrm{f}}}{\partial \mathbf{v}_{\mathrm{C}}^{\mathrm{f}}}, \tag{4.154}$$

$$\mathbf{N}_{\mathrm{C}}^{\mathrm{FS}} = \frac{\partial \mathbf{R}_{\mathrm{C}\perp}^{\mathrm{f}}}{\partial \mathbf{d}_{\mathrm{CC}}^{\mathrm{s}}}, \tag{4.155}$$

$$\mathbf{T}_{\mathrm{C}}^{\mathrm{FS}} = \frac{\partial \mathbf{R}_{\mathrm{C}\parallel}^{\mathrm{f}}}{\partial \mathbf{d}_{\mathrm{C}}^{\mathrm{s}}}, \tag{4.156}$$

$$\mathbf{T}_{\mathrm{C}}^{\lambda} = \frac{\partial \mathbf{R}_{\mathrm{C}\parallel}}{\partial \boldsymbol{\lambda}}, \tag{4.157}$$

$$-\theta\mathbf{D}^{\mathrm{T}} = \frac{\partial \mathbf{R}_{\mathrm{C}}^{\mathrm{f},\lambda}}{\partial \boldsymbol{\lambda}}. \tag{4.158}$$

Solving for the Lagrange multiplier in the Darcy flow equation (forth line in (4.153)) gives

$$\boldsymbol{\lambda}_{n+1}^{i+1} = -\frac{1}{\theta}\mathbf{D}^{-\mathrm{T}} \cdot (-\mathbf{R}_{\mathrm{C}}^{\mathrm{f}} - \mathbf{F}_{\mathrm{CI}} \cdot \Delta\mathbf{v}_{\mathrm{I}}^{\mathrm{f}} - \mathbf{F}_{\mathrm{CC}} \cdot \Delta\mathbf{v}_{\mathrm{C}}^{\mathrm{f}} - \mathbf{C}_{\mathrm{CI}}^{\mathrm{FS}} \cdot \Delta\mathbf{d}_{\mathrm{I}}^{\mathrm{s}} \tag{4.159}$$

$$-\mathbf{C}_{\mathrm{CC}}^{\mathrm{FS}} \cdot \Delta\mathbf{d}_{\mathrm{C}}^{\mathrm{s}} + (1-\theta)\mathbf{D}_{n}^{\mathrm{T}} \cdot \boldsymbol{\lambda}_{n}), \tag{4.160}$$

where all indices referring to the actual time step $n+1$ on the right hand side are omitted for clarity of notation. The Lagrange multipliers are discretized by dual shape functions. This idea was first presented in [255]. Details on the construction approach used here can be found in [193]. Utilizing these shape functions leads to a diagonal matrix $\mathbf{D}^{\mathrm{T}}$ and therefore enables straightforward and efficient evaluation of $\mathbf{D}^{-\mathrm{T}}$, and hence of equation (4.160). By inserting $\boldsymbol{\lambda}_{n+1}^{i+1}$ into the tangential condition (sixth line in (4.153)), the Lagrange multiplier can be condensed out of the system and the original system size is restored.

The final system to be solved by the non-linear algorithm then reads

$$\begin{pmatrix} \mathbf{S}_{\mathrm{II}} & \mathbf{S}_{\mathrm{IC}} & \mathbf{C}_{\mathrm{II}}^{\mathrm{SF}} & \mathbf{C}_{\mathrm{IC}}^{\mathrm{SF}} \\ \mathbf{S}_{\mathrm{CI}} & \mathbf{S}_{\mathrm{CC}} & \mathbf{C}_{\mathrm{CI}}^{\mathrm{SF}} & \mathbf{C}_{\mathrm{CC}}^{\mathrm{SF}} \\ \mathbf{C}_{\mathrm{II}}^{\mathrm{FS}} & \mathbf{C}_{\mathrm{IC}}^{\mathrm{FS}} & \mathbf{F}_{\mathrm{II}} & \mathbf{F}_{\mathrm{IC}} \\ \mathbf{0} & \mathbf{N}_{\mathrm{C}}^{\mathrm{u}} & \mathbf{N}_{\mathrm{I}}^{\mathrm{v}} & \mathbf{N}_{\mathrm{C}}^{\mathrm{v}} \\ \mathbf{A}\cdot\mathbf{C}_{\mathrm{CI}}^{\mathrm{FS}} & \mathbf{A}\cdot\mathbf{C}_{\mathrm{CC}}^{\mathrm{FS}}+\mathbf{T}_{\mathrm{C}}^{\mathrm{u}} & \mathbf{A}\cdot\mathbf{F}_{\mathrm{CI}} & \mathbf{A}\cdot\mathbf{F}_{\mathrm{CC}} \end{pmatrix}_{n+1}^{i} \begin{pmatrix} \Delta\mathbf{d}_{\mathrm{I}}^{\mathrm{s}} \\ \Delta\mathbf{d}_{\mathrm{C}}^{\mathrm{s}} \\ \Delta\mathbf{v}_{\mathrm{I}}^{\mathrm{f}} \\ \Delta\mathbf{v}_{\mathrm{C}}^{\mathrm{f}} \end{pmatrix}_{n+1}^{i+1} = - \begin{pmatrix} \left(\mathbf{R}_{\mathrm{I}}^{\mathrm{s}}\right)_{n+1}^{i} \\ \left(\mathbf{R}_{\mathrm{C}}^{\mathrm{s}}\right)_{n+1}^{i} \\ \left(\mathbf{R}_{\mathrm{I}}^{\mathrm{f}}\right)_{n+1}^{i} \\ \left(\mathbf{R}_{\mathrm{C}\perp}^{\mathrm{f}}\right)_{n+1}^{i} \\ \mathbf{A}\cdot\widetilde{\mathbf{R}_{\mathrm{C}}^{\mathrm{f}}} \end{pmatrix}, \tag{4.161}$$

with $\mathbf{A} = \frac{1}{\theta}\mathbf{T}_{\mathrm{C}}^{\lambda}\cdot\mathbf{D}^{-\mathrm{T}}$. After each iteration, the Lagrange multiplier needs to be recovered by evaluating equation (4.160), as it is required for the calculation of $\mathbf{T}_{\mathrm{C}}^{\lambda}$.

Remark 4.7 *It has to be noted, that the construction of dual shape functions for NURBS is topic of current research [44, 225] and not considered here. Fortunately, the higher continuity of NURBS is not necessary for Darcy flow, as elaborated in Section 4.3.1.*

4.3.4.2.2. No-Slip Condition for Darcy-Brinkman Equation

The methodology to include no-slip constraints into the monolithic solution scheme is very similar to modifications performed in FSI problems, see [148, 168]. After including the no-slip condition (4.104), its consistent linearization, and after adding the additional boundary integrals, the system reads

$$\begin{pmatrix} \mathbf{S}_{\mathrm{II}} & \mathbf{S}_{\mathrm{IC}} & \mathbf{C}_{\mathrm{II}}^{\mathrm{SF}} & \mathbf{C}_{\mathrm{IC}}^{\mathrm{SF}} & \mathbf{0} \\ \mathbf{S}_{\mathrm{CI}} & \mathbf{S}_{\mathrm{CC}} & \mathbf{C}_{\mathrm{CI}}^{\mathrm{SF}} & \mathbf{C}_{\mathrm{CC}}^{\mathrm{SF}} & \mathbf{0} \\ \mathbf{C}_{\mathrm{II}}^{\mathrm{FS}} & \mathbf{C}_{\mathrm{IC}}^{\mathrm{FS}} & \mathbf{F}_{\mathrm{II}} & \mathbf{F}_{\mathrm{IC}} & \mathbf{0} \\ \mathbf{C}_{\mathrm{CI}}^{\mathrm{FS}} & \mathbf{C}_{\mathrm{CC}}^{\mathrm{FS}} & \mathbf{F}_{\mathrm{CI}} & \mathbf{F}_{\mathrm{CC}} & -\theta\mathbf{D}^{\mathrm{T}} \\ \mathbf{0} & -\mathbf{D}^{\mathrm{T}} & \mathbf{0} & \theta\Delta t\mathbf{D}^{\mathrm{T}} & \mathbf{0} \end{pmatrix}_{n+1}^{i} \begin{pmatrix} \Delta\mathbf{d}_{\mathrm{I}}^{\mathrm{s}} \\ \Delta\mathbf{d}_{\mathrm{C}}^{\mathrm{s}} \\ \Delta\mathbf{v}_{\mathrm{I}}^{\mathrm{f}} \\ \Delta\mathbf{v}_{\mathrm{C}}^{\mathrm{f}} \\ \boldsymbol{\lambda} \end{pmatrix}_{n+1}^{i+1} = - \begin{pmatrix} \left(\mathbf{R}_{\mathrm{I}}^{\mathrm{s}}\right)_{n+1}^{i} \\ \widetilde{\mathbf{R}_{\mathrm{C}}^{\mathrm{s}}} \\ \left(\mathbf{R}_{\mathrm{I}}^{\mathrm{f}}\right)_{n+1}^{i} \\ \left(\mathbf{R}_{\mathrm{C}}^{\mathrm{f}}\right)_{n+1}^{i} \\ \mathbf{0} \end{pmatrix}, \tag{4.162}$$

with $\widetilde{\mathbf{R}^{\mathrm{s}}_{\mathrm{C}}} = \mathbf{R}^{\mathrm{s}}_{\mathrm{C}} - (1-\theta)\left(\mathbf{D}^{\mathrm{T}} \cdot \boldsymbol{\lambda}\right)_n$ As done before, $\boldsymbol{\lambda}^{i+1}_{n+1}$ can be condensed out of the system by solving for the Lagrange multiplier $\boldsymbol{\lambda}^{i+1}_{n+1}$ in the Darcy-Brinkman flow equation (forth line in (4.162)). Additionally, the last equation from (4.162), i.e. the identity $\Delta\mathbf{v}^{\mathrm{f}}_{\mathrm{C}} = \frac{1}{\theta\Delta t}\Delta\mathbf{d}^{\mathrm{s}}_{\mathrm{C}}$, is used to condense the fluid velocities on the constraint boundary, further decreasing the number of degrees of freedom. Note, that this simple relation only holds for conforming structure and fluid meshes. In case of non-conforming meshes a projection operator $\mathbf{P}$ is needed to relate velocities and displacements $\Delta\mathbf{v}^{\mathrm{f}}_{\mathrm{C}} = \frac{1}{\theta\Delta t}\mathbf{P}\Delta\mathbf{d}^{\mathrm{s}}_{\mathrm{C}}$. Such an operator can, for instance, be calculated from a mortar approach, as done for FSI with non-matching interfaces [148]. The final condensed system then reads

$$\begin{pmatrix} \mathbf{S}_{\mathrm{II}} & \mathbf{S}_{\mathrm{IC}} - \frac{1}{\theta\Delta t}\mathbf{C}^{\mathrm{SF}}_{\mathrm{IC}} & \mathbf{C}^{\mathrm{SF}}_{\mathrm{II}} \\ \mathbf{S}_{\mathrm{CI}} & \mathbf{S}_{\mathrm{CC}} - \frac{1}{\theta\Delta t}\mathbf{C}^{\mathrm{SF}}_{\mathrm{CC}} & \mathbf{C}^{\mathrm{SF}}_{\mathrm{CI}} \\ \mathbf{C}^{\mathrm{FS}}_{\mathrm{II}} & \mathbf{C}^{\mathrm{FS}}_{\mathrm{IC}} - \frac{1}{\theta\Delta t}\mathbf{F}_{\mathrm{IC}} & \mathbf{F}_{\mathrm{II}} \end{pmatrix}^{i}_{n+1} \begin{pmatrix} \Delta\mathbf{d}^{\mathrm{s}}_{\mathrm{I}} \\ \Delta\mathbf{d}^{\mathrm{s}}_{\mathrm{C}} \\ \Delta\mathbf{v}^{\mathrm{f}}_{\mathrm{I}} \end{pmatrix}^{i+1}_{n+1} = - \begin{pmatrix} \mathbf{R}^{\mathrm{s}}_{\mathrm{I}} \\ \mathbf{R}^{\mathrm{s}}_{\mathrm{C}} \\ \mathbf{R}^{\mathrm{f}}_{\mathrm{I}} \end{pmatrix}^{i}_{n+1}, \tag{4.163}$$

It has to be pointed out, that in this case the Lagrange multiplier does not influence the single non-linear iteration steps directly. It rather plays the role of a boundary traction which can be post-processed after solving one time step. This is because the momentum of the whole mixture already includes the coupling with the fluid stresses, which are equal to the Lagrange multiplier on the constraint boundary and therefore cancels out as described in Section 4.3.2.3.

4.3.4.3. Porous Medium Problem on Non-Matching Meshes

From a numerical point of view an interesting aspect is the consideration of non-matching fluid and solid meshes. If, for instance, the flow is complex, but the deformations are easily resolved, it would be computationally advantageous to only use a very small number of elements to resolve the displacement field while the fluid velocity is approximated with far more elements. Independent meshing of the fluid and the solid also implies the possibility of using different interpolation functions, even if the element sizes do not differ significantly. A general methodology for solving volumetrically coupled multi-field problems is presented in [91]. Therein, two coupling methods are presented: one is based on straightforward interpolation of nodal values on the respective mesh and the other uses a mortar-like coupling of the primary fields. The former will be called collocation approach, while the latter will be referred to as mortar-based approach in the following. In the end, both methods provide the global algorithm with two discrete projection operators $\mathbf{P}_{12}$ and $\mathbf{P}_{21}$, which are used to transfer nodal information from one mesh to the other and vice versa. In this thesis, no further details on the construction of these operators are given. Instead, it is referred to the above contribution. It will be shown here, how this projection is included into the monolithic porous medium system.

The two different discrete domains Ω^{h}_1 and Ω^{h}_2 are considered. Both domains approximate the same continuous porous volume. After spatial discretization, the solid problem is going to be solved on mesh Ω^{h}_1 and the fluid problem on Ω^{h}_2. The two discrete sets of primary unknowns are the skeleton unknowns $\mathbf{d}^{\mathrm{s}}_1$ on Ω^{h}_1 and the fluid unknowns $\mathbf{v}^{\mathrm{f}}_2$ on Ω^{h}_2. The auxiliary counterparts of the primary unknowns are $\mathbf{d}^{\mathrm{s}}_2$ on Ω^{h}_2 and $\mathbf{v}^{\mathrm{f}}_1$ on Ω^{h}_1, respectively. Simply speaking,

both approaches demand the equality of the primary and the corresponding auxiliary variable in a certain sense. The collocation method enforces the coupling in a strong, point-wise sense at each node. The mortar-based approach demands an equality of the two fields in a weak, integral sense. Thereby, so-called dual shape functions [255] are used for efficient calculations. Discretizatuion with standard finite elements then gives the desired projection of the discrete nodel values $\mathbf{d}_2^{\mathrm{s}} = \mathbf{P}_{21}\mathbf{d}_1^{\mathrm{s}}$. Again, it is referred to [91] for details.

Now, the form of the linearized monolithic system will be sketched. The discrete residuals read

$$\mathbf{R}_1^{\mathrm{s}}(\mathbf{d}_1^{\mathrm{s}}, \mathbf{v}_1^{\mathrm{f}}) = \mathbf{0} \qquad \text{and} \qquad \mathbf{R}_2^{\mathrm{f}}(\mathbf{d}_2^{\mathrm{s}}, \mathbf{v}_2^{\mathrm{f}}) = \mathbf{0}. \tag{4.164}$$

As before, the arising system of non-linear discrete algebraic equations is going to be solved in a fully monolithic manner. As iterative non-linear solution technique, a Newton-Raphson method is employed. This requires linearization of the residuals with respect to the primary unknowns, which is obtained from a truncated Taylor expansion:

$$\mathrm{Lin}\ \mathbf{R}_1^{\mathrm{s}}(\mathbf{d}_1^{\mathrm{s},i}, \mathbf{v}_1^{\mathrm{f},i}) = \mathbf{R}_1^{\mathrm{s}}(\mathbf{d}_1^{\mathrm{s},i}, \mathbf{v}_1^{\mathrm{f},i}) + \frac{\partial \mathbf{R}_1^{\mathrm{s}}(\mathbf{d}_1^{\mathrm{s}}, \mathbf{v}_1^{\mathrm{f}})}{\partial \mathbf{d}_1^{\mathrm{s}}}\bigg|^i \Delta\mathbf{d}_1^{\mathrm{s},i+1} + \frac{\partial \mathbf{R}_1^{\mathrm{s}}(\mathbf{d}_1^{\mathrm{s}}, \mathbf{v}_1^{\mathrm{f}})}{\partial \mathbf{v}_1^{\mathrm{f}}}\bigg|^i \Delta\mathbf{v}_1^{\mathrm{f},i+1} = \mathbf{0}, \tag{4.165}$$

$$\mathrm{Lin}\ \mathbf{R}_2^{\mathrm{f}}(\mathbf{d}_2^{\mathrm{s},i}, \mathbf{v}_2^{\mathrm{f},i}) = \mathbf{R}_2^{\mathrm{f}}(\mathbf{d}_2^{\mathrm{s},i}, \mathbf{v}_2^{\mathrm{f},i}) + \frac{\partial \mathbf{R}_2^{\mathrm{f}}(\mathbf{d}_2^{\mathrm{s}}, \mathbf{v}_2^{\mathrm{f}})}{\partial \mathbf{d}_2^{\mathrm{s}}}\bigg|^i \Delta\mathbf{d}_2^{\mathrm{s},i+1} + \frac{\partial \mathbf{R}_2^{\mathrm{f}}(\mathbf{d}_2^{\mathrm{s}}, \mathbf{v}_2^{\mathrm{f}})}{\partial \mathbf{v}_2^{\mathrm{f}}}\bigg|^i \Delta\mathbf{v}_2^{\mathrm{f},i+1} = \mathbf{0}. \tag{4.166}$$

In order to eliminate the auxiliary quantities $\Delta\mathbf{d}_2^{\mathrm{s},i+1}$ and $\Delta\mathbf{v}_1^{\mathrm{f},i+1}$ from the resulting system of equations, the nodal transfer operators $\mathbf{P}_{12}$ and $\mathbf{P}_{21}$ are employed:

$$\Delta\mathbf{d}_2^{\mathrm{s},i+1} = \mathbf{P}_{21}\Delta\mathbf{d}_1^{\mathrm{s},i+1} \qquad \text{and} \qquad \Delta\mathbf{v}_1^{\mathrm{f},i+1} = \mathbf{P}_{12}\Delta\mathbf{v}_2^{\mathrm{f},i+1}. \tag{4.167}$$

Hence, $\mathbf{P}_{12}$ is a projection of nodal values from mesh Ω_2 to mesh Ω_1 and $\mathbf{P}_{21}$ a projection from mesh Ω_1 to mesh Ω_2. Written in matrix form, the off-diagonal blocks of the resulting system of equations are multiplied with the projection operators:

$$\begin{pmatrix} \mathbf{S} & \mathbf{C}^{\mathrm{SF}} \cdot \mathbf{P}_{12} \\ \mathbf{C}^{\mathrm{FS}} \cdot \mathbf{P}_{21} & \mathbf{F} \end{pmatrix}^i_{n+1} \begin{pmatrix} \Delta\mathbf{d}_1^{\mathrm{s}} \\ \Delta\mathbf{v}_2^{\mathrm{f}} \end{pmatrix}^{i+1}_{n+1} = - \begin{pmatrix} \mathbf{R}^{\mathrm{s}} \\ \mathbf{R}^{\mathrm{f}} \end{pmatrix}^i_{n+1}. \tag{4.168}$$

Equations (4.165) and (4.166) have to be fulfilled at each Newton step. After convergence of the Newton scheme, the incremental solutions $\Delta\mathbf{d}_1^{\mathrm{s},i+1}$ and $\Delta\mathbf{v}_2^{\mathrm{f},i+1}$ are used to perform the updates

$$\mathbf{d}_1^{\mathrm{s},i+1} = \mathbf{d}_1^{\mathrm{s},i} + \Delta\mathbf{d}_1^{\mathrm{s},i+1}, \qquad \mathbf{v}_2^{\mathrm{f},i+1} = \mathbf{v}_2^{\mathrm{f},i} + \Delta\mathbf{v}_2^{\mathrm{f},i+1}, \tag{4.169}$$

and the auxiliary quantities are recovered from the primary unknowns employing equation (4.167). The procedure is repeated until a user-defined convergence criterion is fulfilled, as described in Section 4.3.4.

4.4. Numerical Examples

Five examples are presented to demonstrate the numerical properties of the realized computational approach for porous media problems. The first example in Section 4.4.1 is a known benchmark example. It is based on linear theory and very suitable to analyze the utilized stabilization of the porous system. The second example, comprises a simple one-dimensional setting with analytical solution. It is constructed, such that changing porosities occur. This way, the convergence behavior of the proposed numerical approaches can be evaluated in Section 4.4.2. Based on the same problem, the properties of the methodology for non-matching meshes is investigated. The third example in Section 4.4.3 is meant to validate the impermeability boundary conditions. The constraints are tested for dynamic example with curved, moving boundaries. The last two examples presented in Section 4.4.4 and 4.4.5 are three-dimensional problems. The capabilities of the approach are demonstrated for a problem with dynamic boundary conditions and applied to a simplified porous heart model. PSPG stabilization and the stabilization due to the reactive term presented in Section 4.3.3.5 are used within all numerical simulations.

4.4.1. Linear Benchmark: Terzaghi's Consolidation Problem

The first example is Terzaghi's consolidation problem. It was introduced by Karl von Terzaghi in [234]. Even though the problem is one-dimensional, it will be solved within a two-dimensional domain. It is an instructive example and a good test for the Biot stabilization. The results presented here are not new, but stated for the sake of completeness and comprehensiveness of the theory. Similar numerical analysis of Terzaghi's problem can for instance be found in [95, 246]. The setup comprises a porous block (height $2h$), in which deformation and flow are restricted to the vertical direction, see Figure 4.5. Plain strain conditions are assumed. The bottom of the porous block is fixed, while on the top a constant load $q = 1$ is applied. For the fluid, the upper and lower boundaries are considered drained, i.e. a constant pressure $p = 0$ is enforced. Inertia terms are neglected for both the skeleton and the fluid. However, the dynamically changing porosity (with initial value $\phi_0 = 0.2$) is considered via the instationary term in the balance of mass. Linear kinematics are used for this example. A likewise linear stress-strain relation (St.Venant-Kirchhoff law, see equation (2.40)) with a Young's modulus $E = 1.0 \cdot 10^6$ and a Poisson's ratio $\nu = 0.0$ determines the constitutive behavior of the skeleton. An incompressible microscopic solid phase is assumed, which leads to the Biot relation (3.93) with $b = 1.0$ and $1/N = 0.0$. The isotropic permeability is chosen as $k = 1.0 \cdot 10^{-6}$. Under those conditions, the exact solution for the pressure field can be derived [242] as

$$\frac{p}{p_0} = \frac{\pi}{4} \sum_{j=1}^{\infty} \frac{(-1)^{j-1}}{2j-1} \cos\left((2j-1)\left(\frac{\pi\,(h-z)}{2h}\right)\right) \exp\left(-(2j-1)\frac{\pi^2}{4}\frac{c_v t}{h^2}\right), \tag{4.170}$$

with the consolidation coefficient

$$c_v = \frac{kE}{(1.0+\phi)\mu^{\mathrm{f}}}. \tag{4.171}$$

See also Appendix A.3.1 for some explanations of this form of the exact solution. For discretization in space, 470 linear, 3-node elements (approximate element size $h = 0.1$) are used. The one-step-θ scheme with $\theta = 1.0$ and a time step $\Delta t = 1.0 \cdot 10^{-4}$ is applied. The analytical solu-

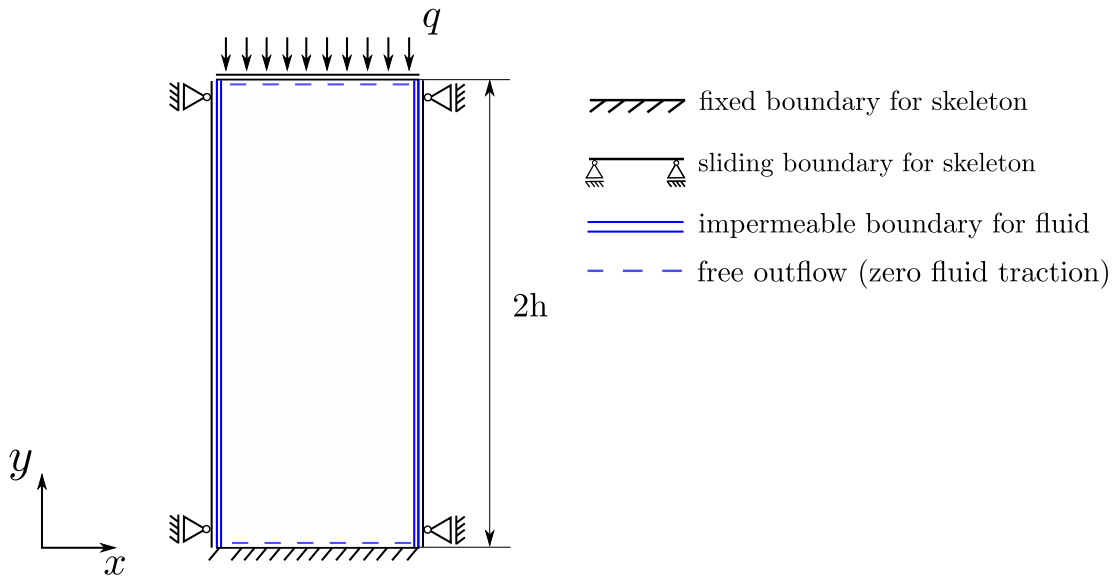

Figure 4.5: Terzaghi consolidation problem: Schematic of geometry and boundary conditions.

tion and the results of the simulation at different time instances without the Biot stabilization are depicted in Figure 4.6. It can be seen, that the sudden application of loading induces a pressure

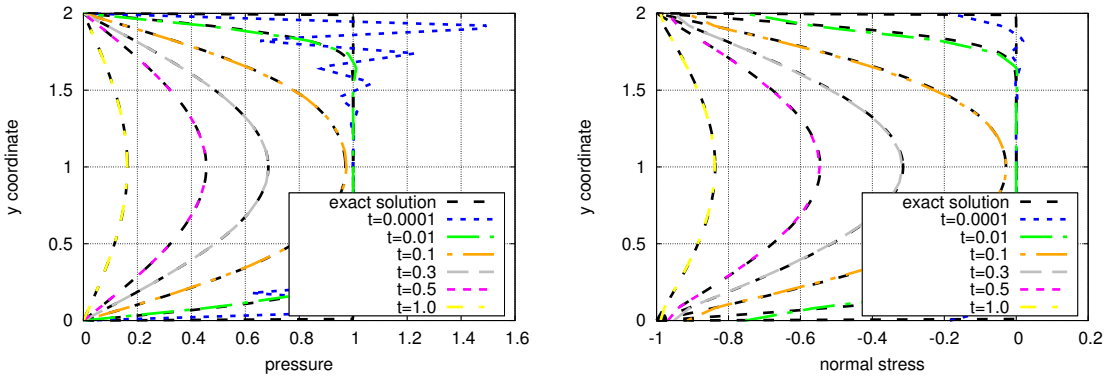

(a) pressure (b) normal skeleton stress

Figure 4.6: Terzaghi consolidation problem: Evolution of fluid pressure and skeleton stresses. Linear 3-node elements without Biot stabilization are used.

jump and unphysical oscillations in the numerical solution predominantly at early times (left Subfigure 4.6). At the beginning, the fluid carries the main part of the load. With time, the loading is redistributed to the skeleton, leading to completely drained conditions at zero pressure in the stationary state. The numerical complexity of the problem originates from the high pressure gradients. This is particularly critical at small values of the dimensionless time $c_v t/h^2$ and small time steps: The smaller the time step is chosen, the higher the pressure gradient, that needs to be resolved, becomes. The skeleton stresses, i.e. $\boldsymbol{\sigma} + p^{\mathrm{f}}\boldsymbol{I}$, exhibit similar oscillations at lower magnitude (right Subfigure 4.6). Note, that this example is particularly designed to amplify the

oscillations. For bigger time steps or moderate permeability, the problem is far less prone to instabilities. Further, it is worth mentioning, that at later times, the oscillations are almost completely annihilated and the numerical solution fits the exact solution very well.

Now, a way to diminish the oscillations is presented. The oscillations can be smoothed by a large enough Biot stabilization, as depicted in Figure 4.7. It significantly improves the initial

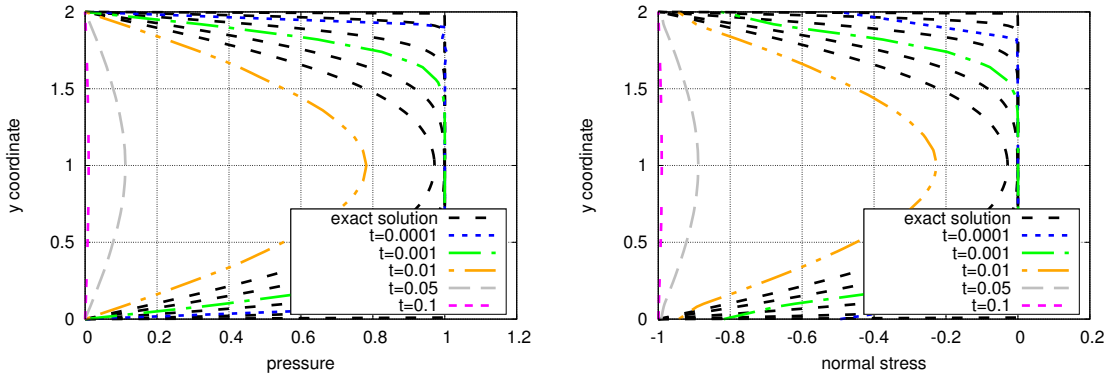

(a) pressure (b) normal skeleton stress

Figure 4.7: Terzaghi consolidation problem: Evolution of fluid pressure and skeleton stresses. Linear 3-node elements with Biot stabilization are used.

pressure and stress solution. However, the stabilization has major drawbacks for linear elements especially at later time instances. As the strong form of the residual is used, the stabilization is not consistent for linear interpolations. The stress divergence term $\boldsymbol{\nabla}_0 \cdot \boldsymbol{P}$ in equation (4.134) cannot be represented (the smoothing mainly stems from the penalization of pressure gradients). Due to this inconsistency, a high numerical damping is introduced into the system. Thus, the pressure and the stress tend much faster to a constant level than the exact solution predicts. Actually, the unstabilized form is far more accurate at later times here. Yet, there are some remedies for this problem. The most straightforward way is to simply use elements, which are more consistent. Of course, this might lead to an increase of computational costs. For quadratic elements, the stress divergence within the strong residual is not vanishing and better results can be obtained, see Figure 4.8. There are still some oscillations at early times, this time most evident in the skeleton stress solution. Note, however, that the stabilization parameter was probably not yet optimal, such that the results could be further improved. Due to the better consistency, also good results are achieved at later time instances. Another approach is the reconstruction of the stress divergence. Also for linear elements, information of the stress divergence can be obtained from the nodal displacements. For instance, a gradient field can be computed by solving a least squares problem, see [127, sec. 4.4.1]. Alternatively, other projection methods can be applied, which even have proven superconvergent characteristics. Results obtained with such a method taken from [269, sec. 15.4] are illustrated in Figure 4.9. Even though the oscillations are still visible and also the dissipative contribution of the stabilization terms can be seen at later times, there is a significant improvement compared to the results without recovery of the stress divergence, cf. Figure 4.7. Other ways to handle the pressure oscillations are even more fundamental. Mathematically, the problem lies in the violation of the inf-sup-condition for dis-

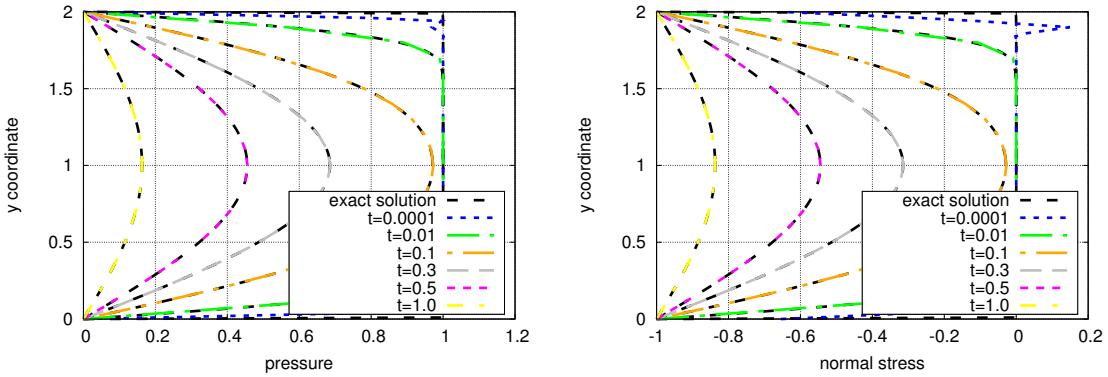

(a) pressure (b) normal skeleton stress

Figure 4.8: Terzaghi consolidation problem: Evolution of fluid pressure and skeleton stresses. Quadratic 9-node elements with Biot stabilization are used.

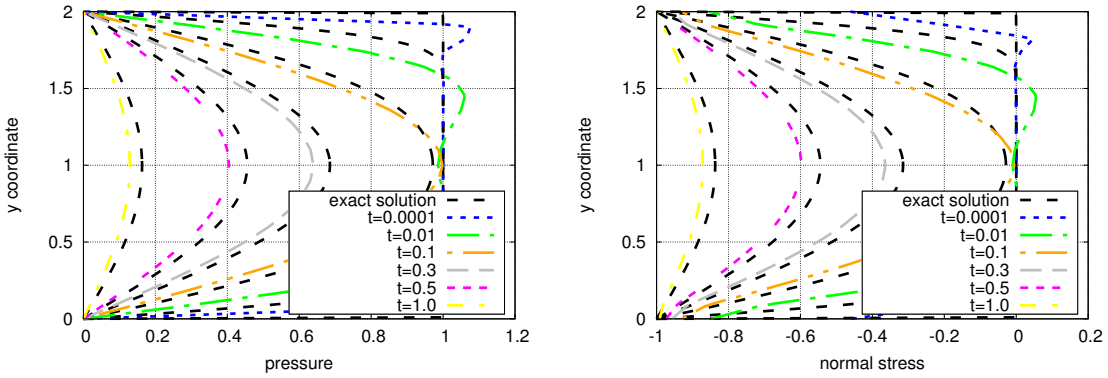

(a) pressure (b) normal skeleton stress

Figure 4.9: Terzaghi consolidation problem: Evolution of fluid pressure and skeleton stresses. Linear 3-node elements with Biot stabilization are used. The stress divergence was computed by a patch-wise recovery [269, sec. 15.4].

placement and pressure. Stabilization techniques as the Biot stabilization used here circumvent the inf-sup-condition. Clearly, another way is to fulfill it. Discontinuous Galerkin methods for porous media have been designed to have this ability [189]. Such methods are not considered in this thesis. Another way, which uses standard Lagrange finite elements, is to choose suitable function spaces to fulfill the inf-sub condition. The simplest example is a Taylor-Hood element for displacement and pressure, see [162] for a discussion. There, quadratic functions are used for the displacements and linear interpolation for the pressure. In this case, no Biot stabilization is necessary, but it implies some more complexity of the element formulation and additional computational costs. This is also not presented here.

4.4.2. Convergence Analysis of Darcy and Darcy-Brinkman Flow

The two following examples are convergence studies. They are meant for validation of the proposed solution approach and the implementation of the porous medium system. The first part analyses the behavior of Darcy and Darcy-Brinkman flow, specifically when significant porosity gradients occur. The second sub-section is dedicated to non-matching fluid and skeleton meshes.

4.4.2.1. Convergence Analysis of Darcy and Darcy-Brinkman Flow on Matching Meshes

This example was presented by the author in [244]. The goal is to analyze the behavior of the presented methodologies for changing porosities in Section 4.3.3. A one-dimensional domain

$$\Omega_0 = [-5, 5] \tag{4.172}$$

is considered. The whole problem is assumed to be stationary, i.e. all inertia terms are neglected. A simple, linear constitutive law for relating pressure, deformation, and porosity is used. It reads

$$p^{\mathrm{f}} = \kappa \left(\phi - \phi_0 - (1 - \phi_0)(J - 1) \right), \tag{4.173}$$

with the bulk modulus κ. The displacement field is prescribed to be

$$\hat{d}^{\mathrm{s}}(x) = 0.5 \cdot \left(1 + \cos\left(\frac{\pi}{5} x \right) \right), \tag{4.174}$$

depending on the spatial coordinate x. Note, that even though the solid deformation is prescribed, the porosity is still allowed to vary due to the pore pressure. The non-homogeneous displacement field (4.174) assures a likewise non-homogeneous porosity field. This implies that the porosity gradient is unequal to zero, which is important to show the differences between the approaches.

Due to the example setup and the assumptions given above, the governing equations simplify significantly. The Darcy equation (3.99) reduces to

$$\frac{\mathrm{d}p^{\mathrm{f}}(x)}{\mathrm{d}x} - \rho_0^{\mathrm{f}} b_{\mathrm{d}}(x) + \mu^{\mathrm{f}} k^{-1} \phi \, v^{\mathrm{f}}(x) = 0. \tag{4.175}$$

Analogously, the Darcy-Brinkman equation (3.100) becomes

$$\frac{\mathrm{d}p^{\mathrm{f}}(x)}{\mathrm{d}x} - \rho_0^{\mathrm{f}} b_{\mathrm{d-b}}(x) + \mu^{\mathrm{f}} k^{-1} \phi \, v^{\mathrm{f}}(x) + 2 \frac{\mu^{\mathrm{f}}}{\phi} \frac{\mathrm{d}}{\mathrm{d}x} \left(\phi \frac{\mathrm{d}v^{\mathrm{f}}(x)}{\mathrm{d}x} \right) = 0. \tag{4.176}$$

The spatial permeability k can be calculated from material permeability K_0 as

$$k(x) = J(x) \cdot K_0 = \frac{1}{1 - \frac{\mathrm{d}\, d(x)}{\mathrm{d}\, x}} \cdot K_0. \tag{4.177}$$

Finally, the continuity equation (3.111) in its one-dimensional form reads

$$\frac{\mathrm{d}\left(\phi(x) v^{\mathrm{f}}(x) \right)}{\mathrm{d}x} = 0. \tag{4.178}$$

For obtaining a simple analytical solution, different body force terms were constructed acting on the fluid for Darcy and Darcy-Brinkman flow. The following body force is applied in the Darcy case on the whole domain

$$b_{\mathrm{d}}(x) = 1 + 0.1\pi \sin\left(0.2\pi\, x\right) - 0.04\pi \cos\left(\frac{\pi}{5} x\right) + 0.01\pi^2 \cdot \frac{\cos\left(0.2\pi\, x\right)}{\left(1 + 0.1\pi\, \sin(0.2\pi\, x)\right)^2}, \quad (4.179)$$

and for Darcy-Brinkman flow

$$\begin{aligned} b_{\mathrm{d-b}}(x) \;=\; & 1 + 0.06\pi \sin\left(0.2\pi\, x\right) + 0.01\pi^2 \frac{\cos\left(0.2\pi\, x\right)}{\left(1 + 0.1\pi \sin\left(0.2\pi\, x\right)\right)^2} \\ & -0.02\pi^2 \frac{\left(0.0016\left(\sin\left(0.2\pi\, x\right)\right)^2 + 0.0056\cos\left(0.2\pi\, x\right) + 0.0016\left(\cos\left(0.2\pi\, x\right)\right)^2\right)}{\left(0.7 + 0.2\cos\left(0.2\pi\, x\right)\right)^3}. \end{aligned} \quad (4.180)$$

The material parameters are the initial porosity $\phi_0 = 0.5$, the bulk modulus $\kappa = 1$, the dynamic viscosity $\mu^{\mathrm{f}} = 0.01$ and the material permeability $K_0 = 0.01$.

Inserting the prescribed displacements (4.174), body forces (4.179) and (4.180) and the given material parameters into the strong form (4.175), (4.178) and (4.176), (4.178), respectively, it can be shown (see Appendix A.3.2 for some comments) that the analytical solution for the porosity, the pressure, and the fluid velocity is for Darcy flow given as

$$\bar{\phi}_{\mathrm{d}}(x) = 0.5 - 0.2\, \sin(0.2\pi\, x), \quad (4.181)$$

$$\bar{p}^{\mathrm{f}}_{\mathrm{d}}(x) = 0.5 - 0.2 \sin(0.2\pi\, x) - \frac{1}{2 + 0.2\pi \sin(0.2\pi\, x)}, \quad (4.182)$$

$$\bar{v}^{\mathrm{f}}_{\mathrm{d}}(x) = \frac{1}{0.5 - 0.2\, \sin(0.2\pi\, x)}, \quad (4.183)$$

and for Darcy-Brinkman flow as

$$\bar{\phi}_{\mathrm{d}-b}(x) = 0.7 + 0.2\, \cos(0.2\pi\, x), \quad (4.184)$$

$$\bar{p}^{\mathrm{f}}_{\mathrm{d-b}}(x) = 0.7 + 0.2 \cos(0.2\pi\, x) - \frac{1}{2 + 0.2\pi \sin(0.2\pi\, x)}, \quad (4.185)$$

$$\bar{v}^{\mathrm{f}}_{\mathrm{d-b}}(x) = \frac{1}{0.7 + 0.2\, \cos(0.2\pi\, x)}. \quad (4.186)$$

First, the convergence behavior of the solution for Darcy flow is analyzed. The 'standard' approach $(\boldsymbol{d}^{\mathrm{s}}, \boldsymbol{v}^{\mathrm{f}}, p^{\mathrm{f}})$, i.e. using solid displacements, fluid velocities and pressure as primary variables, discretized with linear and quadratic Lagrange elements is compared to quadratic NURBS elements, as well as to the mixed approach $(\boldsymbol{d}^{\mathrm{s}}, \phi, \boldsymbol{v}^{\mathrm{f}}, p^{\mathrm{f}})$. As already stated in Section 4.3.1 an important side aspect is the partial integration of the porosity gradient term in the continuity equation. This will also be demonstrated here.

The relative L_2-error norm of the solution variable, this is, $||v^{\mathrm{f}} - \bar{v}^{\mathrm{f}}||_2 / ||\bar{v}^{\mathrm{f}}||_2$ for the fluid velocity, for instance, is evaluated. In Figure 4.10, this error is plotted over the total number of degrees of freedom $\mathrm{n_{dof}}$ for all fields. Therein the results for first- and second-order FE approaches are

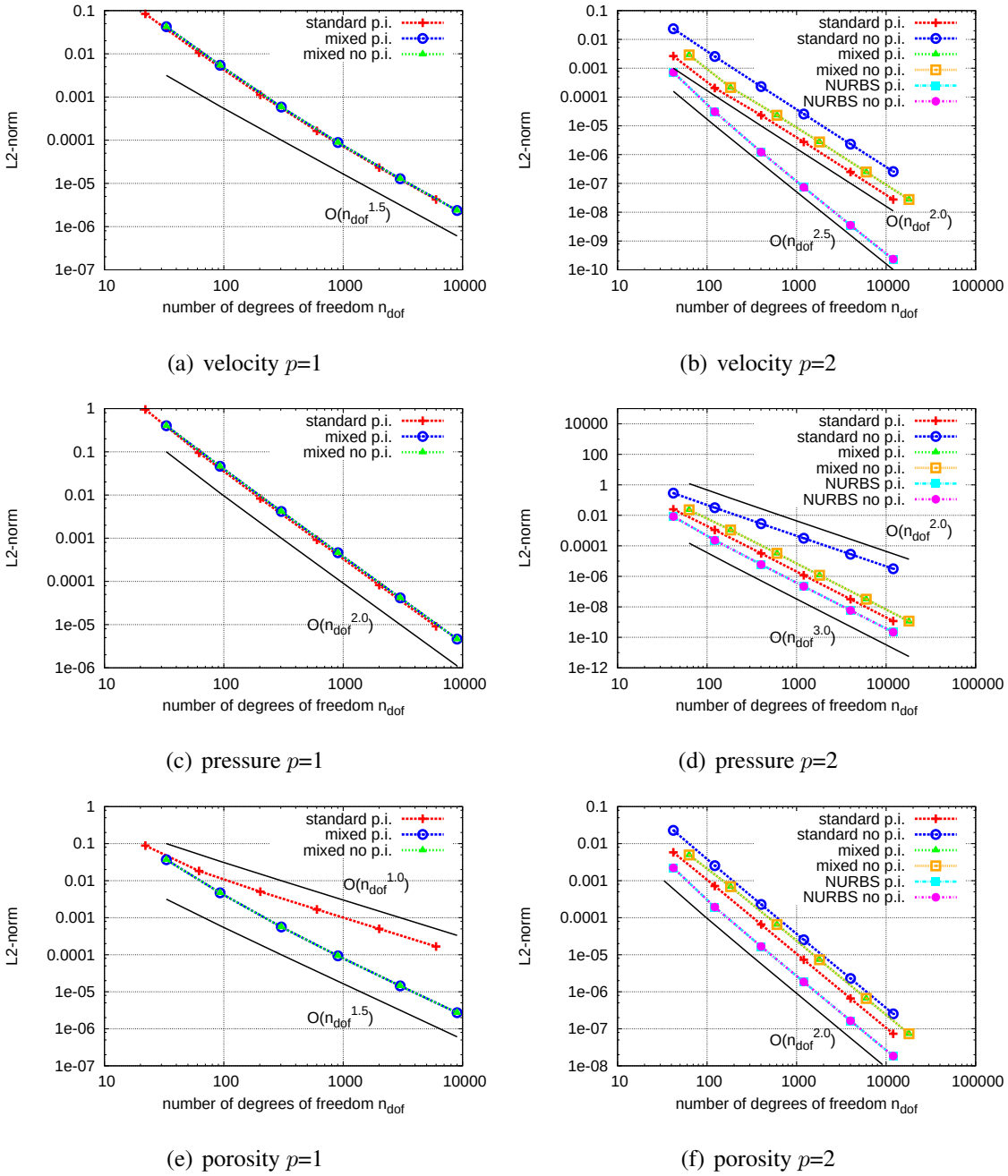

(a) velocity p=1

(b) velocity p=2

(c) pressure p=1

(d) pressure p=2

(e) porosity p=1

(f) porosity p=2

Figure 4.10: Darcy flow: Convergence of relative L_2-error norm for different approaches with shape functions of order p. 'p.i.' indicates partial integration of porosity gradient term in continuity equation, taken from [244].

given. The approaches with first-order shape functions (left column in Figure 4.10), exhibit convergence for all three variants and all solution variables. The convergence rate for the L_2-error of the velocity is approximately of order $O(\mathrm{n}_{\mathrm{dof}}^{1.5})$. The pressure converges with order $O(\mathrm{n}_{\mathrm{dof}}^{2})$. A difference in terms of convergence order can be observed in the porosity. It converges with order $O(\mathrm{n}_{\mathrm{dof}}^{1.5})$ for the mixed approaches and of order $O(\mathrm{n}_{\mathrm{dof}}^{1})$ for the standard approach with

partial integration of the porosity gradient term in the continuity equation. If the porosity gradient is not partially integrated in the standard approach, the Newton scheme does not converge, and therefore no results are obtained for linear elements. This is due to the incompleteness of the approach: for linear elements the second derivatives vanish, which leads to a zero porosity gradient in case of the standard approach.

Further results obtained by using quadratic shape functions are depicted in the right column in Figure 4.10. NURBS-based elements are also applied there. For those, open knot vectors are used, where all knots are equally spaced, apart from the first and last three. All approaches are complete and even the standard approach without partial integration of the porosity gradient converges. However, the latter is theoretically not guaranteed in general. Concerning the velocity field, all approaches converge, see Figure 4.10(b). The NURBS-based approach seems to behave super convergent with order $O(\mathrm{n}_{\mathrm{dof}}^{2.5})$. For all other approaches, the velocity converges with order $O(\mathrm{n}_{\mathrm{dof}}^{2})$. The error of the pressure solution for quadratic elements is depicted in Figure 4.10(d). There, the dominant convergence order is $O(\mathrm{n}_{\mathrm{dof}}^{3})$. Only, the standard approach without partial integration shows slower convergence of order $O(\mathrm{n}_{\mathrm{dof}}^{2})$. Regarding the porosity field, all approaches approximate the exact solution with order $O(\mathrm{n}_{\mathrm{dof}}^{2})$, see Figure 4.10(f).

Also for Darcy-Brinkman flow, studies for linear and quadratic elements were performed, see Figure 4.11. Concerning the linear interpolation in the left column of Figure 4.11, the standard approach does not converge, as expected due its incompleteness and insufficient continuity. The mixed approach reaches the solution for both with and without partial integration of the porosity gradient. The velocity converges with an order of approximately $O(\mathrm{n}_{\mathrm{dof}}^{1.2})$, the pressure and the porosity with an order of $O(\mathrm{n}_{\mathrm{dof}}^{1.25})$.

For quadratic shape functions, see the right column of Figure 4.11, the velocity converges with approximate order of $O(\mathrm{n}_{\mathrm{dof}}^{2})$, the pressure with an order of $O(\mathrm{n}_{\mathrm{dof}}^{2.5})$ and the porosity with an order of $O(\mathrm{n}_{\mathrm{dof}}^{2})$. All approaches behave similarly, even the standard approach, which is still incompatible, but seems to converge for quadratic shape functions, although the convergence order deteriorates for increasing number of degrees of freedom. Also, partial integration of the continuity equation does not significantly alter the results for quadratic elements for all depicted approaches. Furthermore, quadratic NURBS show smaller error norms compared to all other elements presented with comparable number of degrees of freedom.

In conclusion, the results confirm, that for Darcy flow all approaches converge in general, including the standard approach, if the flux term in the continuity equation is partially integrated. In case of Darcy-Brinkman flow, solely the mixed approach is applicable for first-order interpolations, while the standard approach requires the shape functions to be at least of second order. NURBS elements are more accurate than any other element with the same number of degrees of freedom, as was also observed in [132] in a different example. However one has to note that the solver costs per degree of freedom are usually higher for NURBS based elements because of the larger stencil. It should be noted, that for this particular case of a coupled problem no theoretical convergence rates are known to the author, as the approaches and the example are particularly designed for a varying porosity field. For convergence studies concerning Darcy flow with constant porosity, the interested reader is referred to [17, 166, 177]. Therein, similar convergence rates for fluid velocities and pressures are observed.

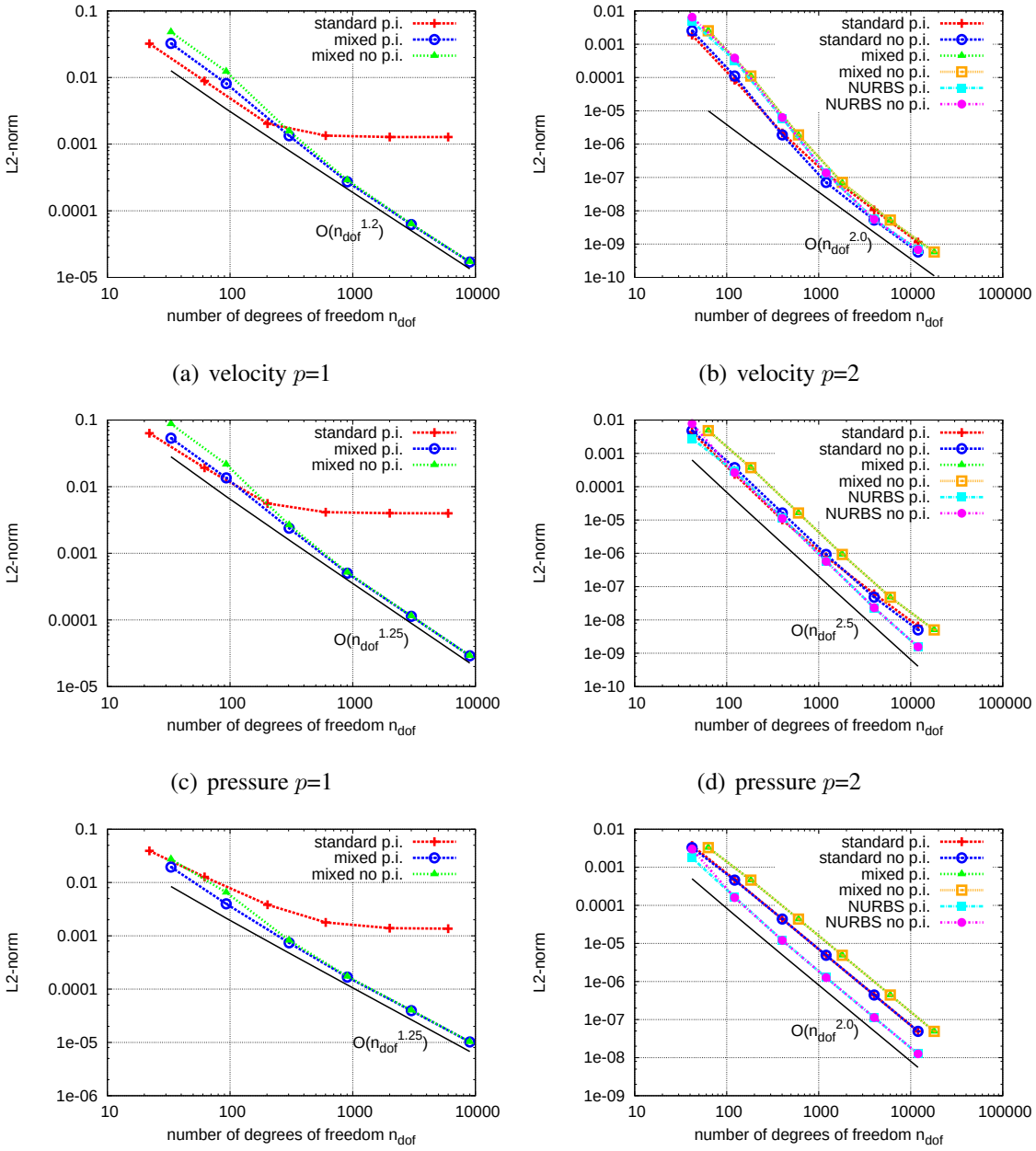

(a) velocity p=1

(b) velocity p=2

(c) pressure p=1

(d) pressure p=2

(e) porosity p=1

(f) porosity p=2

Figure 4.11: Darcy-Brinkman flow: Convergence of relative L_2-error norm for different approaches with shape functions of order p. 'p.i.' indicates partial integration of porosity gradient term in continuity equation

4.4.2.2. Convergence Analysis of Darcy Flow on Non-Matching Meshes

The same setting as in the previous section is analyzed. This time the focus is on non-matching discretizations using the mixed approach. The example is used to examine the convergence behavior of the mortar-based and the collocation approach given in Section 4.3.4.3. The results

were already presented in more detail in [91]. One-dimensional Darcy flow (4.175) is considered. The problem setting is completed by the computational domain given in equation (4.172), the constitutive law for the porosity (4.173), the prescribed displacements (4.174), the variable permeability (4.177), the continuity equation (4.178) and the body forces (4.179). The material parameters are as stated in Section 4.4.2.1. The analytical solution is given in equations (4.181)–(4.183).

Different meshes for discretizing the porosity and for discretizing fluid velocity and pressure, respectively, are used. Even though the problem is actually a one-dimensional problem, the equations are solved on a two-dimensional domain. Two meshes with a ratio of 1:1.5 between the fine and the coarse discretization are depicted exemplary in Figure 4.12. Bi-linear 4-node elements are used for all primary fields.

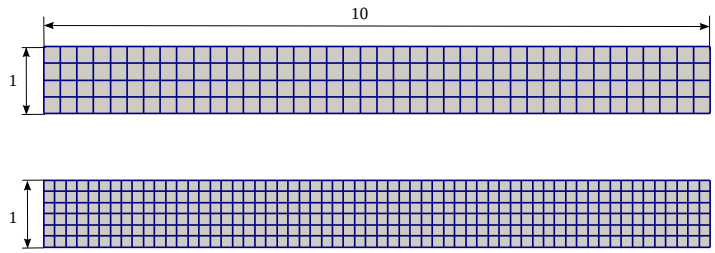

Figure 4.12: Example of two meshes with ratio 1:1.5, taken from [91].

The convergence of the fluid velocity is analyzed in the following. The mortar-based and the collocation approach are compared, while the matching grid solution obtained before serves as a reference. First, the non-matching case with a constant mesh ratio of 1:1.5 of the two meshes is considered. In left Subfigure 4.13 the results are depicted. For each approach, two settings are presented: in one setting, the fluid is solved on the finer mesh and the porosity on the coarser mesh and in the other setting vice versa. From that, it can be deduced, that similar convergence behavior is obtained, if the fluid mesh is chosen as the finer discretization. However, when the smaller elements are used for approximating the porosity, the convergence deteriorates for both the mortar-based and the collocation method. Thus, one can conclude that the porosity solution strongly affects the quality of the velocity field. The convergence of the fluid is restricted by the porosity error on the coarser mesh. On the other hand, a more accurate porosity solution does not affect the convergence of the velocity, such that both approaches converge as good as in the matching case.

Further, the mesh ratio is varied in the right Subfigure 4.13. The setting with the finer fluid mesh is used, as the difference to the matching case is more evident there. Both approaches behave similarly and approach the reference solution for mesh ratios close to 1. In general, it can be seen, that the more different the meshes, the worse the convergence, regarding the error value as well as the convergence order. Still, it is noteworthy, that the mortar approach shows smaller absolute errors than the collocation approach in this example. In the case of a mesh ratio of $1 : 4$ both approaches lead to the same result. As pointed out in [91], in this case, the projection matrices are the same and there is no difference between the two methods due to the

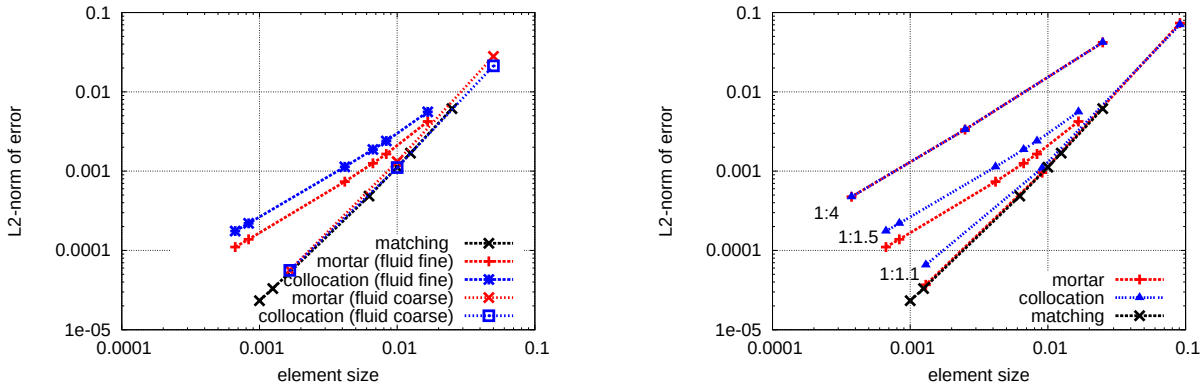

Figure 4.13: Convergence study, taken from [91]. Error norm of the velocity over mesh size of fluid field. Comparison of mortar and collocation method. Left: The mesh ratio is fixed to 1:1.5. Results for fluid unknown on the coarser and finer mesh, respectively. Right: Study for different mesh ratios. The fluid field is solved on a finer mesh than the porosity.

fact that a nested mesh is obtained. This means that the finer mesh is able to exactly represent solutions based on the coarser mesh [91].

In conclusion, this example implies, that, even though techniques for different meshes seem attractive, they are less beneficial for strongly coupled problems like poroelasticity. As the solution quality of the two fields have a great influence on each other, the resolutions of the primary variables can hardly be decoupled. It is expected, that this interdependence is even more evident for larger, more complex settings. Still, the volume coupling approach could be advantageous for porous systems, where a high local resolution for one field is necessary and known a priori, like in case of stress peaks or fluid boundary layers. Clearly, in a more general sense, it can be very well applied to loosely or even one-way coupled multi-physics, or regarding different degrees of interpolation functions, as explained in [91].

4.4.3. Validation of Boundary Conditions

This example shows flow through a deformable porous arc and is mainly meant for validation of the impermeability conditions presented in Section 4.3.4.2. It was presented by the author in [244]. Both Darcy and Darcy-Brinkman flow will be analyzed. The geometry of the arc and the boundary conditions are sketched in Figure 4.14. The inner radius is chosen as $r_\mathrm{i} = 0.7$ and the outer radius as $r_\mathrm{o} = 1.0$. The porous structure is fixed at the inner curved boundary. At the inlet and outlet, the solid is allowed to slide in radial direction. At the inlet boundary, a time varying pressure

$$\hat{p}_i^\mathrm{f}(t) = \begin{cases} 40 \cdot (1.0 - \cos(0.4\pi \cdot t)) & \text{for } t < 2.5, \\ 1 & \text{else,} \end{cases} \tag{4.187}$$

is prescribed, whereas at the outlet boundary a zero-traction boundary condition is applied on the fluid. Also, the fluid is prevented from exiting the arc at the curved boundaries, i.e. a no-penetration constraint in case of Darcy flow and a no-slip constraint in case of Darcy-Brinkman

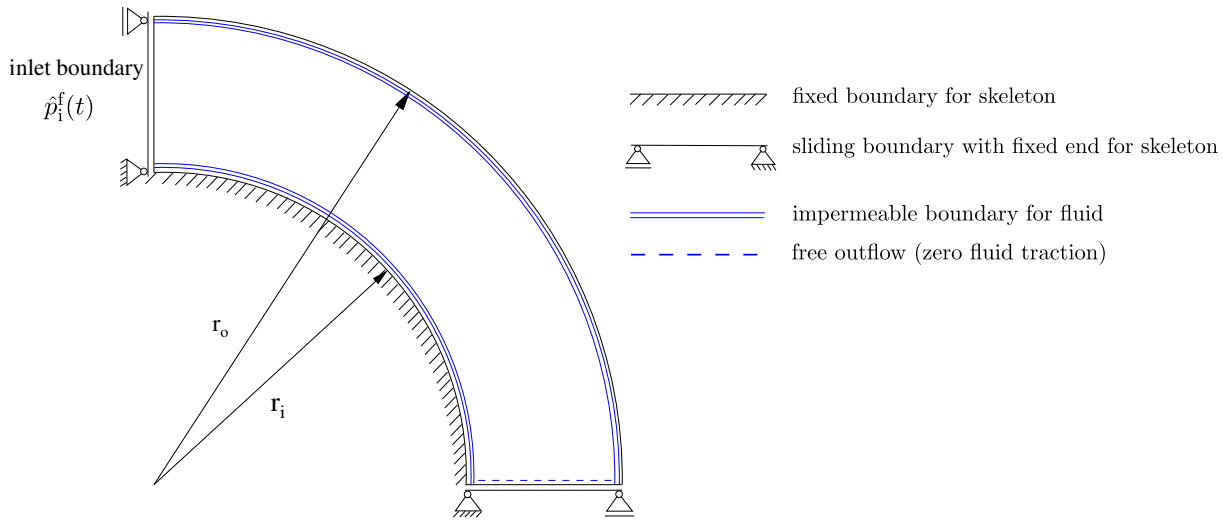

Figure 4.14: Two-dimensional arc: Schematic of geometry and boundary conditions, adapted from [244].

flow is enforced at these boundaries. The density of the solid is $\rho^{\mathrm{s}} = 0.01$, the fluid density $\rho^{\mathrm{f}} = 1.0$ and the fluid viscosity $\mu^{\mathrm{f}} = 0.01$. The initial porosity is set to $\phi_0 = 0.8$ over the whole domain and the material permeability is assumed to be isotropic and constant $K_0 = 0.01$. Assuming a plain-strain state, the Neo-Hookean material model (2.43) is used for the solid skeleton. The Poisson's ratio ν is set to 0.3, the Young's modulus E is 2500. The volumetric part given in equation (3.83) is added to the total strain energy, where the bulk modulus of the skeleton κ is set to 50. As the porous structure will just inflate, no penalty contribution is necessary. Hence, the constitutive relation for the pore pressure reads

$$p^{\mathrm{f}} = \kappa \left(-\frac{1}{1-\phi_0} + \frac{1}{J^{\mathrm{s}}} \right) . \tag{4.188}$$

For time discretization, a backward Euler scheme ($\theta = 1.0$) is applied and a time step $\Delta t = 0.01$ with a total simulation time $t \in [0.0, \ldots, 6.0]$ is used. Different mesh sizes are analyzed, keeping the ratio between the number of elements in circumferential to radial direction constant at 2.5 to 1. Convergence of the non-linear solver is assumed, if all L_2-norms of the residuals and the increments of all primary fields are less than $\epsilon = 1.0 \cdot 10^{-8}$. For Darcy flow quadrilateral elements with bi-linear and bi-quadratic shape functions are used, respectively. The standard approach is utilized for Darcian type of flow, as it was shown in Section 4.3.1 and illustrated in example 4.4.2.1 that it suffices for this setting. For Darcy-Brinkman flow, the mixed approach and the NURBS-based approach are compared.

The porosity field on the undeformed geometry and the pressure field on the deformed geometry for Darcy flow are exemplarily depicted in Figure 4.15. The inflation of the porous structure and significant porosity gradients are visible there. The global solution for pressure and porosity for Darcy-Brinkman flow look similar and will thus not be depicted here. In Figure 4.16 typical flow profiles in this example for Darcy and Darcy-Brinkman flow along the radial axis are depicted. For Darcy flow, the evolution of the velocity in radial direction is nearly linear. The

velocity is higher at the inner boundary, because the pressure gradient driving the flow is higher there than at the outer boundary. As it is common for viscous flow in such settings, the Darcy-Brinkman flow profile exhibits parabolic-like shape. Also, lower velocity magnitudes compared to Darcy flow can be observed, due to the extra resistance induced by the Brinkman term.

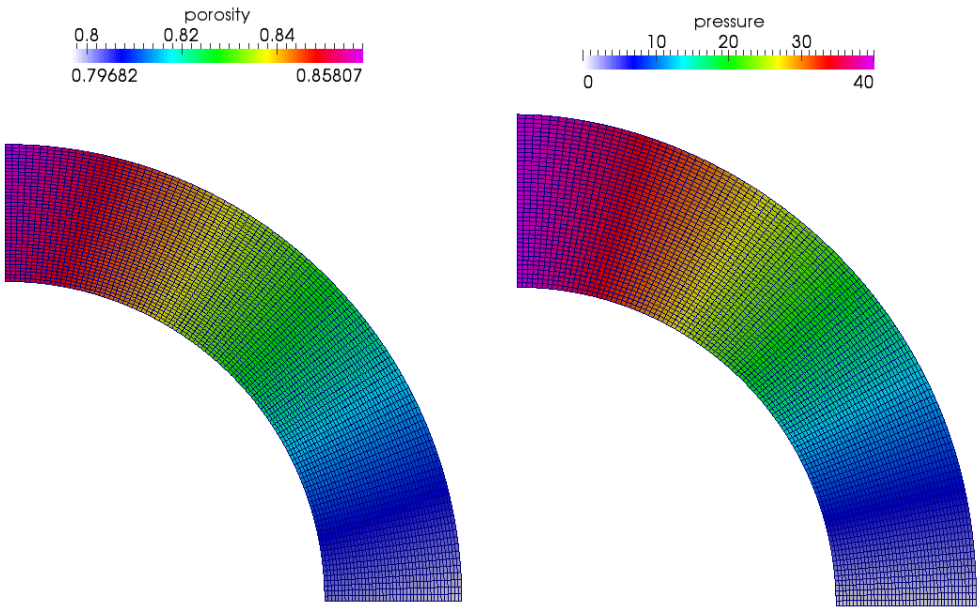

(a) porosity distribution at $t = 6$ on undeformed geometry

(b) pressure distribution at $t = 6$ on deformed geometry

Figure 4.15: Two-dimensional arc: Global solution of porosity and pressure for Darcy flow, taken from [244].

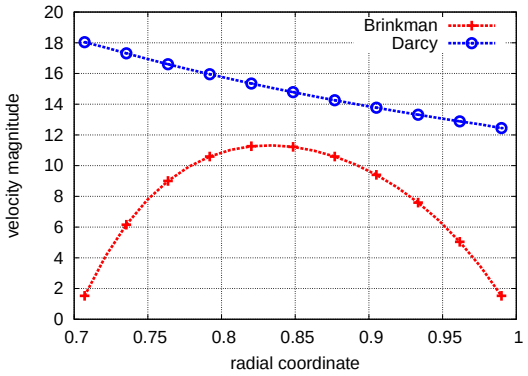

Figure 4.16: Two-dimensional arc: exemplary velocity profiles for Darcy and Darcy-Brinkman flow over the radial coordinate at the middle of the arc at $t = 2.5$, taken from [244].

For validation of the global solution the flow rate across the inlet and outlet is calculated, i.e. $\int (\boldsymbol{v}^{\mathrm{f}} - \boldsymbol{v}^{\mathrm{s}}) \cdot \boldsymbol{n} \, \mathrm{d}\Gamma^{\mathrm{in}} + \int (\boldsymbol{v}^{\mathrm{f}} - \boldsymbol{v}^{\mathrm{s}}) \cdot \boldsymbol{n} \, \mathrm{d}\Gamma^{\mathrm{out}}$, and compared to the change of total fluid mass inside the domain, i.e. $\left(M^{\mathrm{f}}_{n+1} - M^{\mathrm{f}}_{n}\right) / \Delta t$, with $M^{\mathrm{f}} = \int \rho^{\mathrm{f}} \phi \, \mathrm{d}\Omega_t$. Mass conservation dictates,

that these two rates should cancel out (see Figure 4.17(a)). For validation of the no-penetration constraint for Darcy flow, the flux over the constraint boundaries is determined, i.e. $\int (\boldsymbol{v}^{\mathrm{f}} - \boldsymbol{v}^{\mathrm{s}}) \cdot \boldsymbol{n} \, \mathrm{d}\Gamma_t^{\mathrm{c}}$ is evaluated. The results are shown in Figure 4.17(b) for a coarse mesh (5 elements in circumferential direction, 2 elements in radial) and a finer mesh (500 elements in circumferential direction, 200 elements in radial). The flow over the constraint boundary is always around 10^{-10}, showing the fulfillment of the desired constraint.

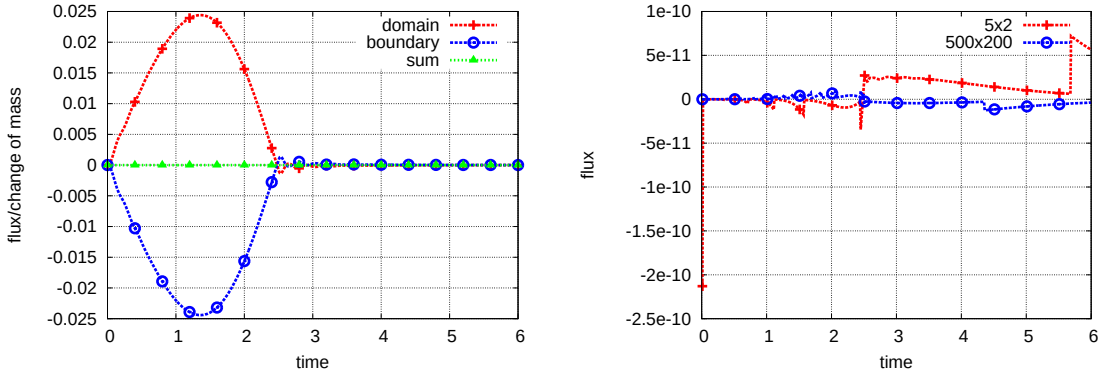

(a) mass balance for coarsest mesh (5×2).

(b) flow over constrained boundaries for coarsest and finest mesh

Figure 4.17: Two-dimensional arc: validation of no-penetration constraint for Darcy flow, taken from [244]. The change of total fluid mass inside the domain $\left(M_{n+1}^{\mathrm{f}} - M_n^{\mathrm{f}}\right)/\Delta t$ is denoted by 'domain', 'boundary' denotes the flow rate across the inlet and outlet $\int (\boldsymbol{v}^{\mathrm{f}} - \boldsymbol{v}^{\mathrm{s}}) \cdot \boldsymbol{n} \, \mathrm{d}\Gamma^{\mathrm{in}} + \int (\boldsymbol{v}^{\mathrm{f}} - \boldsymbol{v}^{\mathrm{s}}) \cdot \boldsymbol{n} \, \mathrm{d}\Gamma^{\mathrm{out}}$, 'sum' is the sum of the two.

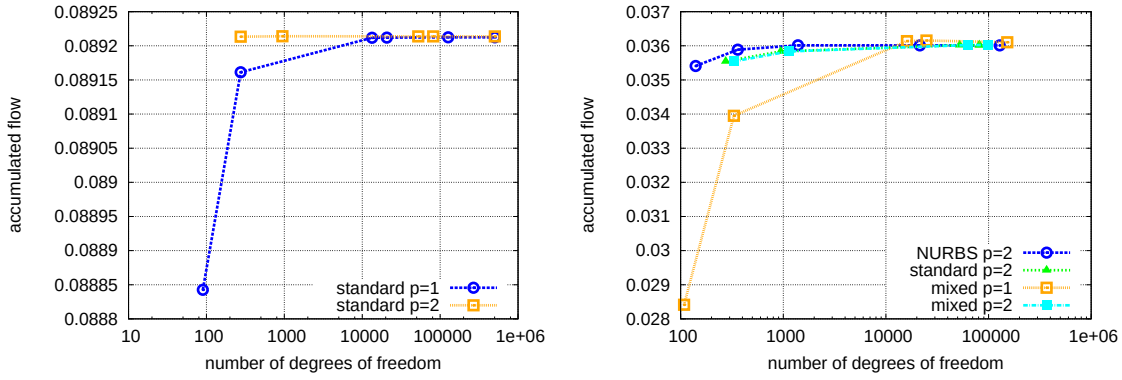

(a) Darcy flow

(b) Darcy-Brinkman flow

Figure 4.18: Two-dimensional arc: Accumulated flow over time for Darcy and Darcy-Brinkman flow for different approaches of order p, taken from [244].

In a mesh refinement study, the accumulated flow over time crossing the outlet, i.e. the expression $\int \int (\boldsymbol{v}^{\mathrm{f}} - \boldsymbol{v}^{\mathrm{s}}) \cdot \boldsymbol{n} \, \mathrm{d}\Gamma^{\mathrm{out}} \, \mathrm{d}t$, is compared for different meshes. The results are depicted in Figure 4.18. Typical convergence behavior can be observed there. All approaches converge to the same value of accumulated flow, for the Darcy and the Darcy-Brinkman case. As expected, the

second-order elements reach the converged value much faster than first-order elements. There are slight, rather insignificant differences in the behavior of mixed and NURBS-based approach.

4.4.4. Pressure Wave through Porous Cylinder

This is a fully coupled, instationary problem in order to demonstrate the capability of the approach to handle dynamic three-dimensional problems, also taken from [244]. It is solved using the mixed and the NURBS-based approach. Darcy-Brinkman flow through a quarter of a hollow cylinder is considered. The inner radius is 0.3, the outer radius is 0.5 and the length of the cylinder is 3 (see Figure 4.19(a)). Both curved boundary surfaces are modeled as impermeable while symmetry conditions are employed on the remaining two boundaries, mimicking a complete hollow cylinder. A high pressure

$$\hat{p}^{\mathrm{f}}(t) = \begin{cases} 5.0 \cdot 10^5 & \text{for } 0.0 \leq t \leq 0.001, \\ 5.0 \cdot 10^5 \cdot (-\frac{0.25}{0.003} t + \frac{13}{12}) & \text{for } 0.001 < t \leq 0.004, \\ 0.75 \cdot 5.0 \cdot 10^5 & \text{else}, \end{cases} \tag{4.189}$$

on the left base surface and a zero traction on the right base surface are applied on the fluid, inducing flow along the cylinder axis. As boundary conditions for the structural side, the inner curved boundary is fixed, while the outer boundary is allowed to move freely under zero traction. Both base surfaces are fixed and the other two boundaries are constrained to move in radial direction only. The material is modeled with the split of the strain energy function from equation (3.82). The macroscopic strain energy function of the skeleton a Saint-Venant-Kirchhoff law (2.39). The volumetric contribution to the strain energy W^{vol}, determining the resistance of the skeleton to pore pressure, is chosen as given in equation (3.83) and the penalty term from equation (3.84). The initial porosity is $\phi_0 = 0.8$, the Young's modulus is $E = 1.0 \cdot 10^6$, the Poisson's ratio $\nu = 0.3$, the bulk modulus $\kappa = 1.0 \cdot 10^6$, the penalty parameter $\eta = 0.01$ and the skeleton density $\rho^{\mathrm{s}} = 1.2$. On the fluid side, the density is $\rho^{\mathrm{f}} = 1.0$, the dynamic viscosity is $\mu^{\mathrm{f}} = 0.03$, the material permeability $K_0 = 1.0 \cdot 10^{-5}$ and Darcy-Brinkman flow is assumed. For discretization tri-linear hexahedral elements for the mixed approach and quadratic functions for the NURBS-based elements are used. For the mixed approach 10 elements in circumferential and radial direction and 30 elements along the axis are utilized. For the NURBS-based approach, the discretization was build similarly in order to result in approximately the same number of degrees of freedom (see Figure 4.19(a)). For time discretization a one-step-θ scheme with $\theta = 0.66$ and a time step $\Delta t = 5 \cdot 10^{-5}$ is applied.

In Figure 4.19, a deformed state is depicted next to the initial geometry. The quick rise in pressure causes the porous structure to inflate next to the inlet, inducing a flow mainly in axial direction. In time, the pressure propagates along the cylinder. This produces according displacements and porosity gradients. In Figure 4.20 the distribution of displacements in radial direction, pressure, porosity, and convective velocity along the cylinder axis at different simulation times are depicted. As both the NURBS based and the mixed approach produce very similar results, only the solutions of the mixed approach are presented in these graphs for the sake of clarity. In terms of performance of the Newton scheme to reach convergence, in this example and for the present implementation, the NURBS based approach required little less iterations compared to the mixed approach (about 7 iterations compared to 9 iterations on average per time step). The

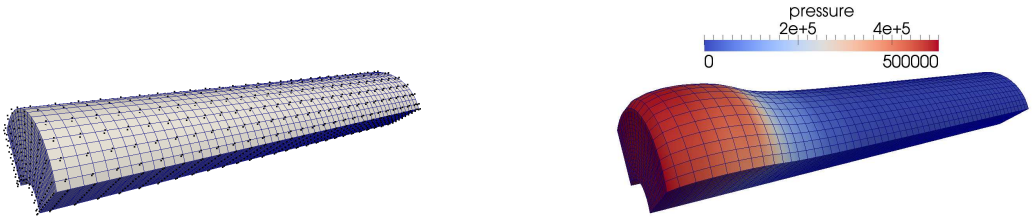

(a) undeformed geometry and mesh (black dots denote control points)

(b) pressure distribution on deformed geometry at $t = 0.00055$

Figure 4.19: Pressure wave through porous cylinder: Initial geometry and pressure field, taken from [244].

convergence tolerances where chosen to be 10^{-8} for the L_2-norm of each field residual and 10^{-6} for all increments of each primary solution variable.

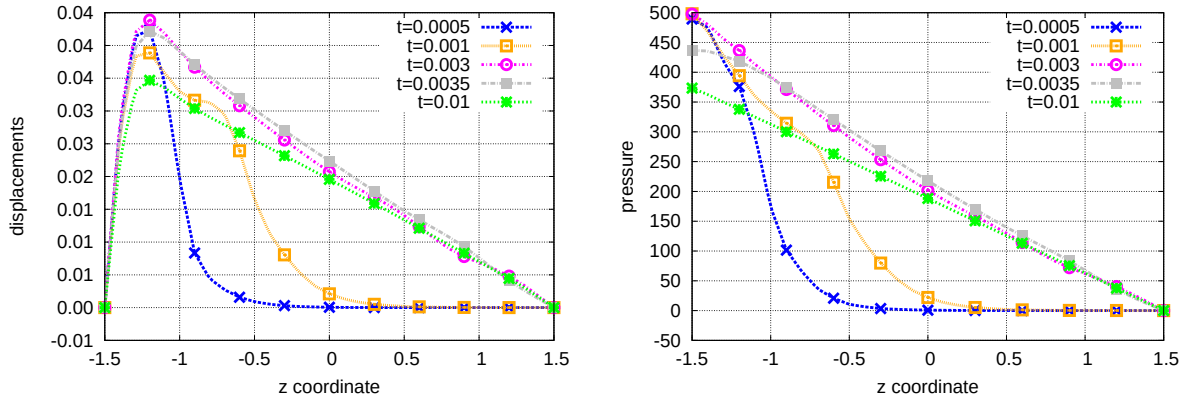

(a) displacement in radial direction

(b) pressure

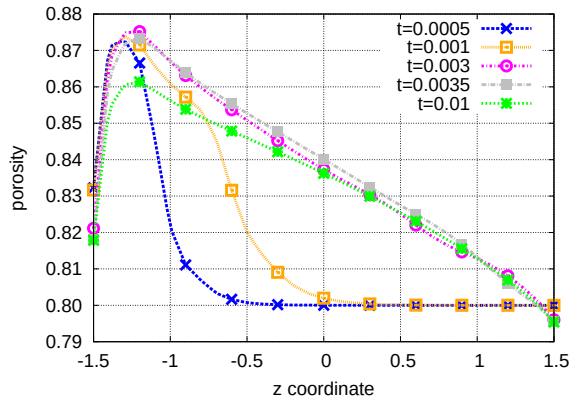

(c) porosity

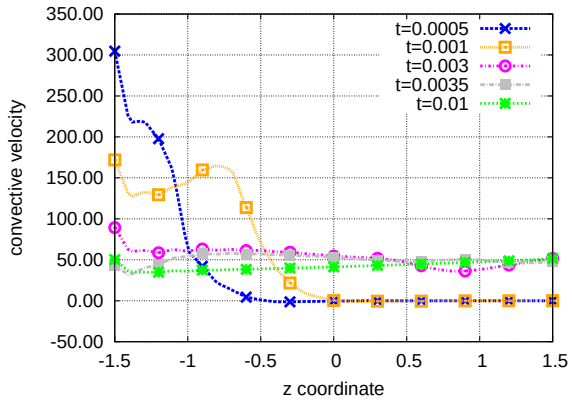

(d) convective velocity in axial direction

Figure 4.20: Pressure wave through porous cylinder: Solution along cylinder axis at $r = 0.3$ and different simulation times, taken from [244].

4.4.5. Contraction of a Porous Heart

The last example considers the contraction of a model of a human heart. One needs to point out that this example is intended to demonstrate the capability of the proposed methodology to simulate examples with more complex geometries and material models and should give an idea of further applications. It is not meant to obtain physiological results, which will be subject of future work. Still, the parameters are chosen to be in a realistic range, if known.

The geometry and most of the general example setting, most importantly the fiber orientation and the active and passive material models for the solid phase, are based on [31, 123] and the references therein. The parameters for the porous fluid are taken from [55]. The skeleton is modeled as a fiber-reinforced material. The fiber orientations were reconstructed from patient-specific diffusion tensor magnetic resonance imaging [31]. The initial geometry and the fiber orientations are depicted in Figure 4.21. The solid part has a density of $\rho^{\mathrm{s}} = 1.0 \cdot 10^{-6}\,\mathrm{kg}/\,\mathrm{mm}^3$

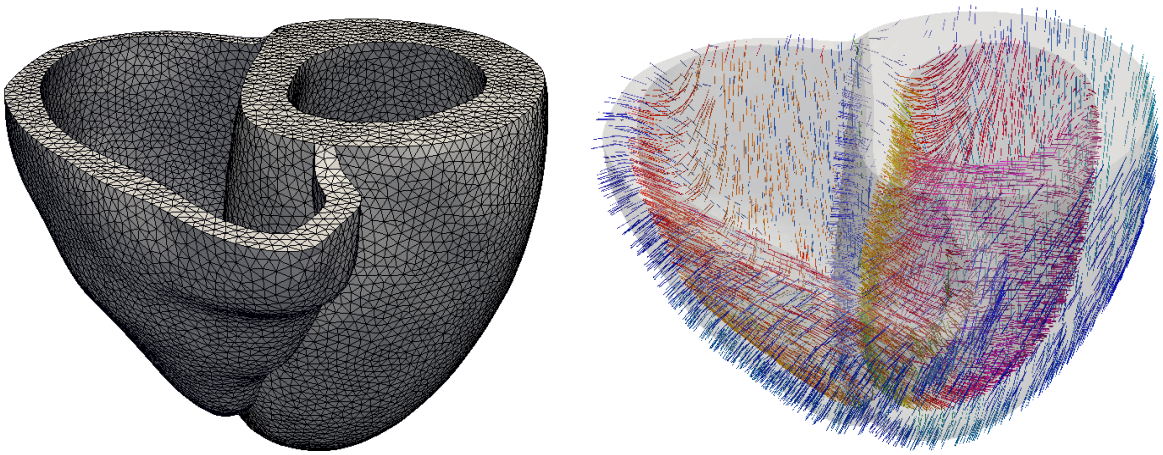

Figure 4.21: Porous heart. Left: Geometry and mesh. Right: Fiber orientations.

and its strain energy function is composed of four additive parts. Three summands determine the passive material behavior and one part gives the active stress contribution. The passive part comprises an isochoric Mooney-Rivlin material (see e.g. [120])

$$\Psi_{\mathrm{MR}} = c_1(\overline{I}_1 - 3) + c_2(\overline{I}_2 - 3), \tag{4.190}$$

an isochoric coupled viscous material based on the pseudo-potential

$$\Psi_{\mathrm{visc}} = \frac{\eta_{\mathrm{v}}}{2}\mathrm{tr}(\dot{\boldsymbol{E}}^2) = \frac{\eta_{\mathrm{v}}}{8}\mathrm{tr}(\dot{\boldsymbol{C}}^2), \tag{4.191}$$

and a penalty contribution

$$\Psi_{\mathrm{pen}} = \epsilon\left(J^{\gamma} + \frac{1}{J^{\gamma}} - 2\right) \tag{4.192}$$

inhibiting volume changes. Therein, $\overline{I}_1$ and $\overline{I}_2$ denote the first and second invariant of the isochoric right Cauchy-Green tensor (which is obtained form an isochoric-volumetric split of the deformation gradient, see e.g. [120]). The active stress is controlled by the activation signal $u(t)$

within the following strain energy contribution

$$\Psi_{\text{active}} = \sigma_{\text{a}}(t)\,(I_4 - 1)\,, \tag{4.193}$$

with the forth pseudo invariant I_4 of the right Cauchy–Green tensor, further depending on the fiber direction [121]. The material parameters in this example are chosen as follows: $c_1 = 4000\ \text{kPa}$, $c_2 = 0.0\ \text{kPa}$, $\eta_{\text{v}} = 0.035\ \text{kPa s}$, $\epsilon = 1.0 \cdot 10^4\ \text{kPa}$, and $\gamma = 1$. The active stress contribution $\sigma_{\text{a}}(t)$ in fiber direction is calculated by solving the following ordinary differential equation

$$\dot{\sigma}_{\text{a}}(t) = |u(t)|\sigma_{\text{a}}(t) + \sigma_0|u(t)|_+, \tag{4.194}$$

with the contractility $\sigma_0 = 400\ \text{kPa}$ and the activation signal

$$\begin{aligned} u(t) = u_{\min} + &\left(0.5 \tanh\left(\frac{t}{10^{-5}\ \text{s}}\right) + 0.5\right) \\ &\cdot \tanh\left(\frac{t}{0.1\ \text{s}}\right) \cdot e^{-\left(\frac{t}{0.54\ \text{s}}\right)^{20}} \cdot (u_{\max} - u_{\min})\,, \end{aligned} \tag{4.195}$$

with $u_{\max} = 5.0\frac{1}{\text{s}}$ and $u_{\min} = -30.0\frac{1}{\text{s}}$ and

$$|u(t)|_+ = \begin{cases} u(t) & \text{if } u(t) > 0.0, \\ 0.0 & \text{else.} \end{cases} \tag{4.196}$$

The activation curve is typical for muscle contraction. Its evolution over time is depicted in Figure 4.22. For the fluid part, Darcy flow is considered. The density is $\rho^{\text{f}} = 1.0 \cdot 10^{-6}\,\text{kg}/\,\text{mm}^3$, the

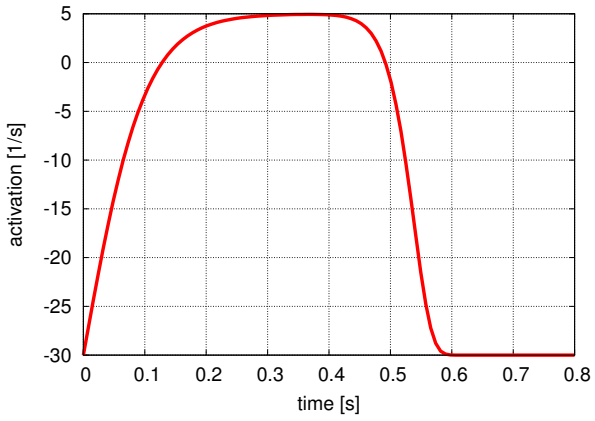

Figure 4.22: Porous heart: Activation signal.

dynamic viscosity $\mu^{\text{f}} = 1.0 \cdot 10^{-4}\,\text{kPa s}$ and the isotropic permeability in material configuration $K_0 = 1.0 \cdot 10^{-5}\,\text{mm}$. Those parameters are in the same range as given in [54]. For the evolution of the porosity, the Neo-Hookean-type law (3.83) for the constitutive relation (3.85) is used. The bulk modulus is set to $\kappa = 1.0 \cdot 10^3\,\text{kPa}$ and the initial porosity to $\phi_0 = 0.15$. The penalty contribution (3.84) is not necessary here. The inner and upper walls of the ventricles are traction-free and impervious. At the outer surfaces, a zero pressure is prescribed for the fluid, and a simple

spring model restricts the movement of the outer surface. Approximately $100,000$ linear, 4-node elements were used for the solid and fluid field, respectively. A one-step-θ scheme with $\theta = 1.0$ and a time step $\Delta t = 0.001\,\mathrm{s}$ is applied.

The resulting deformation and the fluid pressure distribution are depicted in Figure 4.23. One can clearly see the deformation of the ventricle due to the stress field and the fluid pressure induced by this contraction. Note, that the specific pressure values are not meaningful, as a zero pressure at the outer surfaces is not physiological. Still, the general pressure distribution is striking. It does not strictly follow the activation signal. Instead, pressure peaks can be observed in the interior wall of the heart (septum), as its boundaries are impervious and thus giving a high flow resistance.

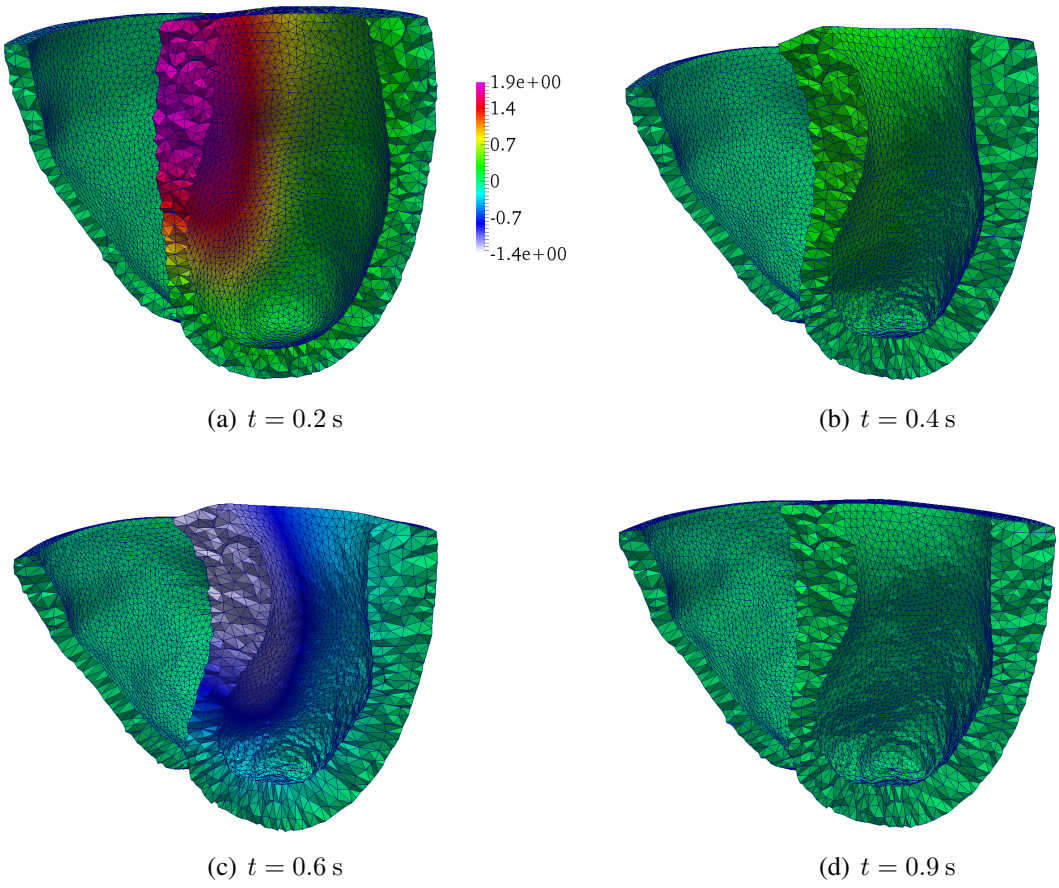

(a) $t = 0.2\,\mathrm{s}$ (b) $t = 0.4\,\mathrm{s}$

(c) $t = 0.6\,\mathrm{s}$ (d) $t = 0.9\,\mathrm{s}$

Figure 4.23: Porous heart: Pressure distribution in $[\,\mathrm{kPa}]$ within actively deforming heart at different time steps. Deformations were scaled with factor 1.5 for visualization.

5. Porous Medium as Part of Coupled Multi-Physics Problem

In the previous chapter, the numerical approach for a porous medium model was presented. Therein, the interaction of the porous medium with its environment was exclusively considered in the boundary conditions. However, for many applications this is not sufficient. There, the porous medium is a part of an interacting multi-physics problem. Such coupled problems are the topic of this chapter. This thesis focuses on the numerical modeling, hence finite element theory is applied to existing continuum mechanical theory. Models for the interaction of an impervious solid and porous medium will be considered in Section 5.1, fluid flow interacting with a porous medium in Section 5.2 and scalar transport within a porous medium in Section 5.3. Even though the physical models are chosen to be as flexible as possible to allow for a large number of applications, one major motivation lies in a model for cell mechanics, which is presented in Section 5.4. All models are illustrated with numerical examples at the end of each section.

5.1. Solid-Porous-Medium and Porous-Medium-Porous-Medium Interaction

In general, solid-porous-medium interaction can occur in two ways. First, one can think of problems, where one part of a body is impervious and the other part porous or both parts are porous with different porosities and permeabilities. This could occur when modeling rock formations or different layers of the aortic wall, for instance. Therein, the structure and the porous medium are tied at their common interface in the reference configuration. The other class of problem is when the impervious structure and the porous medium are actually distinct bodies. Then, the interaction is a contact phenomenon, where the part of the interface, that is acutally in contact, changes in time. The implementation for both classes of problems was realized as part of the student project [254].

5.1.1. Problem Statement

The coupling equations for a mesh tying problem and a contact problem involving a porous medium will be given. For both cases, a formulation based on a dual Lagrange multiplier approach presented in [191, 192, 255] will be used in the following to enforce the interface conditions. This section is restricted to Darcy flow, as it is the most common problem.

5.1.1.1. Fixed Interface (Mesh Tying)

Coupling of an impervious structure and a porous medium and coupling between two porous media is considered in this section. Mathematical analysis of very similar problems can be found in [10, 11, 19]. Therein, domain decomposition techniques and multi-scale couplings for Darcy flow through a rigid porous medium are studied. Even though it is not exactly the same problem and the analysis probably does not hold in the non-linear regime, the coupling conditions are comparable. Applications of such couplings can especially found in geomechanics, see e.g. [248] and the references therein. Kinematic and kinetic constraints have to be fulfilled on the mesh tying interface Γ^{c}. For the coupling of the impervious structure and the porous structure, the displacements at the solid interface $\Gamma_0^{\mathrm{c,s}}$ have to be equal. Thus, the following identity needs to hold:

$$\boldsymbol{d}^{\mathrm{s}} = \widetilde{\boldsymbol{d}}^{\mathrm{s}} \qquad \text{on} \quad \Gamma_0^{\mathrm{c,s}}, \tag{5.1}$$

with $\widetilde{\boldsymbol{d}}^{\mathrm{s}}$ denoting the displacements of the impervious solid. This condition is essentially the same as for standard solid mesh tying problems. As the porous fluid cannot pass the impervious solid, a no-penetration condition holds at the fluid interface $\Gamma_t^{\mathrm{c,f}}$:

$$\phi \boldsymbol{n} \cdot \left(\boldsymbol{v}^{\mathrm{f}} - \boldsymbol{v}^{\mathrm{s}} \right) = 0 \quad \text{on } \Gamma_t^{\mathrm{c,f}}. \tag{5.2}$$

An even more challenging problem is the coupling of two porous media. The two domains are marked with the superscript (1) and (2). The sub-domain (1) is called *slave side* in contrast to the *master side* indicated by (2). The following interface conditions hold: The displacement fields have to be equal

$$\boldsymbol{d}^{\mathrm{s},(1)} = \boldsymbol{d}^{\mathrm{s},(2)} \qquad \text{on} \quad \Gamma_0^{\mathrm{c,s}}, \tag{5.3}$$

and the mass flux over the interface must be conserved

$$\phi^{(1)} \boldsymbol{n}^{(1)} \cdot \left(\boldsymbol{v}^{\mathrm{f},(1)} - \boldsymbol{v}^{\mathrm{s},(1)} \right) = \phi^{(2)} \boldsymbol{n}^{(2)} \cdot \left(\boldsymbol{v}^{\mathrm{f},(2)} - \boldsymbol{v}^{\mathrm{s},(2)} \right) \quad \text{on } \Gamma_t^{\mathrm{c,f}}. \tag{5.4}$$

Note, that this equation only holds if both porous media are fully saturated and filled with the same fluid with equal density. Otherwise, the different mass densities would have be taken into account for the mass balance at the interface and a multiphase fluid model would need to be included.

5.1.1.2. Dynamic Interface (Contact)

Contact problems including porous media are predominantly found in the context of biomechanical applications for modeling of joints. The contact is assumed to be frictionless. For this purpose, a FE algorithm for contact of porous bodies, where the constraints are enforced with Lagrange multipliers was developed for small deformations and two-dimensional problems in [83]. It was extended to three-dimensional problems, large deformations and sliding using an augmented Lagrange formulation in [116, 117, 261] among others. A similar approach was designed for geomechanical problems in [212]. Also motivated by applications in biomechanics, a penalty approach for contact of porous media including solute transport over the interface was presented in [13, 14]. The approach given in this thesis is a mortar-based formulation using Lagrange multipliers to enforce the coupling conditions. In contrast to the references mentioned above,

the applied methodology uses dual Lagrange multiplier interpolations in combination with an primal-dual active set strategy, based on the formulations developed in [191, 192, 255], to solve the contact problem. In this section, the basic coupling equations will be given and first numerical results will be presented. Details on the numerical scheme will be omitted. Instead, it will be refered to the corresponding literature. The main difficulty for contact problems of an impervious structure and a porous structure is that the contact interface changes in time. As a consequence, a numerical scheme for tracking the contact zone is needed as well as an algorithm for integrating over the contact zone. The primal-dual active set strategy for finding the contact zone and the segmentation procedure for performing the numerical integration was adopted from a solid-solid problem (see [191, 192] for details) to a solid-porous solid problem in a straightforward manner. In fact, when considering the contact between the impervious structure and the porous structure without the fluid, the problem formulation is completely the same. Clearly, the two bodies must not overlap. Thus, the *gap function* g is introduced as

$$g = \boldsymbol{n}^{(1)} \cdot \left(\boldsymbol{x}^{(1)} - \tilde{\boldsymbol{x}}^{(2)} \right). \tag{5.5}$$

As for the mesh tying problem, the superscripts (1) and (2) are used to distinguish between slave and master side. The gap is a signed distance function. The coordinate $\tilde{\boldsymbol{x}}^{(2)}$ represents the master point associated with the corresponding slave position $\boldsymbol{x}^{(1)}$. Different procedures to obtain the former coordinate can be applied. Here, $\tilde{\boldsymbol{x}}^{(2)}$ is determined by a smooth interface mapping onto the master surface along the slave side normal field $\boldsymbol{n}^{(1)}$. Again, it is referred to [191, 192] for details. Then, the contact constraint can be formulated as follows

$$g \geq 0,\ p_\perp \leq 0 \quad \text{and} \quad g\, p_\perp = 0, \tag{5.6}$$

with the normal component $p_\perp$ of the interface traction. The first inequality means, that there can be either a positive gap, or the two bodies are in contact. Penetrations must not occur. The second inequality states that there must not be a tensile traction in frictionless contact, as no adhesive effects are modeled. The last equation excludes a positive gap and a contact traction unequal to zero at a time. With the verbal distinction between the active part $\Gamma_{\mathrm{A}}^{(1)}$ as the part of the contact interface $\Gamma_t^{\mathrm{c},(1)}$ actually being in contact and the inactive part $\Gamma_{\mathrm{I}}^{(1)}$, where currently no contact interactions occurs, equation (5.6) can be reformulated to

$$\begin{aligned} p_\perp \leq 0,\ g = 0 \quad & \text{on } \Gamma_{\mathrm{A}}^{(1)}, \\ g > 0,\ p_\perp = 0 \quad & \text{on } \Gamma_{\mathrm{I}}^{(1)}, \\ g\, p_\perp = 0 \quad & \text{on } \Gamma_t^{\mathrm{c},(1)}. \end{aligned} \tag{5.7}$$

The constraints for the pore fluids are the balance of mass flux over the active interface with equal pressures on both sides and zero pressures on the inactive part of the contact interface:

$$\begin{aligned} \phi^{(1)} \left(\boldsymbol{v}^{\mathrm{f},(1)} - \boldsymbol{v}^{\mathrm{s},(1)} \right) \cdot \boldsymbol{n}^{(1)} - \phi^{(2)} \left(\boldsymbol{v}^{\mathrm{f},(2)} - \boldsymbol{v}^{\mathrm{s},(2)} \right) \cdot \boldsymbol{n}^{(1)} = 0 \\ p^{\mathrm{f},(1)} - p^{\mathrm{f},(2)} = 0 \end{aligned} \Bigg\} \quad \text{on} \quad \Gamma_{\mathrm{A}}^{(1)}, \\ p^{\mathrm{f},(1)} = p^{\mathrm{f},(2)} = 0 \qquad\qquad \text{on} \quad \Gamma_{\mathrm{I}}^{(1)}. \tag{5.8}$$

Note, that here it is assumed that both fluids have the same density and are perfectly miscible. Also, the equality of pressures implies that the contact interface is perfectly permeable with respect to fluid flow.

5.1.2. Solution Scheme

The numerical procedure to enforce the respective constraints for mesh tying and contact is very similar to the application of impermeability conditions, presented in Section 4.3.4.2. For details on the formulation and the implementation it is referred to [254]. As presented in [191, 192] for solid problems, the constraints are applied with the Lagrange multiplier method. However, for the constraints on the porous medium, two Lagrange multiplier fields are defined. One corresponds to the porous mixture and one to the fluid phase. In case of mesh tying, the first Lagrange multiplier field is used to enforce the equality of displacements at the interface, i.e. equation (5.1) or (5.3), in a weak sense. This is equivalent to solid mesh tying problems. For details on the theory of solid mesh tying see [197, 198]. In case of contact, the first Lagrange multiplier enforces the conditions (5.7) in a weak sense. See [256] for a mathematical derivation of the corresponding variational inequality. This Lagrange multiplier is identified as the interface traction of the porous medium and the solid body. For frictionless contact, it points in normal direction of the interface in current configuration. The second Lagrange multiplier field requires for both mesh tying and contact mass conservation of the fluid normal mass flux and is also zero in tangential direction. It is identified as the fluid interface traction. In all mortar formulations the Lagrange multiplier field is defined on the slave side and the resulting boundary integrals are evaluated there. Thus, an interface mapping is defined to transfer quantities from the master to the slave side. Again, see [191, 192] for details.

The boundary integrals stemming from the mesh tying and contact conditions, i.e. the weak form of the constraints and the respective force terms in the balance equations, are incorporated into the weak form. For solution of the porous contact problem, the boundary integrals are evaluated on the active part of the slave side boundary (for mesh tying problems, no distinction between active and inactive part is necessary and the integration is performed over the whole interface). Dual shape functions are used for efficient condensation of the Lagrange multiplier degrees of freedom. After consistent linearization for the Newton scheme, these degrees of freedom can be condensed out of the linear system analogously to the methodology for the application of impermeability constraints described in detail in Section 4.3.4.2. The whole problem is embedded within the monolithic porous medium system and solved within one iterative solution scheme. This holds for both mesh tying and contact. Specifically concerning the contact problem, the system of non-linear equations is solved with a semi-smooth Newton method, see e.g. [119] for general mathematical theory.

5.1.3. Numerical Examples

Three examples are shown. A simple patch test is performed as validation of the implementation. A system of two porous media with different porosity is an example for mesh tying of two porous bodies. Lastly, contact between an impervious solid and a porous medium is simulated.

5.1.3.1. Porous-Medium-Solid Interaction with Mesh Tying

A simple benchmark example is presented. It is inspired by standard patch tests from structural mechanics [232, 267]. It is to show, that the formulation can represent a constant stress field. This is an intrinsic feature of the mortar method [198]. An impermeable solid cube (edge length 10) is modeled as hyperelastic body with a Neo-Hookean material (Young's modulus $E = 2.5 \cdot 10^3$ and Poisson's ratio $\nu = 0.3$). The skeleton of the porous block (edge length 10) is modeled

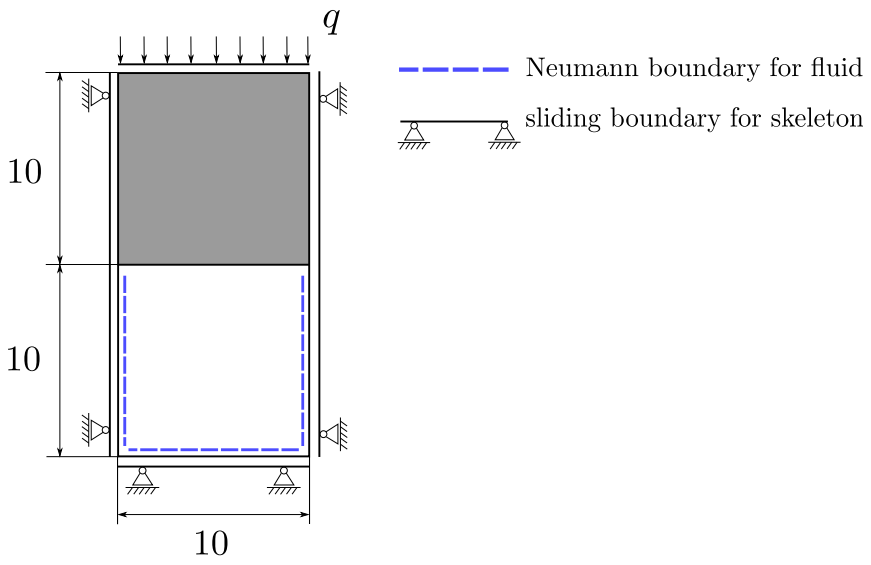

Figure 5.1: Porous medium-solid patch test: Schematic of geometry and boundary conditions. The impermeable solid is colored in grey, the porous medium is white.

by the same macroscopic material law. For the porosity, the non-linear law (3.87) with bulk modulus $\kappa = 500$ and penalty parameter $\eta = 0.0$ is used. The pore fluid is modeled as Darcy flow with dynamic viscosity $\mu^{\mathrm{f}} = 0.1$ and isotropic material permeability $K = 0.01$. Both cubes are tied at the common interface. The lateral boundaries are fixed in normal direction, i.e. only movement in vertical direction is allowed, see Figure 5.1. The bottom of the porous block is fixed and a constant Neumann load of $\hat{p}^{\mathrm{f}} = 1.0$ is applied at all fluid boundaries. At the top, a constant load $q = 4$ is applied. The upper block consists of $5 \times 5 \times 5$ and the lower, porous block of $8 \times 8 \times 8$ tri-linear 8-node elements. Stationary conditions are assumed, thus, inertia terms are neglected. In Figure 5.2 the distribution of the Cauchy stresses in vertical direction and the fluid pressure is depicted. A constant stress field can be seen there. Both blocks exhibit a constant total stress of 4. Within the porous medium, the stress are partitioned between skeleton and fluid, i.e.

$$\boldsymbol{\sigma} = \boldsymbol{\sigma}^{\mathrm{s}} - \mathbf{1} p^{\mathrm{f}}. \tag{5.9}$$

In conclusion, the mesh tying between a impervious solid and a porous medium passes the patch test as expected. The patch test was also performed successfully for a two-dimensional problem and coupling of two porous media [254]. For the sake of brevity, the results will not be shown here.

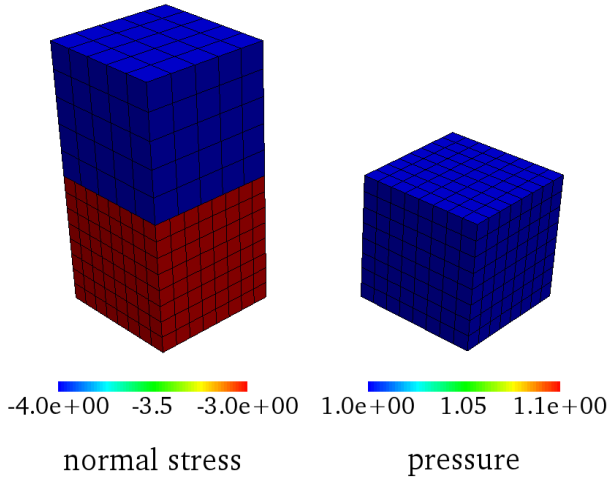

Figure 5.2: Mesh tying example: Patch test. Normal Cauchy stress of the skeleton in vertical direction (left) and fluid pressure (right).

5.1.3.2. Mesh Tying of Two Porous Media

Another application of the presented mesh tying framework is the coupling of two porous media with different characteristics. Flow through a porous structure enclosing another porous medium is shown in this example. Darcy flow with fluid density $\rho^{\mathrm{f}} = 1.0$, dynamic viscosity $\mu^{\mathrm{f}} = 0.1$ and isotropic material permeability $K = 0.01$ is considered. The outer porous medium (density $\rho^{\mathrm{s}} = 3.0$ and initial porosity $\phi_0 = 0.2$) is modeled as a Neo-Hookean material (2.43) with a Young's modulus $E = 2500$ and a Poisson's ratio $\nu = 0.3$. The inclined porous medium (density $\rho^{\mathrm{s}} = 2.0$ and initial porosity $\phi_0 = 0.6$) is considered as Saint-Venant-Kirchhoff material (Young's modulus $E = 5000$ and a Poisson's ratio $\nu = 0.2$). Both porous media include the non-linear porosity law (3.87) with bulk modulus $\kappa = 500$ and penalty parameter $\eta = 0.0$. The dimensions of the geometry and the boundary conditions are depicted in Figure 5.3.

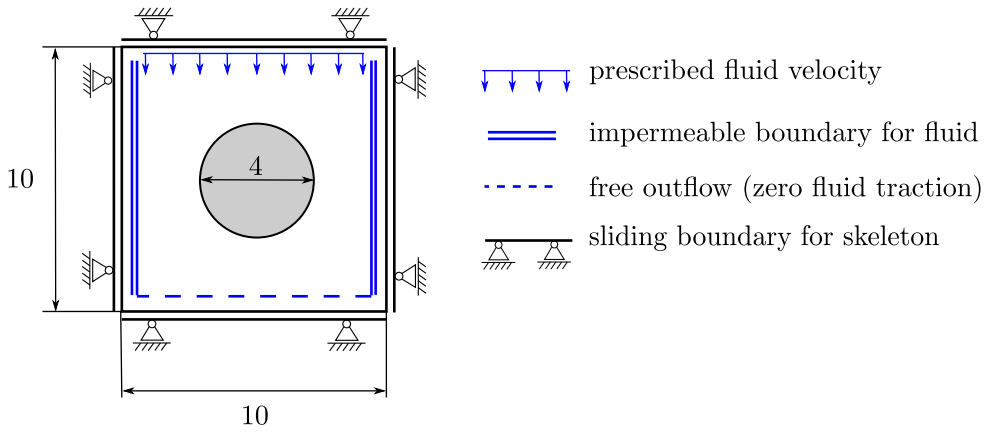

Figure 5.3: Mesh tying of two porous media: Schematic of geometry and boundary conditions. Two different porous domains (white and grey).

At the top boundary a normal velocity

$$\hat{v}_{\perp}^{\mathrm{f}} = \begin{cases} 2.5(1.0 - \cos(0.5\pi t)) & \text{if} \quad t < 2.0, \\ 5.0 & \text{otherwise}, \end{cases} \tag{5.10}$$

is prescribed. The lateral boundaries are impermeable and fixed in normal direction. The lower boundary is a fixed outflow with zero traction. For discretization in space, 2800 bi-linear 4-node elements are used for both fields. A one-step-θ scheme with $\theta = 0.66$ and $\Delta t = 0.05$ is utilized. In Figure 5.4 the global solutions of the fluid pressure, the velocity field and the porosity are depicted. The pressure field is nearly linear in space. The continuity of the pressure

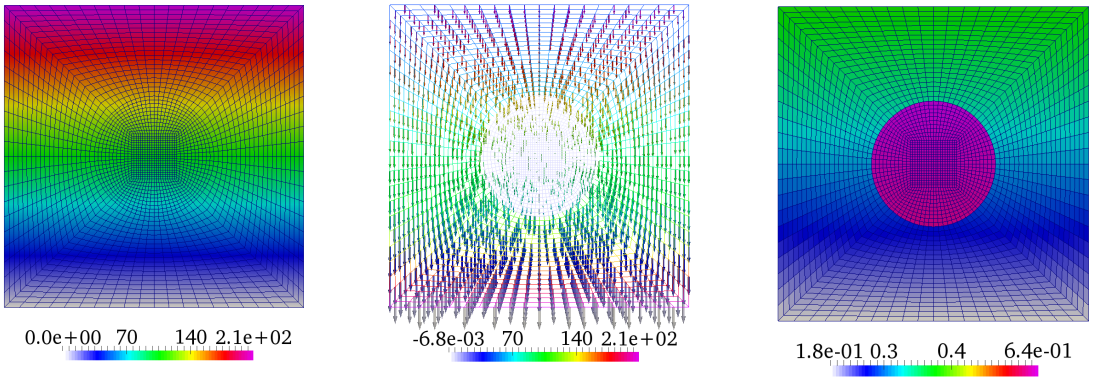

(a) pressure (b) velocity (c) porosity

Figure 5.4: Mesh tying of two porous media: Results at $t = 5$. Pressure field (left), velocity field (middle), porosity field (right). Colors denote respective magnitudes.

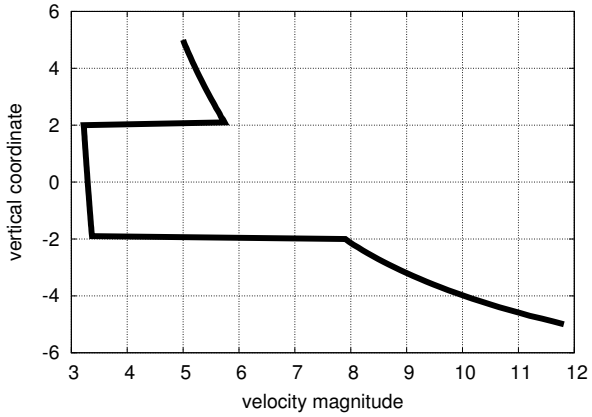

Figure 5.5: Mesh tying of two porous media: Fluid velocity magnitude plotted over vertical coordinate along center line.

at the interface is fulfilled, as enforced by the method. The velocity and the porosity, however, jump at the interface. In Figure 5.5 the velocity magnitude is plotted over the vertical direction.

There, the discontinuity can be seen more clearly. Those jumps are sensible. The porosity field was inhomogeneous from the start and thus the velocity field needs to adapt in order to account for the balance of mass over the interface. Due to the higher porosity in the enclosed area, the velocity decreases there such that the mass flux stays the same.

5.1.3.3. Contact of Porous Medium and Solid

A simple, two-dimensional contact problem of a porous medium and an impervious solid is presented. A pure solid block (edge length 10) is modeled as hyperelastic body with a Neo-Hookean material (density $\rho^{\mathrm{s}} = 0.5$, Young's modulus $E = 2.0{\cdot}10^3$ and Poisson's ratio $\nu = 0.3$). A skeleton of the porous block (width 30 and height 10) is modeled by the same macroscopic material law. For the porosity, the non-linear law (3.87) with bulk modulus $\kappa = 50$ and penalty parameter $\eta = 0.01$. The pore fluid is modeled as Darcy flow with density $\rho^{\mathrm{f}} = 1.0$, dynamic viscosity $\mu^{\mathrm{f}} = 0.01$ and isotropic material permeability $K = 0.01$. The porous body is fixed at the bottom. Its upper and lower boundaries are impervious. The solid block will come into contact with the porous medium and slide in horizontal direction. Note, that modeling the potential contact surface as impervious to fluid flow, is a significant simplification of the problem. Then, the fluid is not influenced by the changing actual contact interface. The spatial discretization consists of 1350 bi-linear, 4-node elements in total (approximate element size $h = 1$). A one-step-θ scheme with $\theta = 1.0$ and $\Delta t = 0.05$ is used for all fields. In Figure 5.6 the results of the simulation at characteristic time instances is depicted. It shows very clearly the pressure waves induced by the initial impact and due to the subsequent sliding of the solid structure.

5.2. Fluid-Porous-Medium Interaction

Flow within a porous medium and its interaction with free flowing fluid can be found in many applications in engineering industry. Flow through porous soil or loose rock is analyzed in the context of ground water pollution due to rainfall or seepage of nuclear waste, see e.g. [92, 149, 170]. In biomechanics, most tissues can be modeled as porous medium interacting with blood flow. For instance, the structure of the aortic wall, being composed of intima, media and adventitia – three different layers of porous structure – significantly influences the loading of the aortic wall, which can be crucial for the formation of arteriosclerosis [200].

Experimental studies of fluid-porous-structure interaction (FPSI) have been performed some decades ago (the arguably most famous is the experiment by Beavers and Joseph [26]) while mathematical and numerical studies are comparatively young. Therein, almost exclusively Darcy flow within the porous medium is considered, which will be done in this thesis also. One has to note, that the exact form of the model, i.e. the form of coupling between the porous medium and the fluid, is very controversial. Promising theoretical efforts have been made [134, 135, 238] leading to formulations which are unfortunately either very complicated and/or need further model assumptions to be applicable in practice. Simply speaking, two general approaches for realizing a fluid-porous-medium coupling exist in practice. The more popular method is to establish the coupling along a dimensional reduced interface [18, 46, 81, 175]. Thereby the free flowing fluid (most often modeled as Stokes or Navier-Stokes flow) is strictly separated from the porous domain. This method is also known as two-domain approach. The primary variables

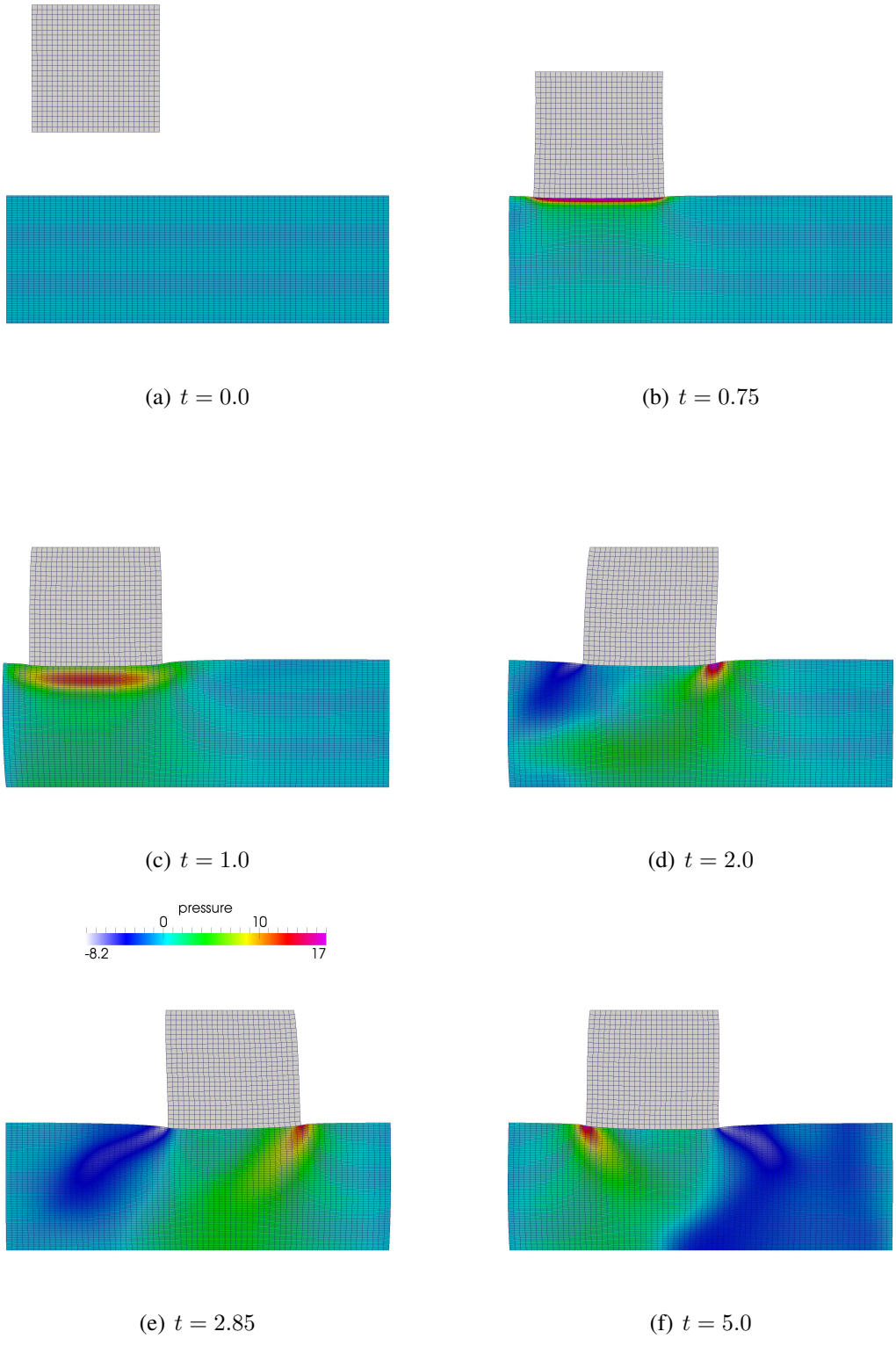

(a) $t = 0.0$ (b) $t = 0.75$

(c) $t = 1.0$ (d) $t = 2.0$

(e) $t = 2.85$ (f) $t = 5.0$

Figure 5.6: Porous medium-solid interaction with contact. Colors denote pressure values.

and/or their fluxes are coupled by given conditions at the porous-fluid interface resulting in potential jumps of some quantities. Even though physically and experimentally motivated, the concrete mathematical form of the coupling is still heuristic and usually includes additional parameters. Alternatively, the coupling can be established within a predefined transition zone. Due to this smooth transition between fluid and porous medium, such concepts are also called one-domain approaches. The idea of one-domain approaches is to circumvent the need for additional model assumptions by resolving the region where the transition takes place [58, 110, 164, 182]. Frequently, the Darcy-Brinkman flow model is used within the transition zone, being 'in the middle' between Navier-Stokes and Darcy flow, as illustrated in Section 3.6.3. Actually, the Darcy-Brinkman equation is often used for the whole domain, reproducing Stokes or Navier-Stokes flow in one part and Darcy flow in the other. The physical quantities are continuous and material parameters are smoothly adapted within the transition zone. Even though estimates for the size of the transition zone exist [109, 156], its form and dimensions and the evolution of the material parameters within this area remain a model uncertaintity. Also, the numerical costs increase due to the high spatial resolution that is necessary within the transition zone. Numerically, for both approaches the stability of the coupling is a highly complex topic. Mathematical analysis and stability conditions can for instance be found in [47, 155, 186]. The interested reader is referred to [80] for a detailed review. In this thesis, the most common approach is used, being a two-domain approach with mass and total pressure continuity and the Beavers-Joseph condition for the tangential stresses. The implementation was realized within the student project [202]. A stabilization for the Navier-Stokes problem and the porous medium problem is utilized similar to [18]. However, a thorough stability analysis of the coupling eludes this thesis.

5.2.1. Problem Statement

The governing equations for incompressible Navier-Stokes flow and the porous medium were already presented in Section 2.4 and 3.7, respectively. Thus, only the coupling conditions at the FPSI interface will be given. Four coupling conditions are applied at the fluid-porous medium interface. First, the balance of tractions between the free fluid and the porous medium

$$\widetilde{\boldsymbol{\sigma}}^{\mathrm{f}} \cdot \widetilde{\boldsymbol{n}}^{\mathrm{f}} + \boldsymbol{\sigma} \cdot \boldsymbol{n} = \boldsymbol{0} \tag{5.11}$$

has to hold. Here, variables associated with the Navier-Stokes fluid are marked with '$\sim$'. Consequently, $\widetilde{\boldsymbol{\sigma}}^{\mathrm{f}}$ and $\widetilde{\boldsymbol{n}}^{\mathrm{f}}$ are the fluid stresses and the outward pointing normal vector of the Navier-Stokes fluid, respectively. Naturally, the continuity of mass flux through the interface can be written as

$$\left(\widetilde{\boldsymbol{v}}^{\mathrm{f}} - \boldsymbol{v}^{\mathrm{s}}\right) \cdot \widetilde{\boldsymbol{n}}^{\mathrm{f}} + \left(\phi(\boldsymbol{v}^{\mathrm{f}} - \boldsymbol{v}^{\mathrm{s}})\right) \cdot \boldsymbol{n} = 0. \tag{5.12}$$

Additionally, the equilibrium of the normal component of the boundary tractions $\widetilde{\boldsymbol{t}}_t^{\mathrm{f}}$ of the Navier-Stokes and the Darcy fluid

$$\widetilde{\boldsymbol{t}}_t^{\mathrm{f}} \cdot \widetilde{\boldsymbol{n}}^{\mathrm{f}} + p^{\mathrm{f}} = 0 \tag{5.13}$$

is enforced. The Beavers-Joseph condition for the shear stresses in tangential direction is used

$$\left(\widetilde{\boldsymbol{v}}^{\mathrm{f}} - \boldsymbol{v}^{\mathrm{s}} - \phi(\boldsymbol{v}^{\mathrm{f}} - \boldsymbol{v}^{\mathrm{s}}) + \frac{\mathrm{tr}\,(\boldsymbol{K})}{\alpha_{\mathrm{BJ}} \widetilde{\mu}^{\mathrm{f}} \sqrt{\mathrm{n}_{\mathrm{sd}}}} \widetilde{\boldsymbol{t}}_t^{\mathrm{f}}\right) \cdot \widetilde{\boldsymbol{\tau}}^{\mathrm{f}} = \boldsymbol{0}, \tag{5.14}$$

with the Beavers-Joseph coefficient α_{BJ} and the matrix of tangential vectors $\widetilde{\boldsymbol{\tau}}^{\mathrm{f}}$.

5.2.2. Solution Scheme

For solving the complete problem, the coupling conditions are integrated into the weak form by substituting the respective boundary integrals on the fluid-porous interface Γ^{c}. Pulling equation (5.11) back to the material configuration and noting that the normals at the interface from both sides only differ in sign, i.e. $\widetilde{\boldsymbol{n}}^{\mathrm{f}} = -\boldsymbol{n}$, gives the boundary traction of the mixture

$$\boldsymbol{t}_0 = (\boldsymbol{F} \cdot \boldsymbol{S}) \cdot \boldsymbol{N} \stackrel{!}{=} \widetilde{\boldsymbol{S}}^{\mathrm{f}} \cdot \boldsymbol{N}, \quad \text{on } \Gamma^{\mathrm{c}}, \tag{5.15}$$

with the second Piola-Kirchhoff stress $\widetilde{\boldsymbol{S}}^{\mathrm{f}}$ of the Navier-Stokes fluid. The conservation of fluid mass (5.12) over the interface is inserted into the continuity equation of the Darcy fluid in the weak form (4.66)

$$\left(\phi(\boldsymbol{v}^{\mathrm{f}} - \boldsymbol{v}^{\mathrm{s}})\right) \cdot \boldsymbol{n} \stackrel{!}{=} \left(\widetilde{\boldsymbol{v}}^{\mathrm{f}} - \boldsymbol{v}^{\mathrm{s}}\right) \cdot \boldsymbol{n}, \quad \text{on } \Gamma^{\mathrm{c}}. \tag{5.16}$$

The remaining two conditions (5.13) and (5.14) determine the current boundary tractions of the Navier-Stokes fluid

$$\widetilde{\boldsymbol{t}}_t^{\mathrm{f}} = \left(\widetilde{\boldsymbol{t}}_t^{\mathrm{f}} \cdot \widetilde{\boldsymbol{n}}^{\mathrm{f}}\right) \cdot \widetilde{\boldsymbol{n}}^{\mathrm{f}} + \widetilde{\boldsymbol{t}}_t^{\mathrm{f}} \cdot \widetilde{\boldsymbol{\tau}}^{\mathrm{f}} \stackrel{!}{=} -p^{\mathrm{f}} \widetilde{\boldsymbol{n}}^{\mathrm{f}} + \frac{\alpha_{\mathrm{BJ}} \widetilde{\mu}^{\mathrm{f}} \sqrt{n_{\mathrm{sd}}}}{\mathrm{tr}\,(\boldsymbol{K})} \left(\widetilde{\boldsymbol{v}}^{\mathrm{f}} - \boldsymbol{v}^{\mathrm{s}} - \phi(\boldsymbol{v}^{\mathrm{f}} - \boldsymbol{v}^{\mathrm{s}})\right) \cdot \widetilde{\boldsymbol{\tau}}^{\mathrm{f}}, \quad \text{on } \Gamma^{\mathrm{c}}. \tag{5.17}$$

The change of the free fluid domain is considered via an ALE approach. For the mesh displacements, a simply elasto-static equation is used. Thus, the following equation is solved for the displacements $\boldsymbol{d}^{\mathrm{g}}$ of the grid

$$\boldsymbol{\nabla}_0 \cdot \boldsymbol{P}(\boldsymbol{d}^{\mathrm{g}}) = \boldsymbol{0}. \tag{5.18}$$

Therein, the linear Saint-Venant-Kirchhoff law (2.39) is used. For the Navier-Stokes fluid, a well-known stabilized equal-order mixed formulation with velocity and pressure as primary variables is applied. Further details concerning the finite element formulation of the Navier-Stokes fluid and the ALE equations are skipped here. It follows the procedure for moving flow problems with moving domains in FSI, which can e.g. be found in [168]. The whole fluid-porous medium system is solved in a monolithic manner. The final global linearized system matrix to be solved at each Newton iteration within a Newton-Raphson scheme can be schematically written as

$$\left(\begin{array}{cc|cc|cc|c}
\mathsf{S}_{\mathrm{II}} & \mathsf{S}_{\mathrm{I\Gamma}} & \mathsf{C}_{\mathrm{II}}^{\mathrm{SF}} & \mathsf{C}_{\mathrm{I\Gamma}}^{\mathrm{SF}} & \mathsf{0} & \mathsf{0} & \mathsf{0} \\
\mathsf{S}_{\mathrm{\Gamma I}} & \mathsf{S}_{\mathrm{\Gamma\Gamma}} & \mathsf{C}_{\mathrm{\Gamma I}}^{\mathrm{SF}} & \mathsf{C}_{\mathrm{\Gamma\Gamma}}^{\mathrm{SF}} & \mathsf{C}_{\mathrm{\Gamma I}}^{\mathrm{S\widetilde{F}}} & \mathsf{C}_{\mathrm{\Gamma\Gamma}}^{\mathrm{S\widetilde{F}}} & \mathsf{0} \\
\hline
\mathsf{C}_{\mathrm{II}}^{\mathrm{FS}} & \mathsf{C}_{\mathrm{I\Gamma}}^{\mathrm{FS}} & \mathsf{F}_{\mathrm{II}} & \mathsf{F}_{\mathrm{I\Gamma}} & \mathsf{0} & \mathsf{0} & \mathsf{0} \\
\mathsf{C}_{\mathrm{\Gamma I}}^{\mathrm{FS}} & \mathsf{C}_{\mathrm{\Gamma\Gamma}}^{\mathrm{FS}} & \mathsf{F}_{\mathrm{\Gamma I}} & \mathsf{F}_{\mathrm{\Gamma\Gamma}} & \mathsf{C}_{\mathrm{\Gamma I}}^{\mathrm{F\widetilde{F}}} & \mathsf{C}_{\mathrm{\Gamma\Gamma}}^{\mathrm{F\widetilde{F}}} & \mathsf{0} \\
\hline
\mathsf{0} & \mathsf{C}_{\mathrm{I\Gamma}}^{\mathrm{\widetilde{F}S}} & \mathsf{0} & \mathsf{0} & \widetilde{\mathsf{F}}_{\mathrm{II}} & \widetilde{\mathsf{F}}_{\mathrm{I\Gamma}} & \mathsf{C}_{\mathrm{II}}^{\mathrm{\widetilde{F}G}} \\
\mathsf{C}_{\mathrm{\Gamma I}}^{\mathrm{\widetilde{F}S}} & \mathsf{C}_{\mathrm{\Gamma\Gamma}}^{\mathrm{\widetilde{F}S}} & \mathsf{C}_{\mathrm{\Gamma I}}^{\mathrm{\widetilde{F}F}} & \mathsf{C}_{\mathrm{\Gamma\Gamma}}^{\mathrm{\widetilde{F}F}} & \widetilde{\mathsf{F}}_{\mathrm{\Gamma I}} & \widetilde{\mathsf{F}}_{\mathrm{\Gamma\Gamma}} & \mathsf{C}_{\mathrm{\Gamma I}}^{\mathrm{\widetilde{F}F}} \\
\hline
\mathsf{0} & \mathsf{C}_{\mathrm{I\Gamma}} & \mathsf{0} & \mathsf{0} & \mathsf{0} & \mathsf{0} & \mathsf{G}_{\mathrm{II}}
\end{array}\right)^{i}_{n+1}
\left(\begin{array}{c}
\Delta \mathbf{d}_{\mathrm{I}}^{\mathrm{s}} \\
\Delta \mathbf{d}_{\mathrm{\Gamma}}^{\mathrm{s}} \\
\hline
\Delta \mathbf{v}_{\mathrm{I}}^{\mathrm{f}} \\
\Delta \mathbf{v}_{\mathrm{\Gamma}}^{\mathrm{f}} \\
\hline
\Delta \widetilde{\mathbf{v}}_{\mathrm{I}}^{\mathrm{f}} \\
\Delta \widetilde{\mathbf{v}}_{\mathrm{\Gamma}}^{\mathrm{f}} \\
\hline
\Delta \mathbf{d}_{\mathrm{I}}^{\mathrm{g}}
\end{array}\right)^{i+1}_{n+1}
= -
\left(\begin{array}{c}
\mathbf{R}_{\mathrm{I}}^{\mathrm{s}} \\
\mathbf{R}_{\mathrm{\Gamma}}^{\mathrm{s}} \\
\hline
\mathbf{R}_{\mathrm{I}}^{\mathrm{f}} \\
\mathbf{R}_{\mathrm{\Gamma}}^{\mathrm{f}} \\
\hline
\widetilde{\mathbf{R}}_{\mathrm{I}}^{\mathrm{f}} \\
\widetilde{\mathbf{R}}_{\mathrm{\Gamma}}^{\mathrm{f}} \\
\hline
\mathbf{R}_{\mathrm{I}}^{\mathrm{g}}
\end{array}\right)^{i}_{n+1}, \tag{5.19}$$

where the subscript 'Γ' denotes degrees of freedom at the interface between fluid and porous medium and the subscript 'I' marks inner degrees freedom. The respective increments of the

solution variables within the Newton-Raphson scheme are denoted by Δ. The matrices $\mathbf{S}$ correspond the porous solid phase, $\mathbf{F}$ to the porous fluid phase, $\widetilde{\mathbf{F}}$ to the Navier-Stokes fluid and $\mathbf{G}$ to the mesh. The coupling blocks are written as $\mathbf{C}$ with corresponding sub- and superscripts. Note, that it is only solved for inner mesh displacements, as the displacements of the interface are determined by the skeleton solution. For solving the linear system, a similar strategy as for the porous medium, see Section 4.3.4.1, adapted from [240] is used. Following standard procedure, see Section 4.3.4, the guess for the unknown solution of the next time step is updated with the solution of the linear system and the iterative procedure is repeated until a user-defined convergence criterion is met.

5.2.3. Numerical Example

Flow over two types of a flexible wall is considered in this example. The wall will either be modeled as porous or impervious. Thus, FPSI is compared to FSI. The geometry is depicted in Figure 5.7. On the left side of the channel, a parabolic inflow profile

$$\hat{\boldsymbol{v}}^{\mathrm{f}}(t,\boldsymbol{x})\cdot\boldsymbol{n} = 6.0(0.6-y)y\cdot\begin{cases} 0.5(1-\cos(10\pi t)) & \text{for } 0.0\leq t\leq 0.1,\\ 1.0 & \text{else,}\end{cases} \tag{5.20}$$

is prescribed pointing in positive x-direction. In tangential directions, the velocity is set to zero. At the outflow (the most right boundary) a zero-traction condition is enforced. A no-slip condition is applied to the upper and lower boundary of the channel, while at the sides (i.e. the boundaries parallel to the flow direction) a slip condition is utilized. In case of an impervious structure, a no-slip condition needs to be fulfilled at the fluid-structure interface, for a porous medium, the above presented conditions (5.11)–(5.14) are used (the Beavers-Joseph coefficient is set to $\alpha_{\mathrm{BJ}} = 10$). For both fluids (pore fluid and free fluid), the dynamic viscosity is set

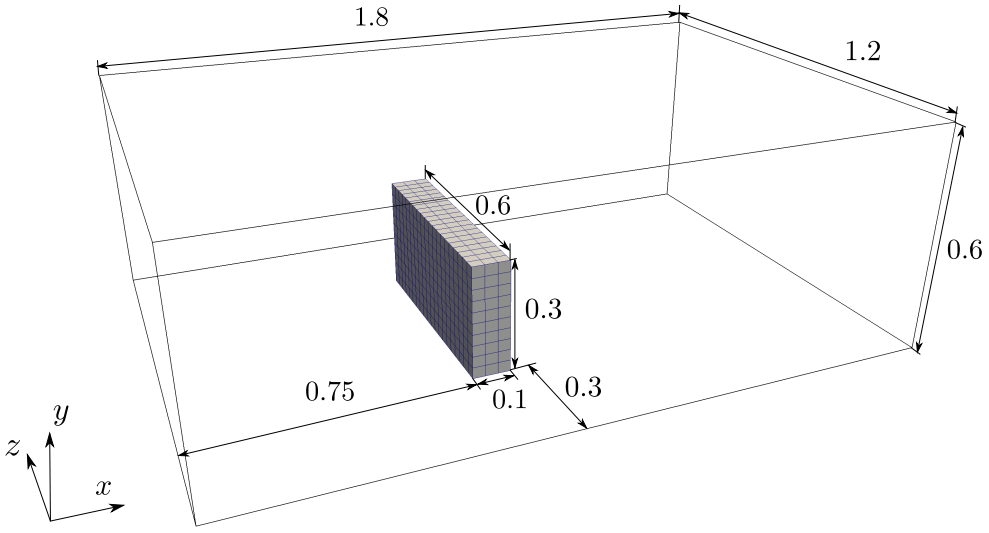

Figure 5.7: Flow over porous wall: Geometric dimensions.

to $\mu^{\mathrm{f}} = 0.001$ and the density to $\rho^{\mathrm{f}} = 1.0$. The solid/skeleton phase ($\rho^{\mathrm{s}} = 1.0$) is modeled

with a Saint-Venant-Kirchhoff material law (2.40) with $E = 600$ and $\nu = 0.39$. The porosity is determined by the Neo-Hookean formulation (3.83)–(3.85) with $\kappa = 2.0 \cdot 10^5$ and $\eta = 0.0$. For discretization in space, tri-linear 8-node Lagrangean elements where used for all fields. The free fluid is discretized with 47400 elements. The same number of elements are used for the ALE mesh. For the solid or skeleton body, 600 elements are used. In case of a porous wall, additionally 600 conforming elements approximate the pore fluid. All fields are integrated in time with the one-step-θ method with $\theta = 0.66$ and time step $\Delta t = 0.01$.

The results are depicted in Figure 5.8. Therein, the velocity streamlines around the deforming structure are depicted at characteristic snapshots. Clearly, the structure starts bending due to the rising flow velocity in both simulations. However, it is worth noting, that the velocity field propagates faster through the channel in case of FSI. This is because, in the porous simulation, parts of the free fluid first penetrate the porous structure. Also, it can be seen, that in the FSI simulation the oscillations of the bending structure are more pronounced. This is the most obvious at $t = 0.4$, where the structure is temporarily bending against the flow. In the FPSI simulation, the oscillations are also present but less obvious, as the porous structure exhibits less drag force due to its permeability. Furthermore, the same effect eventually leads to more vortices in case of the FSI simulation (at $t = 1.0$).

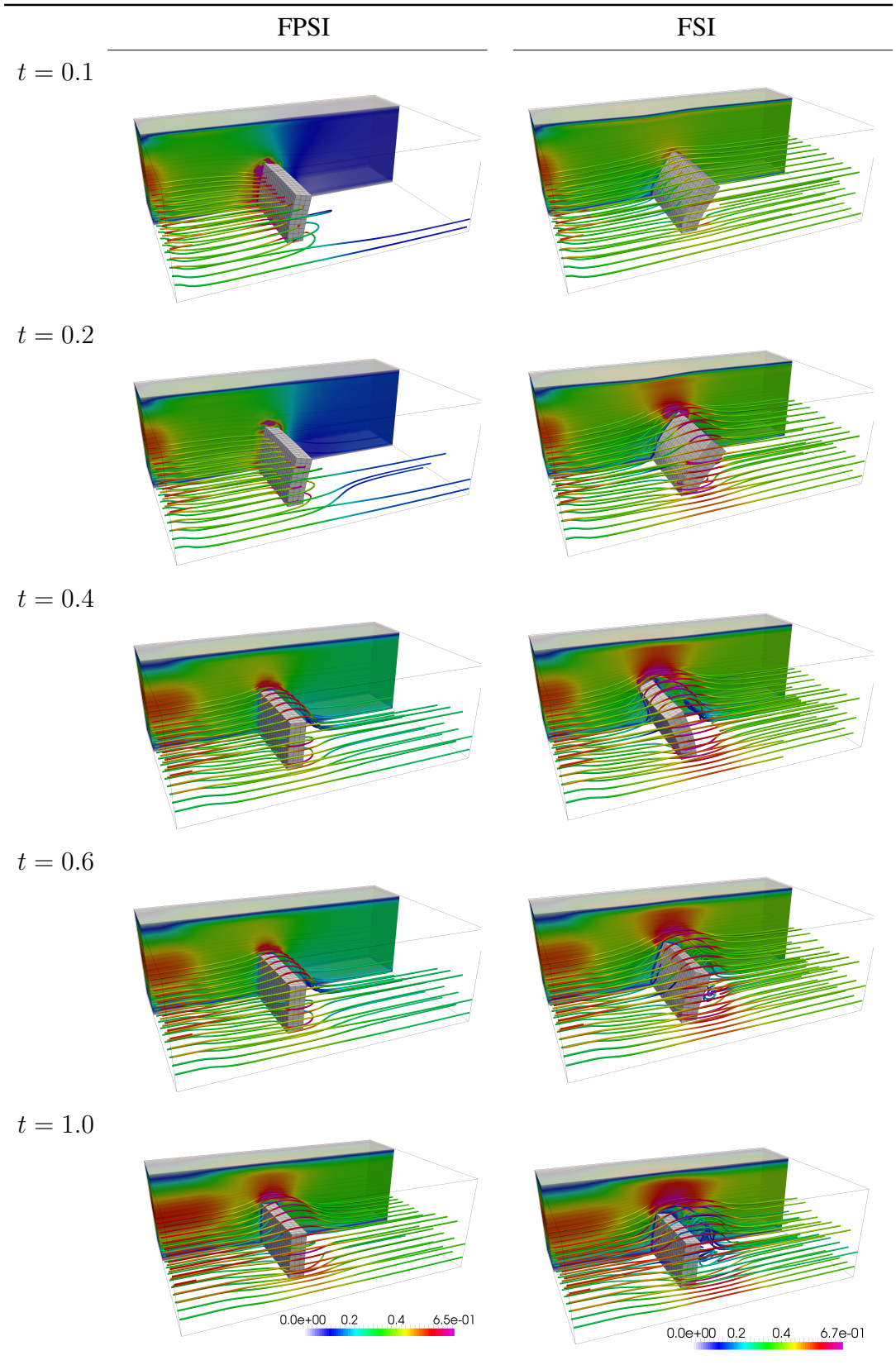

Figure 5.8: Comparison of fluid-porous-structure interaction (FPSI) and fluid-structure interaction (FSI). Streamlines at characteristic time instances. Colors denote velocity magnitude.

5.3. Passive Scalar Transport within Porous Medium

This chapter will treat the model for scalar transport within a porous continuum. Transport processes play an important role in many applications. For instance, in electro-chemical engineering, ion transport within batteries is analyzed, see e.g. [152, 173], and also in biological problems, transport of various chemical species involved in tumor growth [222] and cell mechanics [143] is modeled as such a transport process.

5.3.1. Problem Statement

For describing scalar transport within a porous medium, the governing equations on the microscale are homogenized to the macroscale. It is refered to the textbook [25] for a introduction to the averaging procedure. A system of k scalars is considered. For the i-th scalar c_i^{f}, with $i = 1, \dots, k$, transported within the fluid, one obtains

$$\left.\frac{\partial \phi c_i^{\mathrm{f}}}{\partial t}\right|_{\boldsymbol{x}} + \boldsymbol{\nabla}\cdot\left(\phi c_i^{\mathrm{f}} \boldsymbol{v}^{\mathrm{f}}\right) - \boldsymbol{\nabla}\cdot\left(\phi \boldsymbol{D}_i^{\mathrm{f,eff}} \cdot \boldsymbol{\nabla} c_i^{\mathrm{f}}\right) - \phi \sigma_i^{\mathrm{f}}(\boldsymbol{c}) = 0. \tag{5.21}$$

Therein, the second-order tensor $\boldsymbol{D}_i^{\mathrm{f,eff}}$ denotes the *effective macroscopic diffusivity*. It accounts for all effects that are observed as diffusion-like on the macroscale, see Appendix A.1.2 for further comments. All scalar quantities are summarized within the vector $\boldsymbol{c}$, indicating that the reaction term $\sigma_i^{\mathrm{f}}(\boldsymbol{c})$ potentially depends on all involved scalars. Equation (5.21) represents the conservative formulation of the macroscopic, instationary advection-diffusion-reaction problem in Eulerian form. A detailed derivation can be found in Appendix A.1.2. As the porous medium is deforming, the equation will be reformulated with respect to a moving observer, similar to an Arbitrary-Lagrangean-Eulerian (ALE) formulation. This can be done by replacing the local time derivative $\partial(\phi c_i^{\mathrm{f}})/(\partial t)\big|_{\boldsymbol{x}}$ by

$$\left.\frac{\partial \phi c_i^{\mathrm{f}}}{\partial t}\right|_{\boldsymbol{x}} = \left.\frac{\partial \phi c_i^{\mathrm{f}}}{\partial t}\right|_{\boldsymbol{X}} - \boldsymbol{\nabla}(\phi c_i^{\mathrm{f}}) \cdot \boldsymbol{v}^{\mathrm{s}}, \tag{5.22}$$

using the structural velocity $\boldsymbol{v}^{\mathrm{s}}$ and material time derivatives with respect to the porous solid phase. Here, $\boldsymbol{x}$ and $\boldsymbol{X}$ denote the spatial coordinate and the material coordinate of the macroscopic structure phase, respectively. Inserting equation (5.22) into equation (5.21) leads to

$$\left.\frac{\partial \phi c_i^{\mathrm{f}}}{\partial t}\right|_{\boldsymbol{X}} - \boldsymbol{\nabla}(\phi c_i^{\mathrm{f}}) \cdot \boldsymbol{v}^{\mathrm{s}} + \boldsymbol{\nabla}\cdot\left(\phi c_i^{\mathrm{f}} \boldsymbol{v}^{\mathrm{f}}\right) - \boldsymbol{\nabla}\cdot\left(\phi \boldsymbol{D}_i^{\mathrm{f,eff}} \cdot \boldsymbol{\nabla} c_i^{\mathrm{f}}\right) - \phi \sigma_i^{\mathrm{f}}(\boldsymbol{c}) = 0. \tag{5.23}$$

Applying the product rule and introducing the convective velocity $\boldsymbol{v}^{\mathrm{c}} = \boldsymbol{v}^{\mathrm{f}} - \boldsymbol{v}^{\mathrm{s}}$ yields

$$\begin{aligned} &\phi \left.\frac{\partial c_i^{\mathrm{f}}}{\partial t}\right|_{\boldsymbol{X}} + \phi \boldsymbol{\nabla} c_i^{\mathrm{f}} \cdot \boldsymbol{v}^{\mathrm{c}} - \boldsymbol{\nabla}\cdot\left(\phi \boldsymbol{D}_i^{\mathrm{f,eff}} \cdot \boldsymbol{\nabla} c_i^{\mathrm{f}}\right) + \\ &+ c_i^{\mathrm{f}} \left(\left.\frac{\partial \phi}{\partial t}\right|_{\boldsymbol{X}} + \phi \boldsymbol{\nabla}\cdot\boldsymbol{v}^{\mathrm{f}} + \boldsymbol{\nabla}\phi \cdot \boldsymbol{v}^{\mathrm{c}} \right) - \phi \sigma_i^{\mathrm{f}}(\boldsymbol{c}) = 0. \end{aligned} \tag{5.24}$$

Inserting the conservation of fluid mass, i.e.

$$\left.\frac{\partial \phi}{\partial t}\right|_{\boldsymbol{X}} + \phi \boldsymbol{\nabla} \cdot \boldsymbol{v}^{\mathrm{f}} + \boldsymbol{\nabla} \phi \cdot \boldsymbol{v}^{\mathrm{c}} = 0, \tag{5.25}$$

into equation (5.24) finally gives the convective formulation of the macroscopic, instationary advection-diffusion-reaction problem within a deforming porous continuum:

$$\phi \left.\frac{\partial c_i^{\mathrm{f}}}{\partial t}\right|_{\boldsymbol{X}} + \phi \boldsymbol{\nabla} c_i^{\mathrm{f}} \cdot \boldsymbol{v}^{\mathrm{c}} - \boldsymbol{\nabla} \cdot \left(\phi \boldsymbol{D}_i^{\mathrm{f,eff}} \cdot \boldsymbol{\nabla} c_i^{\mathrm{f}} \right) - \phi \sigma_i^{\mathrm{f}}(\boldsymbol{c}) = 0. \tag{5.26}$$

As boundary condition, the normal diffusive flux is prescribed at the Neumann boundary Γ_i^{N}

$$\hat{h}_i = \left(\phi \boldsymbol{D}_i^{\mathrm{f,eff}} \cdot \boldsymbol{\nabla} c_i^{\mathrm{f}} \right) \cdot \boldsymbol{n}. \tag{5.27}$$

This short derivation has been performed for a scalar c_i^{f} transported within the fluid. For a scalar c_i^{s} transported within the structure phase, analogous calculus leads to

$$(1-\phi) \left.\frac{\partial c_i^{\mathrm{s}}}{\partial t}\right|_{\boldsymbol{X}} - \boldsymbol{\nabla} \cdot \left((1-\phi) \boldsymbol{D}_i^{\mathrm{s,eff}} \cdot \boldsymbol{\nabla} c_i^{\mathrm{s}} \right) - (1-\phi) \sigma_i^{\mathrm{s}}(\boldsymbol{c}) = 0. \tag{5.28}$$

The second-order tensor $\boldsymbol{D}_i^{\mathrm{s,eff}}$ denotes the effective macroscopic diffusivity of the solid phase and $\sigma_i^{\mathrm{s}}(\boldsymbol{c})$ the reaction term. The differences between the equation (5.26) and equation (5.28) are essentially that the porosity ϕ, representing the volume fraction of the fluid is replaced by the volume fraction $1-\phi$ of the solid and that the convective velocity in the solid phase is zero. If no diffusion takes place inside the structure (i.e. $\boldsymbol{D}_i^{\mathrm{s,eff}} = \boldsymbol{0}$), as will be the case for the examples, equation (5.28) simplifies to

$$\left.\frac{\partial c_i^{\mathrm{s}}}{\partial t}\right|_{\boldsymbol{X}} - \sigma_i^{\mathrm{s}}(\boldsymbol{c}) = 0. \tag{5.29}$$

This equation obviously states, that the only driving force of change of a solid-bound scalar is reaction. Often, it is reasonable to utilize this plain form of the transport equation, as diffusion and convection processes inside the solid are very small compared to the corresponding processes in the fluid phase. For instance, the collagen concentration will be calculated according to equation (5.29) in the numerical examples in Section 5.4.5.

5.3.2. Solution Scheme

As for all problems in this thesis, the FEM is used for solving the governing equations of scalar transport. In the following, the FE formulation of equation (5.26) will be given exemplarily. The FE formulation of equations (5.28) and (5.29) can be obtained analogously. After discretization in time (for instance, with the generalized-α method), multiplication with a test function δc and integration over the domain, the following discrete weak form can be derived:

Find $c^{\mathsf{h}} \in \mathcal{S}_{\mathrm{c}}^{\mathsf{h}}$, such that $\forall \delta c^{\mathsf{h}} \in \mathcal{V}_{\mathrm{c}}^{\mathsf{h}}$:

$$\begin{aligned}\left(\delta c^{\mathsf{h}}, \phi^{\mathsf{h}}_{n+\alpha_f} \dot{c}^{\mathsf{h}}_{n+\alpha_m}\right)_{\Omega(t_{n+1})} + \left(\delta c^{\mathsf{h}}, \phi^{\mathsf{h}}_{n+\alpha_f} \boldsymbol{\nabla} c^{\mathsf{h}}_{n+\alpha_f} \cdot \boldsymbol{v}^{\mathrm{c},\mathsf{h}}_{n+\alpha_f}\right)_{\Omega(t_{n+1})} \\ + \left(\boldsymbol{\nabla}\delta c^{\mathsf{h}}, \phi^{\mathsf{h}}_{n+\alpha_f} \boldsymbol{D}^{\mathrm{eff}} \cdot \boldsymbol{\nabla} c^{\mathsf{h}}_{n+\alpha_f}\right)_{\Omega(t_{n+1})} - \left(\delta c^{\mathsf{h}}, \phi^{\mathsf{h}}_{n+\alpha_f} \sigma(\boldsymbol{c}^{\mathsf{h}}_{n+\alpha_f})\right)_{\Omega(t_{n+1})} \\ - \left(\delta c^{\mathsf{h}}, h_{n+\alpha_f}\right)_{\Gamma^{\mathrm{N}}(t_{n+1})} = 0. \qquad (5.30)\end{aligned}$$

Therein, the index 'i' of the considered scalar and the index 'f' denoting the fluid phase were omitted for clarity of notation. The spaces $\mathcal{S}_{\mathrm{c}}^{\mathsf{h}}$ and $\mathcal{V}_{\mathrm{c}}^{\mathsf{h}}$ are the usual finite element spaces. Primarily first-order Lagrange elements will be used. Note that stabilization of the discrete form (5.30) is necessary in case of high convection. Even though Streamline-Upwind-Petrov-Galerkin (SUPG) stabilization [22] has been implemented for this equation, it will not be considered here, since the problems analyzed are diffusion-dominated. The resulting system of non-linear equations is solved with a Newton-Raphson scheme.

In this section, passive transport of scalar quantities is considered. This means that the transport processes are influenced by the solution of the porous medium system, but not vice versa. The fluid and skeleton velocities determine the convective transport, and the movement of the domain is prescribed by the skeleton deformation. The scalar values, however, do not influence the porous medium. Hence, in contrast to the porous medium problem itself, a staggered, one-way coupled methodology is an adequate solution algorithm for this coupled system, schematically depicted in Figure 5.9. Within one time step t_n, the porous medium problem is solved first (still within a monolithic scheme). Then the displacement, velocity and pressure solution is transferred to the transport problem, which is solved afterwards. Subsequently, the algorithm proceeds to the next time step t_{n+1}.

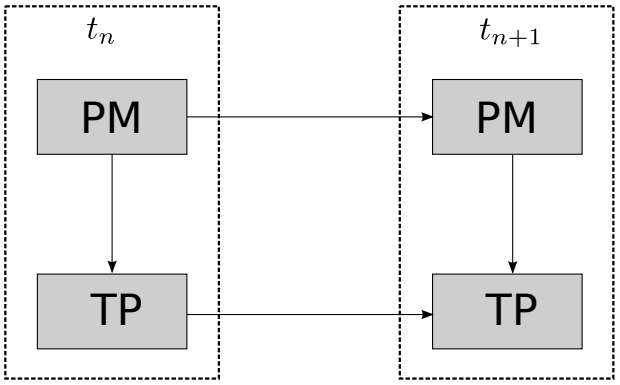

Figure 5.9: Staggered, one-way coupled solution scheme. Within one time step t_n the porous medium problem (PM) is solved. The solution of the PM problem is transferred to the transport problem (TP) and this is solved. Subsequently, the algorithm proceeds to the next time step t_{n+1}.

5.3.3. Numerical Example

A simple validation example for scalar transport within a deforming porous cube (edge length 1) is presented. No reactions are considered and the scalar is transported within the fluid phase. Examples including reactive terms in the fluid and solid phase are presented in the context of the application to cell mechanics in Section 5.4.5. The fluid flow is modeled with the Darcy-Brinkman equation and the mixed approach is utilized. On one side of the cube a fluid inflow

$$\hat{\boldsymbol{v}}^{\mathrm{f}} \cdot \boldsymbol{n} = \begin{cases} 0.25 \cdot (1.0 - \cos(0.2\pi t)) & \text{if} \quad t < 5.0 \\ 0.5 & \text{otherwise} \end{cases} \tag{5.31}$$

pointing in normal direction is prescribed. On the opposite side, the outflow, a zero-pressure boundary condition is applied. All other surfaces are impermeable with respect to fluid flow. The inflow surface is fixed. The whole cube is constrained as such it only deforms in flow direction (see Figure 5.10). The scalar is prescribed to be equal to 5.0 at the inflow surface. On all other surfaces the diffusive flux is zero. The initial porosity of the cube is 0.5. As constitutive equation for the pressure and porosity the Neo-Hookean-like law described in equations (3.82)–(3.84) is used with $\kappa = 5.0 \cdot 10^5$ and $\eta = 0.001$. The skeleton is modeled as Neo-Hookean material ($\rho^{\mathrm{s}} = 2.0$, $E = 1.0 \cdot 10^5$, $\nu = 0.3$). The fluid (density $\rho^{\mathrm{f}} = 1.0$) has a viscosity of $\mu^{\mathrm{f}} = 10.1$ and a constant material permeability of $K = 5 \cdot 10^{-5}$. The diffusivity of the scalar is set to $D = 0.001$. The cube is discretized with $10 \times 10 \times 10$ hexahedral tri-linear elements for each field. The structure, fluid and scalar transport meshes are conforming. The time step is 0.1 and 100 steps are simulated in total. For all fields a one-step-θ time integration scheme with $\theta = 0.66$ is used.

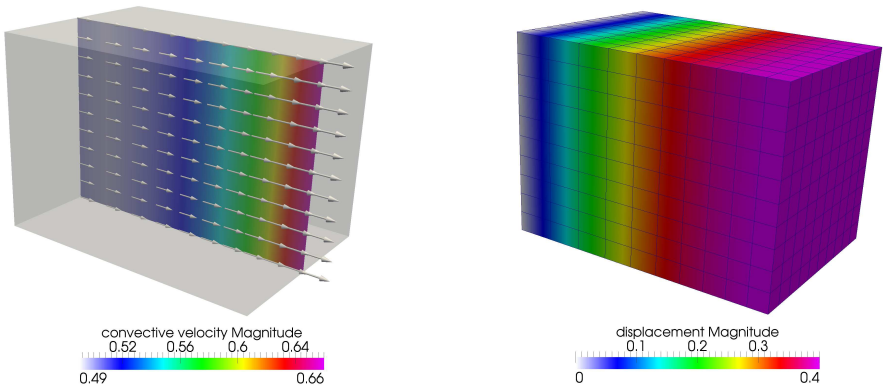

(a) Convective velocity at $t = 10$ (b) Displacement at $t = 10$

Figure 5.10: Scalar transport in porous cube: Global convective velocity field (left) and displacement field (right). Colors denote respective magnitudes.

Global results for convective velocity and displacement field are depicted in Figure 5.10. The cube is deforming in flow direction due to the fluid pressure. The convective velocity rises from inlet to outlet. This corresponds to the change in porosity in flow direction (see Figure 5.11). The scalar concentration is also behaving as expected (see Figure 5.12). The spatial distribution is equilibrating over time, mainly due to convection by the fluid flow. As validation the conservation of mass is checked. The fluxes into and out of the domain, $\int \phi(\boldsymbol{v}^{\mathrm{f}} - \boldsymbol{v}^{\mathrm{s}}) \cdot \boldsymbol{n} \, \mathrm{d}\Gamma$, are equal to the

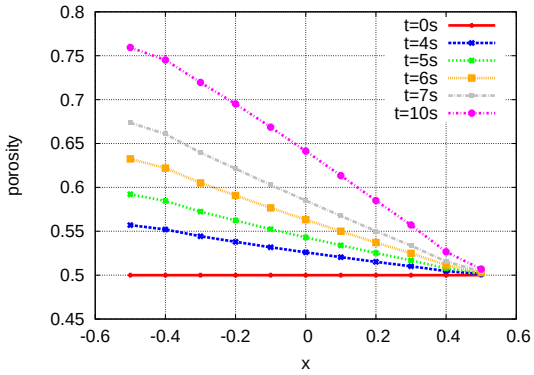

Figure 5.11: Porosity in flow direction at representative time instances.

rate $(M^{n+1} - M^n)/\Delta t$ of the integrated concentration over the porous volume, with the total mass at time step n being $M^n = \int \phi c \, \mathrm{d}\Omega_{t^n}$, see Figure 5.12.

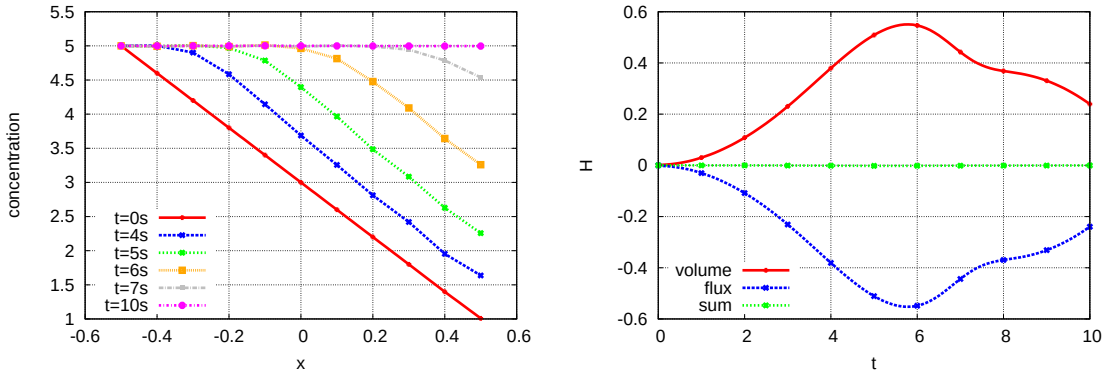

Figure 5.12: Solution for scalar field in porous flow through porous cube. Left: Scalar concentration in flow direction. Right: Conservation of scalar. The fluxes into and out of the domain $\int \phi(\boldsymbol{v}^{\mathrm{f}} - \boldsymbol{v}^{\mathrm{s}}) \cdot \boldsymbol{n} \, \mathrm{d}\Gamma$ are denoted as 'flux', the rate $(M^{n+1} - M^n)/\Delta t$ is denoted as 'volume', with the total mass $M^n = \int \phi c \, \mathrm{d}\Omega_{t^n}$ at time step n . The sum of the two is denoted as 'sum'.

5.4. Towards a Model for Tissue and Cell Mechanics

A deeper understanding of the mechanics of living cells interacting with the extracellular matrix (ECM) is essential for various physiological and pathological processes, e.g., embryonic growth, wound healing, inflammatory response, angiogenesis and tumor metastasis [99]. Despite this outstanding importance, the detailed processes involved are not yet fully understood. Especially the influence of the ECM for regulating cell migration is still topic of current research [70, 257, 258]. Therefore, the long-term aim is to establish a comprehensive model enabling the study of individual cell migration with a specific focus on the influence of physical factors such as matrix stiffness and interstitial flow.

In this thesis a fully coupled model for transport and dissolution processes within a deforming ECM including interstitial flow is proposed, cf. [245]. It is utilized for modeling advection-diffusion-reaction processes within the ECM and on the cell membrane and its coupling to the properties of the mechanical system. A vast number of chemical species and processes interplay on the cellular level [62, 101]. During proteolysis, the ECM is dissolved due to biochemical reactions initiated by the cell. Experimental data suggest that the mechanical state of the ECM influences the dissolution rate [32, 98, 188, 209]. There, it is shown that ECM fibrils often show significantly different reaction kinetics when exposed to loading or strain. However, most mathematical models do not yet consider this specific interaction of mechanics and biochemistry.

The ECM is represented by the two phase porous medium model presented in Chapter 3 and 4. Similar porous medium approaches utilized in other biomechanical applications can e.g. be found in [144, 184, 224]. The flow is described by the Brinkman equation. Therein, considering a variable porosity and its impact on the geometrical structure and mechanical behaviour of the ECM is of major importance when aiming for a realistic model, as the porosity is altered significantly during cell migration either through pure mechanical deformation or biochemical proteolysis. Therefore, the mixed approach presented in Section 4.3.2.2.2 perfectly fits the requirements for this problem and will hence be used. The proteolysis is modeled as a dissolution process of the porous medium. Models for dissolution of porous media are known and often applied in soil mechanics, see e.g. [72, 77, 231]. Such concepts will be adapted for the degradation model. The kinetics of the chemical reactions inducing proteolysis are linked to the mechanical state of the collagen matrix by a change in chemical potential. The cell membrane is represented by a diffusion-reaction model on a curved surface. Also the coupling between species within the ECM volume and on the cell membrane due to chemical reactions is considered. Transport models for cell-interior mechanisms have been developed [78, 241] and also surface-volume coupled models for ECM degradation have been published in recent years [56, 76, 125, 144, 180]. Therein, detailed models for the expression of enzymes at the cell membrane and the advection-diffusion-reaction processes leading to proteolysis are presented. For a review of computational approaches for modeling cellular systems to study anti-angiogenic therapeutics in cancer the interested reader is referred to [97]. Many parameters and model reactions will be incorporated into the model. Still, dispite the growing interest in mathematical models for cellular processes, the influence of the matrix deformation is rarely considered in the literature. An extensive numerical model for cell invasion dynamics into a ECM was presented in [147]. There, the fiber network was resolved explicitly and not included in an averaged sense as in this thesis. The degradability is modeled by crosslinking and uncrosslinking events, i.e. the varying load bearing behaviour of the dissolving matrix is also considered. It further includes similar transport equations as given here and within the references given before, although interstitial flow, i.e. advective transport, is not taken into account. However, more importantly when compared to the model presented here, in [147] the reaction kinetics are assumed to be independent of the mechanical loading. A model which is capable of resolving this missing mechano-chemo coupling is presented here. It based on the explanations given by the author in [245]. Up to the author's knowledge, this is the first time a reactive surface-volume transport model with interstitial flow is extended by including a deformable macroscopic solid phase as well as dissolution processes depending on the structure's thermodynamical state and its influences on the mechanical characteristics of the ECM is proposed.

In Section 5.4.1 the solution scheme for scalar transport on curved boundaries will be presented. It is formulated in a general way and not only applicable to cell mechanics. Then, a short description of the handling of chemical reactions is given in Section 5.4.2. The core of the model is presented in Section 5.4.3 . The mathematical description of the dissolution process is elucidated there. The solution scheme is illustrated in Section 5.4.4 followed by numerical results in Section 5.4.5.

5.4.1. Scalar Transport on Curved Surfaces

Motivated by the application in cell mechanics the scalar transport framework was extended to scalar transport on curved surfaces. Many signaling processes, as well as the formation and dissociation of integrins and various proteolytic reactions take place on the membrane during cell migration, see e.g. [62, 75, 94]. Hence, the goal is to setup a framework for advection-diffusion-reaction equations of multiple scalars on curved surfaces which can be embedded into a bigger model for cell migration. Note, that even though the application is very specific, this sub-module is still independent and can also be applied to other problem settings. Therefore, in this section, the theory and the examples are written in a general way without a direct relation to cell mechanics. Its application to the more complex, coupled model will be addressed in the subsequent sections.

The theory of partial differential equations on manifolds is very extensive. The most popular forms in classical continuum mechanics are shell and beam theory. Therein, tensor analysis, like the definition of local coordinates and the evaluation of covariant derivatives, play a crucial role. For the diffusion equation, the mathematical theory is based on the Laplace-Beltrami operator, being the equivalent of the Laplace operator on curved surfaces. Detailed mathematical analysis of this operator is not in the scope of this thesis. The interested reader is referred to [207] for a thorough introduction to the underlying theory. Numerical analysis for transport processes on curved surfaces have been performed in recent years, see e.g. [86, 221] and the references therein. Also in the context of biomechanics and cell modeling, computational transport models on curved surfaces representing the cell membrane have been used extensively, see e.g. [56, 180, 181, 215, 236]. Here, the equations are restated in a matter-of-fact manner without going into detail about the finite element model.

A system of k scalars is considered. The instationary advection-diffusion-reaction equation for the i-th scalar c_i, with $i = 1, \dots, k$, reads

$$\frac{\partial c_i}{\partial t} + \boldsymbol{v}^{\mathrm{c}} \cdot \boldsymbol{\nabla}_\Gamma c_i + c_i \boldsymbol{\nabla}_\Gamma \cdot \boldsymbol{v} - \boldsymbol{\nabla}_\Gamma \cdot (D \boldsymbol{\nabla}_\Gamma c_i) - \sigma(\boldsymbol{c}) = 0. \tag{5.32}$$

As for scalar transport within a porous medium in Section 5.3.1, the diffusivity is denoted by D, the reactive term by $\sigma(\boldsymbol{c})$, the transport velocity by $\boldsymbol{v}$ and the convective velocity by $\boldsymbol{v}^{\mathrm{c}}$. The operator $\boldsymbol{\nabla}_\Gamma$ denotes the *tangential surface gradient*. It is defined as the projection of the full gradient along the surface normal $\boldsymbol{n}$

$$\boldsymbol{\nabla}_\Gamma = \left(\mathbf{1} - \boldsymbol{n}^{\mathrm{T}} \otimes \boldsymbol{n}\right) \cdot \boldsymbol{\nabla}. \tag{5.33}$$

Consequently, the *Laplace-Beltrami operator* $\boldsymbol{\Delta}_\Gamma$ of a quantity $(\bullet)$ is defined as the surface divergence of the surface gradient

$$\boldsymbol{\Delta}_\Gamma (\bullet) = \boldsymbol{\nabla}_\Gamma \cdot \boldsymbol{\nabla}_\Gamma (\bullet) = \operatorname{tr}\left(\left(\mathbf{1} - \boldsymbol{n}^{\mathrm{T}} \otimes \boldsymbol{n} \right) \cdot \boldsymbol{\nabla} (\bullet) \right). \tag{5.34}$$

The basic assumption behind equation (5.32) is that there is no flux in normal direction

$$\boldsymbol{q} \cdot \boldsymbol{n} = 0. \tag{5.35}$$

Note, that in the form presented here this assumption holds for both convective and diffusive flux. However, this is not necessary in theory. For instance, it might be useful to include convection off the surface. Then, the second term in equation (5.32) would include the full gradient instead of the surface gradient. This form will not be discussed here.The divergence theorem and integration by parts also hold equivalently for the surface gradient and surface divergence [86]. Therefore, the methodology to obtain the weak and discrete form do not change in comparison to scalar transport on plane surfaces or volumes.

5.4.1.1. Solution Approach

The FE scheme is very similar to the one presented in Section 5.3.2. After discretization in time (for instance, with the generalized-α method), multiplication with a test function δc, integration and discretization in space, one obtains the following discrete weak form:

Find $c^{\mathsf{h}} \in \mathcal{S}_{\mathrm{c}}^{\mathsf{h}}$, such that $\forall \delta c^{\mathsf{h}} \in \mathcal{V}_{\mathrm{c}}^{\mathsf{h}}$:

$$\begin{aligned} &\left(\delta c^{\mathsf{h}}, \dot{c}^{\mathsf{h}}_{n+\alpha_m}\right)_{\Omega(t_{n+1})} + \left(\delta c^{\mathsf{h}}, \boldsymbol{v}^{\mathrm{c},\mathsf{h}}_{n+\alpha_f} \cdot \boldsymbol{\nabla}_\Gamma c^{\mathsf{h}}_{n+\alpha_f}\right)_{\Omega(t_{n+1})} + \left(\delta c^{\mathsf{h}}, c^{\mathsf{h}}_{n+\alpha_m} \boldsymbol{\nabla}_\Gamma \cdot \boldsymbol{v}^{\mathsf{h}}_{n+\alpha_m}\right)_{\Omega(t_{n+1})} \\ &+ \left(\boldsymbol{\nabla}_\Gamma \delta c^{\mathsf{h}}, D \boldsymbol{\nabla}_\Gamma c^{\mathsf{h}}_{n+\alpha_f}\right)_{\Omega(t_{n+1})} - \left(\delta c^{\mathsf{h}}, \sigma(c^{\mathsf{h}}_{n+\alpha_f})\right)_{\Omega(t_{n+1})} - \left(\delta c^{\mathsf{h}}, h_{n+\alpha_f}\right)_{\Gamma^{\mathrm{N}}(t_{n+1})} = 0. \end{aligned} \tag{5.36}$$

Therein, the subscript 'i' is omitted for clarity of notation. The spaces $\mathcal{S}_{\mathrm{c}}^{\mathsf{h}}$ and $\mathcal{V}_{\mathrm{c}}^{\mathsf{h}}$ are the usual finite element spaces. Primarily first-order Lagrange elements will be used. The Neumann boundary fluxes are denoted by $h_{n+\alpha_f}$. For a closed surface, this term vanishes. Note, that further stabilization of the discrete form (5.30) is necessary for high convection. Streamline-Upwind-Petrov-Galerkin (SUPG) stabilization, see e.g. [22], is implemented for this equation. If not stated otherwise, it will be neglected in the numerical examples, as the processes on the cell membrane are diffusion-dominated. The resulting system of non-linear equations is solved with a Newton-Raphson scheme.

5.4.1.2. Numerical Examples

The examples presented here are purely academic and meant to validate and analyze different aspects of the formulation and the implementation. Therefore, in all examples, a simplified form of equation (5.32) is solved focusing on specific parts of the transport process. Whenever possible the results will be compared to analytical, exact solutions or to numerical results given in the literature. A more complex coupled example including scalar transport on a curved boundary, is presented later in Section 5.4.5.

5.4.1.2.1. Diffusion on Unit Sphere

The given problem is a unit sphere with the initial field

$$c(\boldsymbol{x}, t = 0) = xy + 10, \tag{5.37}$$

see Figure 5.13. Only diffusive transport and no movement of surface is considered here. Thus,

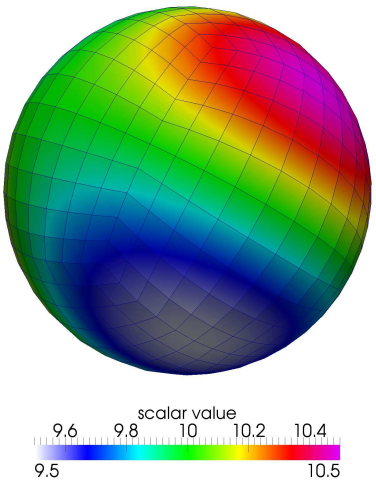

Figure 5.13: Diffusion on unit sphere: Initial scalar field.

the heat equation

$$\frac{\partial c}{\partial t} - D\boldsymbol{\Delta}_\Gamma c = 0 \tag{5.38}$$

is solved on the surface of the sphere. The exact solution $\bar{c}(\boldsymbol{x}, t)$ of this instationary diffusion problem can be derived, see [86] or Appendix A.3.3, as

$$\bar{c}(\boldsymbol{x}, t) = xye^{-6Dt} + 10. \tag{5.39}$$

The solution for the tangential gradient then follows as

$$\boldsymbol{\nabla}_\Gamma \bar{c}(\boldsymbol{x}, t) = (\mathbf{1} - \boldsymbol{n} \otimes \boldsymbol{n}) \cdot \boldsymbol{\nabla} \bar{c} = \begin{pmatrix} (1 - 2x^2)\, y \\ (1 - 2y^2)\, x \\ -2xyz \end{pmatrix} \cdot e^{-6Dt}. \tag{5.40}$$

The total time is $T = 2.0$. For the convergence analysis, the following relative norms are defined

$$L_\infty\left(L_2\right) = \sup_{(0,T)} \frac{||c - \bar{c}||_{L_2}}{||\bar{c}||_{L_2}}, \tag{5.41}$$

$$L_2\left(L_2\right) = \left(\int_0^T \frac{||c - \bar{c}||_{L_2}}{||\bar{c}||_{L_2}} \,\mathrm{d}t\right)^{0.5}, \tag{5.42}$$

$$L_\infty\left(H_1\right) = \sup_{(0,T)} \frac{||c - \bar{c}||_{H_1}}{||\bar{c}||_{H_1}}, \tag{5.43}$$

$$L_2\left(H_1\right) = \left(\int_0^T \frac{||c - \bar{c}||_{H_1}}{||\bar{c}||_{H_1}} \,\mathrm{d}t\right)^{0.5}. \tag{5.44}$$

Figure 5.14 shows the spatial convergence of problem (5.38) with $D = 1$. The time step was adapted to the element size, that is $\Delta t \sim h^2$, starting with $\Delta t = 1.0$ for the coarsest mesh ($h \approx 0.04$). The spatial L_2-norms (5.41) and (5.42) converge with approximate order of $O(\frac{1}{h^2})$, while

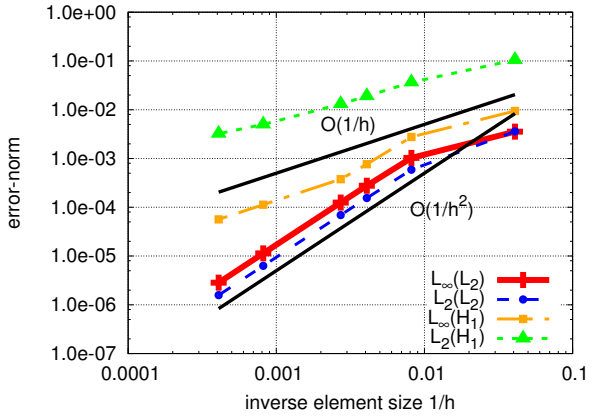

Figure 5.14: Diffusion on unit sphere: Convergence of error norms.

the H_1-norms (5.43) and (5.44) converge with approximate order of $O(\frac{1}{h})$. These convergence rates are in accordance with the results given in [86].

5.4.1.2.2. Advection-Diffusion on Torus

This example is meant to analyze the effect of the convective term. Movement of the surface and reactive terms are neglected in this example. Thus, the equation that is solved reads

$$\frac{\partial c}{\partial t} + \hat{\boldsymbol{v}} \cdot \boldsymbol{\nabla}_\Gamma c - \boldsymbol{\nabla}_\Gamma \cdot (D \boldsymbol{\nabla}_\Gamma c) = 0. \tag{5.45}$$

The geometry is the surface of a torus, see Figure 5.15. For a complete description of the geometry the major radius $R = 5$, the minor radius $r = 1$ and the two angles α and β are introduced in the figure.

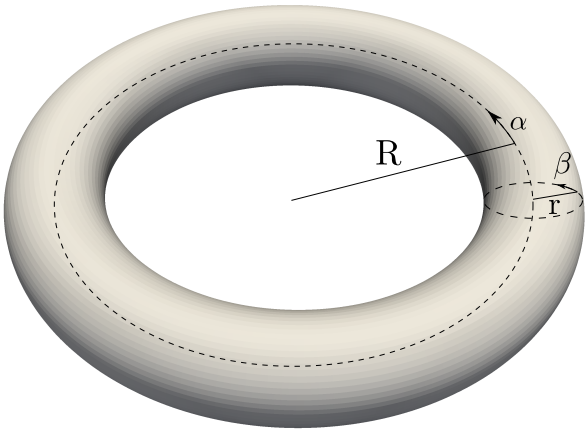

Figure 5.15: Advection-Diffusion on torus: Geometry, with major radius $R = 5$ and minor radius $r = 1$. For parameterization, the angles α and β are used.

As initial field, a Gaussian hill of the form

$$c(\boldsymbol{x}, t = 0) = 1.0 \cdot e^{-\left(\left(\frac{\alpha R}{0.5}\right)^2 + \left(\frac{(\beta - 0.5\pi)r}{0.5}\right)^2\right)} \tag{5.46}$$

is prescribed. The transport velocity field $\boldsymbol{v}$ is defined as follows:

$$\hat{\boldsymbol{v}}(\boldsymbol{x}, t) = \frac{2}{\sqrt{5}\,\|\boldsymbol{e}_\alpha\|}\boldsymbol{e}_\alpha + \frac{1}{\sqrt{5}r}\boldsymbol{e}_\beta, \tag{5.47}$$

with the basis vectors $\boldsymbol{e}_\alpha$ and $\boldsymbol{e}_\beta$ corresponding to the respective angles α and β. For information how the initial scalar field and the velocity can be expressed in Cartesian coordinates, see Appendix A.3.4. For discretization, approximately 19100 bi-linear 4-node elements of size $h = 0.1$ are used and a one-step-θ scheme with $\theta = 0.5$ is applied. SUPG stabilization is utilized. The time step is set to $\Delta t = 0.1$, which corresponds to a *Courant number* of

$$\mathrm{C} = \|\hat{\boldsymbol{v}}\|\,\frac{\Delta t}{h} = 1. \tag{5.48}$$

Different diffusion coefficients D are employed. This way, different *element Péclet numbers*

$$\mathrm{Pe}_e = \|\hat{\boldsymbol{v}}\|\,\frac{h}{2D} \tag{5.49}$$

can be analyzed. The Courant number gives the number of elements passed by a particle within one time step and the element Péclet number relates advective and diffusive flux on an element. In Figure 5.16 the evolution over time of the maximum scalar value is shown. Clearly, the higher the element Péclet number, the less diffusion is within the system. Thus, the maximum value decreases the fastest for the smallest Péclet number. Also, slight oscillations can be observed in Figure 5.16. The amplitude of those oscillations rises with the element Péclet number. Those instabilities are more apparent, when considering the global solution, see Figure 5.17. As seen

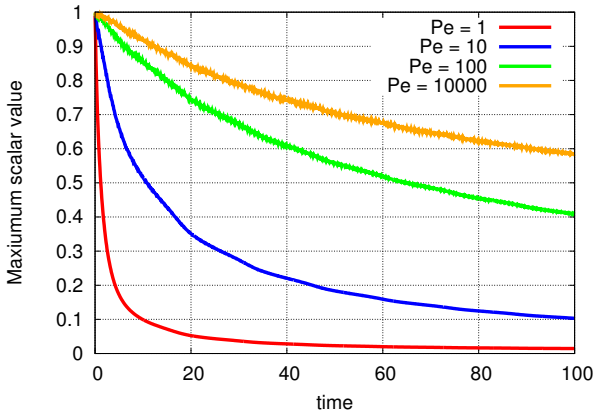

Figure 5.16: Advection-Diffusion on torus: Evolution over time of maximum scalar value. Results for different element Péclet numbers.

before, the scalar diffuses quickly for small element Péclet numbers. For larger values of the element Péclet number, the convection becomes more dominant and the Gaussian hill is still visible at later time instances. Further, oscillations in space are evident especially for higher element Péclet numbers. This phenomenon is known from scalar transport on plane surfaces, see e.g. [82, chap. 5.6.1]. The oscillations originate from time integration errors. Higher-order methods in time or space-time methods can provide a gain in accuracy. As convection dominated problems are not the focus of this thesis, such methods are not discussed further here.

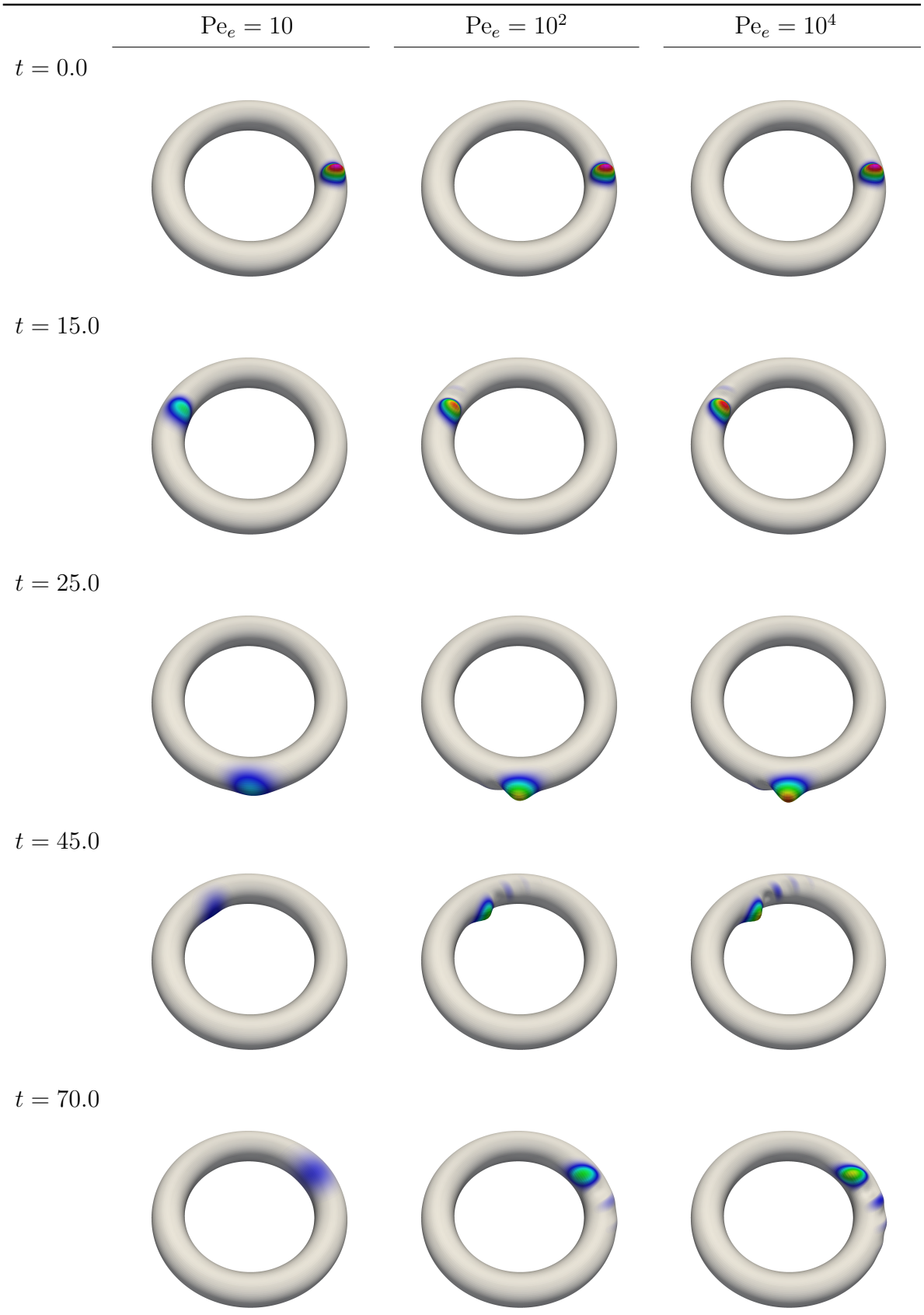

Figure 5.17: Advection-Diffusion on torus: Global solution at different time instances. The scalar value is plotted in normal direction of the surface.

5.4.1.2.3. Reaction-Diffusion on Torus

For validation of the reactive part of the transport equation, a simplified version of the so-called Allen-Cahn equation

$$\frac{\partial c}{\partial t} - \boldsymbol{\Delta}_\Gamma c + \frac{1}{\epsilon^2}\left(c - c^3\right) = 0, \tag{5.50}$$

with the positive parameter ϵ, is solved. The system equation (5.50) is composed of a transient, a diffusive and a non-linear reactive term. In this example, the parameter is set to $\epsilon^2 = 10^3$. The Allen-Cahn equation is used to model the motion of phase boundaries within iron alloys [8]. In this thesis, it is just used as an example for a non-linear reaction-diffusion problem without going into detail regarding the underlying physical assumptions. The problem setting is taken from [87]. The geometry considered is the surface of a torus described by

$$\left\{ \boldsymbol{x} \in \mathbb{R}^3 \,\middle|\, \left(\sqrt{x^2 + y^2} - 1\right)^2 + z^2 = \frac{1}{16} \right\}. \tag{5.51}$$

The initial field is prescribed as

$$c(\boldsymbol{x}, t = 0) = \sin(3\pi z)\cos(3\varphi), \tag{5.52}$$

see Figure 5.18(a). Therein, φ denotes the polar angle in the xy-plane. For discretization of the curved surface, approximately 4300, bi-linear 4-node elements are used. A generalized-α time integration scheme with $\rho_\infty = 0.9$ and time step $\Delta t = 10^{-4}$ is applied. The solution field at different time instances is depicted in Figure 5.18. There, it can be observed, that the distribution quickly rearranges into distinct patches of values -1 and 1 (Figure 5.18(b)). The size of the transition zone between the patches is controlled by the value of ϵ. After some time, this state collapses and the patches start uniting (Figure 5.18(c) and 5.18(d)). These observations are in accordance with the results given in [87].

5.4.1.2.4. Transport on Moving Curved Surfaces

In the previous examples regarding transport on curved boundaries the surface is not moving. This effect will be analyzed in this example. The equation to solve reads

$$\frac{\partial c}{\partial t} + c\boldsymbol{\nabla}_\Gamma \cdot \hat{\boldsymbol{v}} - D\boldsymbol{\Delta}_\Gamma c = 0. \tag{5.53}$$

Again, a very simple setup is chosen in order to verify the implementation. A unit sphere with a constant initial field

$$c(\boldsymbol{x}, t = 0) = 1 \tag{5.54}$$

is inflated by a given velocity field

$$\hat{\boldsymbol{v}}(\boldsymbol{x}, t) = \boldsymbol{n}(\boldsymbol{x}, t). \tag{5.55}$$

Note, that, as $\boldsymbol{v}$ always points in normal direction, the spherical form is preserved. Just its volume is increased. It can be easily derived (see Appendix A.3.4), that the exact surface divergence of

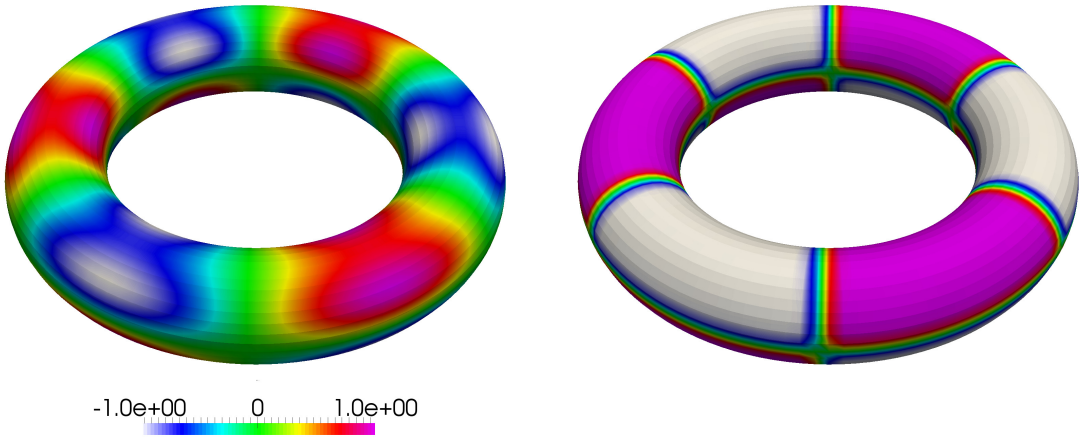

(a) $t = 0.0$ (b) $t = 0.01$

(c) $t = 0.1$ (d) $t = 0.2$

Figure 5.18: Allen-Cahn equation on torus: Solution field at different time instances.

the velocity field reads

$$\boldsymbol{\nabla}_\Gamma \cdot \hat{\boldsymbol{v}}(\boldsymbol{x}, t) = \frac{2}{t+1}, \tag{5.56}$$

and the exact solution for the scalar field immediately follows as

$$\bar{c}(\boldsymbol{x}, t) = \frac{1}{(t+1)^2}. \tag{5.57}$$

It has to be noted, that despite being simple, the presented example is suitable for testing the implementation for transport on moving surfaces. As shown in Appendix A.3.4 the surface divergence of the velocity is non-zero due to the curvature of the domain. This divergence term is the crucial term when moving surfaces are considered and, thus, no convergence could be achieved, if there were a miscalculation of this term. Convergence in time is checked in this example. Hence, for the spatial discretization a very fine mesh composed of 15000 bi-linear,

4-node elements is used. For time discretization, a one-step-θ scheme with $\theta = 1.0$ or $\theta = 0.5$ is applied. The total time is $T = 2.0$. The results for the convergence of the relative L_2-error norm $\int_0^T (||c - \bar{c}||_{L_2})/||\bar{c}||_{L_2} \, \mathrm{d}t$ are depicted in Figure 5.19. It can be seen, that both integration schemes show the theoretical convergence rate, that is first-order for $\theta = 1.0$ and second-order for $\theta = 0.5$.

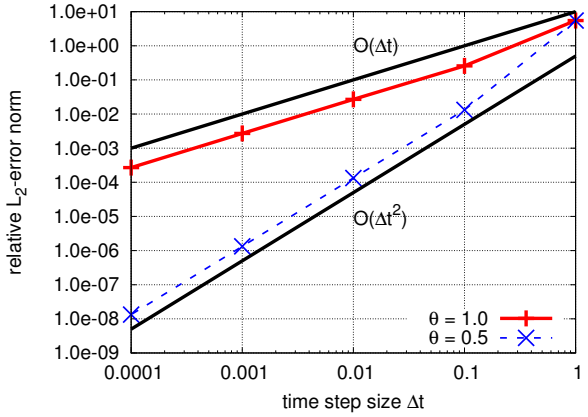

Figure 5.19: Inflated unit sphere: Relative L_2-error norm for different time integration parameters θ.

5.4.2. Chemical Reactions

For modeling chemical processes in cell mechanics, there is the necessity of incorporating a large number of reaction equations into the formulation. The reactions, more precisely the reaction kinetics, determine the form of the reaction terms $\sigma_i(\boldsymbol{c})$ in the transport equations (5.26), (5.28) and (5.32). For instance, for a reversible reaction with two reactants A and B and one product C the reaction equation would read

$$aA + bB \underset{k^-}{\overset{k^+}{\rightleftarrows}} cC, \tag{5.58}$$

with the stoichiometric coefficients a, b and c and the reaction rate coefficients k^+ and k^-. A simple form of a rate law for the respective molar concentrations $[A]$, $[B]$ and $[C]$ giving the corresponding reaction terms could then read

$$\sigma_A = -ak^+[A][B] + ak^-[C], \tag{5.59}$$
$$\sigma_B = -bk^+[A][B] + bk^-[C], \tag{5.60}$$
$$\sigma_C = ck^+[A][B] - ck^-[C]. \tag{5.61}$$

The coupling of the surface and the volume transport problem is established by reactions on the cell membrane including both chemical species bound to the membrane and chemical species transported within the ECM. One has to keep in mind, that a reaction between surface- and volume-bound species is a heterogeneous chemical reaction. Therefore, a characteristic length λ

to scale surface concentrations to volume concentrations is introduced, see e.g. [144]. For instance, if A were a surface-bound scalar and B and C volume-bound, the reaction terms including $[A]$ would be scaled with $1/\lambda$ (which results in a scaled effective reaction rate). The chemical reactions of the proposed model of proteolysis will follow the general scheme presented above. The specific reaction formulations will be elucidated in the respective examples.

5.4.3. Reactive Dissolving Porosity Model

This section is dedicated to a specific phenomenon in cell mechanics. That is, the degradation of the ECM due to chemical substances produced by cells. The idea is to formulate a model in which the porosity will change due to chemical reactions and not only to flow or solid deformation. This reproduces a dissolution effect of the porous medium. The following derivation is based on standard theory from physical chemistry applied on chemical reactions in a porous continuum. The basic theory of dissolving porosity models presented here can be found in more detail in [66]. For more extensive reviews about general thermodynamics in porous media it is referred to [28, 217].

The dissolution process induces the additional dissipation $\Phi^{\mathrm{s}}_{\mathrm{sol}} = -\mu_{\mathrm{sol}}\dot{m}_{\mathrm{s}\to\mathrm{sol}}$, with the chemical potential μ_{sol} of the solvent and the rate $\dot{m}_{\mathrm{s}\to\mathrm{sol}}$ of solid mass dissolving per reference volume. Thus, the total dissipation Φ^{s} of the structural phase, see equation (3.54) using equation (3.78), then reads for isothermal conditions

$$\Phi^{\mathrm{s}} = \boldsymbol{S} : \dot{\boldsymbol{E}} - \phi \boldsymbol{S}^{\mathrm{f}}_{\mathrm{visc}} : \dot{\boldsymbol{E}} + p^{\mathrm{f}} J \boldsymbol{C}^{-1} : \dot{\boldsymbol{E}} - p^{\mathrm{f}} \frac{\mathrm{d}^{\mathrm{s}} J^{\mathrm{s}}}{\mathrm{d}t} - \frac{\mathrm{d}^{\mathrm{s}} \Psi^{\mathrm{s}}}{\mathrm{d}t} - \mu_{\mathrm{sol}} \dot{m}_{\mathrm{s}\to\mathrm{sol}} \geq 0. \tag{5.62}$$

Next, the additional internal variable $\Delta\phi_{\mathrm{sol}} = \dot{m}_{\mathrm{s}\to\mathrm{sol}}/\rho^{\mathrm{s}}_0$ is introduced, representing the additional change of reference porosity (and therefore solid mass) due to the dissolution process. The Helmholtz free energy of the structure $\Psi^{\mathrm{s}}(\boldsymbol{E}, J^{\mathrm{s}}, \Delta\phi_{\mathrm{sol}})$ thus also depends on $\Delta\phi_{\mathrm{sol}}$ (the dependency of the free energy on the temperature is again neglected here). Hence, following standard procedure as in Section 3.5, equation (5.62) can be written as

$$\begin{aligned} \Phi^{\mathrm{s}} \;=\; & \left(\boldsymbol{S} - \phi \boldsymbol{S}^{\mathrm{f}}_{\mathrm{visc}} - \frac{\partial \Psi^{\mathrm{s}}}{\partial \boldsymbol{E}} + p^{\mathrm{f}} J \boldsymbol{C}^{-1} \right) : \dot{\boldsymbol{E}} + \left(p^{\mathrm{f}} + \frac{\partial \Psi^{\mathrm{s}}}{\partial J^{\mathrm{s}}} \right) \frac{\mathrm{d}^{\mathrm{s}} J^{\mathrm{s}}}{\mathrm{d}t} \\ & - \left(\frac{\partial \Psi^{\mathrm{s}}}{\partial (\Delta\phi_{\mathrm{sol}})} + \rho^{\mathrm{s}}_0 \mu_{\mathrm{sol}} \right) \frac{\mathrm{d}^{\mathrm{s}} \Delta\phi_{\mathrm{sol}}}{\mathrm{d}t} \geq 0. \end{aligned} \tag{5.63}$$

From that, the constitutive equations can be derived as

$$\boldsymbol{S} = \phi \boldsymbol{S}^{\mathrm{f}}_{\mathrm{visc}} + \frac{\partial \Psi^{\mathrm{s}}(\boldsymbol{E}, J^{\mathrm{s}}, \Delta\phi_{\mathrm{sol}})}{\partial \boldsymbol{E}} - p^{\mathrm{f}} J \boldsymbol{C}^{-1}, \qquad p^{\mathrm{f}} = -\frac{\partial \Psi^{\mathrm{s}}(\boldsymbol{E}, J^{\mathrm{s}}, \Delta\phi_{\mathrm{sol}})}{\partial J^{\mathrm{s}}}. \tag{5.64}$$

These two equations are constitutive equations of the porous medium very similar to the ones presented in equation (3.59). The only difference is the dependency of the stress and the pressure on $\Delta\phi_{\mathrm{sol}}$. The dissipation inequality that then needs to hold reads

$$- \left(\frac{\partial \Psi^{\mathrm{s}}}{\partial (\Delta\phi_{\mathrm{sol}})} + \rho^{\mathrm{s}}_0 \mu_{\mathrm{sol}} \right) \frac{\mathrm{d}^{\mathrm{s}} \Delta\phi_{\mathrm{sol}}}{\mathrm{d}t} \geq 0. \tag{5.65}$$

Further, using an analysis of the dissipation on the microscale and assuming only small changes of the chemical potential μ^{s} of the solid along the dissolution front, it can be shown [66, chap. 3.6.3] that

$$\rho_0^{\mathrm{s}} \left(\mu^{\mathrm{s}} - \mu_{\mathrm{sol}}\right) \frac{\mathrm{d}^{\mathrm{s}} \Delta\phi_{\mathrm{sol}}}{\mathrm{d}t} \geq 0, \tag{5.66}$$

and comparing equation (5.65) and (5.66) then gives

$$-\frac{\partial \Psi^{\mathrm{s}}}{\partial(\Delta\phi_{\mathrm{sol}})} = \rho_0^{\mathrm{s}} \mu^{\mathrm{s}} = \rho_0^{\mathrm{s}} \mu^{\mathrm{s}} = \rho_0^{\mathrm{s}} \left(\mu_0^{\mathrm{s}} + \Delta\mu^{\mathrm{s}}\right), \tag{5.67}$$

with the chemical potential μ_0^{s} of the undissolved state and the respective change $\Delta\mu^{\mathrm{s}}$ of chemical potential. For modeling the degradation process, the following adapted form of the Helmholtz free energy Ψ^{s} in equation (3.82) is proposed, adding the additional factor $\left(1 - \frac{\Delta\phi_{\mathrm{sol}}}{1-\phi_0}\right)$:

$$\Psi^{\mathrm{s}}(\boldsymbol{E}, J^{\mathrm{s}}, \phi_{\mathrm{ref}}) = \left(1 - \frac{\Delta\phi_{\mathrm{sol}}}{1-\phi_0}\right) W^{\mathrm{skel}}(\boldsymbol{E}) + W^{\mathrm{vol}}(J^{\mathrm{s}}, \phi_{\mathrm{ref}}) + W^{\mathrm{pen}}(\boldsymbol{E}, J^{\mathrm{s}}, \phi_{\mathrm{ref}}) + (1-\phi_{\mathrm{ref}}) \rho_0^{\mathrm{s}} \mu_0^{\mathrm{s}}, \tag{5.68}$$

with the Helmholtz free energy $W^{\mathrm{skel}}(\boldsymbol{E})$ of the undissolved, drained, macroscopic skeleton. Here, the energy term was expressed in terms of the reference porosity

$$\phi_{\mathrm{ref}} = \phi_0 + \Delta\phi_{\mathrm{sol}}, \tag{5.69}$$

which corresponds to the stress-free reference state. For $\Delta\phi_{\mathrm{sol}} = 0$ the original energy function is obtained. Note, that such approaches changing the energy formulation are quite common in continuum mechanics, whenever the reference state is evolving. For instance, damage models are similarly motivated [20]. Using the above presented approach for the strain energy function one then obtains for the pore pressure and the stress

$$p^{\mathrm{f}} = -\frac{\partial W^{\mathrm{vol}}(J^{\mathrm{s}}, \phi_{\mathrm{ref}})}{\partial J^{\mathrm{s}}} - \frac{\partial W^{\mathrm{pen}}(\boldsymbol{E}, J^{\mathrm{s}}, \phi_{\mathrm{ref}})}{\partial J^{\mathrm{s}}}, \tag{5.70}$$

$$\boldsymbol{S} = \phi \boldsymbol{S}_{\mathrm{visc}}^{\mathrm{f}} + \frac{\partial \Psi^{\mathrm{s}}(\boldsymbol{E}, J^{\mathrm{s}}, \phi_{\mathrm{ref}})}{\partial \boldsymbol{E}} - p^{\mathrm{f}} J \boldsymbol{C}^{-}. \tag{5.71}$$

Further, inserting equation (5.68) into equation (5.67) gives

$$\Delta\mu^{\mathrm{s}} = \frac{1}{\rho_0^{\mathrm{s}} \left(1 - \phi_0\right)} W^{\mathrm{skel}} - \frac{1}{\rho_0^{\mathrm{s}}} \frac{\partial \Psi^{\mathrm{s}}(\boldsymbol{E}, J^{\mathrm{s}}, \phi_{\mathrm{ref}})}{\partial \phi_{\mathrm{ref}}}. \tag{5.72}$$

Equation (5.72) represents a model for the change of chemical potential depending on the mechanical state which will be used to establish the mechano-chemical coupling. It is based solely on thermodynamical quantities without any unphysical parameters. As in classical solid continuum mechanics, the choice of the energy formulation Ψ^{s} determines the material behavior.

It should also be noted, that, as the reference porosity is allowed to change, the reference mass of the solid phase equivalently changes:

$$J\rho^{\mathrm{s}}(1-\phi) = \rho_0^{\mathrm{s}}(1-\phi_{\mathrm{ref}}) = m_{\mathrm{ref}}^{\mathrm{s}}. \tag{5.73}$$

This change of reference mass has no effect if quasi-static behavior of the solid phase is assumed. Otherwise, the inertia of the solid phase has to be adapted.

Now, it will be focused on the chemo-mechanical coupling specifically for proteolysis of the ECM. In order to establish a link to the chemical model, a relation between the structural density and the collagen concentration is needed. Providing that collagen is the dominant constituent of the ECM, the reference porosity is related to the molar concentration $[C1]$ of collagen type I by

$$[C1] = \frac{1}{J}\rho_{0,C}(1 - \phi_{\mathrm{ref}}), \tag{5.74}$$

with the molar density of collagen $\rho_{0,C}$ in $[\ \mathrm{mol}/\ \mathrm{m}^3]$. The factor $1/J$ represents a pull-back operation, as the molar concentration $[C1]$ is written with respect to a spatial volume, whereas the reference porosity refers to a volume in the material configuration. Next, the dissolution process due to matrix metalloproteinase (MMP) is considered. Experimental evidence suggest that mechanical strain stabilizes the ECM against proteolysis [32, 50, 98, 260]. Also, there is theoretical work proposing that mechanical strain provides thermodynamical stabilization by loss of configurational entropy of the collagen fibers [171]. However, there are also cases where the opposite is observed. In [6, 7] the preferential degradation due to MMP-1 of loaded collagen is reported. For a review of the current knowledge about collagen degradation mechanisms and the influence of mechanical load on the degradation rate see [53].

While the detailed mechanisms of collagen-enzyme interaction are still unclear, the effect observed in experiments is commonly an increasing or decreasing reaction rate. Here, the following law for a decreasing reaction rate coefficient k is used:

$$k = k_0 \exp\left(\frac{m_{\mathrm{mol,C1}}\Delta\mu^{\mathrm{s}}}{RT}\right), \tag{5.75}$$

with the reaction rate k_0 in the unloaded case, the molecular weight $m_{\mathrm{mol,C1}}$ of collagen, the gas constant R and the Temperature T. The reaction rate changes due to the change $\Delta\mu^{\mathrm{s}}$ of chemical potential of the structural phase. Equation (5.75) is comparable to the reaction rate equation fitted from experimental data in [6]. There, the reaction rate is directly related to the applied force by an exponential function. Hence, the chemical potential is used instead as coupling variable as it is more suitable for thermodynamical analysis and closer to the theoretical results from [171]. Also, note that equation (5.75) is very similar to the Arrhenius equation for reaction rates depending on temperature and activation energy, e.g. in [15], and therefore $\Delta\mu^{\mathrm{s}}$ can be interpreted as a change of the Gibbs energy of activation. The whole ECM degradation model is summarized schematically in Figure 5.20.

5.4.4. Solution Scheme

The porous medium and the scalar transport problem are solved with the FEM as presented in the Section 4 and 5.3. The mixed approach given in Section 4.3.2.2.2 is used for the porous system, as it is suitable for Darcy-Brinkman flow and porosity changes and also convenient for incorporating the dissolution equations altering the reference porosity. In contrast to the coupling between solid and fluid equations within the porous medium, the coupling of the scalar transport equations with the porous medium (solid or fluid) is rather one-directional. The deformation

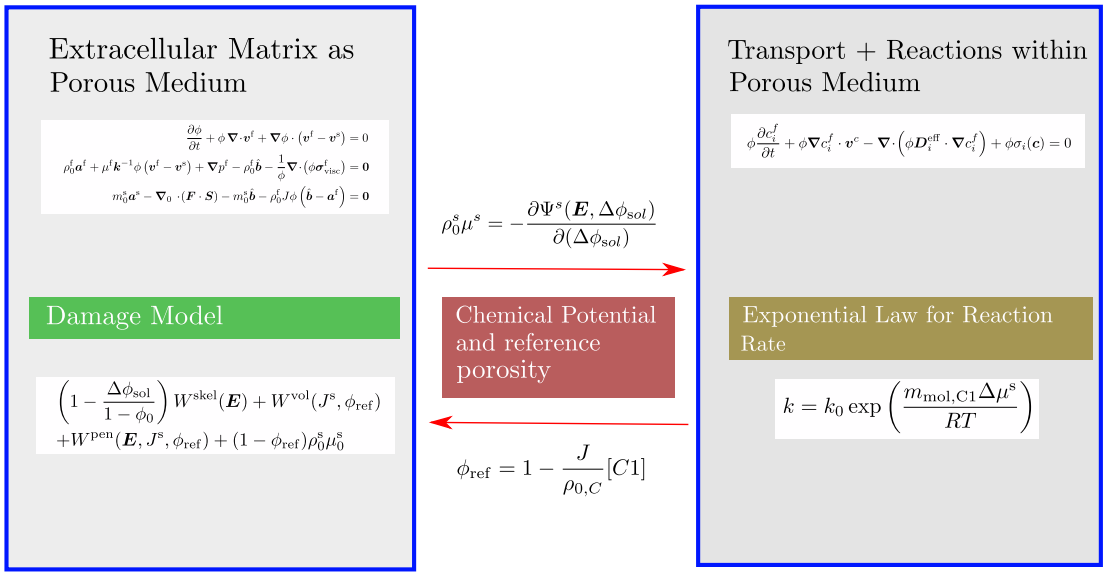

Figure 5.20: Schematic of ECM degradation model: The extracellular matrix is modeled as porous medium with damage model (left). The chemical side is represented by a transport and reaction framework of scalar quantities with changing reaction rate (right). The coupling is based on the chemical potential and a variable reference porosity (middle).

and the fluid velocity influence the scalar transport solution, while for passive transport, there is no coupling back to the porous medium. Even for reactive porous media, the coupling is typically rather weak, as the dissolution kinetics are slow compared to deformation and flow in the considered application. Therefore, a monolithic scheme for the poroelasticity-transport system is not necessary. A partitioned scheme is sufficient. Thus, the algorithm works as follows: Once the porous medium solution is converged, the displacement, porosity and velocity solution are transferred to the scalar transport problem, and any possible couplings (for instance equation (5.75)) are evaluated. The scalar transport fields within the volume and on the surface are also solved within a monolithic algorithm. Subsequently, the scalar solution, i.e. the concentrations of all involved species, are communicated to the porous medium problem and the fulfillment of the governing equations is checked based on the newly computed values. This whole global iteration procedure is repeated until a convergence criterion is met. Then, the algorithm proceeds to the next time step. A schematic of the whole algorithm is depicted in Figure 5.21.

5.4.5. Numerical Examples

The following two examples represent the first steps towards application of the presented methodology to tissue and cell mechanics. It comprises a comparison with experimental data and an extension of an existing numerical approach. The numerical results presented in this section are to be published in [245].

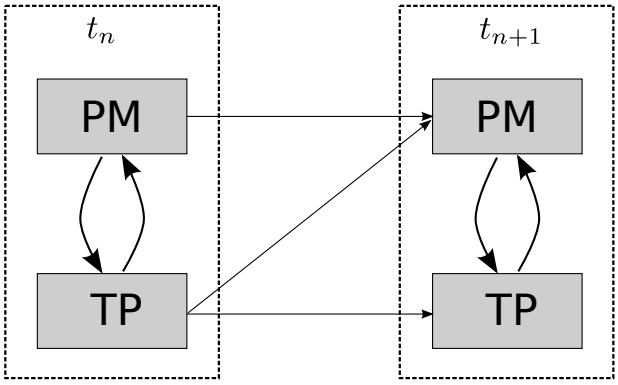

Figure 5.21: Partitioned, strongly coupled solution scheme. Within one time step t_n iterations between the porous medium (PM) and the transport problem (TP) are performed. After a convergence criterion is met, the algorithm proceeds to the next time step t_{n+1}.

5.4.5.1. Dissolution of Strained and Unstrained ECM

This example is motivated by the experimental studies in [32]. There, the strain dependency of the dissolution process was examined. A collagen micronetwork was pre-strained by displacing two micropipettes and exposed to bacterial collagenase. The amount of collagen fibers was estimated from optical images. An edge-intensity image processing method was used in order to obtain a measure for the collagen concentration. It is stated there, that the elapsed time between 5% and 90% edge loss is $\Delta T_{\mathrm{S}} = 1113\mathrm{s} \pm 260\mathrm{s}$ for strained fibrils and $\Delta T_{\mathrm{U}} = 654\mathrm{s} \pm 149\mathrm{s}$ for unstrained fibrils.

A computational model mimicking this experiment is set up and the numerical results are compared to the experimental data from [32]. The transport model comprises the following four chemical substances: Collagen type I $C1$ composing the ECM, the degrading enzyme E, the collagen-enzyme complex $C1E$ and the denatured collagen $C1^*$. The chemical reactions involved can be schematically represented by a Michaelis-Menten mechanism [98, 161]

$$C1 + E \underset{k^-}{\overset{k^+}{\rightleftarrows}} C1E \overset{k^{\mathrm{cat}}}{\rightarrow} C1^* + E, \tag{5.76}$$

where k^+, k^-, and k^{cat} denote the reaction rates. The kinetics are described by the following set of reaction terms

$$\sigma_{C1} = -k^+[C1][E] + k^-[C1E], \tag{5.77}$$
$$\sigma_{E} = -k^+[C1][E] + k^-[C1E] + k^{\mathrm{cat}}[C1E], \tag{5.78}$$
$$\sigma_{C1E} = +k^+[C1][E] - k^-[C1E] - k^{\mathrm{cat}}[C1E], \tag{5.79}$$
$$\sigma_{C1^*} = +k^{\mathrm{cat}}[C1E]. \tag{5.80}$$

The enzyme is transported within the porous fluid, while all other scalar quantities are bound to the solid phase of the ECM. Thus, the governing equation for the enzyme is obtained by inserting the reaction term (5.78) into equation (5.26) and the governing equations for the other species by inserting the respective reaction terms (5.77), (5.79) and (5.80) into equation (5.29).

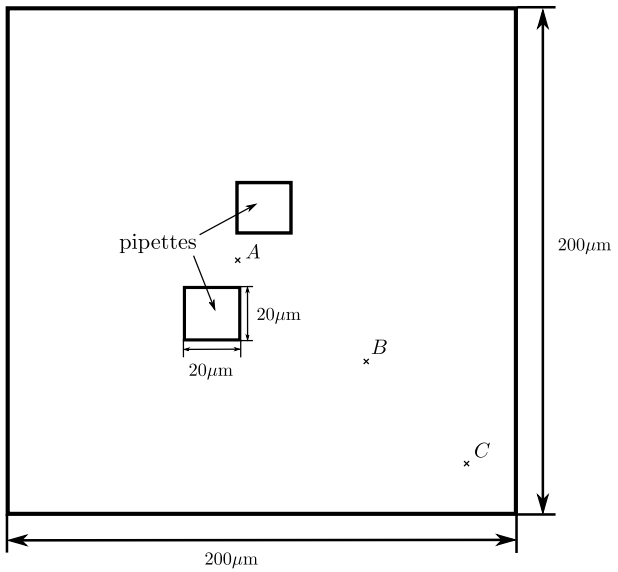

Figure 5.22: Dissolution example: Dimensions of computational domain, taken from [245]. The whole domain is square region with $200\ \mu\mathrm{m}$ edge length. The pipettes domain are two square regions with $20\ \mu\mathrm{m}$ edge length. The points A (center of domain), B and C denote the points where the collagen concentration will be evaluated.

As convective effects are very small, the flow of the fluid within the porous medium is not considered in this example. Instead, the focus lies on the mechano-chemical reaction model. The computational domain is a square of edge length of $200\ \mu\mathrm{m}$, see Figure 5.22. The support of the pipettes is represented by two square regions of edge length $20\,\mu\mathrm{m}$ near the center of the domain. A vertical displacement

$$\hat{d}^{\mathrm{s}}(t) = \begin{cases} \hat{d}^{\mathrm{s}}{}_{\max} \cdot 0.5 \cdot \left(1 - \cos\left(\frac{\pi}{30.0} t\right)\right) & \text{for } 0.0\,\mathrm{s} \leq t \leq 30\,\mathrm{s}, \\ \hat{d}^{\mathrm{s}}{}_{\max} & \text{else}, \end{cases} \tag{5.81}$$

is applied on the the lower pipette, while the upper pipette is fixed. The lower pipette is displaced downwards by a maximum magnitude $\hat{d}^{\mathrm{s}}{}_{\max} = 10\ \mu\mathrm{m}$ in vertical direction. This way, a strain around 50% can be established being similar to the loading in the reference experiment in [32]. The boundaries of the structural phase are modeled as traction free. The initial scalar concentrations are constant on the whole domain and set to

$$[C1]\,(t = 0\,\mathrm{s}) = 17.6 \frac{\mu\mathrm{mol}}{\mathrm{dm}^3}, \tag{5.82}$$

$$[E]\,(t = 0\,\mathrm{s}) = 0.0 \frac{\mu\mathrm{mol}}{\mathrm{dm}^3}, \tag{5.83}$$

$$[C1E]\,(t = 0\,\mathrm{s}) = 0.0 \frac{\mu\mathrm{mol}}{\mathrm{dm}^3}, \tag{5.84}$$

$$[C1^*]\,(t = 0\,\mathrm{s}) = 0.0 \frac{\mu\mathrm{mol}}{\mathrm{dm}^3}. \tag{5.85}$$

The initial value of $C1$ is taken from [144], where it is stated this roughly corresponds to a porosity of 0.99. In the same reference the porosity is calculated via the formula $1-\phi = 1.89\,[C1]_{\mathrm{m}} = 1.89\,m_{\mathrm{mol,C1}}[C1]$, with the mass concentration $[C1]_{\mathrm{m}}$ of collagen. From that, the initial molar density of collagen is deduced as $\rho_{0,C} = (1-\phi_0)/([C1]\,(t=0\,\mathrm{s})) = (1.89\,m_{\mathrm{mol,C1}})^{-1}$. Within the domain occupied by the pipettes, the enzyme concentration is prescribed as

$$[E]\,(t) = \begin{cases} 0.0\,\frac{\mu\mathrm{mol}}{\mathrm{dm}^3} & \text{for } 0\,\mathrm{s} \leq t \leq 30\,\mathrm{s}, \\ [E]_{\max} \cdot 0.5 \cdot \left(1 - \cos\left(\frac{\pi}{70.0}(t-30.0)\right)\right) & \text{for } 30\,\mathrm{s} < t \leq 100\,\mathrm{s}, \\ [E]_{\max} & \text{else}, \end{cases} \tag{5.86}$$

mimicking the dropping of the bacterial collagenase after the full strain was applied. The maximum value is estimated to be $[E]_{\max} = 55\ \mu\mathrm{mol}/\ \mathrm{dm}^3$, which is 3.125 times the initial collagen concentration, as stated in [32]. The enzyme will then diffuse inside the domain with the diffusion coefficient D_E , while collagen and the products of the collagenase are immobile [144], hence their diffusivity is zero. As the matrix is expected to exhibit non-linear constitutive behaviour [32], a Neo-Hookean material law for the mechanical model of the ECM, given by the strain energy function in equation (2.43), is assumed. The dissolution process is inhibited due to mechanical loading by modeling the reaction rate coefficient k^+ as presented in equation (5.75) to be variable, i.e.

$$k^+ = k_0^+ \exp\left(\frac{-m_{\mathrm{mol,C1}}\Delta\mu^{\mathrm{s}}}{RT}\right). \tag{5.87}$$

The other reaction rate coefficients are assumed to be constant. The rate constant k_0^+ is fitted, such that the kinetics of the unstrained collagen dissolution are similar to the experimental results in [32], i.e. that $\Delta T_{\mathrm{U}} \approx 700\,\mathrm{s}$. The rate constant k^- is then chosen as such, that the Michaelis constant $K_{\mathrm{m}} = (k^- + k^{\mathrm{cat}})/k_0^+$ is approximately $3.5\mu\mathrm{mol}$, which is within a realistic range [161]. The mass density $\rho_{0,C}$ of collagen was estimated to be in same order of magnitude as water. All necessary parameters for this example are summarized in Table 5.1. For the finite element discretization of the poroelastic and scalar transport problem, a regular mesh composed of 100×100 bi-linear, 4-node elements is used. The structural problem is assumed to be quasi-static, i.e. inertia terms are neglected. For the diffusion-reaction problem, a one-step-θ time integration scheme with the parameter $\theta = 0.66$ and a time step size $\Delta t = 2.5\,\mathrm{s}$ is utilized. The total simulation time amounts to $2000\,\mathrm{s}$.

The results for the Green-Lagrange strain and the Cauchy stress directly after the full displacement was applied are depicted in Figure 5.23. It shows that due the choice of material parameters of the structural phase, the strains are around 50% as desired and the stress values are also well in the range estimated in [32]. The resulting change in chemical potential is illustrated in Figure 5.24. As expected, it shows a similar spatial distribution as the strain and stress field. The evolution over time of the collagen I concentrations at three different points are shown in Figure 5.25. The point A is placed within the strained region, while the points B and C are located in a certain distance of the center of the domain (see Figure 5.22). As expected from the model formulation, the degradation process is slowed down significantly within the strained region. The point of time, where the degradation process starts, is different for each spatial point observed due to the diffusion time of the enzyme. As the point A is the closest to the pipettes the collagen concentration decreases there first. Only after a certain delay, there is a significant change of concentration in B and C. The degradation dynamics in point B and C do not differ

Quantity	Symbol	Value	Reference/Comment
Molecular mass of collagen	$m_{\mathrm{mol,C1}}$	$0.3\frac{\mathrm{g}}{\mu\mathrm{mol}}$	[144]
Collagen molar density	$\rho_{0,C}$	$1760\frac{\mu\mathrm{mol}}{\mathrm{dm}^3}$	estimated, see text
Collagen mass density	ρ_0^{s}	$1300\frac{\mathrm{g}}{\mathrm{dm}^3}$	see text
Initial porosity	ϕ_0	0.99	assumed
Gas constant	R	$8.3144\frac{\mathrm{J}}{\mathrm{K\,mol}}$	
Temperature	T	$310.15\,\mathrm{K}$	[32]
Reaction rate	k_0^+	$1.0\cdot10^{-4}\frac{\mathrm{dm}^3}{\mu\mathrm{mol\,s}}$	fitted, see text
Reaction rate	k^-	$3.5\cdot10^{-4}\frac{\mathrm{dm}^3}{\mu\mathrm{mol\,s}}$	fitted, see text
Reaction rate	k^{cat}	$3.1\cdot10^{-7}\frac{1}{\mathrm{s}}$	[161]
Young's modulus	E	$1.5\,\mathrm{kPa}$	estimated in [32]
Poisson's ratio	ν	0.3	assumed
Diffusivity of enzyme	D_E	$0.85\cdot10^{-8}\frac{\mathrm{dm}^2}{\mathrm{s}}$	MMP2 in water [30]
Max. enzyme concentration	$[E]_{\max}$	$55\frac{\mu\mathrm{mol}}{\mathrm{dm}^3}$	estimated from [32]
Max. pipette displacement	$\hat{d}^{\mathrm{s}}{}_{\max}$	$10\,\mu\mathrm{m}$	estimated from [32]

Table 5.1.: Dissolution example: Parameters.

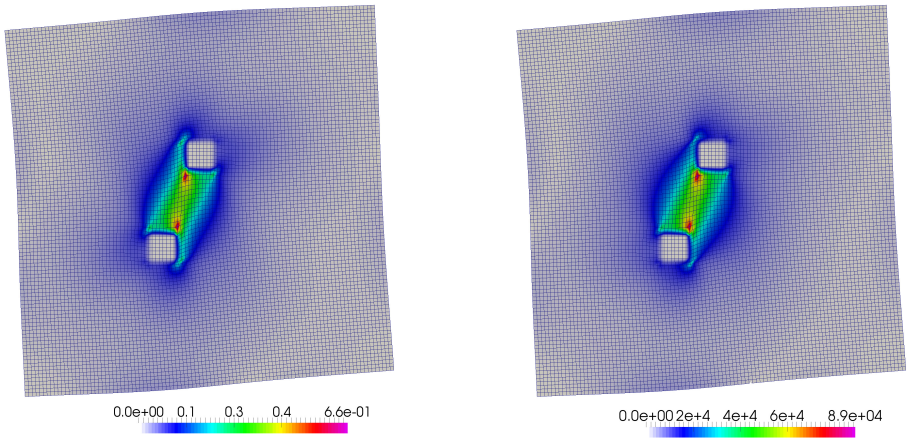

(a) Magnitude of Green-Lagrange strain $[-]$ (b) Magnitude of Cauchy Stress $\left[\frac{\mathrm{g}}{\mathrm{cms}^2}\right]$

Figure 5.23: Dissolution example: Solution field for stress and strain, taken from [245].

significantly, as the strained region is very localized in the area between the pipettes. Thus, the main difference between time evolution at these two points is due to the diffusion delay. The kinetics fit well to the experimental results from [32] with respect to the qualitative behavior as well as to the time scales of collagen dissolution. The time span until a 85% concentration reduction of collagen is reached in the point A, i.e. the strained region, is $\Delta T_{\mathrm{S}} = 1367.5\,\mathrm{s}$, which is in the range given in [32]. Note, that only the unstrained reaction rate, i.e. at point C, has been fitted, the deceleration of the kinetics in point A follows directly from the physical parameters and the proposed model without any further fitting.

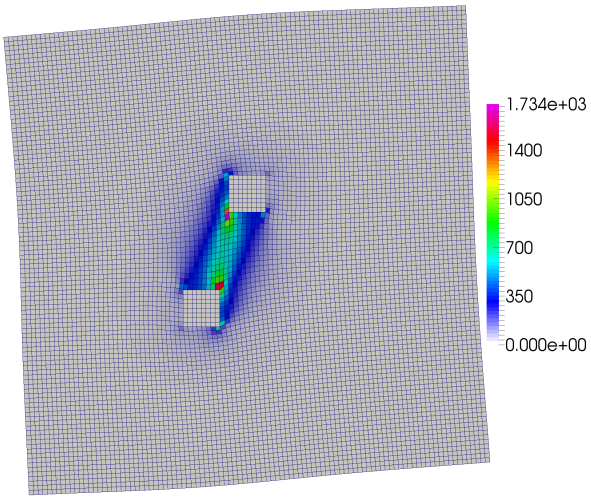

Figure 5.24: Dissolution example: Chemical potential $\left[\frac{\mathrm{dm}^2}{\mathrm{s}^2}\right]$, taken from [245].

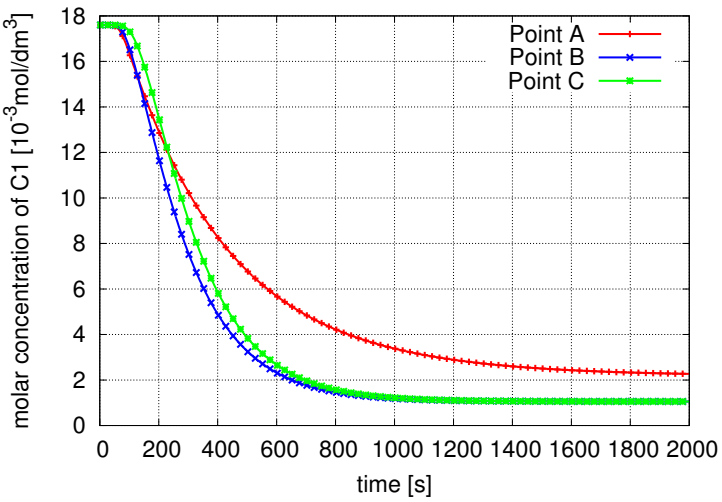

Figure 5.25: Dissolution example: Evolution of $C1$ concentration over time, taken from [245]. The point A is located in the strained region between the pipettes, the points B and C further away, see Figure 5.22.

However, one has to keep in mind that there are still some uncertainties in the model. The material of the solid phase is assumed to be of Neo-Hookean type, which is a simple elastic non-linear constitutive law. It is known, that collagen fibers do not only exhibit non-linear elastic but also viscoelastic behaviour [32, 226]. As the material model primarily determines the change of reaction kinetics, the use of a well-fitted viscoelastic model could improve the results. This could induce additional stabilization of the collagen at early time instances, as the viscous stresses are expected to be high in the beginning before relaxing over time. Actually, one could hypothesize that this produces an effect which can be observed when looking at the early behaviour of the

collagen concentration in the experiments in [32]. The collagen concentration is higher in the strained region than in the unstrained region at all times, whereas in the computational results, the collagen in point A is smaller than in the unstrained points at early times, because it is closer to the enzyme source and therefore more quickly subjected to proteolysis. Not until some diffusion time, the stabilizing effect starts to be visible in the concentration being higher in point A than in point B and C. However, the experimental results could also have other reasons like local matrix compaction or that unpolymerized collagen is attacked first [32]. Still, the model is reasonable in general as it gives good results without the need of unphysical parameters or assumptions. Besides, it is formulated in a general way based on the internal energy, such that other, possibly more suitable material models can be included further improving the results without changing the methodology.

In the following, the influence of certain parameters on the degradation time is studied. The displacements and therefore the resulting strain applied in the experiment in [32] are not easily controlled, however in the simulation it is a given input parameter. Also, the mechanical material behavior of collagen matrices is hard to measure. The degradation enzyme concentration can be controlled in experiments, but the dynamics and the diffusion processes might be of interest. Further, the density of the ECM fibers can only be estimated. In Figure 5.26 the applied displacement, the stiffness, the degradation enzyme concentration and the structural density are varied and their their influence on the degradation time in strained and unstrained regions is evaluated. If one quantity is varied, the others are fixed at the respective value given in Table 5.1. In [32] the time between 95% and 10% of initial collagen concentration was used as a measure for the degradation time. As this value is not always reached in the simulations for every setup with every parameter setting, subsequently the degradation time will be defined as the time span until 20% of the initial collagen remains, starting from the point in time when 95% of the initial collagen concentration is present. In general, all four plots in Figure 5.26 show expected behavior. Higher displacements and hence higher strains stabilize the collagen within the ECM (Figure 5.26(a)). If the applied strain is low, the degradation time in strained regions is even lower than in the unstrained region, which is due to the diffusion delay. Also, the degradation time increases with a stiffer matrix, see Figure 5.26(b). The reason for this is that under the same strain, stiffer material exhibit a higher mechanical energy state, which results in higher chemical potential and stability. Similarly, a lower structural mass density leads to a higher chemical potential under the same loading state, also inducing higher degradation times (Figure 5.26(c)). These three parameters are material characteristics of the mechanical behavior of the ECM. Those parameters do not influence the degradation kinetics of the unstrained region. Clearly, if the enzyme concentration is varied the degradation times in the whole domain change accordingly (Figure 5.26(d)). Still, the stabilizing effect of strain is visible for every analyzed setting. The effect of different ECM porosities, i.e. different matrix densities, is analyzed in Figure 5.27. In order to obtain a similar setting for all simulations, in which the porosity was altered, the initial collagen concentration, the stiffness and the maximum enzyme concentration were adapted accordingly. With rising solid volume, the macroscopic stiffness rises and the amount of degradation enzyme needs to be increased as well to assure the same ratio between collagen and degradation enzyme. For instance, the Young's modulus and the maximum enzyme concentration were increased by a factor of 10 compared to its former values, if the porosity was changed from 0.99 to 0.9 as this corresponds to a change of solid volume fraction from 0.01 to 0.1. Note, that this is a rough approximation concerning the stiffness, as the constitutive behavior is non-linear. Those adaptions lead to the

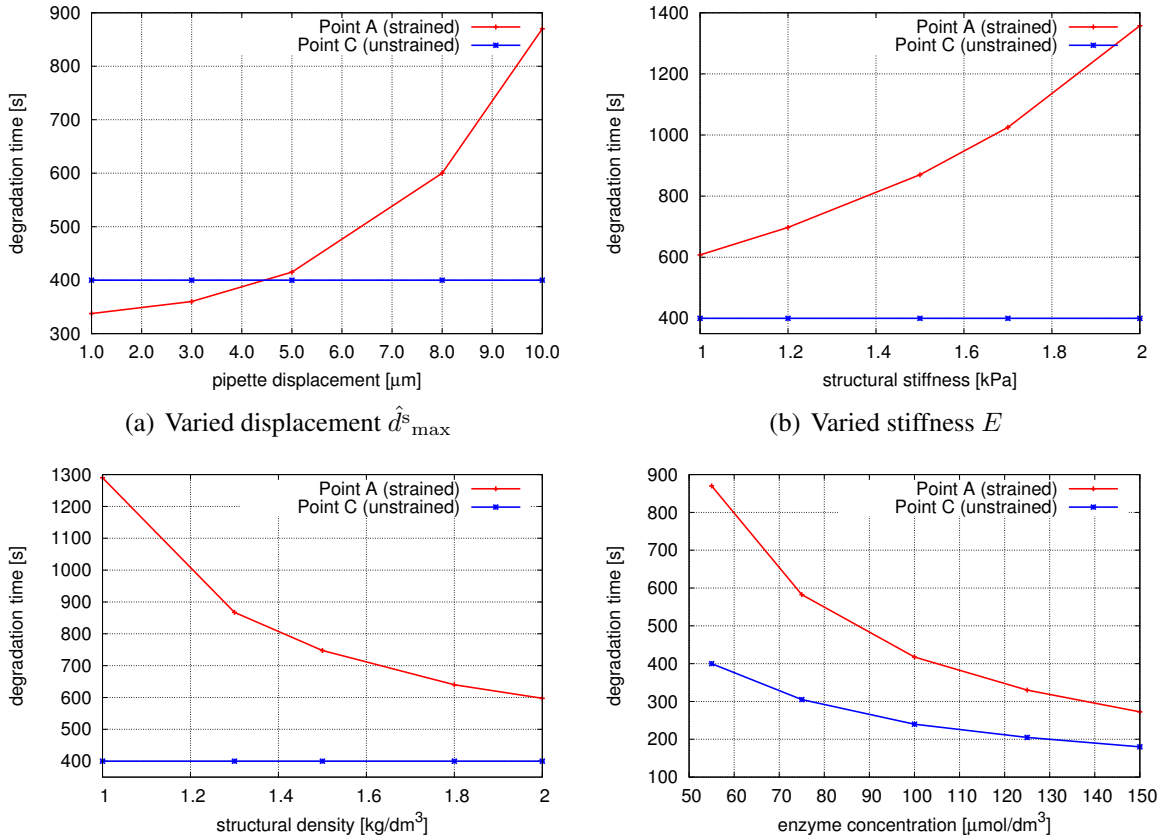

(a) Varied displacement $\hat{d}^{\mathrm{s}}{}_{\max}$

(b) Varied stiffness E

(c) Varied density ρ_0^{s}

(d) Varied maximal enzyme concentration $[E]_{\max}$

Figure 5.26: Dissolution example: Parameter study, taken from [245]. The degradation time within an unstrained and a strained region (point A and C, see Figure 5.22) is compared for for varying model parameters. Degradation time is defined as time span between 95% and 20% of local initial collagen concentration.

results depicted in Figure 5.27(a). There, the stabilizing effect of the applied strain reduces with higher solid volume fraction. However, if the reaction coefficient k_0^+ is decreased in the same way as the solid volume fraction is increased, the stabilization of collagen is evident for all considered porosities, see Figure 5.27(b). If the latter results would be verified experiments, this may indicate, that there is an additional dependency of the reaction rates (k_0^+ or others) on the porosity, which is not yet included in the model. For instance, it might be necessary to incorporate the change of collagen fiber surface, where the degradation takes place, due to a changing collagen fiber volume. In a volume averaged sense, this would lead to an altered effective reaction rate.

5.4.5.2. Cell Proteolysis within ECM

The second example is motivated by the numerical example presented in [144]. Therein, a complex transport model coupled with Brinkman flow for ECM proteolysis is solved. Here, the example is extended by explicitly resolving the cell membrane including diffusion on the membrane and production of $MT1\text{-}MMP$ and other chemical species localized at the root of the

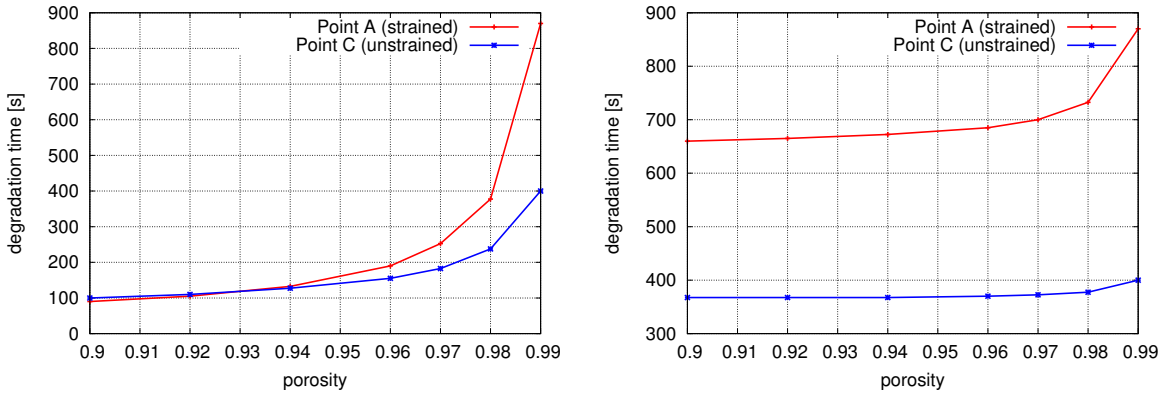

(a) Varied porosity ϕ

(b) Varied porosity ϕ with adapted reaction rate coefficient k_0^+

Figure 5.27: Dissolution example: Parameter study, taken from [245]. The degradation time in an unstrained and a strained region (point A and C, see Figure 5.22) is compared for varying porosity. Left: Young's modulus and maximum enzyme concentration are changed by the same factor as the solid volume fraction $1 - \phi$. Right: reaction rate coefficient is additionally adapted. Degradation time is defined as time span between 95% and 20% of local initial collagen concentration.

pseudopod [147]. Also, a deformable, dissolving solid phase is included into the model, i.e. the collagen matrix, and also the chemo-mechanical coupling is considered, this time induced by a pulling force applied on the ECM by the cell. The geometry of the domain is depicted in Figure 5.28. The cell ($10\ \mu\mathrm{m}$ high and $20\ \mu\mathrm{m}$ long) is placed within a rectangular ECM ($30\ \mu\mathrm{m}$ height, $40\,\mu\mathrm{m}$ width). The ECM is fixed at all outer boundaries. At its right boundary, a spatially constant inflow velocity field in normal direction of magnitude $1.0 \cdot 10^{-4}\,\frac{\mu\mathrm{m}}{\mathrm{s}}$ is prescribed [144]. At the top and bottom boundary a slip condition and on the cell-fluid interface a no-slip condition is applied. The left boundary is an outflow boundary with zero fluid traction. The cell itself is not modeled explicitly, only the transport processes on the cell membrane are considered. Seven species transported within the ECM and five chemical species which are bound to the cell surface are included, similar to [144]. Extending the model given in [144], the diffusion processes of the respective scalar on the membrane are additionally accounted for. The scalars within the ECM are collagen type I $C1$, the matrix-metalloprotease $MMP2$, the proenzyme $pro\text{-}MMP2$, the inhibitor $TIMP2$, the complex $MMP2{\cdot}TIMP2$, the denatured collagen $C1^*$ and the degradation product $MMP2 \cdot C1$. On the cell membrane, the modeled chemical species are the degradation enzyme $MT1\text{-}MMP$, its complex $MT1\text{-}MMP \cdot TIMP2^*$ with inactivated $TIMP2$ and the complexes $MT1{\cdot}TIMP2{\cdot}MMP2$, $MT1{\cdot}TIMP2{\cdot}MMP2{\cdot}MT1$ and $MT1{\cdot}C1$. An overview of the modeled species is given in Table 5.2. In this table, short notations are introduced, that will be used in the following. Also, the type of transport is stated there: 'Immobile' species are not transported (non-diffusive and non-convective), i.e. their local concentrations change only due to reactions, whereas 'mobile' species diffuse through the ECM and are transported by the fluid or diffuse over the cell domain. At the boundary of the protrusion, the cell secrets $M1$, $T2$ and $pM2$ at a constant rate $k_{\mathrm{M1}}^{\mathrm{prod}}$, $k_{\mathrm{T2}}^{\mathrm{prod}}$ and $k_{\mathrm{pM2}}^{\mathrm{prod}}$, respectively. The initial concentrations are set

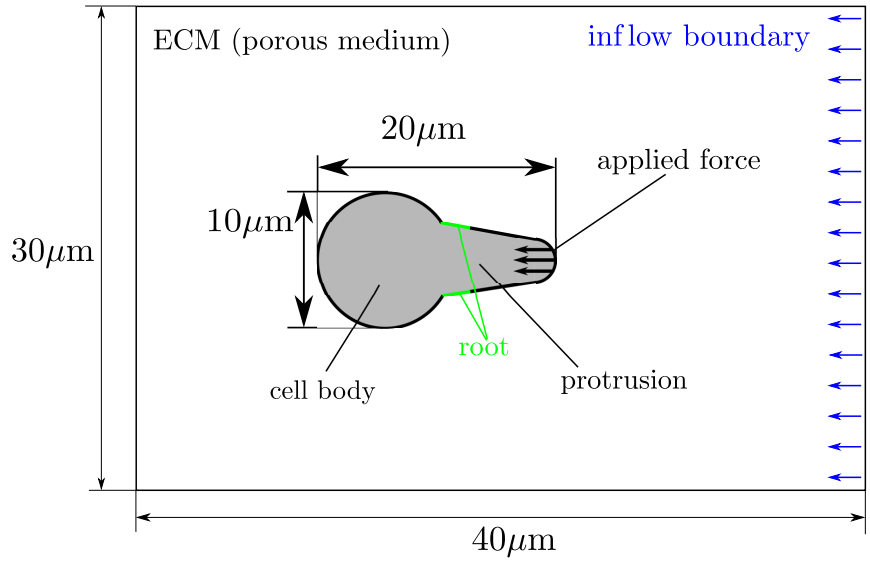

Figure 5.28: Cell example: Dimensions of computational domain, taken from [245]. The whole domain is rectangular region (30 μm height, 40 μm width). The cell geometry is composed by the cell body and a protrusion. At the root ot the protrusion, $MT1$-MMP, $TIMP2$ and pro-$MMP2$ are produced [147]. The cell is 10 μm high and 20 μm long. A pulling force is applied at the leading edge.

to zero apart from

$$[C1]\,(t = 0\,\mathrm{s}) = 176.0 \frac{\mu\mathrm{mol}}{\mathrm{dm}^3}, \tag{5.88}$$

$$[M1]\,(t = 0\,\mathrm{s}) = 1.0 \frac{\mu\mathrm{mol}}{\mathrm{dm}^2}. \tag{5.89}$$

The initial collagen concentration $[C1]\,(t = 0\,\mathrm{s})$ roughly corresponds to a porosity of $\phi_0 = 0.9$, see [144]. The initial concentration $[M1]\,(t = 0\,\mathrm{s})$ is set to a small value to accelerate the proteolytic process (only on the membrane). As boundary conditions for the scalar quantities within the ECM, the scalar values at the inflow are fixed to its respective initial value (i.e. zero for all quantities apart from $C1$, which is set to 176.0 μmol/ dm^3). At all other boundaries including the cell-ECM interface a zero diffusive flux is prescribed as a Neumann condition. The quantities bound to the membrane do not need a boundary condition, as the curved surface is closed. In the following the modeled reaction system is presented.

- Both enzymes $M1$ and $M2$ exert proteolytic activity, i.e. they can degrade the collagen matrix. $M1$ is acting on the cell surface, while $M2$ is transported within the ECM. The Michaelis-Menten mechanism describes the proteolytic reactions:

$$C1 + M2 \underset{k^-_{\mathrm{M2C1}}}{\overset{k^+_{\mathrm{M2C1}}}{\rightleftarrows}} M2C1 \overset{k^{\mathrm{cat}}_{\mathrm{M2C1}}}{\rightarrow} C1^* + M2, \tag{5.90}$$

Scalar quantity	Short notation	Location	Type
$C1$	$C1$	ECM	immobile
$MMP2$	$M2$	ECM	mobile
$pro\text{-}MMP2$	$pM2$	ECM	mobile
$TIMP2$	$T2$	ECM	mobile
$MMP2 \cdot TIMP2$	$M2T2$	ECM	mobile
$C1^*$	$C1^*$	ECM	immobile
$MMP2 \cdot C1$	$M2C1$	ECM	immobile
$MT1\text{-}MMP$	$M1$	membrane	mobile
$MT1\text{-}MMP \cdot TIMP2$	$M1T2$	membrane	mobile
$MT1\text{-}MMP \cdot TIMP2^*$	$M1T2^*$	membrane	mobile
$MT1\text{-}MMP \cdot TIMP2 \cdot pMMP2$	$M1T2pM2$	membrane	mobile
$MT1\text{-}MMP \cdot TIMP2 \cdot pMMP2 \cdot MT1\text{-}MMP$	$M1T2pM2M1$	membrane	mobile
$MT1\text{-}MMP \cdot C1$	$M1C1$	membrane	mobile

Table 5.2.: Cell example: Short notation, location and type of involved chemical species, taken from [245]. 'Immobile' species are not transported (non-diffusive and non-convective), i.e. their local concentrations change only due to reactions, whereas 'mobile' species diffuse through the ECM and are transported by the fluid or diffuse over the cell domain.

$$C1 + M1 \underset{k^-_{\mathrm{M1C1}}}{\overset{k^+_{\mathrm{M1C1}}}{\rightleftarrows}} M1C1 \overset{k^{\mathrm{cat}}_{\mathrm{M1C1}}}{\rightarrow} C1^* + M1. \tag{5.91}$$

- The inhibitor $T2$ can bind both degradation enzymes $M2$ and $M1$:

$$M2 + T2 \underset{k^-_{\mathrm{M2T2}}}{\overset{k^+_{\mathrm{M2T2}}}{\rightleftarrows}} M2T2, \tag{5.92}$$

$$M1 + T2 \underset{k^-_{\mathrm{M1T2}}}{\overset{k^+_{\mathrm{M1T2}}}{\rightleftarrows}} M1T2. \tag{5.93}$$

- The inhibition of $M1$ (5.93) is at the same time the first step towards the activation of $pM2$, which is secreted by the cell at the cell membrane. Here, $M1$ and $M1T2$ act as a catalyst for the production of $M2$:

$$M1T2 + pM2 \underset{k^-_{\mathrm{MTM}}}{\overset{k^+_{\mathrm{MTM}}}{\rightleftarrows}} M1T2pM2, \tag{5.94}$$

$$M1T2pM2 + M1 \underset{k^-_{\mathrm{MTMM}}}{\overset{k^+_{\mathrm{MTMM}}}{\rightleftarrows}} M1T2pM2M1, \tag{5.95}$$

$$M1T2pM2M1 \overset{k^{\text{cat}}_{\text{MTMM}}}{\rightarrow} M1 + M1T2^{*} + M2. \tag{5.96}$$

The corresponding reaction terms are formulated as follows:

$$\begin{aligned}\sigma_{C1} = &-k^{+}_{\text{M2C1}}[C1][M2] + k^{-}_{\text{M2C1}}[M2C1] \\ &-k^{+}_{\text{M1C1}}[C1]\frac{1}{\lambda}[M1] + k^{-}_{\text{M1C1}}\frac{1}{\lambda}[M1C1],\end{aligned} \tag{5.97}$$

$$\begin{aligned}\sigma_{M2} = &-k^{+}_{\text{M2C1}}[C1][M2] + k^{-}_{\text{M2C1}}[M2C1] + k^{\text{cat}}_{\text{M2C1}}[M2C1] \\ &+k^{\text{cat}}_{\text{MTMM}}\frac{1}{\lambda}[M1T2pM2M1],\end{aligned} \tag{5.98}$$

$$\sigma_{pM2} = -k^{+}_{\text{MTM}}[pM2][T2] + k^{-}_{\text{MTM}}\frac{1}{\lambda}[M1T2pM2], \tag{5.99}$$

$$\begin{aligned}\sigma_{T2} = &-k^{+}_{\text{M2T2}}[T2][M2] + k^{-}_{\text{M2T2}}[M2T2] \\ &-k^{+}_{\text{M1T2}}[T2]\frac{1}{\lambda}[M1] + k^{-}_{\text{M1T2}}\frac{1}{\lambda}[M1T2],\end{aligned} \tag{5.100}$$

$$\sigma_{M2T2} = +k^{+}_{\text{M2T2}}[T2][M2] - k^{-}_{\text{M2T2}}[M2T2], \tag{5.101}$$

$$\sigma_{C1^{*}} = +k^{\text{cat}}_{\text{M2C1}}[M2C1] + k^{\text{cat}}_{\text{M1C1}}\frac{1}{\lambda}[M1C1], \tag{5.102}$$

$$\sigma_{M2C1} = +k^{+}_{\text{M2C1}}[C1][M2] - k^{-}_{\text{M2C1}}[M2C1] - k^{\text{cat}}_{\text{M2C1}}[M2C1], \tag{5.103}$$

$$\begin{aligned}\sigma_{M1} = &-k^{+}_{\text{M1C1}}\lambda[C1][M1] + k^{-}_{\text{M1C1}}[M1C1] + k^{\text{cat}}_{\text{M1C1}}[M1C1] \\ &-k^{+}_{\text{MTMM}}[M1T2pM2][M1] + k^{-}_{\text{MTMM}}[M1T2pM2M1] \\ &+k^{\text{cat}}_{\text{MTMM}}[M1T2pM2M1],\end{aligned} \tag{5.104}$$

$$\begin{aligned}\sigma_{M1T2} = &+k^{+}_{\text{M1T2}}\lambda[T2][M1] - k^{-}_{\text{M1T2}}[M1T2] \\ &-k^{+}_{\text{MTM}}[M1T2][pM2] + k^{-}_{\text{MTM}}[M1T2pM2],\end{aligned} \tag{5.105}$$

$$\sigma_{M1T2^{*}} = +k^{\text{cat}}_{\text{MTMM}}[M1T2pM2M1], \tag{5.106}$$

$$\begin{aligned}\sigma_{M1T2pM2} = &+k^{+}_{\text{MTM}}[pM2]\lambda[T2] - k^{-}_{\text{MTM}}[M1T2pM2] \\ &-k^{+}_{\text{MTMM}}[M1T2pM2][M1] + k^{-}_{\text{MTMM}}[M1T2pM2M1],\end{aligned} \tag{5.107}$$

$$\begin{aligned}\sigma_{M1T2pM2M1} = &+k^{+}_{\text{MTMM}}[M1T2pM2][M1] - k^{-}_{\text{MTMM}}[M1T2pM2M1] \\ &-k^{\text{cat}}_{\text{MTMM}}[M1T2pM2M1],\end{aligned} \tag{5.108}$$

$$\sigma_{M1C1} = +k^{+}_{\text{M1C1}}\lambda[C1][M1] - k^{-}_{\text{M1C1}}[M1C1] - k^{\text{cat}}_{\text{M1C1}}[M1C1]. \tag{5.109}$$

Note the appearance of the specific length λ in some reaction terms, accounting for a heterogeneous reaction, as explained in Section 5.4.2. The matrix of the ECM is modeled in a similar

Quantity	Symbol	Value	Reference/Comment
molecular mass of collagen	$m_{\mathrm{mol,C1}}$	$0.3 \frac{\mathrm{g}}{\mu\mathrm{mol}}$	[144]
Collagen molecular density	$\rho_{0,C}$	$1760 \frac{\mu\mathrm{mol}}{\mathrm{dm}^3}$	estimated, see text
Collagen mass density	ρ_0^{s}	$1300 \frac{\mathrm{g}}{\mathrm{dm}^3}$	estimated, see text
Initial porosity	ϕ_0	0.9	assumed
Gas constant	R	$8.3144 \frac{\mathrm{J}}{\mathrm{K\,mol}}$	
Temperature	T	$310.15\ \mathrm{K}$	[32]
Young's modulus	E	$1.5\ \mathrm{kPa}$	estimated in [32]
Poisson's ratio	ν	0.3	assumed
Permeability	K	$1.0\ \mu\mathrm{m}^2$	[187]
Fluid mass density	ρ^{f}	$1000 \frac{\mathrm{g}}{\mathrm{dm}^3}$	water
Dynamic viscosity	μ^{f}	$0.001\ \mathrm{Pa\,s}$	approx. water
Specific length	λ	$0.1\ \mu\mathrm{m}$	[144]

Table 5.3.: Cell example: Parameters.

way as in the previous example. The same Neo-Hookean material model is used for the structural phase given by the strain energy function in equation (2.43). The degradation model for the ECM is included as in the first example, i.e. the collagen degradation depends on the chemical potential as follows

$$k^{+}_{\mathrm{M2C1}} = k^{+}_{0,\mathrm{M2C1}} \exp\left(\frac{-m_{\mathrm{mol,C1}} \Delta\mu^{\mathrm{s}}}{RT}\right). \tag{5.110}$$

The flow is governed by the Darcy-Brinkman equation (3.114). Therein, the influence of changing porosities on the flow is considered. The model parameters for this example are given in Table 5.3. The Poisson's ratio is assumed to be $\nu = 0.3$. The collagen densities ρ_0^{s} and $\rho_{0,C}$ have been approximated in the same way as in the previous example. In accordance to the analysis in [144], the specific length is chosen as $\lambda = 0.1\ \mu\mathrm{m}$ for the surface-volume reactions. The reaction rates of the chemical reactions are listed in Table 5.4. They are all taken from [143, 144]. The production rates $k^{\mathrm{prod}}_{\mathrm{M1}}$, $k^{\mathrm{prod}}_{\mathrm{T2}}$ and $k^{\mathrm{prod}}_{\mathrm{pM2}}$ roughly correspond to a secretion rate of $180,000$ molecules per hour [144]. The diffusion coefficients for the respective transport model in Table 5.5 are also taken from [144] for the species transported in the ECM. All diffusion coefficients on the cell membrane are chosen to be in a realistic order of magnitude [62]. The FE mesh for the fluid, solid and scalar fields comprising the ECM consist of approximately 19200 bi-linear, 4-node elements, respectively (the average edge size of an element is $0.2\ \mu\mathrm{m}$). The mesh for the transport and reactions processes on the cell membrane consists of approximately 280 linear, 2-node elements. As for the previous example, a one-step-θ time integration scheme with $\theta = 0.66$ is applied. A time step of $\Delta t = 0.2\ \mathrm{s}$ is used and $5400\ \mathrm{s}$ were simulated in total.

The results obtained by degradation of the ECM with and without the presence of a pulling force applied by the cell are compared. First, the global solutions will be shown, which give nearly indistinguishable results for both cases. In Figure 5.29, the pressure and velocity field at the end of the simulation are depicted. The laminar flow induces a pressure gradient pointing against the flow direction. The strain solution and the distribution of the chemical potential in the presence of a pulling force at the beginning of the simulation are shown in Figure 5.30. As

Reaction rate coefficient	Value	Reference
$k^{+}_{0,\mathrm{M2C1}}$	$2.6 \cdot 10^{-3} \frac{\mathrm{dm}^3}{\mu\mathrm{mol\,s}}$	[144]
k^{-}_{M2C1}	$2.1 \cdot 10^{-3} \frac{\mathrm{dm}^3}{\mu\mathrm{mol\,s}}$	[144]
$k^{\mathrm{cat}}_{\mathrm{M2C1}}$	$4.5 \cdot 10^{-3} \frac{\mathrm{dm}^3}{\mu\mathrm{mol\,s}}$	[144]
k^{+}_{M1C1}	$2.6 \cdot 10^{-3} \frac{\mathrm{dm}^3}{\mu\mathrm{mol\,s}}$	[143]
k^{-}_{M1C1}	$5.5 \cdot 10^{-3} \frac{\mathrm{dm}^3}{\mu\mathrm{mol\,s}}$	[143]
$k^{\mathrm{cat}}_{\mathrm{M1C1}}$	$2.01 \cdot 10^{-3} \frac{1}{\mathrm{s}}$	[144]
k^{+}_{M2T2}	$5.9 \frac{\mathrm{dm}^3}{\mu\mathrm{mol\,s}}$	[144]
k^{-}_{M2T2}	$6.3 \frac{1}{\mathrm{s}}$	[144]
k^{+}_{M1T2}	$3.54 \frac{\mathrm{dm}^3}{\mu\mathrm{mol\,s}}$	[144]
k^{-}_{M1T2}	$20.2 \frac{1}{\mathrm{s}}$	[144]
k^{+}_{MTM}	$0.14 \frac{\mathrm{dm}^3}{\mu\mathrm{mol\,s}}$	[143]
k^{-}_{MTM}	$4.7 \cdot 10^{-3} \frac{1}{\mathrm{s}}$	[143]
k^{+}_{MTMM}	$3.0 \cdot 10^{-3} \frac{\mathrm{dm}^3}{\mu\mathrm{mol\,s}}$	[143]
k^{-}_{MTMM}	$9.0 \cdot 10^{-4} \frac{1}{\mathrm{s}}$	[143]
$k^{\mathrm{cat}}_{\mathrm{MTMM}}$	$2.0 \cdot 10^{-2} \frac{1}{\mathrm{s}}$	[143]
$k^{\mathrm{prod}}_{\mathrm{M1}}$	$13.84 \frac{\mu\mathrm{mol}}{\mathrm{dm}^2\,\mathrm{s}}$	[144]
$k^{\mathrm{prod}}_{\mathrm{T2}}$	$13.84 \frac{\mu\mathrm{mol}}{\mathrm{dm}^2\,\mathrm{s}}$	[144]
$k^{\mathrm{prod}}_{\mathrm{pM2}}$	$13.84 \frac{\mu\mathrm{mol}}{\mathrm{dm}^2\,\mathrm{s}}$	[144]

Table 5.4.: Cell example: Reaction rate coefficients.

Scalar quantity	Diffusion coefficient	Reference
$M2$	$0.85 \cdot 10^{-8} \frac{\mathrm{dm}^2}{\mathrm{s}}$	[144]
$pM2$	$0.8 \cdot 10^{-8} \frac{\mathrm{dm}^2}{\mathrm{s}}$	[144]
$T2$	$1.1 \cdot 10^{-8} \frac{\mathrm{dm}^2}{\mathrm{s}}$	[144]
$M2T2$	$0.75 \cdot 10^{-8} \frac{\mathrm{dm}^2}{\mathrm{s}}$	[144]
$M1$	$1.0 \cdot 10^{-10} \frac{\mathrm{dm}^2}{\mathrm{s}}$	approximation [62]
$M1T2$	$1.0 \cdot 10^{-10} \frac{\mathrm{dm}^2}{\mathrm{s}}$	approximation [62]
$M1T2^*$	$1.0 \cdot 10^{-10} \frac{\mathrm{dm}^2}{\mathrm{s}}$	approximation [62]
$M1T2pM2$	$1.0 \cdot 10^{-10} \frac{\mathrm{dm}^2}{\mathrm{s}}$	approximation [62]
$M1T2pM2M1$	$1.0 \cdot 10^{-10} \frac{\mathrm{dm}^2}{\mathrm{s}}$	approximation [62]
$M1C1$	$1.0 \cdot 10^{-10} \frac{\mathrm{dm}^2}{\mathrm{s}}$	approximation [62]

Table 5.5.: Cell example: Diffusion coefficients.

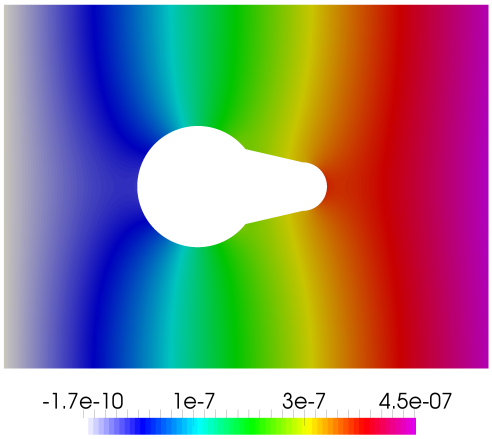

(a) pressure $[10^{-2}\ \mathrm{Pa}]$

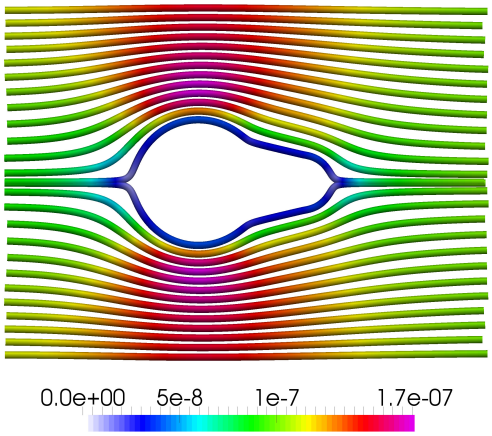

(b) velocity magnitude $\left[\frac{\mu\mathrm{m}}{\mathrm{ms}}\right]$

Figure 5.29: Cell example: Pressure and velocity field at the end of the simulation. Left: colors denote pressure values. Right: Streamlines of velocity. Colors denote velocity magnitude. Results for simulation with force applied by the cell (simulation without force gives nearly indistinguishable results).

expected, both distributions of strain and chemical potential show similar localization and do not change significantly during the simulation. The strain magnitude is small, resulting in moderate values for the chemical potential. In Figure 5.31 the spatial distributions of $T2$ and $pM2$

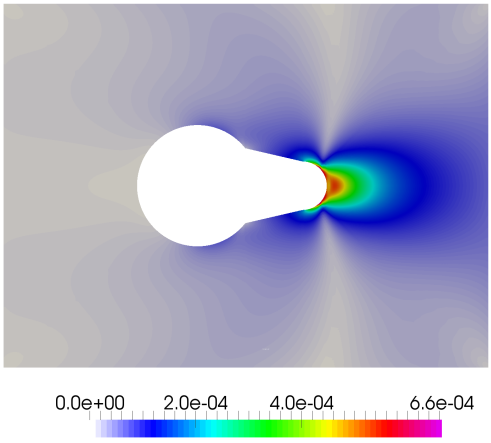

(a) Magnitude of Green-Lagrange strain $[-]$

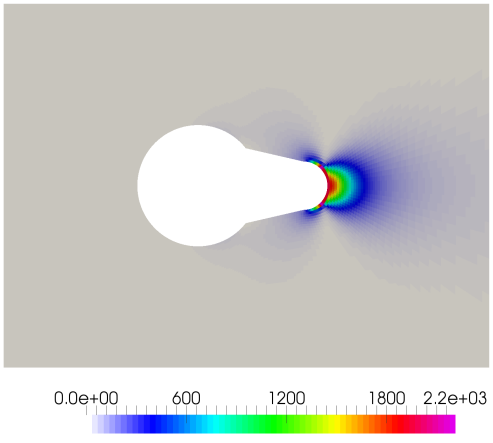

(b) Chemical potential $\left[\frac{\mathrm{dm}^2}{\mathrm{s}^2}\right]$

Figure 5.30: Cell example: Spatial distribution of Green-Lagrange strain and chemical potential at the beginning of the simulation, taken from [245]. Results for simulation with force applied by the cell.

concentration at the end of the simulation ($t = 5400\ \mathrm{s}$) is depicted for the simulation without

applied force on the ECM by the cell. In both figures it can clearly be seen, that the source of $T2$ and $pM2$ is at the root of the protrusion. From there both species are transported to regions preferably in flow direction. Figure 5.32 shows the spatial distribution of $M1$ at two time

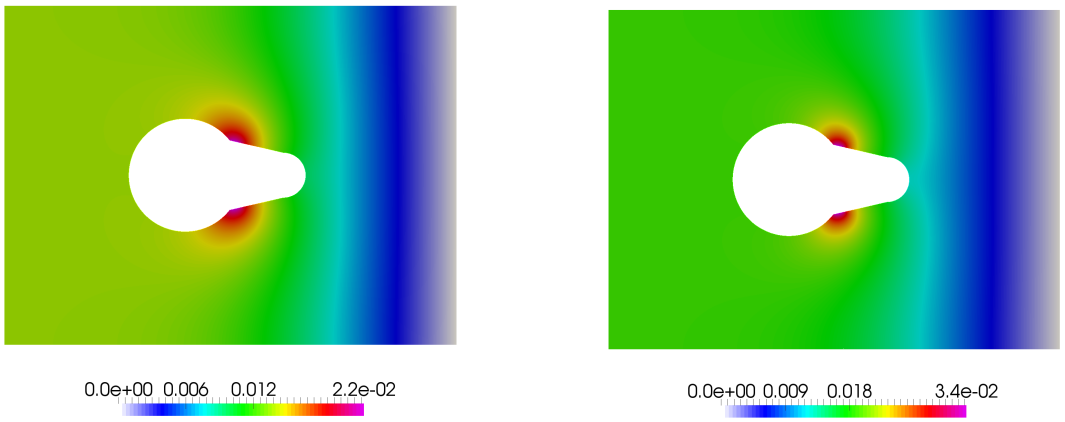

(a) $T2$ concentration $\left[\frac{\mu\text{mol}}{\text{dm}^3}\right]$ (b) $pM2$ concentration $\left[\frac{\mu\text{mol}}{\text{dm}^3}\right]$

Figure 5.31: Cell example: Spatial distribution of $T2$ and $pM2$ concentration at the end of the simulation ($t = 5400$ s). Results for simulation without force applied by the cell (simulation with force gives nearly indistinguishable results).

instances. As enforced by the model, $M1$ is bound to the cell membrane. For $t = 12\,\text{s}$ the spatial variation is very clear (left Subfigure 5.32). The highest concentrations are located at the root of the protrusion, as the $M1$ production has been applied there. At the end of the simulation, the spatial distribution looks very uniform (right Subfigure 5.32). The concentration peak is still present, however small and almost not visible. Also the solutions for the $M2$ concentration and the porosity (which corresponds to the collagen concentration) are depicted in Figure 5.33. The activated $M2$ is transported with the flow showing the highest concentration at the cell rear. The porosity is the highest near the cell membrane, as the degradation process is mainly invoked by $M1$ and $M2$ near the cell. In the vicinity, a very homogeneous porosity field is observed, due to steady $M2$ degradation. For analysis of the kinetics of the collagenolysis, the evolution over time of the $C1$ and $C1^*$ concentration averaged over the domain are depicted in Figure 5.34. There, a difference between both simulations can be observed. The concentrations reach a nearly steady state, however, the simulation with the applied force produces a slightly higher $C1$ concentration and a lower $C1^*$ concentration level. This is expected due to the stabilizing effect of the induced strain. Still, the difference between loaded and unloaded configuration is very small. This has several reasons. First, the induced strain within the ECM by the cell is very small, which in turn produces only small changes in the chemical potential and the reaction rate. Second, only the degradation kinetics of $M2$ are modeled as load dependent. However, the main degradation here is due to $M1$. As already mentioned before, the dependency of the degradation kinetics due to $M1$ is not included although in [6, 7] a increased degradation speed of loaded collagen due to $M1$ is observed in experiments. This dependency is not included for the sake of simplicity and clearance of the interpretation of the results, yet it can be included into the model formulation in

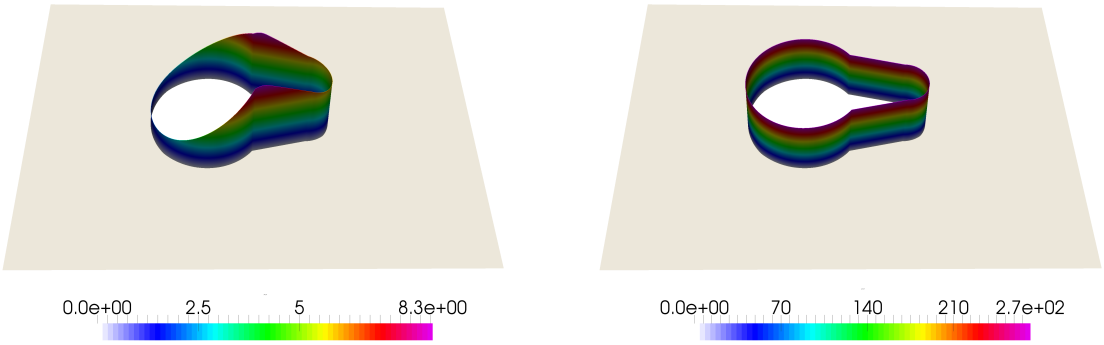

(a) $M1$ concentration $\left[\frac{\mu\text{mol}}{\text{dm}^3}\right]$ at $t = 12\,\text{s}$ (b) $M1$ concentration $\left[\frac{\mu\text{mol}}{\text{dm}^3}\right]$ at $t = 5400\,\text{s}$

Figure 5.32: Cell example: Spatial distribution of $M1$ concentration at $t = 12\,\text{s}$ and at the end of the simulation ($t = 5400\,\text{s}$), taken from [245]. Values are plotted in out-of-plane direction. Results for simulation with force applied by the cell (simulation without force gives nearly indistinguishable results).

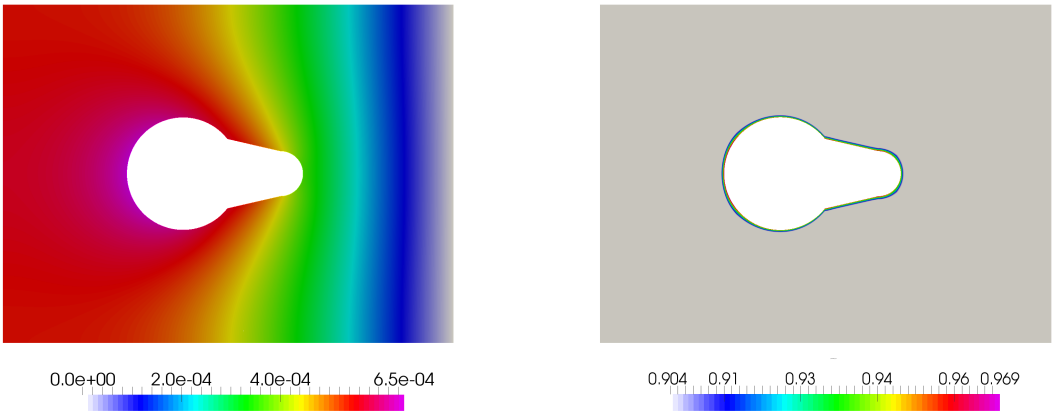

(a) $M2$ concentration $\left[\frac{\mu\text{mol}}{\text{dm}^3}\right]$ (b) porosity $[-]$

Figure 5.33: Cell example: Spatial distribution of $M2$ concentration and porosity at the end of the simulation ($t = 5400\,\text{s}$), taken from [245]. Results for simulation without force applied by the cell (simulation with force gives nearly indistinguishable results).

a straightforward way. In order to amplify the effect of $M2$ degradation another simulation was performed, where the initial concentration of $M2$ is increased to $0.1\ \mu\text{mol}/\ \text{dm}^3$ and also the same constant $M2$ concentration enters at the inflow. The evolution over time of the $C1$ and $C1^*$ concentration averaged over the domain for this setup are depicted in Figure 5.35. There, the collagen dissolution due to $M2$ is emphasized and the difference between the loaded and unloaded case is more evident compared to a zero initial $M2$ concentration, however still small.

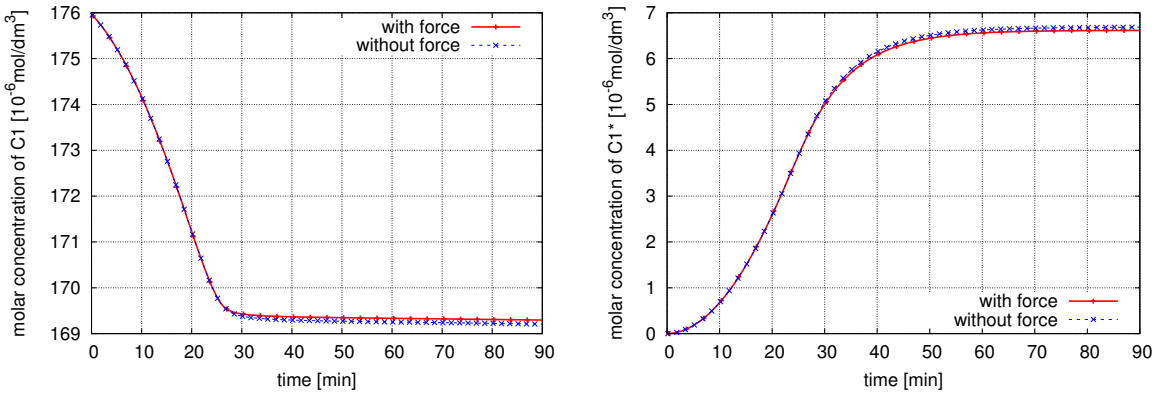

(a) $C1$ concentration $\left[\frac{\mu\text{mol}}{\text{dm}^3}\right]$ (b) $C1^*$ concentration $\left[\frac{\mu\text{mol}}{\text{dm}^3}\right]$

Figure 5.34: Cell example: Temporal evolution of $C1$ and $C1^*$ concentration averaged over the domain, taken from [245]. Comparison of results with and without applied force.

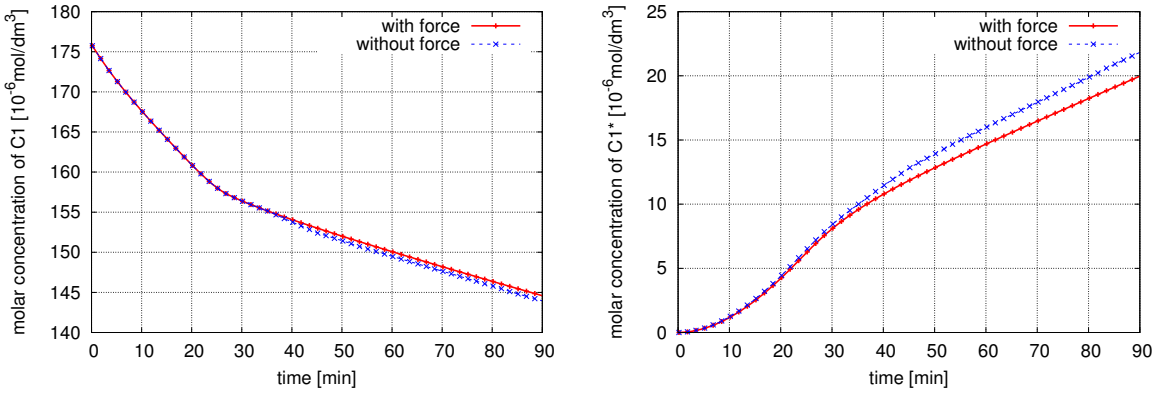

(a) $C1$ concentration $\left[\frac{\mu\text{mol}}{\text{dm}^3}\right]$ (b) $C1^*$ concentration $\left[\frac{\mu\text{mol}}{\text{dm}^3}\right]$

Figure 5.35: Cell example: Temporal evolution of $C1$ and $C1^*$ concentration averaged over the domain with initial presence of $M2$, taken from [245]. Comparison of results with and without applied force.

This example shows the capability of the method to handle complex coupled flow and reaction processes. It implies that the stabilizing effect of mechanical loading is negligible for this scenario. However, this conclusion might be premature, as the model might not yet be complete to capture all relevant processes. More complex reactions with different dependencies of the reaction rates on the loading might be necessary. Additionally, the geometry of the cell and the flow pattern can have large effects on the results. Also, an inhomogeneous ECM, with spatially varying porosities and stiffness might amplify the importance of the mechano-biochemical coupling.

6. Summary and Outlook

In this thesis, a computational approach to porous media problems has been presented. The governing equations are formulated in terms of non-linear kinematic quantities and are hence also valid for large deformations, which constitutes an extension to many existing porous media models. As porous flow equations, general forms of the Darcy and the Darcy-Brinkman equations are considered. The Darcy equation represents the most common form of flow through a porous medium. The Darcy-Brinkman equation is popular in case of high porosities. The new contributions of this thesis, regarding porous media problems, is a solution scheme for the full coupling of both equations under large deformations and a changing porosity in time and space for two- and three-dimensional problems. This includes a consistent linearization of all equations for the monolithic matrix. The pore fluid is modeled as incompressible Newtonian flow. The constitutive law for the total stress has been formulated in such a way that any arbitrary, potential-based, macroscopic material can be utilized. This is especially convenient for applications in biomechanics, where a various number of different non-linear constitutive laws are frequently applied. Also changes in porosity are modeled by a corresponding contribution in the energy function. Different porosity laws, in linear and non-linear forms, have been implemented and tested. The formulation was exemplarily used to simulate the contraction of a porous heart.

Another new contribution of this thesis comprises the analysis and realization of different forms of the finite element discretization specifically designed for large deformation porous media problems. Darcy-Brinkman flow with large deformations of the skeleton requires an accurate evaluation of the spatial porosity gradient. Its influence has been investigated and it was found that it places special continuity requirements on the finite element ansatz functions. Based on this, two approaches have been proposed: an isogeometric approach using the C^1-continuity of NURBS functions and a mixed approach, directly discretizing the porosity. For both approaches a thorough analysis and convergence studies have been performed. Especially the mixed approach shows large potential for further applications, as it is easy to implement and gives large flexibility regarding treatment of the porosity with limited additional costs. Also, it has been shown how complex boundary conditions can be included in the monolithic system via the (dual) Lagrange multiplier method. After condensation of the degrees of freedom associated with the Lagrange multiplier, the original size of the linear system can be preserved, which is convenient for integrating the porous medium into a bigger, coupled problem. Furthermore, a novel volume coupling approach has been successfully applied to the fluid and skeleton problem. It enables non-matching volume discretizations. The coupling operator was built via either a simple collocation approach or a mortar-based method. Both approaches were also tested for convergence.

The flexibility of the realized implementation has been shown by the extension to multi-field problems. The first example given is the interaction between a porous medium and an impervious solid. This can either be realized by a static, permanent interface or a dynamic contact zone. Both coupling constraints established are based on the dual Lagrange multiplier method, well-known from mesh tying and contact solid mechanics. The conditions for the porous fluid at the

interface were formulated and enforced in a consistent manner. Furthermore, the coupling between Navier-Stokes flow and a porous medium was demonstrated. Based on known models and coupling conditions, most importantly the Beavers-Joseph condition, the finite element framework has been enriched by this interaction problem. This is not particularly new, yet noteworthy, as the FPSI problem is intrinsically formulated for large deformations. The non-linear system of equations was solved with a fully linearized monolithic scheme. An example of a volume-coupled problem is transport of a scalar within the porous medium. The governing equations have strong similarities to regular transport processes, apart from the fact that the porous volume fraction influences convection and diffusion and thus acts as a coupling variable. The coupled system of transport and porous medium is solved in a partitioned scheme. Also, a new model for pericellular proteolysis was proposed. It comprises a computational model for the interaction of surface- and volume-bound scalar transport and reaction processes with a deformable porous medium. For the porous medium, the presented mixed finite element approach suitable for high porosity gradients was utilized. The model was applied to specific phenomena in cell and tissue mechanics. For this purpose, a continuum formulation was developed, incorporating the bi-directional coupling between the chemical degradation process and the material behavior of the extracellular matrix. The destabilizing effect of the dissolution process on the structural integrity was considered via a varying reference porosity similar to a damage parameter often applied in solid continuum mechanics. Changes in mechanical energy induce changes in chemical potential, which in turn affect the reaction kinetics. An exponential relation between reaction rate coefficient and chemical potential was postulated based on known experimental and theoretical results. The whole model does not include any unphysical parameters. Up to the author's knowledge, this is the first time a numerical method comprising fully coupled transport-flow-deformation processes within the ECM and on the cell membrane with a dissolving collagen matrix and deformation-dependent dissolution kinetics was presented. Thus, it gives a computational tool to investigate the interplay between biochemical dynamics and mechanical properties in cellular systems. The first numerical example reproduces an experiment, where different dissolution times for strained and unstrained fibers were observed. The computational results are in good agreement with experimental data, even though the dissolution model is still quite simple. A parameter study indicates the influence of the most important material parameters on the degradation time. The second example comprises fluid flow and transport processes within the ECM and the cell membrane. It includes matrix-tethered and free chemical substances involved in the degradation process. The mechano-biochemical coupling is triggered by a pulling force applied by the cell. The capability of the proposed methodology to model complex interactions and analyze specific settings and parameters was demonstrated.

Clearly, even though many aspects of porous media problems were discussed, a number of open questions and possible future projects remain. In terms of modeling, the implementation and validation of other hyperelastic material laws for the skeleton, the porosity and the permeability are just a technical issue. In terms of formulation, other known extensions could be included. For instance, heat transport or sound propagation within a porous system might be of interest, see e.g. [130, 167, 169, 229]. If heat transport is included, the consideration of compressible fluid flow and special kinds of chemical coupling becomes natural as well, see e.g. [88, 89, 157, 204]. Poro-plasticity is also a problem often considered in the literature, see [12, 104, 145]. Furthermore, so-called two-porosity networks are a common problem in soil mechanics, see [59] and the references therein. There, the existence of two, very different types

of pores is assumed. They differ in form as well as in size. Such formulations are utilized to model inter-linked rock formations. Also, multi-phase flow within the pores is computationally very challenging [49, 146, 199, 210, 218, 259]. Such models add further complexity, as the total void fraction has to be split in phase fractions composing the fluid (liquid or gas) phase. Each constituent needs to fulfill its own mass conservation. Mass exchange or reaction processes can be included, while the interfaces remain smeared. An interesting approach to include the constraint that all partial volume fractions must sum up to 1 is presented in [154]. There, the composition of the phase is formulated as a Karush-Kuhn-Tucker condition. The non-linear system is solved with a semi-smooth Newton method and an active set strategy. As such solution schemes were already used in this thesis for the contact constraints in Section 5.1.1.2, it would be compelling to see whether similarities in the mathematical problem and the numerical implementation could be exploited.

From a numerical point of view, the Biot stabilization is a very intriguing aspect, which was just mentioned briefly here. As the definition of the stabilization parameter was taken from an analysis of the linear Biot system in the literature, it is most probably not optimal in the large deformation regime. Actually, it turned out that slight scalings of this stabilization parameter could already lead to significantly improved the results. However, this strongly depends on the example and the parameters involved. Also, for a detailed analysis it would be very interesting to consider a certain aspect of the derivations given in [18]. There, a higher-order stabilization term is added to the balance of linear momentum of the mixture. In the end, this term is not evaluated, as only first-order elements are used, for which this term vanishes. However, it seems like this term is necessary for a consistent stabilization in a general scenario. Furthermore, other locking phenomena have not been addressed at all in this thesis. It is highly likely that especially volume locking occurs in case of a nearly incompressible solid phase. It remains an open question in this thesis whether those effects are already tackled at least partially by the Biot stabilization or further modifications are necessary. In the latter case, it is likely that standard techniques, like reduced integration or enhanced-arbitrary-strains (EAS), can be applied to the porous media formulation. Also, in terms of discretization of the Darcy-Brinkman equation it would be interesting to analyze other smooth shape functions, like Hermite polynomials, and test their performance compared to the mixed and NURBS-based approaches. Another aspect was already mentioned briefly in remark 4.3. It concerns the discretization of the relative fluid mass flux instead of the fluid velocities. Such an approach applied to the general equations for non-constant porosities in this thesis could bring some benefits. For instance, the no-penetration condition for Darcy flow would simplify to $\boldsymbol{w}^{\mathrm{f}} \cdot \boldsymbol{n} = 0$. However, the evaluation of the viscous Brinkman term becomes more complicated and adds further coupling between the fields. Also, the discretization procedure including time integration and stabilization would need to be re-examined.

Regarding multi-field problems, future research topics are also easily found. The coupling in FPSI problems was realized via substitution of the interface terms in the weak form of the governing equations. Such methods often work and give reasonable results. But they could lack accuracy and a mathematical proof of stability. For instance, if an example is constructed where the fluid is flowing perpendicular to the fluid-porous-medium interface, an error in the balance of mass over the interface can be observed, especially in a highly transient regime. Such an error could be controlled by enforcing conservation of mass with a Lagrange multiplier. Also, a Nitsche-type of coupling could give the missing terms for stability at least for a large range of

parameter values. Based on this, more complex, relevant problems, like blood flow through an artery with a porous inclusion, representing an aneurysm, could be analyzed.

The contact formulation can also be extended. Naturally, a dynamic no-penetration condition for the fluid at the contact interface can be beneficial. Furthermore, contact between porous bodies is then straightforward. This has already been realized [254], see Figure 6.1 for a first example. However, instabilities in the pressure field occur if large sliding is considered. This might originate from the non-smooth finite element approximation of the interface or an incomplete stabilization of the contact constraints on the porous fluid. At least the former could be tackled with NURBS functions or a smoothed normal field. Once this is realized, the contact formulation with free fluid flow would give the opportunity to study wet contact in the presence of a porous layer.

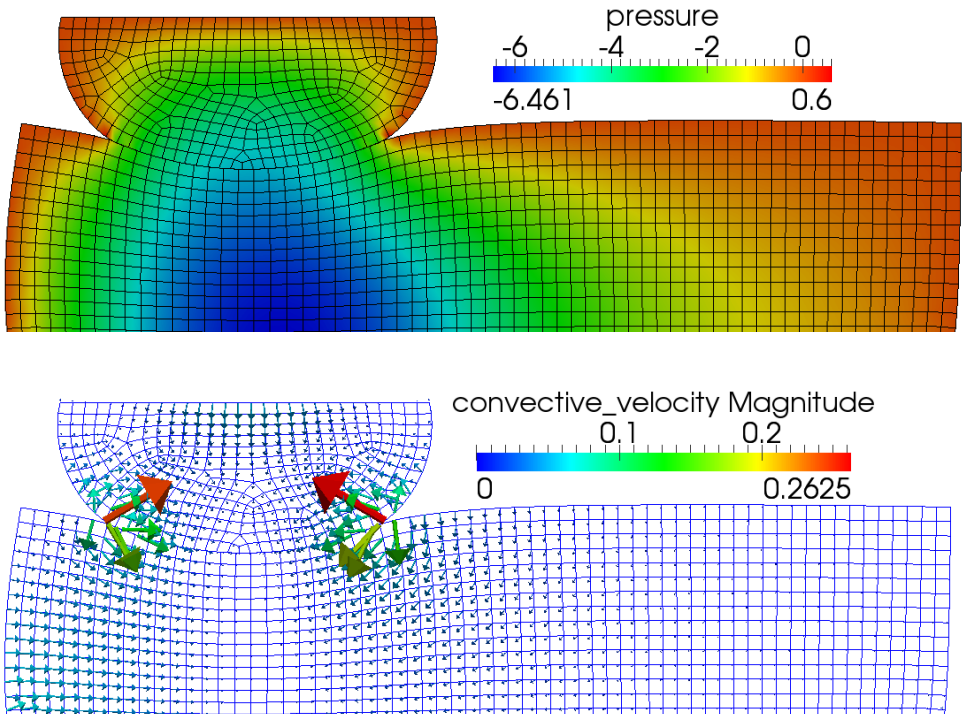

Figure 6.1: Poroelastic contact example: Pressure (top) and relative fluid velocity as arrows colored according to their magnitude (bottom) [254].

Much work is left in the model for cell migration. The proposed methodology is capable of including further chemical interactions and other constitutive laws, like viscoelasticity. As already mentioned before, it has been reported in the literature that collagen fibers exhibit strong viscoelastic behavior [32, 226]. Viscoelasticity can be included in the framework, as in the example in Section 4.4.5. However, for a meaningful application within the ECM model, a thorough study of the material parameters has to be performed. Other future developments may include an extension of the model to incorporate intracellular processes. Most cells are capable of sensing their environment. They react to a number of external cues, like temperature, variations in concentration of certain substances or stiffness gradients. Integrating this, would mean a separate

cell module including growth and active stress models to initiate cell movement. The coupling between cell and ECM has to be formulated in such a way, that the preferred direction of migration is determined by the external information available and internal signaling processes. This introduces a whole new challenge in terms of biological theory and numerical methods. First steps have been made in [201]. Also, more complex material behavior, e.g. anisotropic fiber models and fiber remodeling in the ECM, might be of interest. This could give insights into the dynamics and the persistence of directional proteolytic migration of cells due to durotaxis. As it can be observed that cells trigger remodeling of the collagen structure, a fiber model could provide the necessary directional information. Stress-stabilized fibers would resist degradation representing one form of implicit remodeling. Together with other forms of structural change of the ECM this could possibly reproduce the well-documented 'pathway construction' of mesenchymal cells [101, 258].

A. Appendix

A.1. Examples of Volume Averaging

Even though the main focus of this thesis is rather the numerical treatment of porous media problems and not the fundamental mathematical theory, a short derivation of some balance equations using volume averaging will be given here. In order to give an idea of the underlying methodology, the averaging procedure leading to the balance of momentum will be presented in Section A.1.1 and the necessary steps in order to obtain the transport equation within a porous medium in Section A.1.2. This section is based on the analysis performed in [66, sec. 2.5.1] and [25].

A.1.1. Balance of Momentum using Homogenization

The total stress $\boldsymbol{\sigma}$ of the mixture occurring in equation (3.21) is a macroscopic quantity. It can be expressed in terms of the averaged microscopic stress of both phases:

$$\boldsymbol{\sigma} = (1-\phi)\boldsymbol{\sigma}^{\mathrm{s}} + \phi\boldsymbol{\sigma}^{\mathrm{f}}. \tag{A.1}$$

Hence, the macroscopic stress is a volume weighted average of the microscopic stresses. The fluid stress is weighted with ϕ and the skeleton stress with $(1-\phi)$, respectively. This rather intuitive relation will be derived mathematically in the following using volume averaging.

For convenience of notation $\overline{(\bullet)}$ is defined as the average of a quantity $(\bullet)$ with respect to the total volume V_0 as

$$\overline{(\bullet)} = \frac{1}{V_0}\int_{V^\pi} (\bullet)\ \mathrm{d}V^\pi, \tag{A.2}$$

with $\pi = \mathrm{s}, \mathrm{f}$ denoting fluid or solid phase. The averaged macroscopic densities ρ^{S} and ρ^{F} of the skeleton and of the fluid, respectively, can thus be calculated from the respective intrinsic quantities $\rho^{\mathrm{s}}_{\mathrm{in}}$ and $\rho^{\mathrm{f}}_{\mathrm{in}}$:

$$\rho^{\mathrm{S}} = \overline{\rho^{\mathrm{s}}_{\mathrm{in}}} = \rho^{\mathrm{s}}(1-\phi), \tag{A.3}$$

$$\rho^{\mathrm{F}} = \overline{\rho^{\mathrm{f}}_{\mathrm{in}}} = \rho^{\mathrm{f}}\phi. \tag{A.4}$$

Analogously, the averaged macroscopic stresses $\boldsymbol{\sigma}^{\mathrm{s}}$ and $\boldsymbol{\sigma}^{\mathrm{f}}$ are obtained from the intrinsic stress of both phases $\boldsymbol{\sigma}^{\mathrm{s}}_{\mathrm{in}}$ and $\boldsymbol{\sigma}^{\mathrm{f}}_{\mathrm{in}}$ as

$$\boldsymbol{\sigma}^{\mathrm{S}} = \overline{\boldsymbol{\sigma}^{\mathrm{s}}_{\mathrm{in}}} = \boldsymbol{\sigma}^{\mathrm{s}}(1-\phi), \tag{A.5}$$

$$\boldsymbol{\sigma}^{\mathrm{F}} = \overline{\boldsymbol{\sigma}^{\mathrm{f}}_{\mathrm{in}}} = \boldsymbol{\sigma}^{\mathrm{f}}\phi. \tag{A.6}$$

The index ‘in’ denotes intrinsic, true quantities, in contrast to averaged quantities (microscopic or macroscopic). Here, microscopic quantities like ρ^{s} and $\boldsymbol{\sigma}^{\mathrm{f}}$ are no intrinsic quantities. They

are obtained from the intrinsic quantities by averaging over the respective phase volume. Macroscopic quantities are obtained by averaging over the total volume of the RVE.

For the intrinsic stresses, the balance of momentum of each phase holds:

$$\boldsymbol{\nabla}\cdot\boldsymbol{\sigma}^{\pi}_{\mathrm{in}} + \rho^{\pi}_{\mathrm{in}}\left(\hat{\boldsymbol{b}} - \boldsymbol{a}^{\pi}_{\mathrm{in}}\right) = \boldsymbol{0}. \tag{A.7}$$

It can be shown [66, sec. 2.5.1], that the following identity holds

$$\boldsymbol{\nabla}\cdot\boldsymbol{\sigma}^{\Pi} = \overline{\boldsymbol{\nabla}\cdot\boldsymbol{\sigma}^{\pi}_{\mathrm{in}}} - \underbrace{\frac{1}{V_0}\int_{\Gamma^{\mathrm{fs}}} \boldsymbol{\sigma}^{\pi}_{\mathrm{in}}\cdot\boldsymbol{n}^{\pi}_{\mathrm{in}}\, da}_{\boldsymbol{f}^{\pi}_{\mathrm{sf}}}, \tag{A.8}$$

with $\Gamma^{\mathrm{fs}} = \Gamma^{\mathrm{s}} \cap \Gamma^{\mathrm{f}}$ denoting the interface between fluid and structure phase and $\boldsymbol{n}^{\pi}_{\mathrm{in}}$ the outward pointing normal of the respective phase. The second summand is abbreviated by $\boldsymbol{f}^{\pi}_{\mathrm{sf}}$. It represents an averaged resultant of the interface traction. Thus, the spatial macroscopic divergence of stress $\boldsymbol{\nabla}\cdot\boldsymbol{\sigma}^{\Pi}$ is composed of the averaged microscopic divergence of stress $\overline{\boldsymbol{\nabla}\cdot(\boldsymbol{\sigma}^{\Pi})}$ and a contribution of the interface tractions $\boldsymbol{f}^{\pi}_{\mathrm{sf}}$. Taking an average of the equation (A.7) and using equation (A.8) one obtains

$$\boldsymbol{\nabla}\cdot\boldsymbol{\sigma}^{\Pi} + \rho^{\Pi}\left(\hat{\boldsymbol{b}} - \boldsymbol{a}^{\pi}\right) + \boldsymbol{f}^{\pi}_{\mathrm{sf}} = \boldsymbol{0}. \tag{A.9}$$

By summation of equation (A.9) for skeleton and fluid phase using the balance of tractions at the interface

$$\boldsymbol{\sigma}^{\mathrm{s}}_{\mathrm{in}}\cdot\boldsymbol{n}^{\mathrm{s}}_{\mathrm{in}} + \boldsymbol{\sigma}^{\mathrm{f}}_{\mathrm{in}}\cdot\boldsymbol{n}^{\mathrm{f}}_{\mathrm{in}} = \boldsymbol{0} \qquad \text{on } \Gamma^{\mathrm{fs}}, \tag{A.10}$$

it follows, that both contributions from the interface traction cancel out and one obtains the macroscopic, dynamic balance of linear momentum as

$$\boldsymbol{\nabla}\cdot\left(\boldsymbol{\sigma}^{\mathrm{S}} + \boldsymbol{\sigma}^{\mathrm{F}}\right) + \rho^{\mathrm{s}}\left(\hat{\boldsymbol{b}} - \boldsymbol{a}^{\mathrm{s}}\right) + \rho^{\mathrm{f}}\left(\hat{\boldsymbol{b}} - \boldsymbol{a}^{\mathrm{f}}\right) = \boldsymbol{0}. \tag{A.11}$$

By comparing this to equation (3.21), the definition of the total stress (A.1) can be identified.

A.1.2. Passive Scalar Transport within a Porous Medium

The transport equation (5.21) of a scalar quantity within the fluid phase of a porous medium will be derived. On the microscale, the instationary advection-diffusion-reaction equation of a scalar quantity c with isotropic diffusion reads

$$\frac{\partial c}{\partial t} + \boldsymbol{\nabla}\cdot(c\boldsymbol{v} - D\boldsymbol{\nabla}c) + \sigma(c) = 0. \tag{A.12}$$

Averaging over a *representative elementary volume* V_0 then yields

$$\frac{1}{V_0}\int \frac{\partial c}{\partial t}\,\mathrm{d}V^{\mathrm{f}} + \frac{1}{V_0}\int \boldsymbol{\nabla}\cdot(c\boldsymbol{v} - D\boldsymbol{\nabla}c)\;\mathrm{d}V^{\mathrm{f}} + \frac{1}{V_0}\int \sigma(c)\,\mathrm{d}V^{\mathrm{f}} = 0. \tag{A.13}$$

As already done in appendix A.1.1, for convenience of notation $\overline{(\bullet)}$ is defined as the average of a quantity $(\bullet)$ with respect to the total volume V_0 as

$$\overline{(\bullet)} = \frac{1}{V_0} \int (\bullet) \, \mathrm{d}V^{\mathrm{f}}, \tag{A.14}$$

and analogously $\overline{(\bullet)}^{\mathrm{f}}$ as the average of a quantity $(\bullet)$ with respect to the fluid volume V^{f} (or volumetric intrinsic phase average) as

$$\overline{(\bullet)}^{\mathrm{f}} = \frac{1}{V^{\mathrm{f}}} \int_{V^{\mathrm{f}}} (\bullet) \, \mathrm{d}V^{\mathrm{f}}. \tag{A.15}$$

Hence, using the porosity $\phi = \frac{V^{\mathrm{f}}}{V_0}$, the following identity holds

$$\overline{(\bullet)} = \phi \overline{(\bullet)}^{\mathrm{f}}. \tag{A.16}$$

Using this short notation equation (A.13) can be written as

$$\overline{\frac{\partial c}{\partial t}} + \overline{\boldsymbol{\nabla} \cdot (c\boldsymbol{v} - D\boldsymbol{\nabla} c)} \overline{\sigma c} = 0. \tag{A.17}$$

The goal is to write this equation in terms of the intrinsic averaged quantities $\overline{c}^{\mathrm{f}}$, $\overline{\boldsymbol{v}}^{\mathrm{f}}$ and other macroscopic geometry/problem specific quantities only. Therefore, the terms in (A.17) are evaluated using the relations given in [25], describing the averaging procedure for derivatives in time and space.

- Transient term
  [25, Equ. (2.3.9)] gives

$$\overline{\frac{\partial c}{\partial t}} = \phi \overline{\frac{\partial c}{\partial t}}^{\mathrm{f}} = \frac{\partial \phi \overline{c}^{\mathrm{f}}}{\partial t} - \frac{1}{V_0} \int c\boldsymbol{u} \cdot \boldsymbol{n} \, \mathrm{d}\Gamma^{\mathrm{fs}}, \tag{A.18}$$

  with Γ^{fs} denoting the microscopic fluid-structure interface, $\boldsymbol{u}$ the velocity of the interface and $\boldsymbol{n}$ the surface normal pointing outwards with respect to the fluid phase is applied.

- Flux term
  [25, Equ. (2.3.29)] gives

$$\begin{aligned}
\overline{\boldsymbol{\nabla} \cdot (c\boldsymbol{v} - D\boldsymbol{\nabla} c)} &= \phi \overline{\boldsymbol{\nabla} \cdot (c\boldsymbol{v} - D\boldsymbol{\nabla} c)}^{\mathrm{f}} \\
&= \boldsymbol{\nabla} \cdot \left(\phi \overline{(c\boldsymbol{v} - D\boldsymbol{\nabla} c)}^{\mathrm{f}} \right) + \frac{1}{V_0} \int (c\boldsymbol{v} - D\boldsymbol{\nabla} c) \cdot \boldsymbol{n} \, \mathrm{d}\Gamma^{\mathrm{fs}} \\
&= \boldsymbol{\nabla} \cdot \left(\phi \left(\overline{c\boldsymbol{v}}^{\mathrm{f}} - \overline{D\boldsymbol{\nabla} c}^{\mathrm{f}} \right) \right) + \frac{1}{V_0} \int (c\boldsymbol{v} - D\boldsymbol{\nabla} c) \cdot \boldsymbol{n} \, \mathrm{d}\Gamma^{\mathrm{fs}}.
\end{aligned} \tag{A.19}$$

- Reaction term
  Assuming the reaction coefficient is dependent on the scalar only (i.e. no spatial deriva-

tives) the average of the reaction term is easily calculated as

$$\overline{\sigma c} = \phi \overline{\sigma c}^{\mathrm{f}} = \phi \sigma \overline{c}^{\mathrm{f}}. \tag{A.20}$$

Now, the average of the diffusive flux from (A.19) is further simplified using the following assumptions:

- Constant diffusion coefficient, i.e. $D = \mathrm{const}$

$$\Rightarrow \overline{D \boldsymbol{\nabla} c}^{\mathrm{f}} = D \overline{\boldsymbol{\nabla} c}^{\mathrm{f}}. \tag{A.21}$$

- No diffusive flux over fluid-structure-interface, i.e. $\boldsymbol{\nabla} c \cdot \boldsymbol{n} = 0$ on Γ^{fs}

$$\Rightarrow D \overline{\boldsymbol{\nabla} c}^{\mathrm{f}} = \underbrace{D \boldsymbol{T}^*}_{\boldsymbol{D}^*} \boldsymbol{\nabla} \overline{c}^{\mathrm{f}}. \tag{A.22}$$

  $\boldsymbol{T}^*$ denotes the so-called *tortuosity*. It is a symmetric second-rank tensor and a measure for the curvity of the microstructure. It depends purely on microscopic geometric characteristics of the porous medium, however it in general changes due to deformation and porosity. See [25, sec. 2.3.6] for mathematical definition and detailed analysis. $\boldsymbol{D}^*$ is the so-called *molecular diffusivity* accounting for the effect of microscopic diffusion – i.e. originating from the molecular scale – on the macroscopic diffusion. Also, see [25, Sec. 6.1.2 and 2.6.3] for a thorough derivation of the average of the diffusive flux.

The average of the convective flux in (A.19) can be written as follows (see also [25, Sec. 6.1.1 and 2.6.4]) :

$$\overline{c \boldsymbol{v}}^{\mathrm{f}} = \overline{c}^{\mathrm{f}} \overline{\boldsymbol{v}}^{\mathrm{f}} + \overline{\tilde{c} \tilde{\boldsymbol{v}}}^{\mathrm{f}}, \tag{A.23}$$

with $\tilde{(\bullet)}$ denoting the deviation of a quantity $(\bullet)$ from its intrinsic average $\overline{(\bullet)}^{\mathrm{f}}$. It can be shown [25] that the following identity holds

$$\overline{\tilde{c} \tilde{\boldsymbol{v}}}^{\mathrm{f}} = -\boldsymbol{D}' \cdot \boldsymbol{\nabla} \overline{c}^{\mathrm{f}}. \tag{A.24}$$

Therein, $\boldsymbol{D}'$ is the so-called *advective dispersion*. It is a symmetric second ranked tensor, which depends of the dispersivity of the porous medium, geometric quantities (porosity) and the Péclet number (again, see [25, Sec. 6.1.1] for details). Note that therein, an isochoric fluid motion with uniform density is assumed. Physically speaking, equation (A.24) can be interpreted as such, that the variations of the convective flux at the microscale appear as a diffusive flux on the macroscale, as the small variations of the convective flux are 'unseen' on the coarser description.

Now, having all equations needed at hand, one can insert equations (A.18)–(A.24) into equation (A.17) to obtain

$$\begin{aligned} \frac{\partial \phi \overline{c}^{\mathrm{f}}}{\partial t} + \boldsymbol{\nabla} \cdot (\phi (\overline{c}^{\mathrm{f}} \overline{\boldsymbol{v}}^{\mathrm{f}} \underbrace{- \boldsymbol{D}' \cdot \boldsymbol{\nabla} \overline{c}^{\mathrm{f}} - \boldsymbol{D}^* \boldsymbol{\nabla} \overline{c}^{\mathrm{f}}}_{-\boldsymbol{D}^{\mathrm{eff}} \boldsymbol{\nabla} \overline{c}^{\mathrm{f}}})) \\ + \frac{1}{V_0} \int c (\boldsymbol{v} - \boldsymbol{u}) \cdot \boldsymbol{n} \, \mathrm{d}\Gamma^{\mathrm{fs}} - \frac{1}{V_0} \int D \boldsymbol{\nabla} c \cdot \boldsymbol{n} \, \mathrm{d}\Gamma^{\mathrm{fs}} + \phi \sigma \overline{c}^{\mathrm{f}} = 0. \end{aligned} \tag{A.25}$$

Here, the *effective macroscopic diffusivity* $\boldsymbol{D}^{\mathrm{eff}}$ is defined as the sum of advective dispersion and molecular diffusion, i.e. accounting for all effects that are observed as diffusion-like on the macroscale:

$$\boldsymbol{D}^{\mathrm{eff}} = \boldsymbol{D}' + \boldsymbol{D}^{*}. \tag{A.26}$$

Assuming no diffusive flux, i.e. $\boldsymbol{\nabla} c \cdot \boldsymbol{n} = 0$, (as already in equation (A.22)) and no convective flux, i.e. $(\boldsymbol{v} - \boldsymbol{u}) \cdot \boldsymbol{n} = 0$, on the fluid structure interface Γ^{fs}, both surface integrals in (A.25) vanish. One finally obtains

$$\frac{\partial \phi \overline{c}^{\mathrm{f}}}{\partial t} + \boldsymbol{\nabla} \cdot \left(\phi \overline{c}^{\mathrm{f}} \overline{\boldsymbol{v}}^{\mathrm{f}} \right) - \boldsymbol{\nabla} \cdot \left(\phi \boldsymbol{D}^{\mathrm{eff}} \cdot \boldsymbol{\nabla} \overline{c}^{\mathrm{f}} \right) + \phi \sigma \overline{c}^{\mathrm{f}} = 0, \tag{A.27}$$

which is the macroscopic equation (5.21). Note, that in equation (5.21) and all the main parts of this thesis, the marker $\overline{(\bullet)}$, indicating an averaged quantity, is omitted for the sake of clarity.

A.2. Details on Linearizations

For the Newton scheme, a linearization with respect to the primary unknowns within the coupled problem is necessary. Those involve some intricate derivatives of scalars and tensors. Most of them can be found in [120]. Some will be listed here, from which most of the linearizations needed can be derived.

The linearization of the porosity with respect to pressure and displacements can be calculated as

$$\Delta_{\mathsf{p}} \phi = \frac{\partial \phi}{\partial \mathbf{p}^{\mathrm{f}}} \cdot \Delta \mathbf{p}^{\mathrm{f}} = \frac{\partial \phi}{\partial p^{\mathrm{f}}} \mathbf{N}_{\mathsf{p}} \cdot \Delta \mathbf{p}^{\mathrm{f}}, \tag{A.28a}$$

$$\Delta_{\mathsf{d}} \phi = \frac{\partial \phi}{\partial \mathbf{d}^{\mathrm{s}}} \cdot \Delta \mathbf{d}^{\mathrm{s}} = \frac{\partial \phi}{\partial J} \frac{\partial J}{\partial \mathbf{d}^{\mathrm{s}}} \cdot \Delta \mathbf{d}^{\mathrm{s}}, \tag{A.28b}$$

with the linearization of the jacobian determinant $J = \det \boldsymbol{F}$ with respect to the discrete nodal displacements

$$\Delta_{\mathsf{d}} J = \frac{\partial J}{\partial \boldsymbol{F}} : \Delta_{\mathsf{d}} \boldsymbol{F} = J \boldsymbol{F}^{-\mathrm{T}} : \left(\boldsymbol{\nabla}_0 \left(\Delta_{\mathsf{d}} \boldsymbol{d}^{\mathrm{s}} \right) \right) = J \boldsymbol{\nabla} \cdot \left(\Delta_{\mathsf{d}} \boldsymbol{d}^{\mathrm{s}} \right). \tag{A.29}$$

The derivatives of porosity depend on the constitutive relation applied. For instance, if the nonlinear law (3.87) is used, one obtains for the porosity

$$\phi \left(p^{\mathrm{f}}, J \left(\boldsymbol{d}^{\mathrm{s}} \right) \right) = \frac{1}{2a \left(J, p^{\mathrm{f}} \right)} \left(-b \left(J, p^{\mathrm{f}} \right) \pm c \left(J, p^{\mathrm{f}} \right) \right), \tag{A.30}$$

with the sign of the parameter c chosen such that $0 \leq \phi \leq 1$ holds. The derivatives with respect to pressure and displacements can then be evaluated in a straigthforward way

Further, the gradients of the porosity are linearized. It holds

$$\boldsymbol{\nabla}\phi = \frac{\partial\phi}{\partial p^{\mathrm{f}}}\frac{\partial p^{\mathrm{f}}}{\partial \boldsymbol{x}} + \frac{\partial\phi}{\partial J}\frac{\partial J}{\partial \boldsymbol{x}}, \tag{A.31}$$

$$\boldsymbol{\nabla}_0\phi = \frac{\partial\phi}{\partial p^{\mathrm{f}}}\frac{\partial p^{\mathrm{f}}}{\partial \boldsymbol{X}} + \frac{\partial\phi}{\partial J}\frac{\partial J}{\partial \boldsymbol{X}}, \tag{A.32}$$

with the gradient of the jacobian determinant

$$\frac{\partial J}{\partial \boldsymbol{x}} = \frac{\partial J}{\partial \boldsymbol{F}} : \frac{\partial \boldsymbol{F}}{\partial \boldsymbol{x}} = J\boldsymbol{F}^{-\mathrm{T}} : \left(\boldsymbol{d}^{\mathrm{s}}_{,\boldsymbol{XX}} \cdot \boldsymbol{F}^{-1}\right), \tag{A.33}$$

$$\frac{\partial J}{\partial \boldsymbol{X}} = \frac{\partial J}{\partial \boldsymbol{F}} : \frac{\partial \boldsymbol{F}}{\partial \boldsymbol{X}} = J\boldsymbol{F}^{-\mathrm{T}} : \boldsymbol{d}^{\mathrm{s}}_{,\boldsymbol{XX}}, \tag{A.34}$$

with the second derivative $\boldsymbol{d}^{\mathrm{s}}_{,\boldsymbol{XX}}$ of the displacements with respect to the material coordinate. It can be calculated as

$$\boldsymbol{d}^{\mathrm{s}}_{,AB} = \sum_{k}^{\mathrm{n_{node}}} \frac{\partial^2 \mathsf{N}_{\mathsf{d},k}}{\partial X_A \partial X_B}\mathbf{d}^{\mathrm{s}}_k. \tag{A.35}$$

The directional derivatives of the porosity with respect of the discrete pressure and the discrete displacement values read

$$\Delta_{\mathsf{p}}\boldsymbol{\nabla}\phi = \frac{\partial^2\phi}{\left(\partial p^{\mathrm{f}}\right)^2}\boldsymbol{\nabla}p^{\mathrm{f}} \cdot \left(\mathbf{N}_{\mathsf{p}} \cdot \Delta\mathbf{p}^{\mathrm{f}}\right) + \frac{\partial\phi}{\partial p^{\mathrm{f}}}\boldsymbol{\nabla}\left(\Delta_{\mathsf{p}}p^{\mathrm{f}}\right) + \frac{\partial^2\phi}{\partial p^{\mathrm{f}}\partial J}\frac{\partial J}{\partial \boldsymbol{X}} \cdot \left(\mathbf{N}_{\mathsf{p}} \cdot \Delta\mathbf{p}^{\mathrm{f}}\right), \tag{A.36a}$$

$$\Delta_{\mathsf{d}}\boldsymbol{\nabla}\phi = \left(\frac{\partial^2\phi}{\partial p^{\mathrm{f}}\partial J}\boldsymbol{\nabla}_0 p^{\mathrm{f}} + \frac{\partial^2\phi}{\partial J^2}\boldsymbol{\nabla}_0 J\right) \cdot \Delta_{\mathsf{d}}J + \frac{\partial\phi}{\partial J}J\boldsymbol{\nabla}_0 J \cdot \boldsymbol{F}^{-\mathrm{T}} : \Delta_{\mathsf{d}}\boldsymbol{d}^{\mathrm{s}}_{,\boldsymbol{XX}} \tag{A.36b}$$

and for the respective material gradients

$$\Delta_{\mathsf{p}}\boldsymbol{\nabla}_0\phi = \frac{\partial^2\phi}{\left(\partial p^{\mathrm{f}}\right)^2}\boldsymbol{\nabla}_0 p^{\mathrm{f}} \cdot \left(\mathbf{N}_{\mathsf{p}} \cdot \Delta\mathbf{p}^{\mathrm{f}}\right) + \frac{\partial\phi}{\partial p^{\mathrm{f}}} \cdot \boldsymbol{\nabla}_0\left(\Delta_{\mathsf{p}}p^{\mathrm{f}}\right) + \frac{\partial^2\phi}{\partial p^{\mathrm{f}}\partial J}\boldsymbol{\nabla}_0 J \cdot \left(\mathbf{N}_{\mathsf{p}} \cdot \Delta\mathbf{p}^{\mathrm{f}}\right), \tag{A.37a}$$

$$\Delta_{\mathsf{d}}\boldsymbol{\nabla}_0\phi = \left(\frac{\partial^2\phi}{\partial p^{\mathrm{f}}\partial J}\boldsymbol{\nabla}_0 p^{\mathrm{f}} + \frac{\partial^2\phi}{\partial J^2}\boldsymbol{\nabla}_0 J\right)\Delta_{\mathsf{d}}J + \frac{\partial\phi}{\partial J}J\boldsymbol{\nabla}_0 J \cdot \boldsymbol{F}^{-\mathrm{T}} : \Delta_{\mathsf{d}}\boldsymbol{d}^{\mathrm{s}}_{,\boldsymbol{XX}}. \tag{A.37b}$$

The directional derivative of the inverse of the right Cauchy–Green tensor is given as

$$\begin{aligned}\Delta_{\mathsf{d}}\boldsymbol{C}^{-1} &= -\boldsymbol{F}^{-1} \cdot \left(\left(\boldsymbol{\nabla}\left(\Delta_{\mathsf{d}}\boldsymbol{d}^{\mathrm{s}}\right)\right)^{\mathrm{T}} + \boldsymbol{\nabla}\left(\Delta_{\mathsf{d}}\boldsymbol{d}^{\mathrm{s}}\right)\right) \cdot \boldsymbol{F}^{-\mathrm{T}} \\ &= -2\mathrm{sym}\left(\boldsymbol{\nabla}_0\left(\Delta_{\mathsf{d}}\boldsymbol{d}^{\mathrm{s}}\right) \cdot \boldsymbol{F}^{-1} \cdot \boldsymbol{C}^{-1}\right).\end{aligned} \tag{A.38}$$

The directional derivative of the inverse of the deformation gradient reads

$$\Delta_{\mathrm{d}} \boldsymbol{F}^{-1} = -\boldsymbol{F}^{-1} \cdot \boldsymbol{\nabla} \left(\Delta_{\mathrm{d}} \boldsymbol{d}^{\mathrm{s}} \right) = -\boldsymbol{F}^{-1} \cdot \boldsymbol{\nabla}_0 \left(\Delta_{\mathrm{d}} \boldsymbol{d}^{\mathrm{s}} \right) \cdot \boldsymbol{F}^{-1}. \tag{A.39}$$

The directional derivative of virtual Green-Lagrange strains can be calculated as

$$\begin{aligned} \Delta_{\mathrm{d}} \delta \boldsymbol{E} &= \left(\frac{\partial^2 \boldsymbol{E}}{\left(\partial \boldsymbol{d}^{\mathrm{s}}\right)^2} \cdot \delta \boldsymbol{d}^{\mathrm{s}} \right) \cdot \Delta \mathbf{d}^{\mathrm{s}} = \frac{1}{2} \left(\left(\boldsymbol{\nabla}_0 (\Delta \boldsymbol{d}^{\mathrm{s}}) \right)^{\mathrm{T}} \cdot \boldsymbol{\nabla}_0 (\Delta_{\mathrm{d}} \boldsymbol{d}^{\mathrm{s}}) + \left(\boldsymbol{\nabla}_0 (\Delta_{\mathrm{d}} \boldsymbol{d}^{\mathrm{s}}) \right)^{\mathrm{T}} \cdot \boldsymbol{\nabla}_0 (\Delta_{\mathrm{d}} \boldsymbol{d}^{\mathrm{s}}) \right) \\ &= \operatorname{sym} \left(\left(\boldsymbol{\nabla}_0 (\Delta_{\mathrm{d}} \boldsymbol{d}^{\mathrm{s}}) \right)^{\mathrm{T}} \cdot \boldsymbol{\nabla}_0 (\Delta_{\mathrm{d}} \boldsymbol{d}^{\mathrm{s}}) \right). \end{aligned} \tag{A.40}$$

A.3. Details on Setup of some Examples

A.3.1. Terzaghi's Consolidation Problem

Here, the major steps for the derivation of the solution of Terzaghi's consolidation problem considered in Section 4.4.1 will be sketched. It is based on the derivation given in [242, chap. 2.4.1]. The full one-dimensional equation solved there reads

$$(\alpha + \phi\beta) \frac{\partial p^{\mathrm{f}}}{\partial t} = -\alpha \frac{\partial \sigma_{yy}}{\partial t} + \frac{k}{\mu^{\mathrm{f}}} \frac{\partial^2 p^{\mathrm{f}}}{\partial y^2}, \tag{A.41}$$

with α and β denoting the compressibility of the solid and fluid, respectively.

Remark A.1 *Note, that actually, there is a changed sign in the stress term in equation* (A.41) *compared to its original form in [242]. This is due to a different sign convention. In the reference, stresses are positive for compression, which is common soil mechanics practice. Here, the usual sign convention in solid mechanics (positive for extension, negative for compression) is used.*

In order to obtain the initial distribution of the pressure corresponding to the initial loading, this equation is integrated over a short time Δt. Assuming $\Delta t \to 0$ gives

$$\Delta p^{\mathrm{f}} = -\frac{\alpha}{\alpha + \phi\beta} \Delta \sigma_{yy}. \tag{A.42}$$

As the boundary conditions, state that the initial loading jumps from 0 to q, the initial pressure reads

$$p^{\mathrm{f}}(t = 0) = p_0^{\mathrm{f}} = \frac{\alpha}{\alpha + \phi\beta} q. \tag{A.43}$$

For the solution of equation (A.41), the time derivative of the normal stress is zero, as the loading remains constant after it has been applied. Hence, the one-dimensional equation to be solved reads

$$\frac{\partial p^{\mathrm{f}}}{\partial t} = c_v \frac{\partial^2 p^{\mathrm{f}}}{\partial y^2}, \tag{A.44}$$

with the consolidation coefficient

$$c_v = \frac{k}{(\alpha + \phi\beta)\mu^{\mathrm{f}}}. \tag{A.45}$$

The boundary conditions are

$$p^{\mathrm{f}}(y=0) = p^{\mathrm{f}}(y=2h) = 0. \tag{A.46}$$

The problem can be solved using the Laplace transform method. The Laplace transform of the pressure is

$$\tilde{p}^{\mathrm{f}} = \int_0^\infty p^{\mathrm{f}} e^{-st}, \tag{A.47}$$

depending on the positive parameter s. The Laplace transformation of equation (A.44) reads

$$s\tilde{p}^{\mathrm{f}} - p_0^{\mathrm{f}} = c_v \frac{\partial^2 \tilde{p}^{\mathrm{f}}}{\partial^2 y}. \tag{A.48}$$

This ordinary differential equation can solved with the general solution

$$\tilde{p}^{\mathrm{f}} = \frac{p_0^{\mathrm{f}}}{s} + A \exp\left(y\sqrt{\frac{s}{c_v}}\right) + B \exp\left(-y\sqrt{\frac{s}{c_v}}\right). \tag{A.49}$$

The solution in the frequency domain using the boundary conditions can then be derived as

$$\frac{\tilde{p}^{\mathrm{f}}}{p_0^{\mathrm{f}}} = \frac{1}{s} - \frac{\cosh\left((h-y)\sqrt{\frac{s}{c_v}}\right)}{s\cosh\left(h\sqrt{\frac{s}{c_v}}\right)}. \tag{A.50}$$

The back transform of this solution can be derived [242] as

$$\frac{p}{p_0} = \frac{\pi}{4}\sum_{j=1}^{\infty} \frac{(-1)^{j-1}}{2j-1} \cos\left((2j-1)\left(\frac{\pi\,(h-z)}{2h}\right)\right) \exp\left(-(2j-1)\frac{\pi^2}{4}\frac{c_v t}{h^2}\right). \tag{A.51}$$

The question remains, how the one-dimensional equation (A.41) is related to the coupled system (3.117) given in this thesis and how the consolidation coefficient can be expressed in terms of the material parameters used here. As in this thesis only incompressible flow is considered, the compressibility β needs to be set to zero. Then, equation (A.41) can be derived from (3.117) as follows. All time instationary terms apart from the derivative of the porosity are neglected and small deformations are assumed. Further, body forces are neglected. Then, the balance equations from (3.117) with Darcy flow reduce to

$$\mathring{\phi} + \phi\,\boldsymbol{\nabla}\cdot\boldsymbol{v}^{\mathrm{s}} + \boldsymbol{\nabla}\cdot\left(\phi\left(\boldsymbol{v}^{\mathrm{f}} - \boldsymbol{v}^{\mathrm{s}}\right)\right) = 0, \tag{A.52}$$

$$\boldsymbol{\nabla} p^{\mathrm{f}} + \mu^{\mathrm{f}}\phi\boldsymbol{k}^{-1}\cdot\left(\boldsymbol{v}^{\mathrm{f}} - \boldsymbol{v}^{\mathrm{s}}\right) = \boldsymbol{0}, \tag{A.53}$$

$$-\boldsymbol{\nabla}\cdot\boldsymbol{\sigma} - \phi\boldsymbol{\nabla} p^{\mathrm{f}} - \mu^{\mathrm{f}}\phi^2\boldsymbol{k}^{-1}\cdot\left(\boldsymbol{v}^{\mathrm{f}} - \boldsymbol{v}^{\mathrm{s}}\right) = \boldsymbol{0}. \tag{A.54}$$

Solving equation (A.53) for the fluid flux $\phi\left(\boldsymbol{v}^{\mathrm{f}}-\boldsymbol{v}^{\mathrm{s}}\right)$, inserting this into the other two equation and assuming a constant permeability and viscosity, gives

$$\frac{\partial\phi}{\partial p^{\mathrm{f}}}\frac{\partial p^{\mathrm{f}}}{\partial t}+\frac{\partial\phi}{\partial\mathrm{tr}(\boldsymbol{\epsilon})}\frac{\partial\mathrm{tr}(\boldsymbol{\epsilon})}{\partial t}+\phi\,\boldsymbol{\nabla}\cdot\boldsymbol{v}^{\mathrm{s}}-\frac{\boldsymbol{k}}{\mu^{\mathrm{f}}}\boldsymbol{\Delta}p^{\mathrm{f}}=0, \tag{A.55}$$

$$\boldsymbol{\nabla}\cdot\boldsymbol{\sigma}=\boldsymbol{0}. \tag{A.56}$$

The porosity was expressed in terms of pressure and deformation. Noting that

$$\boldsymbol{\nabla}\cdot\boldsymbol{v}^{\mathrm{s}}=\frac{\partial\mathrm{tr}(\boldsymbol{\epsilon})}{\partial t} \tag{A.57}$$

gives for the one-dimensional case

$$\frac{\partial\phi}{\partial p^{\mathrm{f}}}\frac{\partial p^{\mathrm{f}}}{\partial t}+\left(\frac{\partial\phi}{\partial\epsilon_{yy}}+\phi\right)\frac{\partial\epsilon_{yy}}{\partial t}-\frac{k}{\mu^{\mathrm{f}}}\frac{\partial^2 p^{\mathrm{f}}}{\partial y^2}=0, \tag{A.58}$$

$$\frac{\partial\sigma_{yy}}{\partial y}=0. \tag{A.59}$$

The second equation simply states that the stress is constant. For a linear stress-strain relation, no viscous stresses and small deformations, the constitutive law (3.81) reads

$$\sigma_{yy}=E\epsilon_{yy}-p^{\mathrm{f}}. \tag{A.60}$$

Solving this identity for the strains and inserting them into equation (A.58) and using the linear biot law (3.93), i.e. $\partial\phi/\partial p^{\mathrm{f}}=1/N$ and $\partial\phi/\partial\epsilon_{yy}=b$ leads to

$$\left(\frac{1}{N}+\frac{1}{E}\left(b+\phi\right)\right)\frac{\partial p^{\mathrm{f}}}{\partial t}+\frac{1}{E}\left(b+\phi\right)\frac{\partial\sigma_{yy}}{\partial t}-\frac{k}{\mu^{\mathrm{f}}}\frac{\partial^2 p^{\mathrm{f}}}{\partial y^2}=0. \tag{A.61}$$

By comparing the coefficients of this equation and equation (A.41) (as stated before with $\beta=0$) one obtains

$$\frac{1}{N}=0,\qquad \alpha=\frac{1}{E}\left(b+\phi\right). \tag{A.62}$$

For the consolidation coefficient used in the example in equation (4.171) the above relations with $b=1$ and $\beta=0$ were inserted into equation (A.45).

A.3.2. Analytical Solution of 1D Porous Medium Example

A short derivation of the analytical solution used in Section 4.4.2 is given. The solution was obtained by postulating sensible solution fields for the porosity, pressure and velocity for Darcy (equations (4.181)–(4.183)) and Darcy–Brinkman flow (equations (4.184)–(4.186)). For both problems, the porosity and the velocity solution are chosen, such that the following identity holds:

$$\phi(x)v^{\mathrm{f}}(x)=1. \tag{A.63}$$

Thus, the continuity equation (4.178) is fulfilled. An important detail is the application of the displacement field in equation (4.174). It is written in terms of the spatial coordinate. As the

Dirichlet boundary conditions are applied with respect to the material coordinate, a separate problem is solved with a Newton scheme to evaluate the Dirichlet boundary conditions for the skeleton. The determinant of the deformation gradient for the calculation of the spatial permeability (4.177) can determined via

$$J = \frac{\mathrm{d}\, x}{\mathrm{d}\, X} = 1 + \frac{\mathrm{d}\, d^{\mathrm{s}}}{\mathrm{d}\, X} = 1 + \frac{\mathrm{d}\, d^{\mathrm{s}}}{\mathrm{d}\, x} \underbrace{\frac{\mathrm{d}\, x}{\mathrm{d}\, X}}_{J} \tag{A.64}$$

and thus

$$J = \frac{1}{1 - \frac{\mathrm{d}\, d^{\mathrm{s}}(x)}{\mathrm{d}\, x}}. \tag{A.65}$$

Using this, all terms can be expressed as functions of the spatial coordinate x. Inserting this into the respective flow equations, they can be solved for the body forces, resulting in equations (4.179) and (4.180).

A.3.3. Analytical Solution of Diffusion on Unit Sphere

Here, it will be shown that equation (5.39) and (5.40) are the analytical solution of the heat equation on a unit sphere, as stated in Section 5.4.1.2.1. The equation to solve reads

$$\frac{\partial c}{\partial t} - D \boldsymbol{\Delta}_{\Gamma} c = 0, \tag{A.66}$$

Separation of variables

$$c(\boldsymbol{x}, t) = v(t) w(\boldsymbol{x}) + c_o, \tag{A.67}$$

with the constant c_0, gives

$$v' w - D v \boldsymbol{\Delta}_{\Gamma} w = 0, \tag{A.68}$$

and thus

$$\frac{v'}{Dv} = \frac{\boldsymbol{\Delta}_{\Gamma} w}{w} = \text{const.} \tag{A.69}$$

The time dependent part immediately follows as

$$v(t) = c_1 e^{\lambda t}, \tag{A.70}$$

with the constants c_1 and λ. Now, it will be shown that

$$w(\boldsymbol{x}) = xy \tag{A.71}$$

is a solution of equation (A.69). The surface Laplacian can be calculated as

$$\boldsymbol{\Delta}_{\Gamma} w = \mathrm{tr}\left((\mathbf{1} - \boldsymbol{n} \otimes \boldsymbol{n}) \cdot \boldsymbol{\nabla} \left(\boldsymbol{\nabla}_{\Gamma} w \right) \right). \tag{A.72}$$

The surface gradient is defined as

$$\boldsymbol{\nabla}_{\Gamma} w = (\mathbf{1} - \boldsymbol{n} \otimes \boldsymbol{n}) \cdot \boldsymbol{\nabla} w. \tag{A.73}$$

which reads in index notation for Cartesian coordinates

$$(\boldsymbol{\nabla}_\Gamma w)_i = (\delta_{ij} - n_i n_j)\, w_{,j} = w_{,i} - n_i n_j w_{,j}. \tag{A.74}$$

Therefore, the Laplacian can be written as

$$\boldsymbol{\Delta}_\Gamma w = \delta_{ij} \left((\delta_{ik} - n_i n_k) \left(\boldsymbol{\nabla}_\Gamma w \right)_{k,j} \right) = \left(\boldsymbol{\nabla}_\Gamma w \right)_{i,i} - n_i n_k \left(\boldsymbol{\nabla}_\Gamma w \right)_{k,i}. \tag{A.75}$$

Inserting equation (A.73) into equation (A.75) gives

$$\boldsymbol{\Delta}_\Gamma w = w_{,ii} - (n_{i,i} n_j w_{,j} + n_i n_{j,i} w_{,j} + n_i n_j w_{,ji}) - n_i n_k \left(w_{,k} - n_k n_j w_{,j} \right)_{,i}. \tag{A.76}$$

For the outward pointing normal of a unit sphere, it holds

$$n_i = \frac{1}{r} x_i, \quad r = x^2 + y^2 + z^2 = 1. \tag{A.77}$$

Equation (A.77) and (A.71) inserted into equation (A.75) and evaluating all derivatives give

$$\boldsymbol{\Delta}_\Gamma w = -\frac{6}{r^2} w = -6w. \tag{A.78}$$

From this relation, it is clear that equation (A.71) fulfills equation (A.69). Hence, a solution for the heat equation on a unit sphere reads

$$c(\boldsymbol{x}, t) = c_1 e^{\lambda t} x_1 x_2 + c_o. \tag{A.79}$$

The missing constants can be evaluated easily be inserting this solution into the partial differential equation (A.66) and considering the initial condition (5.13). The constants follow as

$$c_0 = 10, \quad c_1 = 1, \quad \lambda = -6D, \tag{A.80}$$

resulting in the analytical solution (5.39).

A.3.4. Velocity Field for Convection-Diffusion on Surface of Torus

It will be presented how the initial distribution and the velocity field for the example of convection-diffusion on a surface of a torus in Section 5.4.1.2.2 can be expressed in Cartesian coordinates. This can be useful as input for the simulation which is referring to a globally fixed Cartesian coordinate system. A parametrization of the surface can be written as

$$x = (R + r\cos\beta)\cos\alpha, \tag{A.81}$$
$$y = (R + r\cos\beta)\sin\alpha, \tag{A.82}$$
$$z = r\sin\beta. \tag{A.83}$$

Therein, R denotes the major radius and r the minor radius of the torus, see Figure 5.15. From this, the following useful identities can be derived:

$$\sin\alpha = \frac{y}{\sqrt{x^2+y^2}}, \quad \cos\alpha = \frac{x}{\sqrt{x^2+y^2}}, \quad \tan\alpha = \frac{y}{x} \tag{A.84}$$

$$\sin\beta = \frac{z}{r}, \quad \cos\beta = \frac{\sqrt{x^2+y^2}-R}{r} \tag{A.85}$$

Hence, the initial scalar distribution (5.46) can easily be written in terms of the Cartesian coordinates by solving any equation of (A.84) and (A.85) for α and β.

As stated in Section 5.4.1.2.2, α and β are angles used for description of the geometry. The basis vectors $\boldsymbol{e}_\alpha$ and $\boldsymbol{e}_\beta$ are defined as

$$\boldsymbol{e}_\alpha = \frac{\partial}{\partial\alpha}\begin{pmatrix} x \\ y \\ z \end{pmatrix} = \begin{pmatrix} -(R+r\cos\beta)\sin\alpha \\ (R+r\cos\beta)\cos\alpha \\ 0 \end{pmatrix} = \begin{pmatrix} -y \\ x \\ 0 \end{pmatrix}, \tag{A.86}$$

$$\boldsymbol{e}_\beta = \frac{\partial}{\partial\beta}\begin{pmatrix} x \\ y \\ z \end{pmatrix} = r\begin{pmatrix} -\sin\beta\cos\alpha \\ -\sin\beta\sin\alpha \\ \cos\beta \end{pmatrix} = \begin{pmatrix} -\frac{xz}{\sqrt{x^2+y^2}} \\ -\frac{yz}{\sqrt{x^2+y^2}} \\ \sqrt{x^2+y^2}-R \end{pmatrix}. \tag{A.87}$$

As stated in equation (5.47), the velocity field is chosen as a unit vector, which creates an angle of $30°$ with $\boldsymbol{e}_\alpha$, see Figure A.1. Inserting equations (A.86) and (A.87) into (5.47) gives the velocity field in Cartesian coordinates.

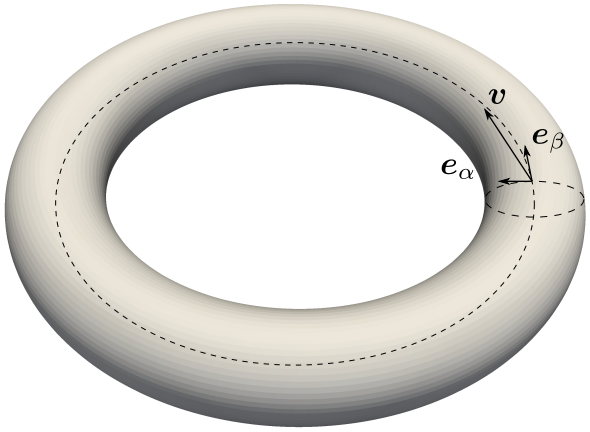

Figure A.1: Advection-diffusion on torus: Basis vectors and velocity.

A.3.5. Surface Divergence of Velocity Field on Moving Curved Surface

Two different ways to obtain the surface divergence given in equation (5.56) of Section 5.4.1.2.4 are presented.

1. From the physical interpretation of the scalar as mass density (and also from the form of the transport equation in the material configuration) it is intuitive that the solution has to read

$$\bar{c} = c_0 \frac{A_0}{A(t)}, \tag{A.88}$$

with the initial concentration $c_0 = 1$ and the initial surface area A_0 and the current surface area $A(t)$. This means, that, as the surface is closed, the total mass has to be conserved. The prescribed velocity field (5.55) can be rewritten in terms of a prescribed radius as

$$r(t) = t + r_0, \tag{A.89}$$

with the initial radius $r_0 = 1$. For a sphere the solution can then be calculated depending on the prescribed radius as

$$\bar{c} = c_0 \frac{A_0}{A(t)} = c_0 \frac{4\pi r_0^2}{4\pi \left(r(t)\right)^2} = \frac{1}{t+1}, \tag{A.90}$$

being the analytical solution (5.57). This solution can be inserted in the partial differential equation and solved for $\boldsymbol{\nabla}_\Gamma \cdot \boldsymbol{v}$, which results in equation (5.56).

2. The surface divergence can be calculated directly via tensor calculus. Spherical coordinates can be defined by

$$\boldsymbol{x}(\varphi, \phi, r) = r \sin\varphi \sin\phi \boldsymbol{e}_1 + r \cos\phi \boldsymbol{e}_2 + r \cos\phi \boldsymbol{e}_3, \tag{A.91}$$

with $\{\boldsymbol{e}_1, \boldsymbol{e}_2, \boldsymbol{e}_3\}$ forming the Cartesian basis. The given velocity (5.55) can be expressed in spherical coordinates as:

$$\boldsymbol{v} = \boldsymbol{n} = \begin{pmatrix} 0 \\ 0 \\ 1 \end{pmatrix}_{(\varphi,\phi,r)}. \tag{A.92}$$

and the surface divergence as

$$\boldsymbol{\nabla}_\Gamma \cdot \boldsymbol{v} = \operatorname{tr}\left(\left(\mathbf{1} - \boldsymbol{n}^{\mathrm{T}} \otimes \boldsymbol{n}\right) \cdot \boldsymbol{\nabla}\boldsymbol{v}\right). \tag{A.93}$$

Hence, once the gradient $\boldsymbol{\nabla}\boldsymbol{v}$ is evaluated, the surface divergence can be obtained in a straightforward calculation. The components of the gradient are the covariant derivatives $v^i|_j$, which are defined as

$$\left[\boldsymbol{\nabla}\boldsymbol{v}\right]^i_{\ j} = v^i|_j = v^i_{,j} + v^k \Gamma^i_{kj}, \tag{A.94}$$

with the *Christoffel symbols of second kind* Γ^i_{kj}. All Christoffel symbols vanish for Cartesian coordinates. For spherical coordinates, however, the Christoffel symbols can be derived [133] as

$$[\Gamma^1_{ij}] = \begin{bmatrix} 0 & \cot\phi & \frac{1}{r} \\ \cot\phi & 0 & 0 \\ \frac{1}{r} & 0 & 0 \end{bmatrix}, \tag{A.95}$$

$$[\Gamma^2_{ij}] = \begin{bmatrix} -\sin\phi\cos\phi & 0 & 0 \\ 0 & 0 & \frac{1}{r} \\ 0 & \frac{1}{r} & 0 \end{bmatrix}, \tag{A.96}$$

$$[\Gamma^3_{ij}] = \begin{bmatrix} -r\sin^2\phi & 0 & 0 \\ 0 & -r & 0 \\ 0 & 0 & 0 \end{bmatrix}. \tag{A.97}$$

With this, one obtains for the velocity gradient

$$[\boldsymbol{\nabla} \boldsymbol{v}]^i_{\ j} = \begin{bmatrix} \frac{1}{r} & 0 & 0 \\ 0 & \frac{1}{r} & 0 \\ 0 & 0 & 0 \end{bmatrix} \tag{A.98}$$

and the surface divergence follows from equation (A.93) as

$$\boldsymbol{\nabla}_\Gamma \cdot \boldsymbol{v} = \frac{2}{r}. \tag{A.99}$$

With $r = t + 1$, one obtains equation (5.56).

Bibliography

[1] https://de.wikipedia.org/wiki/Leichtbauweise, . Accessed: 2016-03-02.

[2] https://en.wikipedia.org/wiki/Limestone, . Accessed: 2016-03-02.

[3] https://en.wikipedia.org/wiki/Wood, . Accessed: 2016-03-02.

[4] R. Ababou, D. McLaughlin, L. Gelhar, and A. Tompson, Numerical simulation of three-dimensional saturated flow in randomly heterogeneous porous media, *Transport in Porous Media* **4**, 549–565, 1989.

[5] B. L. Aboustit, S. H. Advani, and J. K. Lee, Variational principles and finite element simulations for thermo-elastic consolidation, *International Journal for Numerical and Analytical Methods in Geomechanics* **9**, 49–69, 1985.

[6] A. S. Adhikari, J. Chai, and A. R. Dunn, Mechanical load induces a 100-fold increase in the rate of collagen proteolysis by MMP-1, *Journal of the American Chemical Society* **133**, 1686–1689, 2011.

[7] A. S. Adhikari, E. Glassey, and A. R. Dunn, Conformational dynamics accompanying the proteolytic degradation of trimeric collagen I by collagenases, *Journal of the American Chemical Society* **134**, 13259–13265, 2012.

[8] S. M. Allen and J. W. Cahn, A microscopic theory for antiphase boundary motion and its application to antiphase domain coarsening, *Acta Metallurgica* **27**, 1085–1095, 1979.

[9] E. S. Almeida and R. L. Spilker, Finite element formulations for hyperelastic transversely isotropic biphasic soft tissues, *Computer methods in applied Mechanics and Engineering* **151**, 513–538, 1998.

[10] T. Arbogast, L. C. Cowsar, M. F. Wheeler, and I. Yotov, Mixed Finite Element Methods on Nonmatching Multiblock Grids, *SIAM Journal on Numerical Analysis* **37**, 1295–1315, 2000.

[11] T. Arbogast, G. Pencheva, M. F. Wheeler, and I. Yotov, A Multiscale Mortar Mixed Finite Element Method, *Multiscale Modeling & Simulation* **6**, 319–346, 2007.

[12] F. Armero, Formulation and finite element implementation of a multiplicative model of coupled poro-plasticity at finite strains under fully saturated conditions, *Computer Methods in Applied Mechanics and Engineering* **171**, 205–241, 1999.

[13] G. A. Ateshian, S. Maas, and J. A. Weiss, Finite Element Algorithm for Frictionless Contact of Porous Permeable Media Under Finite Deformation and Sliding, *Journal of Biomechanical Engineering* **132**, 2010.

[14] G. A. Ateshian, S. Maas, and J. A. Weiss, Solute transport across a contact interface in deformable porous media, *Journal of Biomechanics* **45**, 1023–1027, 2012.

[15] P. Atkins and J. de Paula, *Atkins' Physical Chemistry*, Oxford University Press, 9 Edition, 2010.

[16] J.-L. Auriault, C. Geindreau, and L. Orgas, Upscaling Forchheimer law, *Transport in Porous Media* **70**, 213–229, 2007.

[17] S. Badia and R. Codina, Stabilized continuous and discontinuous Galerkin techniques for Darcy flow, *Computer Methods in Applied Mechanics and Engineering* **199**, 1654–1667, 2010.

[18] S. Badia, A. Quaini, and A. Quarteroni, Coupling Biot and Navier-Stokes equations for modelling fluid-poroelastic media interaction, *Journal of Computational Physics* **228**, 7986–8014, 2009.

[19] M. T. Balhoff, S. G. Thomas, and M. F. Wheeler, Mortar coupling and upscaling of pore-scale models, *Computational Geosciences* **12**, 15–27, 2008.

[20] D. Balzani, S. Brinkhues, and G. A. Holzapfel, Constitutive framework for the modeling of damage in collagenous soft tissues with application to arterial walls, *Computer Methods in Applied Mechanics and Engineering* **213–216**, 139–151, 2012.

[21] Batchelor, *An introduction to fluid dynamics*, Cambridge University Press, 2000.

[22] G. Bauer, V. Gravemeier, and W. A. Wall, A stabilized finite element method for the numerical simulation of multi-ion transport in electrochemical systems, *Computer Methods in Applied Mechanics and Engineering* **223–224**, 199–210, 2012.

[23] Y. Bazilevs, V. M. Calo, J. A. Cottrell, J. A. Evans, T. J. R. Hughes, S. Lipton, M. A. Scott, and T. W. Sederberg, Isogeometric analysis using T-splines, *Computer Methods in Applied Mechanics and Engineering* **199**, 229–263, 2010.

[24] J. Bear, *Dynamics of fluids in porous media*, Dover Publications, New York, NY, 1988.

[25] J. Bear and Y. Bachmat, *Introduction to Modeling of Transport Phenomena in Porous Media*, Kluwer Academic Publishers, Dordrecht, 1991.

[26] G. S. Beavers and D. D. Joseph, Boundary conditions at a naturally permeable wall, *Journal of Fluid Mechanics* **30**, 197–207, 1967.

[27] T. Belytschko, W. K. Liu, and B. Moran, *Nonlinear finite elements for continua and structures*, Wiley, 2000.

[28] L. S. Bennethum, M. Murad, and J. Cushman, Macroscale thermodynamics and the chemical potential for swelling porous media, *Transport in Porous Media* **39**, 187–225, 2000.

[29] L. Berger, R. Bordas, K. Burrowes, V. Grau, S. Tavener, and D. Kay, A poroelastic model coupled to a fluid network with applications in lung modelling, *International Journal for Numerical Methods in Biomedical Engineering* **32**, 2016.

[30] D. Berk, F. Yuan, M. Leunig, and R. Jain, Fluorescence photobleaching with spatial fourier analysis: measurement of diffusion in light-scattering media, *Biophysical Journal* **65**, 2428 – 2436, 1993.

[31] C. Bertoglio, A. Nagler, M. Ortiz, and W. A. Wall, Detailed fiber modeling and estimation in the heart : a computational framework and examples using real DTMRI data, *submitted*, 2014.

[32] A. P. Bhole, B. P. Flynn, M. Liles, N. Saeidi, C. A. Dimarzio, and J. W. Ruberti, Mechanical strain enhances survivability of collagen micronetworks in the presence of collagenase: implications for load-bearing matrix growth and stability, *Philosophical transactions. Series A, Mathematical, physical, and engineering sciences* **367**, 3339–3362, 2009.

[33] M. A. Biot, Consolidation settlement under a rectangular load distribution, *Journal of Applied Physics* **12**, 426–430, 1941.

[34] M. A. Biot, Theory of elasticity and consolidation for a porous anisotropic solid, *Journal of Applied Physics* **26**, 182–185, 1955.

[35] M. A. Biot, Theory of deformation of a porous viscoelastic anisotropic solid, *Journal of Applied Physics* **27**, 459–467, 1956.

[36] M. A. Biot, General solutions of the equation of elasticity and consolidation for a porous material, *Journal of Applied Mechanics* **78**, 91–96, 1956.

[37] M. A. Biot, Theory of Stability and Consolidation of a Porous Medium Under Initial Stress, *Journal of Mathematics and Mechanics* **12**, 521–542, 1963.

[38] M. A. Biot, General theory of three-dimensional consolidation, *Journal of Applied Physics* **12**, 155–164, 1941.

[39] M. A. Biot, Generalized Theory of Acoustic Propagation in Porous Dissipative Media, *The Journal of the Acoustical Society of America* **34**, 1254–1264, 1962.

[40] J. Bonet and R. D. Wood, *Nonlinear Continuum Mechanics for Finite Element Analysis*, Cambridge University Press, 1997.

[41] J. Booker and C. Savvidou, Consolidation around a spherical heat source, *International Journal of Solids and Structures* **20**, 1079–1090, 1984.

[42] B. P. Boudreau, The diffusive tortuosity of fine-grained unlithified sediments, *Geochimica et Cosmochimica Acta* **60**, 3139–3142, 1996.

[43] F. Brezzi and M. Fortin, *Mixed and hybrid finite element methods*, Springer Series in Computational Mathematics, Springer, New York, NY, 2002.

[44] E. Brivadis, A. Buffa, B. I. Wohlmuth, and L. Wunderlich, Isogeometric mortar methods, *Computer Methods in Applied Mechanics and Engineering* **284**, 292–319, 2015.

[45] P. D. Buhan, X. Chateau, and L. Dormieux, The constitutive equations of finite strain poroelasticity in the light of a micro-macro approach, *European Journal for Mechanics A/Solids* **17**, 909–921, 1998.

[46] M. Bukač, I. Yotov, R. Zakerzadeh, and P. Zunino, Partitioning strategies for the interaction of a fluid with a poroelastic material based on a Nitsche's coupling approach, *Computer Methods in Applied Mechanics and Engineering* **292**, 138–170, 2015.

[47] E. Burman and P. Hansbo, A unified stabilized method for Stokes and Darcy's equations, *Journal of Computational and Applied Mathematics* **198**, 35–51, 2007.

[48] C. Callari and A. Abati, Finite element methods for unsaturated porous solids and their application to dam engineering problems, *Computers & Structures* **87**, 485–501, 2009.

[49] C. Callari and A. Abati, Hyperelastic Multiphase Porous Media with Strain-Dependent Retention Laws, *Transport in Porous Media* **86**, 155–176, 2011.

[50] R. J. Camp, M. Liles, J. Beale, N. Saeidi, B. P. Flynn, E. Moore, S. K. Murthy, and J. W. Ruberti, Molecular Mechanochemistry: Low force switch slows enzymatic cleavage of human type I collagen monomer, *Journal of the American Chemical Society* **133**, 4073–4078, 2011.

[51] P. C. Carman, Fluid flow through granular beds, *Transactions of the Institution of Chemical Engineers* **15**, 155–166, 1937.

[52] J. P. Carter, J. R. Booker, and J. C. Small, The analysis of finite elasto-plastic consolidation, *International Journal for Numerical and Analytical Methods in Geomechanics* **3**, 107–129, 1979.

[53] S. W. Chang and M. J. Buehler, Molecular biomechanics of collagen molecules, *Materials Today* **17**, 70–76, 2014.

[54] D. Chapelle and P. Moireau, General coupling of porous flows and hyperelastic formulations - From thermodynamics principles to energy balance and compatible time schemes, *European Journal of Mechanics - B\Fluids* **46**, 82–96, 2014.

[55] D. Chapelle, J.-F. Gerbeau, J. Sainte-Marie, and I. Vignon-Clementel, A poroelastic model valid in large strains with applications to perfusion in cardiac modeling, *Computational Mechanics* **46**, 91–101, 2009.

[56] Q. Chaudhry, M. Hanke, R. Morgenstern, and K. Dreij, Surface reactions on the cytoplasmatic membranes–Mathematical modeling of reaction and diffusion systems in a cell, *Journal of Computational and Applied Mathematics* **262**, 244–260, 2014.

[57] G. Chavent and J. E. Roberts, A unified physical presentation of mixed, mixed-hybrid finite elements and standard finite difference approximations for the determination of velocities in waterflow problems, *Advances in Water Resources* **14**, 329–348, 1991.

[58] H. Chen and X.-P. Wang, A one-domain approach for modeling and simulation of free fluid over a porous medium, *Journal of Computational Physics* **259**, 650–671, 2014.

[59] J. Choo and R. I. Borja, Stabilized mixed finite elements for deformable porous media with double porosity, *Computer Methods in Applied Mechanics and Engineering* **293**, 131–154, 2015.

[60] J. T. Christian and J. W. Boehmer, Plane strain consolidation by finite elements, *Journal of Soil Mechanics & Foundations Div* **96**, 1435–1457, 1970.

[61] J. Chung and G. M. Hulbert, A Time Inegration Algorithm for Stuctural Dynamics With Improved Numerical Dissipation: The Generalized-α Method, *Journal of Applied Mechanics* **60**, 371–375, 1993.

[62] I. E. Collier, W. Legant, B. Marmer, O. Lubman, S. Saffarian, T. Wakatsuki, E. Elson, and G. I. Goldberg, Diffusion of MMPs on the surface of collagen fibrils: The mobile cell surface - collagen substratum interface, *PLoS ONE* **6**, 1–14, 2011.

[63] M. R. Correa and A. F. D. Loula, Stabilized velocity post-processings for darcy flow in heterogeneous porous media, *Communications in Numerical Methods in Engineering* **23**, 461–489, 2007.

[64] J. A. Cottrell, T. J. R. Hughes, and A. Reali, Studies of refinement and continuity in isogeometric structural analysis, *Computer Methods in Applied Mechanics and Engineering* **196**, 4160–4183, 2007.

[65] O. Coussy, *Mechanics of Porous Continua*, John Wiley and Sons, West Sussex, 1995.

[66] O. Coussy, *Poromechanics*, John Wiley and Sons, West Sussex, 2004.

[67] A. L. G. A. Coutinho, C. M. Dias, J. L. D. Alves, L. Landau, A. F. D. Loula, S. M. C. Malta, R. Castro, and E. L. M. Garcia, Stabilized methods and post-processing techniques for miscible displacements, *Computer Methods in Applied Mechanics and Engineering* **193**, 1421 – 1436, 2004.

[68] S. C. Cowin, Bone poroelasticity, *Journal of Biomechanics* **32**, 217–238, 1999.

[69] S. C. Cowin, The relationship between the elasticity tensor and the fabric tensor, *Mechanics of Materials* **4**, 137–47, 1985.

[70] E. Cukierman, R. Pankov, and K. M. Yamada, Cell interactions with three-dimensional matrices, *Current Opinion in Cell Biology* **14**, 633–639, 2002.

[71] H. Darcy, *Les fontaines publiques de la ville de Dijon*, Dalmont, 1856.

[72] R. de Boer, On the thermodynamics of pressure solution–interaction between chemical and mechanical forces, *Geochimica et Cosmochimica Acta* **41**, 249–256, 1977.

[73] R. de Boer, Development of Porous Media Theories - A Brief Historical Review, *Transport in Porous Media* **9**, 155–164, 1992.

[74] R. de Boer, *Theory of Porous Media: Highlights in Historical Development and Current State*, Springer Berlin Heidelberg, 2012.

[75] I. de Curtis and J. Meldolesi, Cell surface dynamics - how Rho GTPases orchestrate the interplay between the plasma membrane and the cortical cytoskeleton, *Journal of Cell Science* **125**, 4435–4444, 2012.

[76] N. E. Deakin and M. A. J. Chaplain, Mathematical modeling of cancer invasion: the role of membrane-bound matrix metalloproteinases, *Frontiers in oncology* **3**, 1–9, 2013.

[77] J. Deśarnaud, O. Grauby, P. Bromblet, J. M. Vallet, and A. Baronnet, Growth and dissolution of crystal under load: New experimental results on kcl, *Crystal Growth and Design* **13**, 1067–1074, 2013.

[78] V. S. Deshpande, M. Mrksich, R. M. McMeeking, and A. G. Evans, A bio-mechanical model for coupling cell contractility with focal adhesion formation, *Journal of the Mechanics and Physics of Solids* **56**, 1484–1510, 2008.

[79] H.-J. G. Diersch and O. Kolditz, Variable-density flow and transport in porous media: approaches and challenges, *Advances in Water Resources* **25**, 899–944, 2002.

[80] M. Discacciati and A. Quarteroni, Navier-stokes/darcy coupling: modeling, analysis, and numerical approximation, *Revista Matemática Complutense* **22**, 2009.

[81] M. Discacciati, E. Miglio, and A. Quarteroni, Mathematical and numerical models for coupling surface and groundwater flows, *Applied Numerical Mathematics* **43**, 57–74, 2002.

[82] J. Donéa and A. Huerta, *Finite element methods for flow problems*, Chichester : Wiley, 2003.

[83] P. S. Donzelli and R. L. Spilker, A contact finite element formulation tissues for biological soft hydrated, *Computer Methods in Applied Mechanics and Engineering* **153**, 63–79, 1998.

[84] J. J. Douglas, R. E. Ewing, and M. F. Wheeler, The approximation of the pressure by a mixed method in the simulation of miscible displacement, *RAIRO Analyse Numérique/Numerical Analysis* **17**, 17–33, 1983.

[85] L. J. Durlofsky, A Triangle Based Mixed Finite ElementFinite Volume Technique for Modeling Two Phase Flow through Porous Media, *Journal of Computational Physics* **105**, 252–266, 1993.

[86] G. Dziuk and C. M. Elliott, Finite elements on evolving surfaces, *IMA Journal of Numerical Analysis* **27**, 262–292, 2007.

[87] G. Dziuk and C. M. Elliott, Surface finite elements for parabolic equations, *Journal of Computational Mathematics* **25**, 385–407, 2007.

[88] W. Ehlers, Challenges of porous media models in geo- and biomechanical engineering including electro-chemically active polymers and gels, *International Journal of Advances in Engineering Sciences and Applied Mathematics* **1**, 1–24, 2009.

[89] S. Ekbote and Y. Abousleiman, Porochemoelastic Solution for an Inclined Borehole in a Transversely Isotropic Formation, *Journal of Engineering Mechanics* **132**, 754–763, 2006.

[90] R. E. Ewing, R. Lazarov, and Y. Lin, Finite volume element approximations of nonlocal reactive flows in porous media, *Numerical Methods for Partial Differential Equations* **16**, 285–311, 2000.

[91] P. Farah, A.-T. Vuong, W. A. Wall, and A. Popp, Volumetric coupling approaches for multiphysics simulations on non-matching meshes, *International Journal for Numerical Methods in Engineering*, n/a–n/a. doi: 10.1002/nme.5285, 2016.

[92] J. Faulkner, B. X. Hu, S. Kish, and F. Hua, Laboratory analog and numerical study of groundwater flow and solute transport in a karst aquifer with conduit and matrix domains, *Journal of Contaminant Hydrology* **110**, 34–44, 2009.

[93] H. E. Fayed, N. A. Sheikh, and O. Iliev, On Laminar Flow of Non-Newtonian Fluids in Porous Media, *Transport in Porous Media* **111**, 253–264, 2016.

[94] G. R. Fedorchak, A. Kaminski, and J. Lammerding, Cellular mechanosensing: Getting to the nucleus of it all, *Progress in Biophysics and Molecular Biology* **115**, 76–92, 2014.

[95] M. Ferronato, N. Castelletto, and G. Gambolati, A fully coupled 3-D mixed finite element model of Biot consolidation, *Journal of Computational Physics* **229**, 4813–4830, 2010.

[96] J. P. Feser, A. K. Prasad, and S. G. Advani, Experimental characterization of in-plane permeability of gas diffusion layers, *Journal of Power Sources* **162**, 1226–1231, 2006.

[97] S. D. Finley, L.-H. Chu, and A. S. Popel, Computational systems biology approaches to anti-angiogenic cancer therapeutics, *Drug Discovery Today* **20**, 187–197, 2015.

[98] B. P. Flynn, A. P. Bhole, N. Saeidi, M. Liles, C. A. Dimarzio, and J. W. Ruberti, Mechanical strain stabilizes reconstituted collagen fibrils against enzymatic degradation by mammalian collagenase matrix metalloproteinase 8 (MMP-8), *PLoS ONE* **5**, 21–23, 2010.

[99] J. Folkman, Tumor angiogenesis: Therapeutic implications, *New England Journal of Medicine* **285**, 1182–1186, 1971.

[100] P. Forchheimer, Wasserbewegung durch boden, *Z. Ver. Deutsch. Ing* **45**, 1788, 1901.

[101] P. Friedl and K. Wolf, Proteolytic interstitial cell migration: A five-step process, *Cancer and Metastasis Reviews* **28**, 129–135, 2009.

[102] A. Gajo, A general approach to isothermal hyperelastic modelling of saturatued porous media at finite strains with compressible solid constituents, *Proceedings of the Royal Society A: Mathematical, Physical and Engineering Sciences* **466**, 3061–3087, 2010.

[103] A. Gajo and R. Denzer, Finite element modelling of saturated porous media at finite strains under dynamic conditions with compressible constituents, *International Journal for Numerical Methods in Engineering* **85**, 1705–1736, 2011.

[104] A. Gajo and B. Loret, Finite element simulations of chemo-mechanical coupling in elastic-plastic homoionic expansive clays, *Computer Methods in Applied Mechanics and Engineering* **192**, 3489–3530, 2003.

[105] P. Gamnitzer and G. Hofstetter, A cap model for soils featuring a smooth transition from partially to fully saturated state, *PAMM* **13**, 169–170, 2013.

[106] D. Gawin, P. Baggio, and B. A. Schrefler, Coupled heat, water and gas flow in deformable porous media, *International Journal for Numerical Methods in Fluids* **20**, 969–978, 1995.

[107] M. Gee, U. Küttler, and W. Wall, Truly monolithic algebraic multigrid for fluid-structure interaction, *International Journal for Numerical Methods in Engineering* **85**, 987–1016, 2011.

[108] J. Ghaboussi and E. L. Wilson, Flow of compressible fluid in porous elastic media, *International Journal for Numerical Methods in Engineering* **5**, 419–442, 1973.

[109] A. Goharzadeh, A. Khalili, and B. B. Jørgensen, Transition layer thickness at a fluid-porous interface, *Physics of Fluids* **17**, 2005.

[110] B. Goyeau, D. Lhuillier, D. Gobin, and M. G. Velarde, Momentum transport at a fluid-porous interface, *International Journal of Heat and Mass Transfer* **46**, 4071–4081, 2003.

[111] R. A. Granger, *Fluid mechanics*, Dover Publications, 1996.

[112] W. G. Gray and C. T. Miller, Thermodynamically constrained averaging theory approach for modeling flow and transport phenomena in porous medium systems: 5. Single-fluid-phase transport, *Advances in Water Resources* **32**, 681–711, 2009.

[113] W. G. Gray and B. A. Schrefler, Thermodynamic approach to effective stress in partially saturated porous media, *European Journal for Mechanics A/Solids* **20**, 521–538, 2001.

[114] W. G. Gray and C. T. Miller, A generalization of averaging theorems for porous medium analysis, *Advances in Water Resources* **62, Part B**, 227–237, 2013.

[115] W. G. Gray, C. T. Miller, and B. A. Schrefler, Averaging theory for description of environmental problems: What have we learned?, *Advances in Water Resources* **51**, 123–138, 2013.

[116] H. Guo and R. L. Spilker, An augmented Lagrangian finite element formulation for three-dimensional contact of biphasic tissues, *Computer Methods in Biomechanics and Biomedical Engineering* **17**, 1206–1216, 2014.

[117] H. Guo, M. Shah, and R. L. Spilker, A finite element implementation for biphasic contact of hydrated porous media under finite deformation and sliding, *Proceedings of the Institution of Mechanical Engineers. Part H, Journal of engineering in medicine* **228**, 225–236, 2014.

[118] P. Guo, Dependency of Tortuosity and Permeability of Porous Media on Directional Distribution of Pore Voids, *Transport in Porous Media* **95**, 285–303, 2012.

[119] M. Hintermüller, K. Ito, and K. Kunisch, The Primal-Dual Active Set Strategy as a Semismooth Newton Method, *SIAM Journal on Optimization* **13**, 865–888, 2002.

[120] G. A. Holzapfel, *Nonlinear Solid Mechanics*, John Wiley and Sons, West Sussex, 2000.

[121] G. A. Holzapfel and T. C. Gasser, A viscoelastic model for fiber-reinforced composites at finite strains: Continuum basis, computational aspects and applications, *Computer Methods in Applied Mechanics and Engineering* **190**, 4379–4403, 2001.

[122] M. Hori and S. Nemat-Nasser, On two micromechanics theories for determining micro-macro relations in heterogeneous solids, *Mechanics of Materials* **31**, 667–682, 1999.

[123] J. M. Hörmann, C. Bertoglio, A. Nagler, M. R. Pfaller, F. Bourier, H. Martin, I. Deisenhofer, and W. A. Wall, Quantification of left atrial hemodynamic performance for standard ablation strategies: an in silico study Article, *submitted*, 2016.

[124] U. Hornung, *Homogenization and Porous Media*, Springer-Verlag, New York, NY, 1997.

[125] D. Hoshino, N. Koshikawa, T. Suzuki, V. Quaranta, A. M. Weaver, M. Seiki, and K. Ichikawa, Establishment and Validation of Computational Model for MT1-MMP Dependent ECM Degradation and Intervention Strategies, *PLoS Computational Biology* **8**, 2012.

[126] R. Huber and R. Helmig, Multiphase flow in heterogeneous porous media: A classical finite element method versus an implicit pressure-explicit saturation-based mixed finite element-finite volume approach, *International Journal for Numerical Methods in Fluids* **29**, 899–920, 1999.

[127] T. J. R. Hughes, *The Finite Element Method: Linear Static and Dynamic Finite Element Analysis*, Dover Civil and Mechanical Engineering, Dover Publications, 2012.

[128] T. J. R. Hughes, J. A. Cottrell, and Y. Bazilevs, Isogeometric analysis: CAD, finite elements, NURBS, exact geometry and mesh refinement, *Computer Methods in Applied Mechanics and Engineering* **194**, 4135–4195, 2005.

[129] T. J. R. Hughes, A. Reali, and G. Sangalli, Efficient quadrature for NURBS-based isogeometric analysis, *Computer Methods in Applied Mechanics and Engineering* **199**, 301–313, 2010.

[130] J. M. Huyghe and J. D. Janssen, Thermo-Chemo-Electro-Mechanical Formulation of Saturated Charged Porous Solids, *Transport in Porous Media* **34**, 129–141, 1999.

[131] C. T. Hwang, N. R. Morgenstern, and D. W. Murray, On solutions of plane strain consolidation problems by finite element methods, *Canadian Geotechnical Journal* **8**, 109–118, 1971.

[132] F. Irzal, J. Remers, C. V. Verhoosel, and R. de Borst, Isogeometric finite element analysis of poroelasticity, *International Journal for Numerical and Analytical Methods in Geomechanics* **37**, 1891–1907, 2013.

[133] M. Itskov, *Tensor Algebra and Tensor Analysis for Engineers: With Applications to Continuum Mechanics*, Springer Publishing Company, Incorporated, Berlin, Heidelberg, 2nd Edition, 2009.

[134] W. Jäger and A. Mikelić, On the boundary conditions at the contact interface between a porous medium and a free fluid, *Annali della Scuola Normale Superiore di Pisa - Classe di Scienze (4)* **23**, 403–465, 1996.

[135] W. Jäger and A. Mikelić, On the Interface Boundary Condition of Beavers, Joseph, and Saffman, *SIAM Journal on Numerical Analysis* **60**, 1111–1127, 2000.

[136] M. Jakobsen, T. A. Johansen, and C. McCann, The acoustic signature of fluid flow in complex porous media, *Journal of Applied Geophysics* **54**, 219–246, 2003.

[137] K. E. Jansen, C. H. Whiting, and G. M. Hulbert, A Generalized-α Method for Integrating the Filtered Navier-Stokes Equations with a Stabilized Finite Element Method, *Computer Methods in Applied Mechanics and Engineering* **190**, 305–319, 2000.

[138] P. Jenny, S. H. Lee, and H. A. Tchelepi, Adaptive Multiscale Finite-Volume Method For Multiphase Flow And Transport In Porous Media, *Multiscale Modeling and Simulation* **3**, 50–64, 2004.

[139] P. Jenny, S. H. Lee, and H. A. Tchelepi, Adaptive fully implicit multi-scale finite-volume method for multi-phase flow and transport in heterogeneous porous media, *Journal of Computational Physics* **217**, 627–641, 2006.

[140] D. L. Johnson, J. Koplik, and R. Dashen, Theory of dynamic permeability and tortuosity in fluid-saturated porous media, *Journal of Fluid Mechanics* **176**, 379–402, 1987.

[141] H. Jourde, P. Fenart, M. Vinches, S. Pistre, and B. Vayssade, Relationship between the geometrical and structural properties of layered fractured rocks and their effective permeability tensor. A simulation study, *Journal of Hydrology* **337**, 117–132, 2007.

[142] Q. Kang, L. Chen, A. J. Valocchi, and H. S. Viswanathan, Pore-scale study of dissolution-induced changes in permeability and porosity of porous media, *Journal of Hydrology* **517**, 1049–1055, 2014.

[143] E. D. Karagiannis and A. S. Popel, A theoretical model of type I collagen proteolysis by matrix metalloproteinase (MMP) 2 and membrane type 1 MMP in the presence of tissue inhibitor of metalloproteinase 2, *Journal of Biological Chemistry* **279**, 39105–39114, 2004.

[144] E. D. Karagiannis and A. S. Popel, Distinct modes of collagen type I proteolysis by matrix metalloproteinase (MMP) 2 and membrane type I MMP during the migration of a tip endothelial cell: Insights from a computational model, *Journal of Theoretical Biology* **238**, 124–145, 2006.

[145] N. Khalili and B. Loret, An elasto-plastic model for non-isothermal analysis of flow and deformation in unsaturated porous media: Formulation, *International Journal of Solids and Structures* **38**, 8305–8330, 2001.

[146] A. R. Khoei and T. Mohammadnejad, Numerical modeling of multiphase fluid flow in deforming porous media: A comparison between two- and three-phase models for seismic analysis of earth and rockfill dams, *Computers and Geotechnics* **38**, 142–166, 2011.

[147] M.-C. Kim, J. Whisler, Y. R. Silberberg, R. D. Kamm, and H. H. Asada, Cell Invasion Dynamics into a Three Dimensional Extracellular Matrix Fibre Network, *PLOS Computational Biology* **11**, 1–29, 2015.

[148] T. Klöppel, A. Popp, U. Küttler, and W. A. Wall, Fluid-structure interaction for non-conforming interfaces based on a dual mortar formulation, *Computer Methods in Applied Mechanics and Engineering* **200**, 3111–3126, 2011.

[149] O. Kolditz, S. Bauer, N. Böttcher, D. Elsworth, U. J. Görke, C. I. McDermott, C. H. Park, a. K. Singh, J. Taron, and W. Wang, Numerical simulation of two-phase flow in deformable porous media: Application to carbon dioxide storage in the subsurface, *Mathematics and Computers in Simulation* **82**, 1919–1935, 2012.

[150] J. Kozeny, Über kapillare Leitung des Wassers im Boden, *Sitzungsber Akad. Wiss* **136**, 271–306, 1927.

[151] U. Küttler, M. W. Gee, C. Förster, A. Comerford, and W. A. Wall, Coupling strategies for biomedical fluid-structure interaction problems, *International Journal for Numerical Methods in Biomedical Engineering* **26**, 305–321, 2010.

[152] M. Landstorfer and T. Jacob, Mathematical modeling of intercalation batteries at the cell level and beyond, *Chem. Soc. Rev.* **42**, 3234–3252, 2013.

[153] D. Lasseux, A. Ahmadi, and A. A. A. Arani, Two-Phase Inertial Flow in Homogeneous Porous Media: A Theoretical Derivation of a Macroscopic Model, *Transport in Porous Media* **75**, 371–400, 2008.

[154] A. Lauser, C. Hager, R. Helmig, and B. Wohlmuth, A new approach for phase transitions in miscible multi-phase flow in porous media, *Advances in Water Resources* **34**, 957–966, 2011.

[155] W. J. Layton, F. Schieweck, and I. Yotov, Coupling Fluid Flow with Porous Media Flow, *SIAM Journal on Numerical Analysis* **40**, 2195–2218, 2003.

[156] M. Le Bars and M. G. Worster, Interfacial conditions between a pure fluid and a porous medium: implications for binary alloy solidification, *Journal of Fluid Mechanics* **550**, 149–173, 2006.

[157] X. Lei, H. Wong, A. Fabbri, A. Limam, and Y. Cheng, A thermo-chemo-electro-mechanical framework of unsaturated expansive clays, *Computers and Geotechnics* **62**, 175–192, 2014.

[158] R. W. Lewis and B. A. Schrefler, *The finite element method in the deformation and consolidation of porous media*, John Wiley and Sons, Chichester, 1987.

[159] R. W. Lewis, G. K. Roberts, and O. C. Zienkiewicz, A non-linear flow and deformation analysis of consolidation problems, *Numerical methods in geomechanics* **2**, 1106–1118, 1976.

[160] R. W. Lewis, C. E. Majorana, and B. A. Schrefler, A coupled finite element model for the consolidation of nonisothermal elastoplastic porous media, *Transport in Porous Media* **1**, 155–178, 1986.

[161] H. Lin, D. O. Clegg, and R. Lal, Imaging real-time proteolysis of single collagen I molecules with an atomic force microscope, *Biochemistry* **38**, 9956–9963, 1999.

[162] H. Liu, P. R. Patil, and U. Narusawa, On Darcy-Brinkman equation: Viscous flow between two parallel plates packed with regular square arrays of cylinders, *Entropy*, 118–131, 2007.

[163] L. Luquot and P. Gouze, Experimental determination of porosity and permeability changes induced by injection of CO2 into carbonate rocks, *Chemical Geology* **265**, 148–159, 2009.

[164] N. Martys, D. P. Bentz, and E. J. Garboczi, Computer simulation study of the effective viscosity in brinkmans equation, *Physics of Fluids* **6**, 1434–1439, 1994.

[165] Y. J. Masson and S. R. Pride, On the correlation between material structure and seismic attenuation anisotropy in porous media, *Journal of Geophysical Research: Solid Earth* **119**, 2848–2870, 2014.

[166] A. Masud and T. J. R. Hughes, A stabilized mixed finite element method for Darcy flow, *Computer Methods in Applied Mechanics and Engineering* **191**, 4341–4370, 2002.

[167] P. J. Matuszyk and L. F. Demkowicz, Solution of coupled poroelastic/acoustic/elastic wave propagation problems using automatic -adaptivity, *Computer Methods in Applied Mechanics and Engineering* **281**, 54–80, 2014.

[168] M. Mayr, T. Klöppel, W. A. Wall, and M. W. Gee, A temporal consistent monolithic approach to fluid-structure interaction enabling single field predictors, *SIAM Journal on Scientific Computing* **37**, B30–B59, 2015.

[169] N. Mendes, P. Philippi, and R. Lamberts, A new mathematical method to solve highly coupled equations of heat and mass transfer in porous media, *International Journal of Heat and Mass Transfer* **45**, 509–518, 2002.

[170] E. Miglio, A. Quarteroni, and F. Saleri, Coupling of free surface and groundwater flows, *Computers & Fluids* **32**, 73–83, 2003.

[171] C. A. Miles and M. Ghelashvili, Polymer-in-a-box mechanism for the thermal stabilization of collagen molecules in fibers, *Biophysical Journal* **76**, 3243–3252, 1999.

[172] M. Minale, Modelling the flow of a second order fluid through and over a porous medium using the volume averages. I. The generalized Brinkmans equation, *Physics of Fluids* **28**, 023102, 2016.

[173] D. Miranda, C. M. Costa, and S. Lanceros-Mendez, Lithium ion rechargeable batteries: State of the art and future needs of microscopic theoretical models and simulations, *Journal of Electroanalytical Chemistry* **739**, 97–110, 2015.

[174] M. R. K. Mofrad, Rheology of the cytoskeleton, *Annual Review of Fluid Mechanics* **41**, 433–453, 2009.

[175] K. Mosthaf, K. Baber, B. Flemisch, R. Helmig, A. Leijnse, I. Rybak, and B. Wohlmuth, A coupling concept for two-phase compositional porous-medium and single-phase compositional free flow, *Water Resources Research* **47**, 2011.

[176] S. Multon, A. Sellier, and B. Perrin, Numerical analysis of frost effects in porous media. benefits and limits of the finite element poroelasticity formulation, *International Journal for Numerical and Analytical Methods in Geomechanics* **36**, 438–458, 2012.

[177] K. B. Nakshatrala, D. Z. Turner, K. D. Hjelmstad, and A. Masud, A stabilized mixed finite element method for Darcy flow based on a multiscale decomposition of the solution, *Computer Methods in Applied Mechanics and Engineering* **195**, 4036–4049, 2006.

[178] D. Nemec and J. Levec, Flow through packed bed reactors: 1.Single-phase flow, *Chemical Engineering Science* **60**, 6947–6957, 2005.

[179] D. A. Nield and A. Bejan, *Convection in Porous Media*, Springer-Verlag, New York, NY, 1998.

[180] I. L. Novak and B. M. Slepchenko, A conservative algorithm for parabolic problems in domains with moving boundaries, *Journal of Computational Physics* **270**, 203–213, 2014.

[181] I. L. Novak, F. Gao, Y.-S. Choi, R. Diana, J. C. Schaff, and B. M. Slepchenko, Diffusion on a Curved Surface Coupled to Diffusion in the Volume: Application to Cell Biology, *Journal of Computational Physics* **226**, 1271–1290, 2007.

[182] J. A. Ochoa-Tapia and S. Whitaker, Momentum transfer at the boundary between a porous medium and a homogeneous fluid – I. Theoretical development, *International Journal of Heat and Mass Transfer* **38**, 2635–2646, 1995.

[183] H. Okabe and M. J. Blunt, Prediction of permeability for porous media reconstructed using multiple-point statistics, *Phys. Rev. E* **70**, 066135, 2004.

[184] K. J. Painter, Modelling cell migration strategies in the extracellular matrix, *Journal of Mathematical Biology* **58**, 511–543, 2009.

[185] Y. A. N. Pan and R. N. Horne, Generalized Macroscopic Models for Fluid Flow in Deformable Porous Media I : Theories, *Transport in Porous Media* **45**, 1–27, 2001.

[186] L. E. Payne and B. Straughan, Analysis of the boundary condition at the interface between a viscous fluid and a porous medium and related modelling questions, *Journal de Mathématiques Pures et Appliquées* **77**, 317–354, 1998.

[187] J. A. Pedersen, S. Lichter, and M. A. Swartz, Cells in 3D matrices under interstitial flow: Effects of extracellular matrix alignment on cell shear stress and drag forces, *Journal of Biomechanics* **43**, 900–905, 2010.

[188] S. R. Peyton, C. M. Ghajar, C. B. Khatiwala, and A. J. Putnam, The emergence of ECM mechanics and cytoskeletal tension as important regulators of cell function, *Cell Biochemistry and Biophysics* **47**, 300–320, 2007.

[189] P. J. Phillips and M. F. Wheeler, Overcoming the problem of locking in linear elasticity and poroelasticity: An heuristic approach, *Computational Geosciences* **13**, 5–12, 2009.

[190] L. Piegl and W. Tiller, *The NURBS Book*, Springer, New York, 2 Edition, 1997.

[191] A. Popp, M. W. Gee, and W. A. Wall, A finite deformation mortar contact formulation using a primal-dual active set strategy, *International Journal for Numerical Methods in Engineering* **79**, 1354–1391, 2009.

[192] A. Popp, M. Gitterle, M. W. Gee, and W. A. Wall, A dual mortar approach for 3D finite deformation contact with consistent linearization, *International Journal for Numerical Methods in Engineering* **83**, 1428–1465, 2010.

[193] A. Popp, B. I. Wohlmuth, M. W. Gee, and W. A. Wall, Dual quadratic mortar finite element methods for 3D finite deformation contact, *SIAM Journal on Scientific Computing* **34**, B421–B446, 2012.

[194] J. H. Prevost, Nonlinear transient phenomena in saturated porous media, *Computer Methods in Applied Mechanics and Engineering* **30**, 3–18, 1982.

[195] J. H. Prevost, Implicit-explicit schemes for nonlinear consolidation, *Computer Methods in Applied Mechanics and Engineering* **39**, 225–239, 1983.

[196] J. H. Prevost, Wave propagation in fluid-saturated porous media: An efficient finite element procedure, *International Journal of Soil Dynamics and Earthquake Engineering* **4**, 183–202, 1985.

[197] M. A. Puso and T. A. Laursen, Mesh tying on curved interfaces in 3D, *Engineering Computations* **20**, 305–319, 2003.

[198] M. A. Puso, A 3D mortar method for solid mechanics, *International Journal for Numerical Methods in Engineering* **59**, 315–336, 2004.

[199] C. Z. Qin and S. M. Hassanizadeh, Multiphase flow through multilayers of thin porous media: General balance equations and constitutive relationships for a solidgasliquid threephase system, *International Journal of Heat and Mass Transfer* **70**, 693–708, 2014.

[200] A. Quarteroni, M. Tuveri, and A. Veneziani, Computational vascular fluid dynamics: problems, models and methods, *Computing and Visualization in Science* **2**, 163–197, 2014.

[201] A. D. Rauch, A.-T. Vuong, and W. A. Wall, A Computational Multiphysics Framework Covering Comprehensively the Mesenchymal Cell Migration Cycle, *in preparation*, 2016.

[202] A. D. Rauch. Kopplungskonzepte und Finite Elemente Formulierung zur Interaktion freier Strömungen mit gesättigten poroelastischen Medien. Diploma thesis, Technical University of Munich, 2013.

[203] P.-A. Raviart and J.-M. Thomas, A mixed finite element method for 2-nd order elliptic problems, In *Mathematical aspects of finite element methods*, pages 292–315, Springer, 1977.

[204] C. Rawal and A. Ghassemi, A reactive thermo-poroelastic analysis of water injection into an enhanced geothermal reservoir, *Geothermics* **50**, 10–23, 2014.

[205] D. F. Rogers, *An Introduction to NURBS: With Historical Perspective*, The Morgan Kaufmann Series in Computer Graphics, Elsevier Science, 2000.

[206] T. Roose, S. Chapman, and P. Maini, Mathematical models of avascular tumor growth, *SIAM Review* **49**, 179–208, 2007.

[207] S. Rosenberg, *The Laplacian on a Riemannian Manifold: An Introduction to Analysis on Manifolds*, EBSCO ebook academic collection, Cambridge University Press, 1997.

[208] C. J. Roth, A. Ehrl, T. Becher, I. Frerichs, J. Schittny, N. Weller, and W. A. Wall, Correlation between alveolar ventilation and electrical properties of lung parenchyma, *Physiological Measurement* **36**, 2015.

[209] J. W. Ruberti and N. J. Hallab, Strain-controlled enzymatic cleavage of collagen in loaded matrix, *Biochemical and Biophysical Research Communications* **336**, 483–489, 2005.

[210] I. Rybak, W. G. Gray, and C. Miller, Modeling two-fluid-phase flow and species transport in porous media, *Journal of Hydrology* **521**, 565–581, 2015.

[211] Y. Saad and M. H. Schultz, GMRES: A Generalized Minimal Residual Algorithm for Solving Nonsymmetric Linear Systems, *SIAM Journal on Scientific and Statistical Computing* **7**, 856–869, 1986.

[212] H. Sabetamal, M. Nazem, S. W. Sloan, and J. P. Carter, Frictionless contact formulation for dynamic analysis of nonlinear saturated porous media based on the mortar method, *International Journal for Numerical and Analytical Methods in Geomechanics* **40**, 25–61, 2016.

[213] M. Sahimi, G. R. Gavalas, and T. T. Tsotsis, Statistical and continuum models of fluid-solid reactions in porous media, *Chemical Engineering Science* **45**, 1443 – 1502, 1990.

[214] E. Sanchez-Palencia, *Non-homogeneous media and vibration theory*, Springer-Verlag, Berlin, 1980.

[215] I. F. Sbalzarini, A. Hayer, A. Helenius, and P. Koumoutsakos, Simulations of (an)isotropic diffusion on curved biological surfaces, *Biophysical Journal* **90**, 878–885, 2006.

[216] R. L. Schiffman, A. T. Chen, and J. C. Jordan, An analysis of consolidation theories, *Journal of Soil Mechanics & Foundations Div* **95**, 285–312, 1969.

[217] B. A. Schrefler, Mechanics and thermodynamics of saturated/unsaturated porous materials and quantitative solutions, *Applied Mechanics Reviews* **55**, 351, 2002.

[218] B. A. Schrefler, Multiphase flow in deforming porous material, *International Journal for Numerical Methods in Engineering* **60**, 27–50, 2004.

[219] B. A. Schrefler and A. Scotta, A fully coupled dynamic model for two-phase fluid flow in deformable porous media, *Computer Methods in Applied Mechanics and Engineering*, 3223–3246, 2001.

[220] L. Schreyer-Bennethum, Theory of flow and deformation of swelling porous materials at the macroscale, *Computers and Geotechnics* **34**, 267–278, 2007.

[221] P. Schwartz, D. Adalsteinsson, P. Colella, A. P. Arkin, and M. Onsum, Numerical computation of diffusion on a surface, *Proceedings of the National Academy of Sciences of the United States of America* **102**, 11151–11156, 2005.

[222] G. Sciumè, W. G. Gray, M. Ferrari, P. Decuzzi, and B. A. Schrefler, On Computational Modeling in Tumor Growth, *Archives of Computational Methods in Engineering* **20**, 327–352, 2013.

[223] G. Sciumè, W. G. Gray, F. Hussain, M. Ferrari, P. Decuzzi, and B. A. Schrefler, Three phase flow dynamics in tumor growth, *Computational Mechanics* **53**, 465–484, 2014.

[224] G. Sciumè, R. Santagiuliana, M. Ferrari, P. Decuzzi, and B. A. Schrefler, A tumor growth model with deformable ECM, *Physical Biology* **11**, 2014.

[225] A. Seitz, P. Farah, J. Kremheller, B. I. Wohlmuth, W. A. Wall, and A. Popp, Isogeometric dual mortar methods for computational contact mechanics, *Computer Methods in Applied Mechanics and Engineering* **301**, 259–280, 2016.

[226] Z. L. Shen, H. Kahn, R. Ballarini, and S. J. Eppell, Viscoelastic Properties of Isolated Collagen Fibrils, *Biophysical Journal* **100**, 3008–3015, 2011.

[227] J. Small, J. Booker, and E. Davis, Elasto-plastic consolidation of soil, *International Journal of Solids and Structures* **12**, 431–448, 1976.

[228] T. Sochi, Non-Newtonian flow in porous media, *Polymer* **51**, 5007–5023, 2010.

[229] X. Song and R. I. Borja, Mathematical framework for unsaturated flow in the finite deformation range, *International Journal for Numerical Methods in Engineering* **97**, 658–682, 2014.

[230] W. Strychalski, C. A. Copos, O. L. Lewis, and R. D. Guy, A poroelastic immersed boundary method with applications to cell biology, *Journal of Computational Physics* **282**, 77–97, 2015.

[231] J. Taron, D. Elsworth, and K. B. Min, Numerical simulation of thermal-hydrologic-mechanical-chemical processes in deformable, fractured porous media, *International Journal of Rock Mechanics and Mining Sciences* **46**, 842–854, 2009.

[232] R. L. Taylor, J. C. Simo, O. C. Zienkiewicz, and A. C. H. Chan, The patch test–a condition for assessing FEM convergence, *International Journal for Numerical Methods in Engineering* **22**, 39–62, 1986.

[233] K. Terzaghi, Die Berechnung der Durchlässigkeitsziffer des Tones aus dem Verlauf der hydrodynamischen Spannungserscheinungen, *Ak. der Wissenschaften in Wien, Sitzungsberichte mathematisch-naturwissenschaftliche Klasse* **132**, 125–138, 1923.

[234] K. Terzaghi, *Theoretical soil mechanics*, J. Wiley and Sons, inc, 1943.

[235] M. M. Tomadakis, Viscous Permeability of Random Fiber Structures: Comparison of Electrical and Diffusional Estimates with Experimental and Analytical Results, *Journal of Composite Materials* **39**, 163–188, 2005.

[236] A. R. Tzafriri, M. Bercovier, and H. Parnas, Reaction diffusion model of the enzymatic erosion of insoluble fibrillar matrices, *Biophysical Journal* **83**, 776–793, 2002.

[237] K. Vafai and S. J. Kim, On the limitations of the Brinkman-Forchheimer-extended Darcy equation, *International Journal of Heat and Fluid Flow* **16**, 11–15, 1995.

[238] F. J. Valdés-Parada, J. Alvarez-Ramírez, B. Goyeau, and J. A. Ochoa-Tapia, Computation of jump coefficients for momentum transfer between a porous medium and a fluid using a closed generalized transfer equation, *Transport in Porous Media* **78**, 439–457, 2009.

[239] F. J. Valdes-Parada, J. A. Ochoa-Tapia, and J. Alvarez-Ramírez, Validity of the permeability Carman-Kozeny equation: A volume averaging approach, *Physica A: Statistical Mechanics and its Applications* **388**, 789–798, 2009.

[240] F. Verdugo and W. A. Wall, Unified framework for the efficient solution of n-field coupled problems with monolithic schemes, *arXiv preprint arXiv:1605.01522 [math.NA]*, 2016.

[241] F. J. Vernerey and M. Farsad, A constrained mixture approach to mechano-sensing and force generation in contractile cells, *Journal of the Mechanical Behavior of Biomedical Materials* **4**, 1683–1699, 2011.

[242] A. Verruijt, *Computational geomechanics*, Volume 7, Springer Science & Business Media, Dordrecht, 1995.

[243] A.-T. Vuong, L. Yoshihara, and W. A. Wall, A general approach for modeling interacting flow through porous media under finite deformations, *Computer Methods in Applied Mechanics and Engineering* **283**, 1240–1259, 2015.

[244] A.-T. Vuong, C. Ager, and W. Wall, Two finite element approaches for Darcy and Darcy-Brinkman flow through deformable porous media–Mixed method vs. NURBS based (isogeometric) continuity, *Computer Methods in Applied Mechanics and Engineering* **305**, 634–657, 2016.

[245] A.-T. Vuong, A. D. Rauch, and W. A. Wall, A Computational Model for Coupled Surface-Volume Scalar Transport within a Deformable Porous Medium with Application to Pericellular Proteolysis in Tissue Mechanics, *submitted*, 2016.

[246] J. Wan, *Stabilized Finite Element Methods for Coupled Geomechanics and Multiphase Flow*, PhD thesis, Stanford University, 2002.

[247] T. Weinstein and L. Schreyer-Bennethum, On the derivation of the transport equation for swelling porous materials with finite deformation, *International Journal of Solids and Structures* **44**, 1408–1422, 2006.

[248] M. F. Wheeler, J. A. Wheeler, and M. Peszynska, A Distributed Computing Portal for Coupling Multi-Physics And Multiple Domains In Porous Media, *Computational Methods in Water Resources* **12**, 167–174, 2000.

[249] S. Whitaker, Flow in porous media III: Deformable media, *Transport in Porous Media* **1**, 127–154, 1986.

[250] S. Whitaker, Flow in porous media II: The governing equations for immiscible, two-phase flow, *Transport in Porous Media* **1**, 105–125, 1986.

[251] S. Whitaker, Flow in porous media I: A theoretical derivation of Darcy's law, *Transport in Porous Media* **1**, 3–25, 1986.

[252] S. Whitaker, The Forchheimer equation: A theoretical development, *Transport in Porous Media* **25**, 27–61, 1996.

[253] S. Whitaker, Flow in porous media III: Deformable media, *Transport in Porous Media* **1**, 127–154, 1986.

[254] H. Willmann. Finite Element Formulation for Mesh-Tying and Contact Problems in Nonlinear Poroelasticity. Master's thesis, Technical University of Munich, 2015.

[255] B. I. Wohlmuth, A Mortar Finite Element Method Using Dual Spaces for the Lagrange Multiplier, *SIAM Journal on Numerical Analysis* **38**, 989–1012, 2000.

[256] B. I. Wohlmuth, Variationally consistent discretization schemes and numerical algorithms for contact problems, *Acta Numerica* **20**, 569–734, 2011.

[257] K. Wolf and P. Friedl, Extracellular matrix determinants of proteolytic and non-proteolytic cell migration, *Trends in Cell Biology* **21**, 736–744, 2011.

[258] K. Wolf, M. te Lindert, M. Krause, S. Alexander, J. te Riet, A. L. Willis, R. M. Hoffman, C. G. Figdor, S. J. Weiss, and P. Friedl, Physical limits of cell migration: Control by ECM space and nuclear deformation and tuning by proteolysis and traction force, *Journal of Cell Biology* **201**, 1069–1084, 2013.

[259] Y.-S. Wu and G. Qin, A Generalized Numerical Approach for Modeling Multiphase Flow and Transport in Fractured Porous Media, *Communications in Computational Physics* **6**, 85–108, 2009.

[260] K. E.-K. Wyatt, J. W. Bourne, and P. A. Torzilli, Deformation-dependent enzyme mechanokinetic cleavage of type I collagen, *Journal of biomechanical engineering* **131**, 051004, 2009.

[261] T. Yang and R. L. Spilker, A Lagrange multiplier mixed finite element formulation for three-dimensional contact of biphasic tissues, *Journal of Biomechanical Engineering* **129**, 457–71, 2007.

[262] Y. Yokoo, K. Yamagata, and H. Nagaoka, Finite element method applied to biot's consolidation theory, *Soils and Foundations* **11**, 29–46, 1971.

[263] L. You and L. Hongtan, A two-phase flow and transport model for the cathode of PEM fuel cells, *International Journal of Heat and Mass Transfer* **45**, 2277–2287, 2002.

[264] O. C. Zienkiewicz, Basic formulation of static and dynamic behaviours of soil and other porous media, *Applied Mathematics and Mechanics* **3**, 457–468, 1982.

[265] O. C. Zienkiewicz and T. Shiomi, Dynamic behaviour of saturated porous media; the generalized biot formulation and its numerical solution, *International Journal for Numerical and Analytical Methods in Geomechanics* **8**, 71–96, 1984.

[266] O. C. Zienkiewicz, C. Humpheson, and R. W. Lewis, A unified approach to soil mechanics problems (including plasticity and viscoplasticity), *Finite elements in geomechanics* **8**, 151–178, 1977.

[267] O. C. Zienkiewicz, S. Qu, R. L. Taylor, and S. Nakazawa, The patch test for mixed formulations, *International Journal for Numerical Methods in Engineering* **23**, 1873–1883, 1986.

[268] O. C. Zienkiewicz, D. K. Paul, and A. H. C. Chan, Unconditionally stable staggered solution procedure for soil-pore fluid interaction problems, *International Journal for Numerical Methods in Engineering* **26**, 1039–1055, 1988.

[269] O. C. Zienkiewicz, R. L. Taylor, and J. Z. Zhu, *The Finite Element Method: Its Basis and Fundamentals*, Butterworth-Heinemann, Oxford, seventh Edition, 2013.

[270] O. C. Zienkiewicz, R. L. Taylor, and D. Fox, *The Finite Element Method for Solid and Structural Mechanics*, Butterworth-Heinemann, Oxford, seventh Edition, 2014.

[271] O. C. Zienkiewicz, R. L. Taylor, and P. Nithiarasu, *The Finite Element Method for Fluid Dynamics*, Butterworth-Heinemann, Oxford, seventh Edition, 2014.

Verzeichnis der betreuten Studienarbeiten

Im Rahmen dieser Dissertation entstanden am Lehrstuhl für Numerische Mechanik (LNM) in den Jahren von 2011 bis 2016 unter wesentlicher wissenschaftlicher, fachlicher und inhaltlicher Anleitung des Autors die im Folgenden aufgeführten studentischen Arbeiten. Der Autor dankt allen Sudierenden für Ihr Engagement bei der Unterstützung dieser wissenschaftlichen Arbeit.

Studierende(r)	**Studienarbeit**
Jasper Rieser	*Wachstumsmodell zur Finite-Elemente-Simulation biologischer Materialien*, Bachelorarbeit, 2013
Andreas Rauch	*Kopplungskonzepte und Finite Elemente Formulierung zur Interaktion freier Strömungen mit gesättigten poroelastischen Medien*, Diplomarbeit, 2013, eingeflossen in Abschnitt 5.2
Jonas Eichinger	*Nichtlineares, anisotropes und aktives Materialmodell für die lebende tierische Zelle*, Semesterarbeit, 2014
Johannes Hermann	*Enhancement of Established Material Models for Cells Towards Physiological Migration Patterns by Incorporating Observed Microscale Processes*, Master Thesis, 2015
Harald Willmann	*Finite Element Formulation for Mesh-tying and Contact Problems in Nonlinear Poroelasticity*, Master Thesis, 2015, eingeflossen in Abschnitt 5.1
Raphael Gebhart	*Mixed finite element approach based on dual shape functions for nearly incompressible elasticity*, Bachelorarbeit, 2015
Marc Kornmesser	*Finite Elemente Simulation proteolytischer Prozesse innerhalb der extrazellulären Matrix*, Bachelorarbeit, 2015
Roxana Künzel	*FEM Simulation of a Model for the Proteolytic Step in Mesenchymal Cell Migration*, Semesterarbeit, 2016
Suhaib Koji Baydoun	*Finite Element Formulation and Partitioned Solution of Elasto-Hydrodynamic Lubrication Problems*, Masterarbeit, 2016
Anton Shu	*The Hu-Washizu approach for nonlinear finite elements based on dual shape functions for nearly incompressible elasticity*, Semesterarbeit, 2016
Naeimeh Hosseini	*A Computational Finite Element Model for Anisotropy in Extracellular Matrices*, Masterarbeit, 2016
Philip Bilfinger	*Numerical stability analysis of transport problems for interface-coupled discretizations*, Bachelorarbeit 2016